



Chirality in the ^{13}Nd and ^{13}Nd nuclei

Bingfeng Lv

► To cite this version:

Bingfeng Lv. Chirality in the ^{13}Nd and ^{13}Nd nuclei. Nuclear Experiment [nucl-ex]. Université Paris Saclay (COmUE), 2019. English. NNT : 2019SACLS353 . tel-02347000

HAL Id: tel-02347000

<https://theses.hal.science/tel-02347000>

Submitted on 5 Nov 2019

HAL is a multi-disciplinary open access archive for the deposit and dissemination of scientific research documents, whether they are published or not. The documents may come from teaching and research institutions in France or abroad, or from public or private research centers.

L'archive ouverte pluridisciplinaire **HAL**, est destinée au dépôt et à la diffusion de documents scientifiques de niveau recherche, publiés ou non, émanant des établissements d'enseignement et de recherche français ou étrangers, des laboratoires publics ou privés.

Chirality in the ^{136}Nd and ^{135}Nd nuclei

Thèse de doctorat de l'Université Paris-Saclay
préparée à l'Université Paris-Sud

École doctorale n°576 particules hadrons énergie et noyau: instrumentation, image,
cosmos et simulation (PHENIICS)
Spécialité de doctorat : Structure et réactions nucléaires

Thèse présentée et soutenue à Orsay, le 11 octobre 2019, par

BINGFENG LV

Composition du Jury :

MME AMEL KORICHI Directrice de Recherche, CSNSM	Présidente
MME ELENA LAWRIE Professeure associée, iThemba Labs, South Africa	Rapporteur
MME NADINE REDON Directrice de Recherche, IP2I Lyon	Rapporteur
M. ZHONG LIU Professeur des Universités, Chinese Academy of Sciences, IMP, China	Examineur
M. COSTEL PETRACHE Professeur des Universités, Paris-Sud/Paris Saclay	Directeur de thèse

Acknowledgements

I would like to express my sincere gratitude to those who helped me and shared their experiences during my PhD. The work presented here would have been impossible to conclude without their guidance and assistance.

First and foremost, I would like to express my sincere gratitude to my supervisor Professor Costel Petrache, for his systematic teaching and training me in experimental nuclear structure research. It is my great honor to have a supervisor who is so famous and highly respected in the nuclear physics. Also, I want to express my deepest grateful to him for his take care of me, and all the things he has done for me even if he never told me. In addition, for sure, his personal qualities, like work hard, great passion for research, explorative spirit, will influence me more in the future. For me, he is not only a mentor in my work, but also in my life.

I would like to also thank my CSNSM colleagues. Alain Astier help will never be forgotten due to his selfless shared many data analysis skills used in present work. I feel very lucky that I had a very nice officemate, Etienne Dupont, who assisted me a lot in my daily life in France. I want to say "Merci beaucoup, monsieur Etienne Dupont ". I also would like to thank Amel Korichi, Araceli Lopez-Martens, Jérémie Jacob, Nicolas Dosme and all the other colleagues in CSNSM for their assistance.

I also thank the nuclear structure group of IMP, Lanzhou, in particular, Xiaohong Zhou, my supervisor, also Guo Song and Jianguo Wang for initiating me in experimental nuclear physics research. In particular, I would like to thank Dr. Guo Song for establishing the collaboration between Professor Costel Petrache group and the nuclear structure group in IMP, which provided me the opportunity to do my PhD in CSNSM, Orsay, France.

I also would like to thank another one of my supervisors, Wenhui Long from Lanzhou University for his continue support and very wisdom advice for my future career.

I would like to thank all our collaborators, in particular to Prof. Meng Jie and Dr. Qibo Chen for their excellent theoretical work made for the interpretation of the present data.

I am thankful to the jury members of my PhD defense, Dr. Amel Korichi (CSNSM, Orsay), Dr. Elena Lawrie (iThemba Labs, South Africa), Dr. Nadine Redon (IP2I Lyon), and Dr. Zhong Liu (IMP, Lanzhou) for having spent their valuable time to evaluate my PhD work and read my thesis, also to give suggestions and comments on my manuscript.

I would like to also thank the financial support of China Scholarship Council (CSC) and CSNSM, CNRS.

Finally, I would like to express my heartfelt gratitude to my parents for their love, care and constant spiritual support in my 22 years student career. Also, thanks to my girl friend Cui Xiaoyun for her understanding, accompany and endless encouragement.

Contents

Acknowledgements	3
1 Introduction	17
1.1 Chirality	18
1.1.1 Nuclear Chirality	19
1.1.2 Multiple chiral doublets ($M_{\chi D}$)	20
1.2 Fingerprints of the chiral bands	21
1.2.1 Energy spectra	21
1.2.2 Electromagnetic transitions rates	21
1.2.3 Other fingerprints	22
1.3 Motivation of this study	23
1.4 Outline of thesis	23
2 Theoretical background	25
2.1 Liquid drop model	25
2.2 The shell model	26
2.3 The deformed shell model	28
2.3.1 Deformed parameters	28
2.3.2 The Nilsson model	32
2.4 Particle-rotor model	37
2.4.1 Strong coupling	38
2.4.2 The decoupling limit	38
2.4.3 Four- j shells particle-rotor model	39
2.5 Cranked Nilsson-Strutinsky model	41
2.5.1 Cranking model	41
2.5.2 The rotating liquid drop model	45
2.5.3 The configuration-dependent CNS approach	46
2.6 Tilted axis cranking covariant density functional theory	47
2.6.1 Tilted axis cranking	47
2.6.2 TAC-CDFT	50
2.7 Transition probabilities	52

3	Experimental techniques	53
3.1	Heavy-ion fusion-evaporation reactions	53
3.2	Interaction mechanisms of the γ -rays with matter	55
3.2.1	Photoelectric absorption	55
3.2.2	Compton scattering	55
3.2.3	Pair production	56
3.3	High-purity Germanium γ -ray detector	56
3.4	The JUROGAM II array	58
3.5	The RITU gas-filled recoil separator	59
3.6	The GREAT spectrometer	61
3.7	Total-Data Readout (TDR)	62
4	Experimental details and processing of the data	65
4.1	Experimental details	65
4.2	Data processing	65
4.2.1	Energy calibrations and gain matching	65
4.2.2	Efficiency calibrations for Ge detectors	66
4.2.3	Doppler shift correction	67
4.2.4	Add-back for the clover detectors	67
4.2.5	Spin and parity assignments	68
5	Towards complete spectroscopy of ^{136}Nd	71
5.1	Experimental results and level scheme	71
5.1.1	The low-spin γ band and bands N1, N2	72
5.1.2	The medium-spin bands L and T	73
5.1.3	The dipole bands	75
5.1.4	The highly-deformed bands	81
5.2	Discussion	98
5.2.1	$M\chi D$ interpretation of the chiral bands within TAC- CDFT framework	98
5.2.2	$M\chi D$ interpretation of the chiral bands within PRM framework	103
5.2.3	CNS interpretation of all rotational bands	108
6	Evidence of $M\chi D$ in the odd-A nucleus ^{135}Nd	123
6.1	Introduction	123
6.2	Experimental results and level scheme	124
6.3	Discussion	127
7	Search for long-lived isomeric states	139
7.1	Introduction	139
7.2	The recoil-decay tagging technique	139
7.3	Results of the focal plane	140

Synthèse	145
Conclusions and Outlook	147
Appendix A JUROGAM II detector angles	149

List of Figures

1.1	Left- and right-handed chiral systems for a triaxial odd-odd nucleus. The symbols \vec{J} , \vec{R} , \vec{j}_ν , and \vec{j}_π denote respectively the total angular momentum, the angular momenta of the core, of the neutron and of the proton, respectively. Figure adopted from Ref. [1].	19
1.2	The nuclides with chiral doublet bands (red circles) and M χ D (blue pentagons) observed in the nuclear chart. The black squares represent stable nuclides. Figure adopted from Ref. [2].	22
2.1	Schematic nuclear levels calculated by the shell model including the l^2 and $\vec{l} \cdot \vec{s}$ terms. Figure adapted from Ref. [3].	29
2.2	The lowest four vibrations of a nucleus. The dashed lines show the spherical equilibrium shape and the solid lines show an instantaneous view of the vibrating surface. Figure adapted from Ref. [4].	30
2.3	Plot of the Eq. 2.12, for $k=1, 2, 3$, corresponding to the increase in the axis lengths in the x , y , and z directions. Figure adopted from Ref. [5].	31
2.4	Schematic of nuclear shapes with respect to the deformation parameters (β_2, γ) , as defined in the Lund convention. Figure adapted from Ref. [6].	32
2.5	Schematic of the quantum numbers which can describe the deformed nucleus. Λ , Ω , Σ , and K are the projections of the orbital angular momentum l , of the total angular momentum of the particle j , of the spin of the particle s , and of the total angular momentum J onto the symmetry axis, respectively. In addition, \vec{R} is the angular momentum of the core and M is the projection of the total angular momentum onto the laboratory axis.	34
2.6	Nilsson diagram for protons in the $50 \leq Z \leq 80$ region showing the single-particle energies as a function of the deformation parameter ϵ_2 . For $\epsilon_2 > 0$, corresponding to the prolate shape; for $\epsilon_2 = 0$, corresponding to the spherical shape; for $\epsilon_2 < 0$, corresponding to the oblate shape. Labels obey the $\Omega^\pi[Nn_z\Lambda]$ rule.	35

2.7	Nilsson diagram for neutrons in the $50 \leq N \leq 80$ region showing the single-particle energies as a function of the deformation parameter ϵ_2 . For $\epsilon_2 > 0$, corresponding to the prolate shape; for $\epsilon_2 = 0$, corresponding to the spherical shape; for $\epsilon_2 < 0$, corresponding to the oblate shape. Labels obey the $\Omega^\pi[Nn_z\Lambda]$ rule.	36
2.8	Schematic diagram of the strong coupling limit in the particle-rotor model.	39
2.9	Schematic diagram of the decoupling limit in the particle-rotor model.	39
2.10	Discrete symmetries of the mean field of a rotating triaxial reflection symmetric nucleus. The axis of rotation (z) is marked by the circular arrow. The rotational band structures associated with each symmetry type are presented on the right side. This figure was taken from Ref. [7].	49
3.1	Schematic illustration the heavy-ion fusion-evaporation reaction forming a compound nucleus and its decay.	54
3.2	(a) Photoelectric absorption, (b) Compton scattering, (c) Pair production.	55
3.3	Reverse bias of the p-n junction.	57
3.4	The schematic configuration of a BGO anti-Compton shield of a HPGe detector.	58
3.5	JUROGAM II array.	59
3.6	Scheme of gas-filled recoil separator RITU. The figure is taken from Ref. [8].	60
3.7	Schematic diagram of GREAT septrometer.	61
3.8	Schematic illustration of a typical RDT setup and the signal times for each detector relative to the an event stamp in the DSSDs. This figure is adapted from Ref. [9].	63
4.1	A sample of calibrated overlaid energy spectra of ^{152}Eu for some Ge detectors of the JUROGAM II array. The peaks corresponding to the contaminating transitions are indicated with asterisks.	66
4.2	Geometry of the detector arrangement with the beam as orientation axis.	69
5.1	Partial level scheme of ^{136}Nd showing the low- and medium-spin bands.	72
5.2	Double-gated spectra for the γ band of ^{136}Nd . The peaks corresponding to the γ rays of ^{136}Nd are indicated with their energies, while those of the contaminating transitions are indicated with an asterisk.	73

5.3	Double-gated spectra for the band N2 of ^{136}Nd . The peaks corresponding to the contaminating transitions are indicated with asterisks.	74
5.4	Double-gated spectrum for band L4 of ^{136}Nd	74
5.5	Sum of spectra obtained by double-gating on all combinations of in-band transitions of band T2. The peaks corresponding to the contaminating transitions are indicated with asterisks. . .	75
5.6	Partial level scheme of ^{136}Nd showing the dipole bands.	76
5.7	a) Sum of spectra obtained by double-gating on all combinations of the 220-, 254- and 294-keV transitions of band D1. b) Spectrum obtained by double-gating on the 220- and 254-keV transitions of band D1. The peaks corresponding to the in-band transitions of band D1-chiral and to the connecting transitions to band D1 are indicated with asterisks.	77
5.8	Spectra constructed by double-gating on transitions of band D2 which shows the connecting transitions of band D2-chiral. The transitions marked with asterisks indicate low-lying transitions in ^{136}Nd . The red lines show how the connecting transitions disappear when gating on successive higher-lying transitions of band D2.	78
5.9	Double-gated spectrum on the 249- and 345-keV transitions of band D3, showing the connecting transitions of band D3-chiral to band D3, which are indicated with asterisks.	79
5.10	Double-gated spectrum on the 309- and 357-keV transitions of band D4. The peaks corresponding to the connecting transitions of band D4-chiral to band D4 are indicated with asterisks. . .	80
5.11	Sum of spectra obtained by double-gating on all combinations of the 230-, 284-, 345-, 388- and 463-keV transitions of band D5. The peaks corresponding to the in-band transitions of band D5-chiral and to the connecting transitions to band D5 are indicated with asterisks.	80
5.12	Sum of spectra obtained by double-gating on all combinations of in-band transitions of: a) band HD1 and b) band HD2. The peaks corresponding to the in-band transitions of each band are indicated with asterisks.	81
5.13	Sum of spectra obtained by double-gating on all combinations of in-band transitions of: a) band HD3, b) band HD4, and c) HD5. The peaks corresponding to the in-band transitions of each band are indicated with asterisks.	82
5.14	Partial level scheme of ^{136}Nd showing the T bands.	83
5.15	Partial level scheme of ^{136}Nd showing the HD bands.	83
5.16	Excitation energies and $\hbar\omega$ vs I calculated by TAC-CDFT for the positive (left panel) and negative (right panel) chiral rotational bands of ^{136}Nd	100

5.17	Quasiparticle alignments calculated by TAC-CDFT for the positive-parity (left panel) and negative-parity (right panel) chiral rotational bands of ^{136}Nd . Solid and open circles with the same color represent experimental data of one pair of nearly degenerate bands, and different lines denote the theoretical results based on different configurations.	100
5.18	Values of transition probabilities $B(M1)/B(E2)$ of ^{136}Nd calculated by TAC-CDFT, in comparison with experimental data (solid and open symbols).	101
5.19	Evolution of the azimuth angle ϕ as a function of rotational frequency, for the total angular momentum of the configuration D^* assigned to band D3, calculated by 3D TAC-CDFT	102
5.20	(Color online) The energy spectra of bands D1-D6 and their partners calculated by PRM in comparison with corresponding data. The excitation energies are relative to a rigid-rotor reference.	103
5.21	(Color online) The staggering parameters of bands D1-D6 calculated by PRM in comparison with corresponding data.	105
5.22	(Color online) The $B(M1)/B(E2)$ of bands D1-D6 and their partners calculated by PRM in comparison with corresponding data.	106
5.23	(Color online) The root mean square components along the intermediate (i -, squares), short (s -, circles) and long (l -, triangles) axes of the rotor, valence protons, and valence neutrons angular momenta calculated as functions of spin by PRM for the doublet bands D2 and D2-C in ^{136}Nd	106
5.24	(Color online) Same as Fig. 5.23, but for D4 and D4-C.	107
5.25	(Color online) Same as Fig. 5.23, but for D5 and D5-C.	108
5.26	(Color online) Energies relative to a standard rotating liquid drop reference calculated for the experimental bands observed in ^{136}Nd . With an odd number of $h_{11/2}$ neutron holes, two signature degenerate bands are formed which are shown by the same color and symbols.	110
5.27	The same as in Fig. 5.26 but for the bands L and T.	110
5.28	The same as in Fig. 5.26 but for the dipole bands.	111
5.29	The same as in Fig. 5.26 but for the bands HD.	112
5.30	(Color online) The observed low-spin bands of ^{136}Nd are shown relative to a rotating liquid drop reference in panel (a), with the calculated configurations assigned to these bands given relative to the same reference in panel (b). The panel (c) provides the difference between calculations and experiment.	113
5.31	(Color online) The same as in Fig. 5.30 but for the medium-spin bands L.	114
5.32	(Color online) The same as in Fig. 5.30 but for the medium-spin bands T.	116

5.33	(Color online) The same as in Fig. 5.30 but for the bands D. . .	118
5.34	(Color online) The same as in Fig. 5.30 but for the HD bands. . .	120
6.3	(Color online) Comparison between the experimental excitation energies relative to a reference rotor (symbols) and the particle-rotor model calculations (lines) for the bands D1-D6.	128
6.4	(Color online) The experimental quasi-particle alignments for the chiral rotational bands of ^{135}Nd	129
6.5	(Color online) Comparison between experimental ratios of transitions probabilities $B(M1)/B(E2)$ (symbols) and the particle-rotor calculations (lines) for the bands D1-D6.	131
6.6	(Color online) The root mean square components along the intermediate (i —, squares), short (s —, circles) and long (l —, triangles) axes of the rotor, valence protons, and valence neutrons angular momenta calculated as functions of spin by PRM for the doublet bands D3 and D4 of ^{135}Nd	132
7.1	γ -Time matrix for the clovers at the focal plane. The transitions marked with asterisks represent the β -decay contaminants from the nuclei produced in this experiment: 665 keV, 783 keV, 828 keV and 872 from the β -decay of ^{135}Ce , 761 keV and 925 keV from the β -decay of ^{137}Nd	141
7.2	Partial level scheme of ^{138}Nd related to the isomeric state. . .	142
7.3	Spectrum of prompt transitions measured by JUROGAM II gated with selected clean transitions in ^{138}Nd (521, 729, 884, and 973 keV) measured by the clovers placed at the focal plane. . .	142
7.4	Time spectra extracted from γ -T matrix at the focal plane transitions (521, 729, 884, and 973 keV) deexciting the 10^+ isomer in ^{138}Nd . The red line is fitted to the data.	143

List of Tables

5.1	Experimental information including the γ -ray energies, energies of the initial levels E_i , intensities I_γ , anisotropies R_{DCO} and or R_{ac} , multipolarities, and the spin-parity assignments to the observed states in ^{136}Nd . The transitions listed with increasing energy are grouped in bands. The deduced values for R_{DCO} with a stretched quadrupole gate are ≈ 1 for stretched quadrupole and ≈ 0.46 for dipole transitions, while the ratio is close to 1 for a dipole and 2.1 for a quadrupole transition when the gate is set on a dipole transition. The R_{ac} values for stretched dipole and quadrupole transitions are ≈ 0.8 and ≈ 1.4	84
5.2	Experimental information including the γ ray energies, energies of the initial levels E_i and the tentative spin-parity assignments to the observed states in ^{136}Nd	97
5.3	Unpaired nucleon configurations labeled A-H and the corresponding parities, calculated by constrained CDFT. The excitation energies E_x (unit MeV) and quadrupole deformation parameters (β, γ) are also presented.	99
5.4	The parities, unpaired nucleon configurations, quadrupole deformation parameters (β, γ) , moments of inertia \mathcal{J}_0 (unit \hbar^2/MeV), and Coriolis attenuation factors ξ used in the PRM calculations for bands D1-D6 and their partners.	104
5.5	Configuration assignments and deformation information to the bands of ^{136}Nd	119

6.1	Experimental information including the γ -ray energies, energies of the initial levels E_i , intensities I_γ , anisotropies R_{DCO} and or R_{ac} , multipolarities, and the spin-parity assignments to the observed states in ^{135}Nd . The transitions listed with increasing energy are grouped in bands and the transitions connecting a given band to low-lying states are listed at the end of each band separated by a blank line. The deduced values for R_{DCO} with a stretched quadrupole gate are ≈ 1 for stretched quadrupole and ≈ 0.46 for dipole transitions, while the ratio is close to 1 for a dipole and 2.1 for a quadrupole transition when the gate is set on a dipole transition. The R_{ac} values for stretched dipole and quadrupole transitions are ≈ 0.8 and ≈ 1.4	133
A.1	The information of JUROGAM II detector angles.	149

Chapter 1

Introduction

The atomic nucleus is a strongly interacting quantum many-body system composed of protons and neutrons. The nuclei can contain nucleons from a few to several hundred. This finite number of nucleons makes the nucleus become a unique system which cannot be treated in a statistical way, and its behaviour at a phase change is very different from that of ordinary matter. The finiteness of the nucleus is also manifest in the influence that just one nucleon may have on determining the nuclear properties, particularly the nuclear shape. The main aim of the nuclear structure is to understand the distribution and motion of the nucleons inside the nucleus and also to study the collective motion and shape of the whole nucleus.

The work presented in this thesis is centred around two nuclei: ^{135}Nd and ^{136}Nd , which are located in the $A \approx 130$ mass region, a fertile field of study of the transitional nuclei with shapes that can vary between strongly deformed in the middle of the major shell $50 < Z, N < 82$ to nearly spherical close to the shell closure [10]. A variety of shapes can also be present in a single nucleus in different spin ranges.

At low spins, axial asymmetry was suggested for the ground states of nuclei centered around $Z = 62, N = 76$ [10], in which a regular increase of the level energies of the observed low-lying γ band, considered a sign of rigid triaxiality has been observed, while in the surrounding nuclei the level energies present a staggering, which is considered a sign of soft triaxial shapes.

At medium spins, the shape can change under the polarizing effect of unpaired nucleons resulting from broken pairs. In certain cases the triaxial shape becomes more rigid, being based on a deeper minimum of the potential energy surface, induced by the protons occupying low- Ω orbitals in the lower part of the $h_{11/2}$ subshell, or by neutrons excited from orbitals below $N = 82$ to low- Ω ($h_{9/2}, f_{7/2}$) orbitals lying above $N = 82$ (see, e.g., [11, 12] and references therein).

At high spins, the nuclei with several holes in the $N = 82$ shell closure, a multitude of triaxial bands have been observed in several Ce and Nd nuclei, giving strong support for the existence of stable triaxial shape up to very high

spins. In addition, nuclei of the $A \approx 130$ mass region can also present other coexisting shapes, e.g., axially deformed, highly deformed, and even superdeformed at high spins. This is the case for ^{140}Nd , in which states based on a spherical shape have been observed up to spins as high as $27 \hbar$ coexisting with triaxial shapes, and in which axial superdeformed and highly deformed shapes coexist at very high spin [13,14]. In this nucleus, the bridge between the regions of highly deformed bands present in $A \approx 130$ nuclei and the superdeformed bands present in $A \approx 150$ nuclei provides an insight into the development of the deformation between these two regions of superdeformation [14].

An additional feature of nuclei in this mass region is the presence of isomeric states, e.g., the 10^+ , $T_{1/2} = 370$ ns isomer of ^{138}Nd , the 10^+ , $T_{1/2} = 308$ ns isomer of ^{134}Ce , the $11/2^-$, $T_{1/2} = 2.7 \mu\text{s}$ isomer of ^{137}Pr , and the 6^+ , $T_{1/2} = 90$ ns isomer of ^{136}Pr [15], populated in the reaction used in the present work, which interrupts and fragments the decay flux.

The $A \approx 130$ mass region is also characterized by the existence of two unique fingerprints of a triaxial nuclear shape: chirality and wobbling. Chirality represents a novel feature of triaxial nuclei rotating around an axis which lies outside the three principal planes of the triaxial ellipsoidal shape, which will be discussed in detail in Section 1.1. The wobbling motion has been discussed by Bohr and Mottelson in the triaxial even-even nuclei many years ago [16]. This mode represents the quantized oscillations of the principal axes of an asymmetric top relative to the space-fixed angular momentum vector or, in the body fixed frame of reference, the oscillations of the angular momentum vector about the axis of the largest moment of inertia [17]. Recently, the wobbling interpretation has been proposed for low-lying bands observed in ^{135}Pr [17].

Thus, this region of the nuclear chart is an ideal testing ground to investigate the competition between various deformations and their evolution with spins, as well as the competition between single-particle and collective modes of excitation.

1.1 Chirality

The term chirality, was first time introduced by Lord Kelvin in 1904 in his Baltimore Lectures [18]:

"I call any geometrical figure, or group of points, chiral, and say it has chirality, if its image in a plane mirror, ideally realized, can not be brought to coincide with itself."

Chirality commonly exists in nature, and has important consequences in fields of science as diverse as biology, chemistry, and physics. The best known examples of geometrically chiral objects are the human hands and the microscopic handedness of certain molecules. Chiral symmetry is also well known in particle physics, where it is of a dynamic nature distinguishing between the two possible orientations of the intrinsic spin with respect to the momentum

of the particle [19].

1.1.1 Nuclear Chirality

In nuclear physics, chirality was suggested in 1997 by Frauendorf and Meng [20]. It shows up in a triaxial nucleus which rotates about an axis out of the three principal planes of the ellipsoidal nuclear shape.

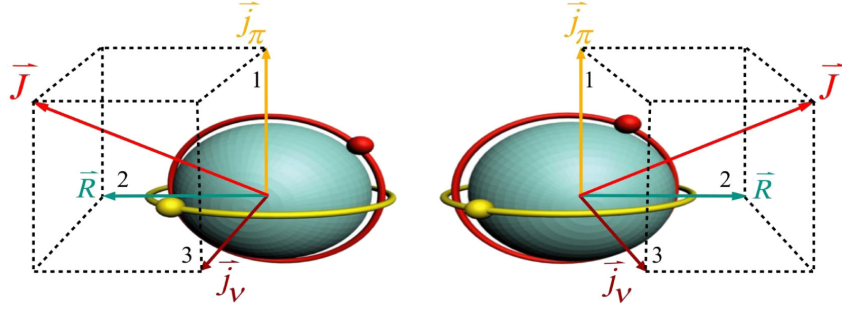


Figure 1.1: Left- and right-handed chiral systems for a triaxial odd-odd nucleus. The symbols \vec{J} , \vec{R} , \vec{j}_ν , and \vec{j}_π denote respectively the total angular momentum, the angular momenta of the core, of the neutron and of the proton, respectively. Figure adopted from Ref. [1].

The simplest chiral geometry is expected in an odd-odd nucleus when the angular momenta of the valence proton, of the valence neutron, and of the core tend to be mutually perpendicular. This occurs when the collective angular momentum is oriented along the intermediate axis (this happens if one assumes hydrodynamical moments of inertia), and the angular momentum of the high- j quasiparticle and quasihole are aligned along the short and long axes, respectively, minimizing thus the interaction energy. These three mutually perpendicular angular momenta can be arranged into a left- or a right-handed system (see Fig. 1.1), which differ by intrinsic chirality; the two systems are related by the chiral operator of the form $\chi = TR(\pi)$, where $R(\pi)$ corresponds to a rotation of 180° , while T is the time reversal and therefore changes to opposite the directions of all angular momentum vectors. Chiral symmetry in an atomic nucleus is observed because quantum tunneling occurs between systems with opposite chirality. When chiral symmetry is thus broken in the body-fixed frame, the restoration of the symmetry in the laboratory frame is manifest as degenerate doublet $\Delta I = 1$ bands with the same parity, called chiral doublet bands [21, 22]. In practice, chiral bands are near degenerate, and show similar properties. The chiral symmetry can be identified if similarities between a specific band and its partner band are observed. The specific fingerprints used to identify chiral doublet bands will be discussed in Section 1.2.

It should be pointed out that the chirality in the nature is often static, like in the molecules, in the DNA. In the case of nucleus, the chirality is dynamic, since it is the angular momentum vector that defines a direction with respect to which the semi-axes (1, 2, 3) form a left- or right-handed system. The non-rotating nuclei are achiral.

1.1.2 Multiple chiral doublets (M χ D)

Adiabatic and configuration-fixed constrained triaxial relativistic mean field (RMF) approaches were developed to investigate the triaxial shape co-existence and possible chiral doublet bands in 2006 [23], which predicted a new phenomenon, the existence of multiple chiral doublets (M χ D), i.e., more than one pair of chiral doublet bands, in one single nucleus. This phenomenon was suggested for ^{106}Rh after examining the possible existence of triaxial deformation and of the corresponding high- j proton-hole and neutron-particle configurations. Such investigation has been extended to the rhodium isotopes and the existence of M χ D has been suggested in $^{104,106,108,110}\text{Rh}$ [24]. The investigation predicted M χ D not only in ^{106}Rh , but also in other mass regions, i.e., $A \approx 80$, and $A \approx 130$.

Recently, M χ D bands have been identified in $A \approx 130$, $A \approx 110$, and $A \approx 80$ mass regions. The first experimental evidence for the existence of M χ D in the $A \approx 130$ mass region was reported in ^{133}Ce in 2013 [25]. It was found that the negative-parity bands 2 and 3, and the positive-parity bands 5 and 6 based on the 3-quasiparticle configurations $\pi[(1h_{11/2})^1(1g_{7/2})^{-1}] \otimes \nu(1h_{11/2})^{-1}$ and $\pi(1h_{11/2})^2 \otimes \nu(1h_{11/2})^{-1}$, respectively, are nearly degenerate and have similar properties. Later, Kuti *et al.* reported a novel type of M χ D bands in ^{103}Rh [26], where an "excited" chiral doublet of a configuration is seen together with the "yrast" one. This observation showed that chiral geometry can be robust against the increase of the intrinsic excitation energy. In ^{78}Br , two pairs of positive- and negative-parity doublet bands together with eight strong electric dipole transitions linking the yrast positive- and negative-parity bands have been identified [27]. They were interpreted as M χ D bands with octupole correlations, being the first example of chiral geometry in octupole soft nuclei and indicating that nuclear chirality can be robust against the octupole correlations.

It should be noted that until now all the observed M χ D bands are only in odd-odd, odd-even, and even-odd nuclei. It inspired us to search for the M χ D bands in even-even nuclei. This is one of the main aims of the experiment presented in this thesis.

1.2 Fingerprints of the chiral bands

From an experimental point of view, the doublet bands must satisfy a set of criteria in order to be recognized as chiral bands, among which the most important are the energy separation between the partners and their electromagnetic transitions rates.

1.2.1 Energy spectra

Firstly, the appearance of near degenerate $\Delta I = 1$ bands with the same parity is considered to be one fingerprint for the chiral bands. The energies of the partner bands should be close to each other, i.e. be nearly degenerate. What does near degenerate mean is not precisely defined since it depends on the deformation, valence nucleon configuration and their couplings. Normally, the acceptance of a near degenerate energy is below 200 keV.

From the measured energies one can derive other observables, like the energy staggering parameter $S(I) = [E(I) - E(I - 2)]/2I$ which can also serve as fingerprint for chiral partner bands.

Experimentally, the signature splitting between the odd- and even-spins sequences of a given dipole band is quantified by the energy staggering $S(I)$. When the rotation axis is tilted outside the principal planes, the signature is not a good quantum number and therefore it is more appropriate to speak about the odd/even spin dependence of $S(I)$. The expected typical behaviour of $S(I)$ in a chiral band is a small odd/even staggering at low spins, which diminishes with increasing spin, and finally, becomes constant. Therefore, the energy staggering parameter should be almost constant and equal for the states of the same I , in the two chiral partners [28].

1.2.2 Electromagnetic transitions rates

The electromagnetic transitions rates in chiral doublet bands obey important selection rules. Thus, for odd-odd nuclei, with the $\nu h_{11/2} \otimes \pi h_{11/2}^{-1}$ configuration coupled to a rigid triaxial rotor with $\gamma = 30^\circ$, the selection rules for electromagnetic transitions in the chiral bands has been proposed in Ref. [29], including the odd-even staggering of intraband $B(M1)/B(E2)$ ratios, the interband $B(M1)$ values, as well as the vanishing of the interband $B(E2)$ transitions in the high spin region.

The fingerprints of the electromagnetic transitions probabilities in the chiral bands also depend on the deformation, valence nucleon configuration and their coupling. It is found that the $B(M1)$ staggering depends strongly on the character of the nuclear chirality, i.e., the staggering is weak in chiral vibration region and strong in the static chirality region. For partner bands the similar $B(M1)$, $B(E2)$ transitions, and the strong $B(M1)$ staggering can be used as a fingerprint for the static chiral rotation [30]. This result agrees

with the lifetime measurements for the doublet bands in ^{128}Cs [31], but not in ^{135}Nd which shows a chiral vibration [32].

1.2.3 Other fingerprints

To identify chiral doublet bands besides energy spectra and electromagnetic transitions rates, as arguments in favor of chirality there are some other specific fingerprints. Experimentally, almost constant energy difference between partners, and similar moment of inertia are always used in the discussion of the chiral doublet bands. In addition, one can examine the similarities of the configurations for chiral doublet bands by analysing the $I-\hbar\omega$ relation, where $\hbar\omega$ is the rotational frequency defined as $\hbar\omega = [E(I+1) - E(I-1)]/2$. Generally speaking, the $I-\hbar\omega$ relation for the yrast band and its partner band should be similar. Furthermore, one can also examine the angular momentum geometries of the observed doublet bands by calculating the expectation values of the angular momentum components of the core, of the valence protons and of the valence neutrons, along the intermediate, short, and long axes.

Experimentally, the chiral phenomenon has been reported in a number of odd-odd and odd-A nuclei in the mass $A \approx 80$, $A \approx 100$, $A \approx 130$, $A \approx 190$ regions; see e.g., Refs. [21, 22, 25–27, 31–39]. The distribution of the observed chiral nuclei in the nuclear chart is given in Fig. 1.2.

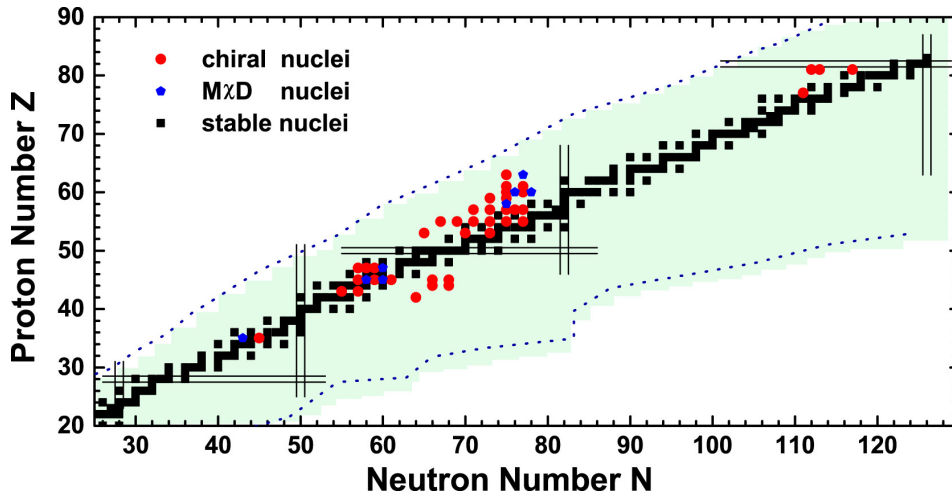


Figure 1.2: The nuclides with chiral doublet bands (red circles) and $M\chi D$ (blue pentagons) observed in the nuclear chart. The black squares represent stable nuclides. Figure adopted from Ref. [2].

1.3 Motivation of this study

The existence of triaxially deformed nuclei has been the subject of a long standing debate. It appears questionable how well the non-axial shape is stabilized. The intimate mechanism which induces such a behavior needs detailed and accurate investigations, both from the experimental and theoretical points of view. Recently, the wobbling and chirality, as the two unique fingerprints of triaxiality in nuclei, have been intensively studied.

The main part of present work was undertaken with the aim of searching for multiple chiral bands in ^{136}Nd , a nucleus which is the nearest even-even neighbor of the first chiral candidate ^{134}Pr [20] and the first reported wobblers ^{135}Pr outside of the $A \approx 160$ region [17]. In addition, an important effort was devoted to the detailed spectroscopy of ^{136}Nd since most of the experimental results reported previously were obtained more than twenty years ago with less efficient detector arrays.

The other aim of the present work was focused on a detailed study of the chirality in ^{135}Nd , to search for multiple chiral bands similar to those observed in the ^{133}Ce isotone [25]. The nucleus ^{135}Nd is one of the best known examples of chiral vibration [32, 33].

In addition to the study of the chiral bands of ^{135}Nd and ^{136}Nd , we devoted an important effort to searching for long-lived isomers in the populated nuclei, in particular in ^{135}Nd and ^{136}Nd , using the RITU+GREAT setup and the recoil tagging technique. This effort was motivated by the existence of long-lived isomers in ^{134}Nd , ^{137}Nd , ^{138}Nd , ^{139}Nd , and ^{140}Nd [15], but not in ^{135}Nd and ^{136}Nd .

1.4 Outline of thesis

The remaining chapters of this thesis will be organized as follows:

The relevant nuclear models needed to understand the experimental results presented in this work are described in Chapter 2.

Details of the experimental techniques, and the data analysis procedures are outlined in Chapter 3 and Chapter 4, respectively.

The experimental results and discussion of ^{136}Nd and ^{135}Nd are reported in Chapter 5 and Chapter 6, respectively.

The search for possible long-lived isomeric states in the populated nuclei, in particular in ^{136}Nd and ^{135}Nd are presented in Chapter 7.

The detailed information of JUROGAM II detectors are given in Appendix A.

Chapter 2

Theoretical backgroud

In this chapter, some of the nuclear structure models relevant to the present work will be presented. The specific mechanism leading to the chiral mode of excitation will also be briefly discussed.

2.1 Liquid drop model

The liquid drop model (LDM) [40] of the nucleus was historically the first model proposed to describe the different properties of the nucleus. The idea of considering the nucleus as a liquid drop originally came from considerations about its saturation properties and from the fact that nucleus has a low compressibility and a well defined surface [3].

One of the basic properties of a nucleus is its binding energy $B(N, Z)$, where N and Z are the number of neutrons and protons, respectively. Many attempts were made to reproduce the nuclear binding energy B , but the liquid drop model proposed by Weizsäcker [41] and Bethe [42] is one of the successful ones.

The *semi-empirical* mass formula of the Weizsäcker and Bethe for the nuclear binding energy reads:

$$\begin{aligned} B &= (Nm_n + Zm_p - m)c^2 \\ &= a_{vol}A - a_{surf}A^{2/3} - a_{coul}\frac{Z^2}{A^{1/3}} - a_{asym}\frac{(N - Z)^2}{A} + \delta(A), \end{aligned} \quad (2.1)$$

where m_n and m_p are the masses of neutron and proton, respectively, and A is the mass number. The five coefficients a_{vol} , a_{surf} , a_{coul} , a_{asym} , and δ are obtained by fitting the experimental data. The physical meaning of Eq. 2.1 is the following:

- the first term is usually called the *volume term*, because it is proportional to the mass number A ;

- the second term, called the *surface term*, is proportional to the nuclear surface area $A^{2/3}$;

- the third term called the *Coulomb term* derives from the Coulomb interaction among protons, and is proportional to Z^2 ;
- the fourth term called the *asymmetry term* reflects the fact that nuclear force favour equal numbers of neutrons and protons, or $N = Z$;
- the last term called the *pairing term* favours configurations where two identical fermions are paired. It can be rewritten as follows:

$$\delta(A) = \begin{cases} a_p A^{-3/4}, & \text{for even - even nuclei;} \\ 0, & \text{for even - odd nuclei;} \\ -a_p A^{-3/4}, & \text{for odd - odd nuclei.} \end{cases}$$

where $a_p \approx 34$ MeV [43].

The LDM was very successful in predicting the nuclear binding energy and describing how a nucleus can deform and undergo fission. As a collective model, it is also particularly useful in describing the macroscopic behaviour of the nucleus. However, this is a crude model that does not explain all the properties of the nucleus and nuclear shell structure. In particular, it fails when it is used to explain the nuclei with *magic numbers* (N or Z equal 2, 8, 20, 28, 50, 82, and 126). A more sophisticated model must to be developed to solve this problem.

2.2 The shell model

As mention above, one of most important information on the shell structure is the presence of *magic numbers*. If one of the proton or neutron numbers is equal to a magic number, then the nucleus is more stable compared with the neighbors, has a larger total binding energy, a much larger energy of the first excited state, and a larger energy required to separate one nucleon.

The shell model was firstly proposed by Mayer and Jensen [44,45] in 1949 to interpret the observed shell structure in nuclei. The basic assumptions of shell model is that each nucleon moves independently in an average potential created by other nucleons. The assumption made is that motion of the nucleons is quite similar to the motion of electrons in an atom. The Schrödinger equation for a given potential $V(r)$, is written as

$$\left(-\frac{\hbar^2}{2m}\nabla^2 + V(r)\right)\psi_i(r) = \epsilon_i\psi_i(r), \quad (2.2)$$

where $\psi_i(r)$ and ϵ_i are the eigenstates and eigenvalues representing the wave functions and energies, respectively. Various potential wells have been used, for example square well, infinite harmonic oscillator well, and Woods-Saxon potential.

Harmonic oscillator potential

The harmonic oscillator potential has the form

$$V(r) = \frac{1}{2}m\omega^2 r^2, \quad (2.3)$$

where m is the mass of the nucleon and ω is the angular frequency of the oscillator. The Schrödinger equation of motion for harmonic oscillator is written as:

$$\left(-\frac{\hbar^2}{2m}\nabla^2 + \frac{1}{2}m\omega^2 r^2\right)\psi_i(r) = \epsilon_i\psi_i(r). \quad (2.4)$$

The energy eigenvalues are:

$$\epsilon_N = \hbar\omega\left(N + \frac{3}{2}\right), \quad (2.5)$$

where

$$N = 2(n - 1) + l, \quad (2.6)$$

with $n = 1, 2, 3, \dots$, and $l = 0, 1, 2, \dots, n - 1$. N is the principal quantum number, n is the radial quantum number. l is angular momentum, and it often referred to using the spectroscopic notations, s, p, d, f, g, h, \dots corresponding to $l = 0, 1, 2, 3, 4, 5, \dots$.

In this case, all levels with the same principal quantum number N are degenerate, where the degeneracy is given by $2(2l + 1)$. The parity of each level is given by $\pi = (-1)^N$. This potential can only reproduce the magic numbers 2, 8 and 20, implying that the model needs to be modified if one wants to reproduce higher magic numbers.

Woods-Saxon potential

To improve the model, the more realistic Woods-Saxon potential [46] can also be employed. It has the form

$$V(r) = -\frac{V_0}{1 + e^{(r-R)/a}}, \quad (2.7)$$

where $R = r_0 A^{1/3}$ is the mean radius of the nucleus, $V_0 \simeq 50$ [MeV] is the depth of the potential well, and a describes the diffuseness of the nuclear surface, $a \simeq 0.5$ [fm].

Compared with the harmonic oscillator potential it removes the l degeneracies of the major shells, filling the shells in order with $2(2l+1)$ levels, but also in this case only the magic numbers 2, 8 and 20 are reproduced. In addition, its eigenfunctions can not be solved analytically, and must be treated numerically.

Spin orbit coupling

To reproduce all the magic numbers, a quite different suggestion was put forward independently by Mayer [44] and by Haxel, Jensen and Suess [45]. They added a strong spin-orbit coupling term $\vec{l} \cdot \vec{s}$ into the single-particle Hamiltonian.

The addition of this term splits the states with the same orbital angular momentum l into two. The single particle total angular momentum is defined by $j = l + s$, and then the j values of the split-up levels are $j = l \pm \frac{1}{2}$. By including the spin-orbit coupling term all magic numbers are successfully reproduced, see Fig. 2.1. Other properties, like the spins and parities of the ground states of most spherical nuclei, and the ground state magnetic moments of nuclei are also well described. But the shell model with the spin-orbit coupling term is still not accurate for the description of nuclei far away from the closed shells. These difficulties were overcome by Nilsson who introduced the *deformed shell model* [47].

2.3 The deformed shell model

2.3.1 Deformed parameters

The nucleus is considered as an incompressible liquid drop with a sharp surface or surface oscillations. In order to investigate these oscillations, we can parametrize them in some way. The length of the radius vector $R(\theta, \phi)$ pointing from the origin to the surface can be written as

$$R(\theta, \phi) = R_0 \left[1 + \sum_{\lambda=0}^{\infty} \sum_{\mu=-\lambda}^{\lambda} \alpha_{\lambda\mu} Y_{\lambda\mu}(\theta, \phi) \right], \quad (2.8)$$

where R_0 is the radius at the spherical equilibrium with the same volume, $Y_{\lambda\mu}$ are the spherical harmonics. Each spherical harmonic component will have an amplitude $\alpha_{\lambda\mu}$, where λ represents different modes of deformations. The general expansion of the nuclear surface in Eq. 2.8 allows to describe different shapes, as displayed in Fig. 2.2.

The lowest order multipole term, $\lambda = 1$, does not correspond to a deformation of the nucleus, but rather to a shift of the position of the center of mass. Thus, the deformation of order $\lambda = 1$ is equivalent to a translation of the nucleus that should be neglected for nuclear excitations.

The $\lambda = 2$ multipole term corresponds to the quadrupole deformation which looks like ellipsoidal deformation. In this case, the nucleus shape could be oblate, prolate or triaxial. It turns out to be the most important mode of excitation of the nucleus, therefore only the $\lambda = 2$ will be considered in the following discussion.

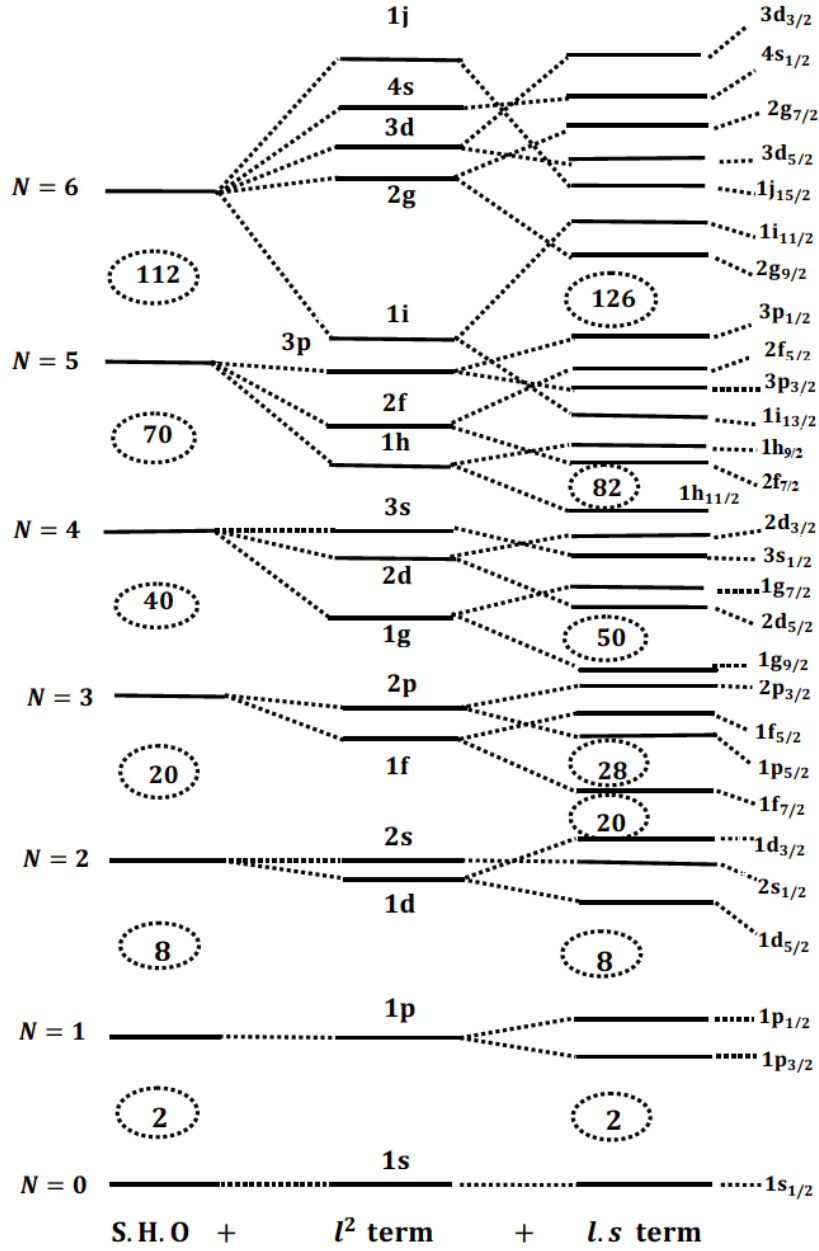


Figure 2.1: Schematic nuclear levels calculated by the shell model including the l^2 and $\vec{l} \cdot \vec{s}$ terms. Figure adapted from Ref. [3].

The octupole deformation corresponding to $\lambda = 3$, is the principal asymmetric mode of deformation of the nucleus and is associated with a pear shape.

The term $\lambda = 4$ (hexadecapole) and higher order terms are small and often can be neglected.

In the case of quadrupole deformation, there are five shape parameters $\alpha_{\lambda\mu}$; three of these shape parameters are equivalent to classical Euler angles,

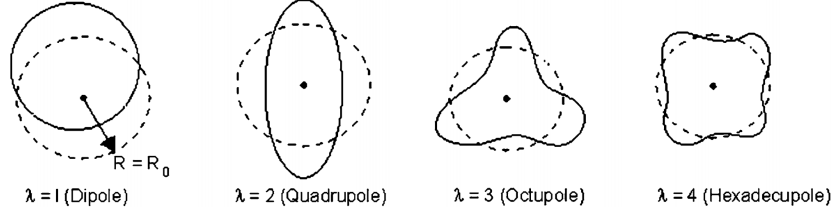


Figure 2.2: The lowest four vibrations of a nucleus. The dashed lines show the spherical equilibrium shape and the solid lines show an instantaneous view of the vibrating surface. Figure adapted from Ref. [4].

which are related to the relative orientation of the drop in space. By a suitable rotation, we can transform to the body-fixed system characterized by three axes 1, 2, 3, which coincide with the principle axes of the mass distribution of the drop. Thus, the five coefficients $\alpha_{2\mu}$ reduce to two real independent variables α_{20} and $\alpha_{22} = \alpha_{2-2}$ ($\alpha_{21} = \alpha_{2-1} = 0$), which together with the three Euler angles, give a complete description of the system [3]. The two remaining parameters (α_{20} , α_{22}) are more convenient to be expressed in Hill-Wheeler [48] coordinates β_2 and γ , as follows

$$\begin{aligned}\alpha_{20} &= \beta_2 \cos \gamma, \\ \alpha_{22} = \alpha_{2-2} &= \frac{1}{\sqrt{2}} \beta_2 \sin \gamma,\end{aligned}\tag{2.9}$$

which satisfy the condition,

$$\sum_{\mu} |\alpha_{2\mu}|^2 = \alpha_{2-2}^2 + 2\alpha_{22}^2 = \beta_2^2,\tag{2.10}$$

where β_2 is the quadrupole deformation parameter of the nucleus, while the γ parameter describes the degree of triaxiality of the nuclear system, measuring the deviation from axial symmetry.

From the above definitions we can rewrite $R(\theta, \phi)$ as

$$R(\theta, \phi) = R_0 \left\{ 1 + \beta_2 \sqrt{\frac{5}{16\pi}} [\cos \gamma (3\cos^2 \theta - 1) + \sqrt{3} \sin \gamma \sin^2 \theta \cos 2\phi] \right\}.\tag{2.11}$$

The increments of the three axes in the body-fixed frame can be written in terms of the β_2 and γ parameters as follow

$$\frac{R_k - R_0}{R_0} = \beta_2 \sqrt{\frac{5}{4\pi}} \cos\left(\gamma - \frac{2\pi k}{3}\right), \quad k = 1, 2, 3,\tag{2.12}$$

where $k = 1, 2, 3$ correspond to the x , y , and z direction, respectively.

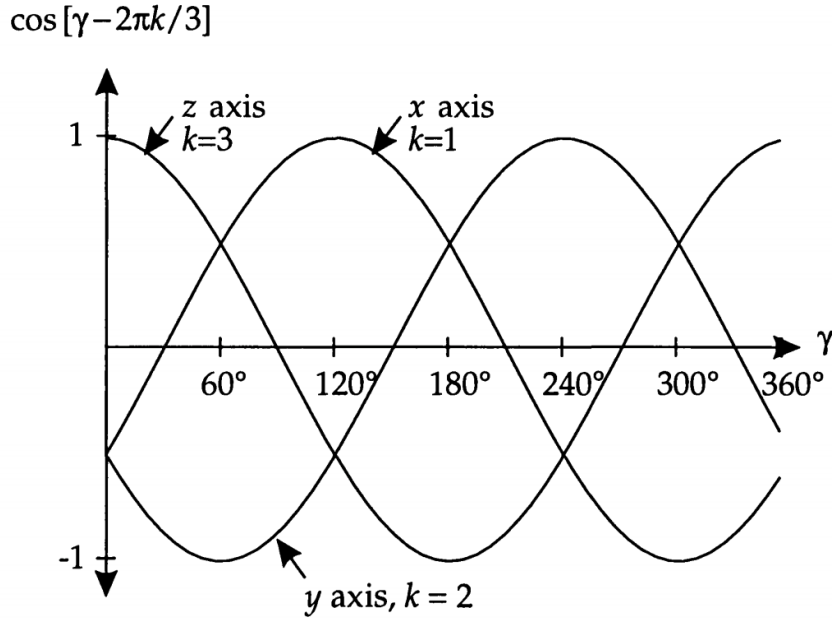


Figure 2.3: Plot of the Eq. 2.12, for $k=1, 2, 3$, corresponding to the increase in the axis lengths in the x , y , and z directions. Figure adopted from Ref. [5].

To easily see the evolution of the axis lengths with γ , a plot of the functions $\beta_2 \cos(\gamma - \frac{2\pi k}{3})$ with various γ and k are given in Fig. 2.3. One can see that at $\gamma = 0^\circ$ the nucleus is elongated along the z axis, while the length of x and y axes are equal (axially symmetric). With increasing γ , the x axis grows at the expense of the y and z axes, until the length of x and z axes are equal at $\gamma = 60^\circ$. This pattern is repeated each 60° .

According to the Lund convention [49], the different nuclear shapes corresponding to the various (β_2, γ) are shown in Fig. 2.4. In this convention, for $\gamma = 0^\circ$ and -120° , the nucleus is prolate, while it is oblate for $\gamma = -60^\circ$ and 60° . Note that there are two different types of rotations for pure prolate and oblate shapes which can be collective- and non-collective. Collective rotation, which occurs when $\gamma = 0^\circ$ or $\gamma = -60^\circ$, the rotational axis of nucleus is perpendicular to the symmetry axis. For non-collective rotation which occurs when $\gamma = 60^\circ$ or $\gamma = -120^\circ$, the rotational axis of nucleus is along the symmetry axis. When γ is not a multiple of 60° one has a triaxial shape. There are discrete symmetries, namely, one can interchange all three axes without changing the shape, which mean an invariance under the point group D_2 [3]. However, the interval $0^\circ < \gamma < 60^\circ$ is sufficient to describe all the $\lambda = 2$ shapes.

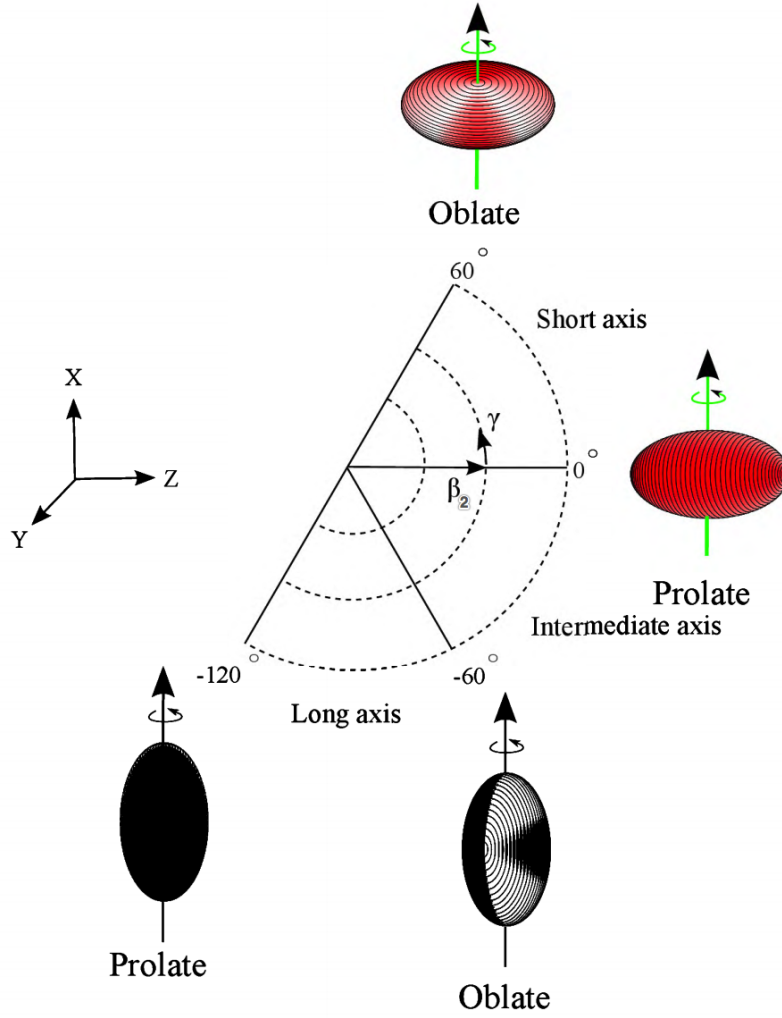


Figure 2.4: Schematic of nuclear shapes with respect to the deformation parameters (β_2, γ) , as defined in the Lund convention. Figure adapted from Ref. [6].

2.3.2 The Nilsson model

The deformed shell model was originally introduced by S. G. Nilsson [47], which is also often referred to the Nilsson model. In this model, the anisotropic harmonic oscillator potential is used as average field, so the single-particle Hamiltonian is expressed as,

$$H = -\frac{\hbar^2}{2m}\nabla^2 + \frac{m}{2}(\omega_x^2 x^2 + \omega_y^2 y^2 + \omega_z^2 z^2) - C\vec{l} \cdot \vec{s} - D l^2, \quad (2.13)$$

where ω_x , ω_y , and ω_z are the oscillator frequencies, x , y , and z are the coordinates of a particle in the intrinsic reference system. The parameters C and D control the strength of the spin-orbit and l^2 term, respectively. However, for large N quantum numbers, the l^2 -term shift is too strong and Nilsson replaced

the last term with the following form

$$D(l^2 - \langle l^2 \rangle_N), \quad (2.14)$$

where $\langle l^2 \rangle_N = \frac{1}{2}N(N+3)$ is the expectation values of l^2 averaged over one major shell with quantum number N . The three frequencies are chosen proportional to the inverse of the half axes a_x , a_y , and a_z of the ellipsoid:

$$\omega_i = \omega_o \frac{R_0}{a_i} \quad i = x, y, z. \quad (2.15)$$

If one only take into account the anisotropic harmonic oscillator Hamiltonian, the eigenstates are characterized by the number of oscillator quanta n_x , n_y , n_z , and the eigenvalues are

$$\epsilon_0(n_x, n_y, n_z) = \hbar\omega_x(n_x + \frac{1}{2}) + \hbar\omega_y(n_y + \frac{1}{2}) + \hbar\omega_z(n_z + \frac{1}{2}). \quad (2.16)$$

In the case of axially symmetric shapes, one usually choose the z -axis as symmetry axis and further introduce one single parameter of deformation δ , so

$$\begin{aligned} \omega_\perp^2 &= \omega_x^2 = \omega_y^2 = \omega^2(\delta) \left(1 + \frac{2}{3}\delta\right), \\ \omega_z^2 &= \omega^2(\delta) \left(1 - \frac{4}{3}\delta\right). \end{aligned} \quad (2.17)$$

The condition of constant volume of the nucleus leads to

$$\omega_x\omega_y\omega_z = \text{const.} = \omega_0^3, \quad (2.18)$$

ω_0 is the value of $\omega(\delta)$ for $\delta = 0$. From Eq. 2.17 and Eq. 2.18, we can get

$$\omega(\delta) = \omega_0 \left(1 - \frac{4}{3}\delta^2 - \frac{16}{27}\delta^3\right)^{-1/6}, \quad (2.19)$$

leading in second order to

$$\omega(\delta) = \omega_0 \left[1 + \left(\frac{2}{3}\delta\right)^2\right]. \quad (2.20)$$

The quantity δ is related to the deformation parameter β_2 , as follows [47]

$$\delta \approx \frac{3}{2} \sqrt{\frac{5}{4\pi}} \beta_2 \approx 0.95 \beta_2. \quad (2.21)$$

In the case of axial symmetry, it is more convenient to use cylindrical coordinates, and in this case the eigenvalues can be written as

$$\begin{aligned} \epsilon_0(n_z, n_\rho, n_l) &= \hbar\omega_z(n_z + \frac{1}{2}) + \hbar\omega_\perp(2n_\rho + m_l + 1) \\ &\approx \hbar\omega_0(N + \frac{3}{2}) + \delta(\frac{N}{3} - n_z), \end{aligned} \quad (2.22)$$

with

$$N = n_z + 2n_\rho + m_l = n_x + n_y + n_z. \quad (2.23)$$

Now, if one treats Eq. 2.13 by using the first order perturbation theory [43], we can obtain

$$\begin{aligned} E &= \langle N n_z \Lambda \Omega | H | N n_z \Lambda \Omega \rangle \\ &= (N + \frac{3}{2}) \hbar \omega_0 + \frac{1}{3} \delta \hbar \omega_0 (N - 3n_z) - 2\kappa \hbar \Lambda \Sigma \\ &\quad - \mu' \hbar \omega_0 (\Lambda^2 + 2n_\perp n_z + 2n_z + n_\perp - \frac{N(N+3)}{2}), \end{aligned} \quad (2.24)$$

where N is the principal quantum number, Σ is projection of the spin of the particle s on the symmetry axis, Λ is projection of the orbital angular momentum on the symmetry axis, and n_z is number of oscillator quanta (see Fig. 2.5).

The Nilsson orbitals are often denoted by a set of quantum numbers

$$\Omega^\pi [N n_z \Lambda],$$

where Ω is projection of single-particle angular momentum on the symmetry axis, and π is the parity of the state [$\pi = (-1)^l = (-1)^N$].

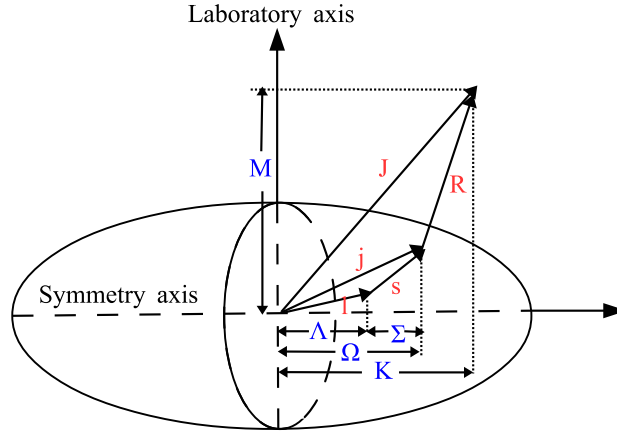


Figure 2.5: Schematic of the quantum numbers which can describe the deformed nucleus. Λ , Ω , Σ , and K are the projections of the orbital angular momentum l , of the total angular momentum of the particle j , of the spin of the particle s , and of the total angular momentum J onto the symmetry axis, respectively. In addition, \vec{R} is the angular momentum of the core and M is the projection of the total angular momentum onto the laboratory axis.

The Nilsson orbitals as function of the ϵ_2 deformation are often summarized in a Nilsson diagram. Parts of Nilsson diagram for neutrons and protons in the $A \approx 130$ mass region are given in Fig. 2.6 and Fig. 2.7, respectively.

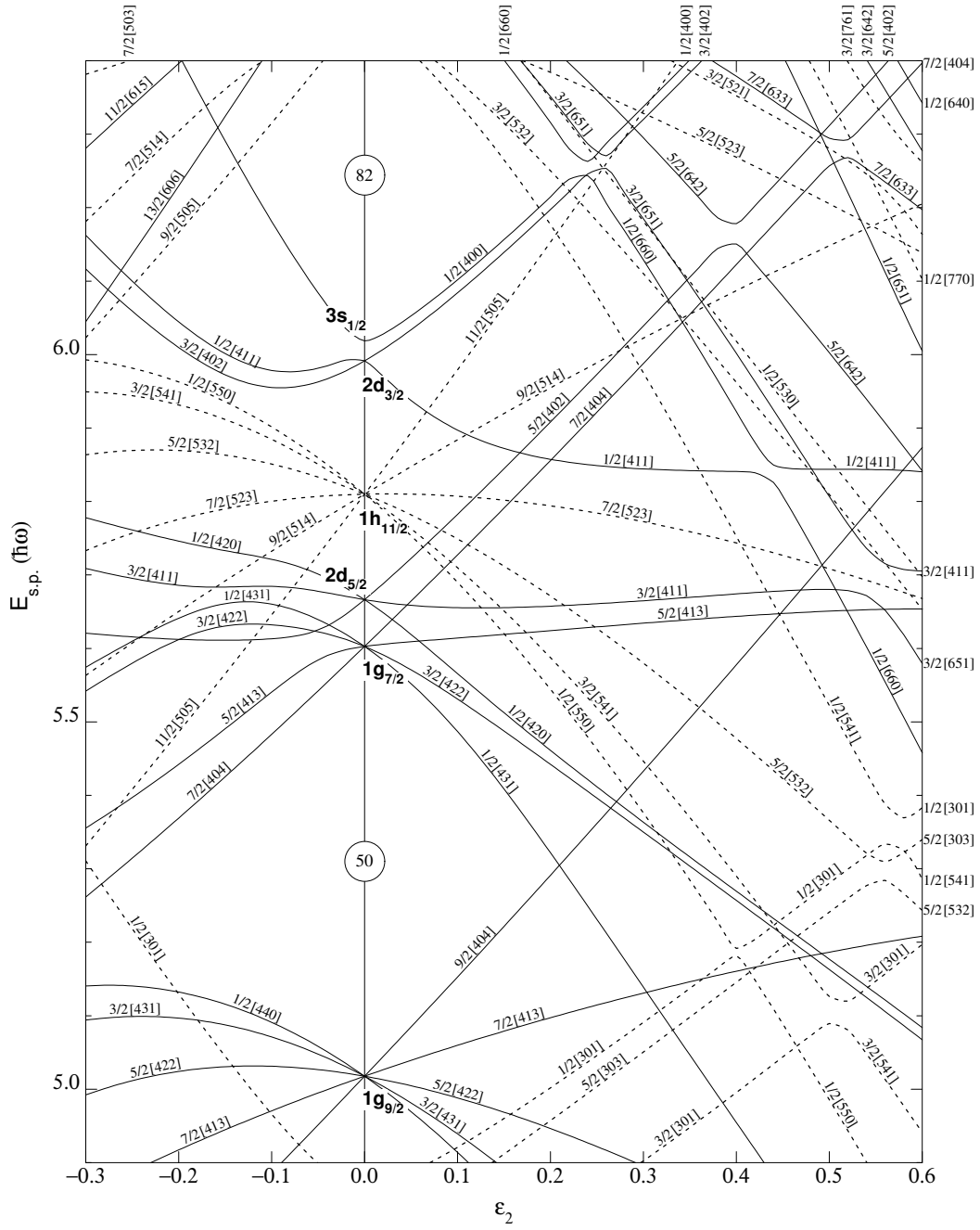


Figure 2.6: Nilsson diagram for protons in the $50 \leq Z \leq 80$ region showing the single-particle energies as a function of the deformation parameter ϵ_2 . For $\epsilon_2 > 0$, corresponding to the prolate shape; for $\epsilon_2 = 0$, corresponding to the spherical shape; for $\epsilon_2 < 0$, corresponding to the prolate shape. Labels obey the $\Omega^\pi[Nn_z\Lambda]$ rule.

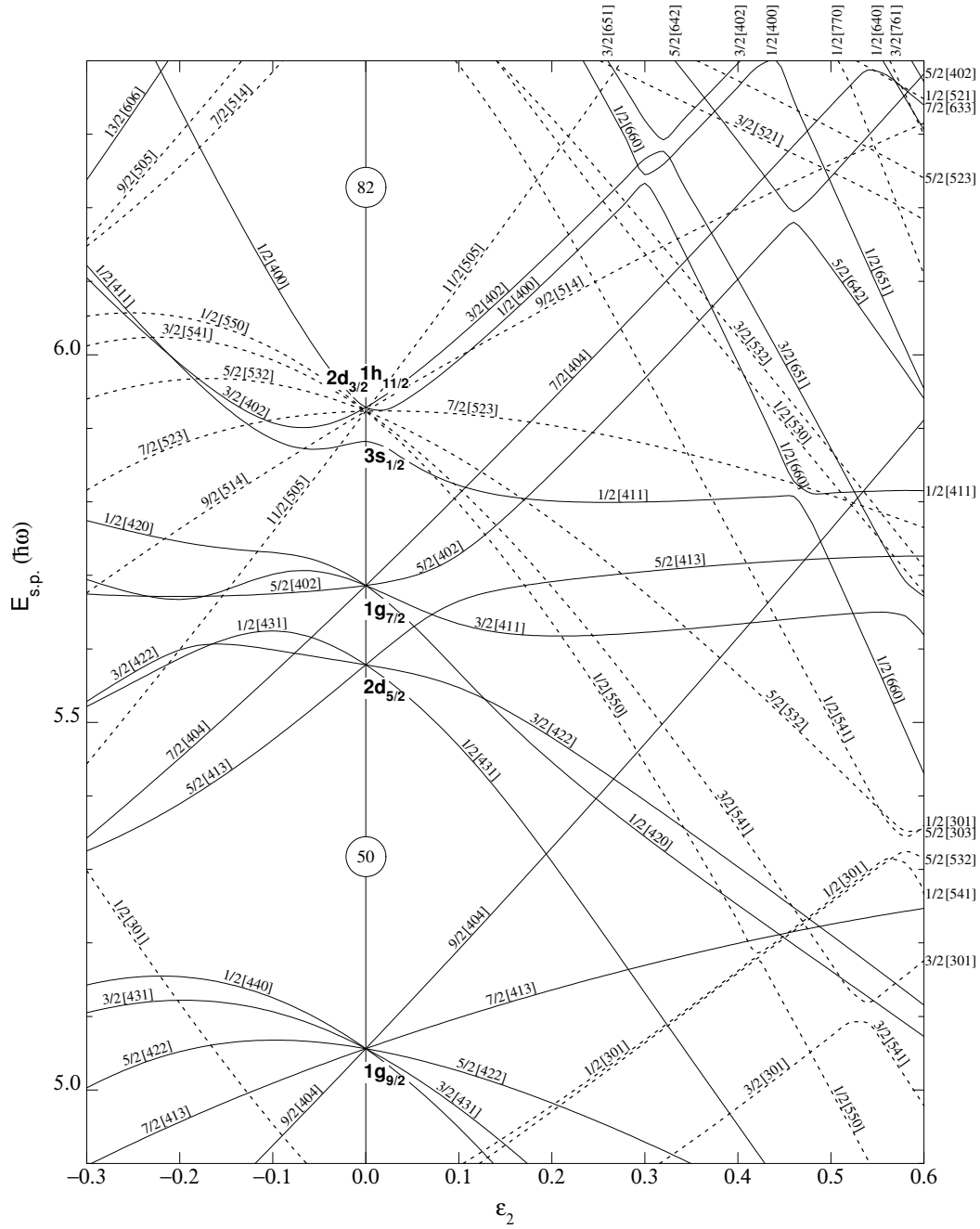


Figure 2.7: Nilsson diagram for neutrons in the $50 \leq N \leq 80$ region showing the single-particle energies as a function of the deformation parameter ϵ_2 . For $\epsilon_2 > 0$, corresponding to the prolate shape; for $\epsilon_2 = 0$, corresponding to the spherical shape; for $\epsilon_2 < 0$, corresponding to the oblate shape. Labels obey the $\Omega^\pi[Nn_z\Lambda]$ rule.

2.4 Particle-rotor model

The unified nuclear model and its consequences, especially for the nuclear properties pertaining to the ground states and to the low energy region of excitation has been proposed by Bohr and Mottelson in 1953 [50]. It core describes the interplay between the motion of particles and of the collective. In this model, one considers only a few valence particles which move more or less independently in the deformed potential well of the core, and one couple them to a collective rotor which represents the rest of the particles.

The simplest model consists of a particle in a single shell coupled to a rotor. Generally speaking, one divides the Hamiltonian into two parts: an intrinsic part H_{intr} , which describes microscopically a valence particle, and a collective rotor part H_{rot} , which describes the rotations of the inert core. The total Hamiltonian is written as

$$H = H_{intr} + H_{rot}. \quad (2.25)$$

The intrinsic part has the form

$$H_{intr} = \sum_{i=1}^4 \sum_{\nu} \varepsilon_{i,\nu} a_{i,\nu}^{\dagger} a_{i,\nu} + \frac{1}{4} \sum_{klmn} \bar{v}_{klmn} a_k^{\dagger} a_l^{\dagger} a_n a_m, \quad (2.26)$$

where $\varepsilon_{i,\nu}$ is the single-particle energy in the i -th single- j shell and \bar{v} is the interaction between the valence particles (residual interaction) which is often neglected.

The collective rotor Hamiltonian reads:

$$H_{rot} = \frac{R_1^2}{2\mathcal{J}_1} + \frac{R_2^2}{2\mathcal{J}_2} + \frac{R_3^2}{2\mathcal{J}_3}, \quad (2.27)$$

where the R_i are the body-fixed components of the collective angular momentum of the core. The total angular momentum is $I = R + j$, where j is the angular momentum of the valence nucleons. Thus, H_{rot} can be expanded into three parts:

$$H_{rot} = \sum_{i=1}^3 \frac{I_i^2}{2\mathcal{J}_i} + \sum_{i=1}^3 \frac{j_i^2}{2\mathcal{J}_i} - \sum_{i=1}^3 \frac{I_i j_i}{\mathcal{J}_i}, \quad i = 1, 2, 3. \quad (2.28)$$

The first term is a pure rotational operator of the rotor which acts only on the intrinsic coordinates; the second term called recoil term, acts on the coordinates of the valence particle; the third term couples the degrees of freedom of the valence particles to the degrees of the freedom of the rotor.

According to the physical situation, there are two important limit cases of the above Hamiltonian, namely, *strong coupling (deformation alignment)* and *decoupling (rotation alignment)*.

2.4.1 Strong coupling

Assuming that the rotor has the 3-axis being the symmetry axis, the moments of inertia $\mathcal{J}_1 = \mathcal{J}_2 = \mathcal{J}$ and $K = \Omega$, the corresponding rotor Hamiltonian can be rewritten as

$$\begin{aligned} H_{rot} &= \frac{1}{2\mathcal{J}} [(I_1 - j_1)^2 + (I_2 - j_2)^2] \\ &= \frac{1}{2\mathcal{J}} [I^2 + (j_1^2 + j_2^2 - j_3^2) - (I_+ j_- + I_- j_+)], \end{aligned} \quad (2.29)$$

where $I_{\pm} = I_1 \pm I_2$ and $j_{\pm} = j_1 \pm j_2$. The term $(I_+ j_- + I_- j_+)$ corresponds to the classically Coriolis and centrifugal forces, which generates a coupling between the particle motion and the collective rotation. For small I , we can assume that this term is small and we just need to take into account its diagonal contributions, i.e., it's treated in first order perturbation theory. This approximation, in which it is assumed that the influence of the rotational motion in the intrinsic frame of the nucleus can be ignored, is always referred to as the adiabatic approximation or the strong coupling limit [43].

In this strong coupling case, K is a good quantum number. The angular momentum j of the valence particle is strongly coupled to the the motion of the rotor (see Fig. 2.8), leading to j perpendicular to the R : this gives rise to a band $I = K, I = K + 1, I = K + 2, \dots$. The total energy is given by

$$E_{IK} = E_K + \frac{1}{2\mathcal{J}} [I(I + 1) - K^2], \quad K \neq \frac{1}{2}, \quad (2.30)$$

where E_K is the quasiparticle energy.

For $K = \frac{1}{2}$, the total energy is

$$E_{IK} = E_K + \frac{1}{2\mathcal{J}} [I(I + 1) + a(-1)^{I+1/2}(I + 1/2)], \quad (2.31)$$

where a is the decoupling factor which is calculated by

$$a = - \sum_{nj} |C_{nj}|^2 (-1)^{j+1/2} (j + \frac{1}{2}). \quad (2.32)$$

2.4.2 The decoupling limit

In the decoupling case, the Coriolis force is strong and the coupling of the active particle to the deformed core can be neglected. The total angular momentum I is parallel to the single-particle angular momentum j (see Fig. 2.9). This gives rise to the typical $\Delta I = 2$ bands. For a more detailed discussion see Refs. [3, 43].

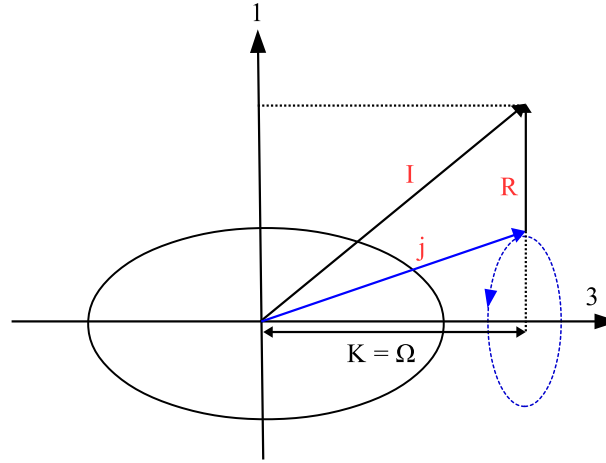


Figure 2.8: Schematic diagram of the strong coupling limit in the particle-rotor model.

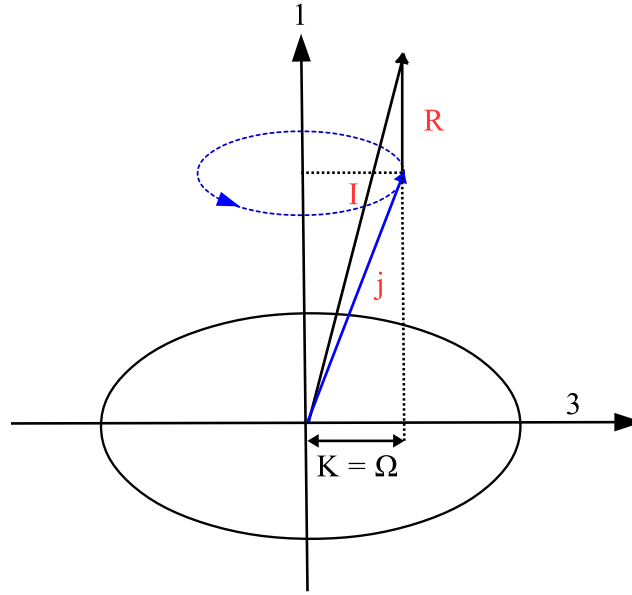


Figure 2.9: Schematic diagram of the decoupling limit in the particle-rotor model.

2.4.3 Four- j shells particle-rotor model

Theoretically, various particle-rotor models have been developed to investigate the exotic nuclear structure, in particular the nuclear chirality. For example, one-particle-one-hole PRM combined with the tilted axis cranking (TAC) approximation was first developed to study the chirality in the odd-odd nuclei [20]. Later, in order to treat more than one valence proton and one valence neutron, and also to study the nuclear chirality, the n -particle-

n -hole PRM with nucleons in two single- j shells [51, 52] and three single- j shells [25, 26, 53, 54] have been developed, respectively. In the present work, we observed five pairs of doublet bands in ^{136}Nd , with configurations involving four different single- j shells, which can not be treated by any PRM model available at the time when the experimental results were obtained. Inspired by the new obtained results in ^{136}Nd , a n -particle- n -hole version of the PRM with nucleons in four single- j shells was developed [55].

The total Hamiltonian of the PRM model which couples nucleons in four single- j shells to a triaxial rotor is similar to that of Eq. 2.25. The collective rotor Hamiltonian H_{rot} is expressed as

$$H_{rot} = \sum_{k=1}^3 \frac{R_k^2}{2\mathcal{J}_k} = \sum_{k=1}^3 \frac{(I_k - j_k)^2}{2\mathcal{J}_k}, \quad (2.33)$$

where the indexes $k = 1, 2$, and 3 refer to the three principal axes of the body-fixed frame, R_k , I_k , and j_k denote the angular momentum of the core, of the total nucleus, and of the valence nucleon, respectively. The moments of inertia of the irrotational flow [3] are adopted, i.e., $\mathcal{J}_k = \mathcal{J}_0 \sin^2(\gamma - 2k\pi/3)$. Additionally, the intrinsic Hamiltonian for valence nucleons is written as

$$H_{intr} = \sum_{i=1}^4 \sum_{\nu} \varepsilon_{i,\nu} a_{i,\nu}^{\dagger} a_{i,\nu}, \quad (2.34)$$

where $\varepsilon_{i,\nu}$ is the single-particle energy in the i -th single- j shell given by

$$h_{sp} = \pm \frac{1}{2} C \left\{ \cos \gamma \left[j_3^2 - \frac{j(j+1)}{3} \right] + \frac{\sin \gamma}{2\sqrt{3}} (j_+^2 + j_-^2) \right\}, \quad (2.35)$$

where the plus sign refers to a particle, the minus to a hole, and the parameter C is responsible for the level splitting in the deformed field and directly proportional to the quadrupole deformation β_2 as in Ref. [56].

The single-particle state and its time reversal state are expressed as

$$a_{\nu}^{\dagger} |0\rangle = \sum_{\alpha\Omega} c_{\alpha\Omega}^{\nu} |\alpha, j\Omega\rangle, \quad (2.36)$$

$$a_{\bar{\nu}}^{\dagger} |0\rangle = \sum_{\alpha\Omega} (-1)^{j-\Omega} c_{\alpha\Omega}^{\nu} |\alpha, j-\Omega\rangle, \quad (2.37)$$

where Ω is the projection of the single-particle angular momentum j along the 3-axis of the intrinsic frame and restricted to $\dots, -3/2, 1/2, 5/2, \dots$ due to the time-reversal degeneracy, and α denotes the other quantum numbers. For a system with $\sum_{i=1}^4 N_i$ valence nucleons (N_i denotes the number of the nucleons in the i -th single- j shell), the intrinsic wave function is given as

$$|\varphi\rangle = \prod_{i=1}^4 \left(\prod_{l=1}^{n_i} a_{i,\nu_l}^{\dagger} \right) \left(\prod_{l=1}^{n'_i} a_{i,\bar{\mu}_l}^{\dagger} \right) |0\rangle, \quad (2.38)$$

with $n_i + n'_i = N_i$ and $0 \leq n_i \leq N_i$.

The total wave function can be expanded into the strong coupling basis

$$|IM\rangle = \sum_{K\varphi} c_{K\varphi} |IMK\varphi\rangle, \quad (2.39)$$

with

$$|IMK\varphi\rangle = \frac{1}{\sqrt{2(1 + \delta_{K0}\delta_{\varphi,\bar{\varphi}})}} [|IMK\rangle |\varphi\rangle + (-1)^{I-K} |IM-K\rangle |\bar{\varphi}\rangle], \quad (2.40)$$

where $|IMK\rangle$ is the Wigner function $\sqrt{\frac{2I+1}{8\pi^2}} D_{MK}^I$, and φ is a shorthand notation for the configurations in Eq. 2.38. The basis states are symmetrized under the point group D_2 , which leads to $K - \frac{1}{2} \sum_{i=1}^4 (n_i - n'_i)$ being an even integer.

Once obtained the wave functions of the PRM, the reduced transition probabilities $B(M1)$ and $B(E2)$ can be calculated with the $M1$ and $E2$ operators [57].

Note that due to the inclusion of n -particle- n -hole configurations with four single- j shells, the size of the basis space is quite large. It is rather time-consuming in the diagonalization of the PRM Hamiltonian matrix. In order to solve this problem, a properly truncated basis space by introducing a cutoff for the configuration energy $\sum_{i,\nu} \varepsilon_{i,\nu}$ was adapted which is similar in the shell-model-like approach (SLAP) [58, 59]. In this way, the dimension of the PRM matrix is reduced to ~ 5000 - 10000 , while maintaining the energy uncertainty within 0.1% [55].

This new version of the PRM has been applied to investigate the energy spectra, the electromagnetic transition probabilities, as well as the angular momentum geometries of the five pairs of nearly degenerate doublet bands in ^{136}Nd , which are discussed in detail in Section. 5.2.2.

2.5 Cranked Nilsson-Strutinsky model

One of the most important and widely used models in the high-spin study is the cranked Nilsson-Strutinsky (CNS) model [60–63], which successfully describes the high-spin states of nuclei. In the present work, this model was applied to discuss the various band structures in ^{136}Nd (see Section. 5.2.3). In the Nilsson-Strutinsky method, the total energy of the nucleus is split into an average part, parametrized by a macroscopic expression, and a fluctuating part extracted from the variation of the level density around the Fermi surface. The microscopic part using the Strutinsky shell correction [63].

2.5.1 Cranking model

To get a deeper insight into the properties of rotating nuclei from a microscopic point of view, the cranking model was introduced by Inglis [64, 65]. The

basic idea of the cranking model is the following classical assumption: if one introduces a coordinate system which rotates with constant angular velocity ω around x -axis, the motion of the nucleon in the rotating frame is rather simple when the angular frequency is properly chosen; in particular, the nucleons can be thought of as independent particles moving in an average potential well which is rotating with the coordinate frame [3].

The single-particle Hamiltonian in the rotating system h_ω is given as,

$$h_\omega = h - \omega j_x, \quad (2.41)$$

where h is the single-particle Hamiltonian in the laboratory system and j_x is the x -component of the single-particle angular momentum.

Thus, the total energy in the laboratory system is calculated as,

$$E_{tot} = \sum_i \langle \Phi_i^\omega | h | \Phi_i^\omega \rangle = \sum_i e_i^\omega + \sum_i \omega \langle \Phi_i^\omega | j_x | \Phi_i^\omega \rangle, \quad (2.42)$$

and the total spin I is

$$I \approx I_x = \sum_i \langle \Phi_i^\omega | j_x | \Phi_i^\omega \rangle, \quad I \gg 1, \quad (2.43)$$

where Φ_i^ω are the single-particle eigenfunction in the rotating system and $e_i^\omega = \langle \Phi_i^\omega | h_\omega | \Phi_i^\omega \rangle$ the corresponding eigenvalues, also called single-particle *Routhians*. The slope of the Routhian corresponds to the alignments i_x . It is written as

$$i_x = -\frac{de_i^\omega}{d\omega}. \quad (2.44)$$

Note that the Eq. 2.41 Hamiltonian is dependent on the rotational frequency ω , and therefore it breaks the time-reversal symmetry, but remains invariant with respect to space inversion (parity invariance), which means that the parity (π) is a good quantum number. In addition, the cranking Hamiltonian is invariant with respect to rotation through an angle π around the rotating axis [60].

$$R_x(\pi) = e^{-i\pi j_x}, \quad (2.45)$$

with eigenvalue

$$r = e^{-i\pi\alpha}, \quad (2.46)$$

where α is the signature quantum number. The single-particle orbitals can be classified with respect to the signature quantum number α , which can take values $\alpha_i = +\frac{1}{2}$ ($r_i = -i$) or $\alpha_i = -\frac{1}{2}$ ($r_i = i$). In addition, the signature α relates to the total angular momentum.

For a system with an even number of nucleons,

$$\begin{aligned} \alpha = 0 \quad (r = +1), \quad I = 0, 2, 4, \dots, \\ \alpha = 1 \quad (r = -1), \quad I = 1, 3, 5, \dots \end{aligned} \quad (2.47)$$

For a system with an odd number of nucleons,

$$\begin{aligned}\alpha &= +\frac{1}{2} \ (r = -i), \quad I = \frac{1}{2}, \frac{5}{2}, \frac{9}{2} \dots, \\ \alpha &= -\frac{1}{2} \ (r = +i), \quad I = \frac{3}{2}, \frac{7}{2}, \frac{11}{2} \dots.\end{aligned}\tag{2.48}$$

As mentioned above, the parity π is a good quantum number, which together with the signature α can be used to describe the Routhians of the quasiparticles.

The advantage of using the cranking model is that it gives a microscopic description of rotating nuclei, in which the total angular momentum is the sum of single-particle angular momenta, and thus collective and non-collective rotations can be treated on the same footing. However, this model is a semi-classical approximation due to the fact that the rotation is imposed externally. A fixed rotation axis is used in the model which also breaks the rotational invariance. In addition, another important shortcoming of the cranking model is that the wave functions are not eigenstates of the angular momentum operator, which causes difficulties, i.e., a proper calculation of the electromagnetic transition probabilities [43, 60].

The rotating harmonic oscillator

Many features of the high-spin structure of nuclei can be easily illustrated with the rotating (cranked) harmonic oscillator potential because of its simplicity, and allowing to express in analytic form all matrix elements.

If only the orbital angular momentum is considered, the cranking Hamiltonian reads

$$h^\omega = h_{osc} - \omega l_1, \tag{2.49}$$

where

$$h_{osc} = -\frac{\hbar^2}{2m} \Delta + \frac{m}{2} (\omega_1^2 x_1^2 + \omega_2^2 x_2^2 + \omega_3^2 x_3^2), \tag{2.50}$$

and

$$l_1 = x_2 p_3 - x_3 p_2. \tag{2.51}$$

The oscillator frequencies ω_1 , ω_2 and ω_3 are expressed in the standard way through the deformation coordinates ϵ_2 and γ [66]:

$$\omega_i = \omega_0(\epsilon_2, \gamma) \left[1 - \frac{2}{3} \epsilon_2 \cos(\gamma + i \frac{2\pi k}{3}) \right] \quad i = 1, 2, 3. \tag{2.52}$$

Introducing boson creation and annihilation operators, a_i^+ and a_i , see Ref. [60], the cranking Hamiltonian Eq. 2.49 can be written in the form

$$h^w = \sum_{i=1}^3 \hbar \omega_i (a_i^+ a_i + \frac{1}{2}) - \omega l_1, \tag{2.53}$$

where

$$l_1 = \frac{\omega_2 + \omega_3}{2(\omega_2\omega_3)^{1/2}}(a_2^\dagger a_3 + a_3^\dagger a_2) - \frac{\omega_2 - \omega_3}{2(\omega_1\omega_3)^{1/2}}(a_2^\dagger a_3^\dagger + a_2 a_2). \quad (2.54)$$

Now, we can get the single-particle eigenvalues of h^ω [43]

$$e_v^\omega = \hbar\omega_1(n_1 + \frac{1}{2}) + \hbar\omega_\alpha(n_\alpha + \frac{1}{2}) + \hbar\omega_\beta(n_\beta + \frac{1}{2}), \quad (2.55)$$

where n_1, n_α and n_β specify the number of quanta in the three normal-mode degrees of freedom (*directions*).

A further quantity of interest is the expectation value of l_1 . The diagonal parts of this operator are easily obtained and thus, for an orbital that is characterized by the occupation numbers n_1, n_α and n_β :

$$\langle l_1 \rangle \approx (\frac{p}{1+p^2})^{1/2}(n_\beta - n_\alpha). \quad (2.56)$$

The total quantities of the A -particle system will now be considered with the A -particles generally filling the lowest or close-to-lowest energy orbitals of the cranked harmonic oscillator. For this purpose, we define the quantities

$$\Sigma_k = \sum_{\nu \text{ occ}} \langle \nu | a_k^\dagger a_k + \frac{1}{2} | \nu \rangle = \sum_{\nu \text{ occ}} (n_k + \frac{1}{2})_\nu. \quad (2.57)$$

The index k takes the values $k = 1, \alpha$, and β (or $k = 1, 2$ and 3 for $\omega = 0$) and the summation extends over the occupied orbitals, $|\nu\rangle$. Then the specific configuration in the rotating frame is defined by $(\Sigma_1, \Sigma_\alpha, \Sigma_\beta)$.

The total energy in the rotating system is given by

$$E = \sum_{\nu \text{ occ}} \langle \nu | h^\omega | \nu \rangle = \hbar\omega_1 \Sigma_1 + \hbar\omega_\alpha \Sigma_\alpha + \hbar\omega_\beta \Sigma_\beta. \quad (2.58)$$

The total energy in the laboratory system is calculated as the sum of expectation values of the Hamiltonian h_{osc}

$$E = \sum_{\nu \text{ occ}} \langle \nu | h_{osc} | \nu \rangle = \sum_{\nu \text{ occ}} \langle \nu | h^\omega + \omega l_1 | \nu \rangle = E^\omega + \omega I. \quad (2.59)$$

In addition, for a fixed configuration $(\Sigma_1, \Sigma_\alpha, \Sigma_\beta)$ and spin I , the minimized energy E can be obtained.

The cranked single-particle Nilsson Hamiltonian

The cranked single-particle Nilsson Hamiltonian h^ω is given by [61]

$$h^\omega = h_{h.o.}(\epsilon_2, \gamma) + 2\hbar\omega_0\rho^2\epsilon_4 V_4(\gamma) + V' - \omega j_x, \quad (2.60)$$

where $h_{h.o.}(\epsilon_2, \gamma)$ is the anisotropic harmonic oscillator Hamiltonian, ρ is the radius in the stretched coordinate system.

The hexadecapole deformation potential $V_4(\gamma)$ is defined to obtain a smooth variation in the γ -plane, so it does not break the axial symmetry when $\gamma = -120^\circ, -60^\circ, 0^\circ$, and 60° . It has the form

$$V_4(\gamma) = a_{40}Y_{40} + a_{42}(Y_{42} + Y_{4-2}) + a_{44}(Y_{44} + Y_{4-4}), \quad (2.61)$$

where the parameters a_{4i} are chosen as

$$a_{40} = \frac{1}{6}(5\cos^2\gamma + 1), \quad a_{42} = -\frac{1}{12}\sqrt{30}\sin 2\gamma, \quad a_{44} = \frac{1}{12}\sqrt{70}\sin^2\gamma. \quad (2.62)$$

The term V' is the Nilsson potential which as defined in Ref. [47].

The diagonalization of the Hamiltonian of Eq. 2.60 gives the eigenvalues e_i^ω and eigenfunctions of the eigenvectors Φ_i^ω . Furthermore, the single-particle energies in the laboratory system and the single-particle angular momentum alignments in the rotating system can be obtained.

Note that the sum over the occupied single-particle states from phenomenological potentials, such as the Nilsson or Woods-Saxon potentials, turned out to yield poor approximations to average nuclear properties and their deformation dependence [3]. To overcome these problems, the total energies are renormalized to a rotating liquid drop behaviour.

2.5.2 The rotating liquid drop model

The energy of a rotating nuclear liquid drop at the fixed spin I_0 has the form

$$E_{RLD}(I_0) = E_{LD}(I = 0) + \frac{1}{2\mathcal{J}_{rig}(\bar{\epsilon})}I_0^2, \quad (2.63)$$

where $\mathcal{J}_{rig}(\bar{\epsilon})$ is the rigid body moment of inertia and $\bar{\epsilon} = (\epsilon_2, \gamma, \epsilon_4 \dots)$. The total energy in the liquid-drop model is given by [60]

$$\begin{aligned} E_{RLD}(I_0) = & -a_v \left[1 - k_v \left(\frac{N-Z}{A} \right)^2 \right] A + \frac{3}{5} \frac{e^2 Z^2}{R_c} [B_c(\bar{\epsilon}) - \frac{5\pi^2}{6} \left(\frac{d}{R_c} \right)^2] \\ & + a_s \left[1 - k_s \left(\frac{N-Z}{A} \right)^2 \right] A^{2/3} B_s(\bar{\epsilon}), \end{aligned} \quad (2.64)$$

where $B_c(\bar{\epsilon})$ and $B_s(\bar{\epsilon})$ are the coulomb and surface energies of a nucleus with a sharp surface in units of their corresponding values at a spherical shape [60], respectively. The second term in the Coulomb energy is a (shape-independent) diffuseness correction with d being the diffuseness. In addition, we often define the Coulomb energy constant a_c as $a_c = \frac{3}{5} \frac{e^2}{R_c}$.

2.5.3 The configuration-dependent CNS approach

Following the standard Nilsson-Strutinsky method [61, 67], the total nuclear energy E_{tot} at a specific deformation $\bar{\epsilon}$ and a specific spin I_0 is obtained as a sum of the rotating liquid drop energy and the shell correction energy

$$E_{tot}(\bar{\epsilon}, I_0) = E_{LD}(\bar{\epsilon}, I = 0) + \frac{1}{2\mathcal{J}_{rig}(\bar{\epsilon})}I_0^2 + E_{sh}(\bar{\epsilon}, I_0). \quad (2.65)$$

The shell correction energy is defined as the difference between the discrete and smoothed single-particle energy sums,

$$E_{sh}(I_0) = \sum e_i(\omega, \bar{\epsilon}) \Big|_{I=I_0} - \sum \tilde{e}_i(\tilde{\omega}, \bar{\epsilon}) \Big|_{\tilde{I}=I_0}, \quad (2.66)$$

where the smoothed sum (indicated by \sim) is calculated using the Strutinsky procedure [43, 67]. In the numerical calculations, it is parametrized as

$$\sum \tilde{e}_i(\tilde{\omega}, \bar{\epsilon}) \Big|_{\tilde{I}=I_0} = \sum \tilde{e}_i(\tilde{\omega}, \bar{\epsilon}) \Big|_{\tilde{I}=0} + \frac{1}{2\mathcal{J}_{str}(\bar{\epsilon})}I_0^2 + bI_0^4, \quad (2.67)$$

where \mathcal{J}_{str} is the (Strutinsky) smoothed moment of inertia and E_0 is the value of $\sum \tilde{e}_i(\tilde{\omega}, \bar{\epsilon}) \Big|_{\tilde{I}=I_0}$ for $\tilde{I} = 0$. The E_0 , I_0^2 , and bI_0^4 terms were introduced in Ref. [49]. The constants \mathcal{J}_{str} , E_0 , and b are determined by calculating the smoothed sum at the different frequencies (see Ref. [49]). Using these formulas, we can calculate the total nuclear energy as a function of spin I at any deformation.

Furthermore, in order to get a better physical understanding of the relation between the level density and the shell energy, it is useful to rewrite these equations slightly and make some approximations. A quasi-shell energy is defined as

$$E_{quasi-sh}(\omega, \bar{\epsilon}) = \sum e_i(\omega, \bar{\epsilon}) - \sum \tilde{e}_i(\omega, \bar{\epsilon}). \quad (2.68)$$

This definition is important because it shows that the numerical values of E_{sh} and $E_{quasi-sh}$ are very similar. The E_{sh} is defined exactly analogous to the static shell energy. Thus, ω enters very much as a deformation and we can take over all our experience from the static case.

In order to obtain the renormalized frequency, the formulas above are combined by rewriting the total energy as

$$E_{tot}(I_0) = \sum e_i(\omega, \bar{\epsilon}) \Big|_{I=I_0} + E_{LD}(\bar{\epsilon}, I = 0) - E_0 + \left\{ \frac{1}{2\mathcal{J}_{rig}} - \frac{1}{2\mathcal{J}_{str}} \right\} I_0^2 - bI_0^4. \quad (2.69)$$

With the frequency given by $\partial E / \partial I$, the resulting renormalized frequency is

$$\omega_{ren}(I_0) = \omega + \left(\frac{1}{2\mathcal{J}_{rig}} - \frac{1}{2\mathcal{J}_{str}} \right) I_0 + bI_0^4, \quad (2.70)$$

where b value is always very small, thus we can neglect the bI_0^4 term. Furthermore, for highly deformed bands with no pairing $I = \mathcal{J}_{str}\omega$, using this approximation, we can obtain

$$\omega_{ren} = (\mathcal{J}_{str}/\mathcal{J}_{rig})\omega. \quad (2.71)$$

With this renormalization being in the range 1.2-1.3, depending on the deformation, frequencies in Routhian diagrams are directly comparable with experimentally observed frequencies only if the Routhians are plotted as a function of ω_{ren} .

Note that in the present used version of the cranked Nilsson-Strutinsky model the pairing correlations have been neglected. The neglect of pairing has an advantage in that the tracing of a fixed configuration undergoing drastic deformation changes becomes possible over the considerable spin range of a band up to termination. Furthermore, in the present study, we are mainly interested in the very high spin states of nuclei, for which the deformation changes play an more important role than the pairing.

2.6 Tilted axis cranking covariant density functional theory

Magnetic rotation is an exotic rotational phenomenon observed in weakly deformed or near-spherical nuclei which are interpreted in terms of the shears mechanism [68]. Since their first observation, the magnetic bands have been mainly investigated in the framework of tilted axis cranking (TAC) [20, 69, 70]. In the last decades, the covariant density functional theory (CDFT) and its extensions have been proved to be successful in describing a series of nuclear properties, like ground-states and excited states, radii, single-particle spectra, magnetic rotation, and collective motions, etc. Recently, the tilted axis cranking covariant density functional theory (TAC-CDFT) [71–75] has been developed and applied for the description of the chiral bands.

2.6.1 Tilted axis cranking

In the standard cranking model, it is assumed that the rotational axis coincides with one of the principal axes of the deformed density distribution. Such principal axis cranking (PAC) solutions always exist. In the TAC approach, the rotational axis does not coincide with any principal axis. At difference from the PAC model, the signature is not a good quantum number. The TAC model is based on the mean field theory that permits the calculation of the orientation of the deformed field in space together with the parameters that define its shape. Thus, one may easily study multi-quasiparticle excitations, and the consequences of changes of the deformation or the pairing. It

gives transparent classical vector diagram pictures of the angular momentum coupling, which is of great help to understand the structure of rotation bands. The drawback of the TAC model is that it cannot describe the gradual onset of signature splitting as well as the mixing of bands with substantially different quasiparticle angular momentum as in the standard cranking theory [71].

Assuming that the rotational axis is the z -axis and with a constant angular velocity ω , the corresponding Hamiltonian in intrinsic frame is given as

$$H' = H - \omega J_z. \quad (2.72)$$

In Ref. [70], the H term is defined as a sum of the spherical Hamiltonian and the pairing plus quadrupole interaction,

$$H = H_{sph} - \frac{\chi}{2} \sum_{\mu=-2}^2 Q_{\mu}^+ Q_{\mu} - GP^+P - \lambda N, \quad (2.73)$$

with the spherical part

$$H_{sph} = \sum_k \epsilon_k c_k^+ c_k, \quad (2.74)$$

where H_{sph} is parameterized in the same way as the Nilsson Hamiltonian, the pairing interaction is defined by the monopole pair field P^+ , the quadrupole interaction is defined by the operators Q_{μ} , and λ is the chemical potential. As written above all expressions are only accounting for one kind of particles. Thus, they are understood as sums of a proton and a neutron part, and the terms $-GP^+P$ and $-\lambda N$ for both protons and neutrons. In practice, the actual values of the force constants χ and G depend on the configuration space under consideration and are determined from experimental data. A detailed description of the TAC model can be found in the Refs. [3, 7, 69, 70]. As in the present work we are interested in the chiral motion, in the following we will examine the TAC solutions for specific rotation axes.

Rotation about a principal axis

If the axis of rotation (z) coincides with one of the principal axes, the orientation angles defined as in the case of spherical coordinates, are satisfying the condition:

$$\theta = 0, \quad \frac{\pi}{2}; \quad \phi = 0, \quad \frac{\pi}{2}. \quad (2.75)$$

The upper panel of Fig. 2.10 shows this case, in which J has the direction of one of the principal axes and $R_z(\pi)$ satisfies the relation

$$R_z(\pi)|\rangle = e^{-i\alpha\pi}|\rangle, \quad (2.76)$$

which means that the signature quantum number α takes the values $I = \alpha + 2n$, $n = \pm 1, \pm 2, \dots$, giving rise to a band characterized by $\Delta I = 2$ transitions.

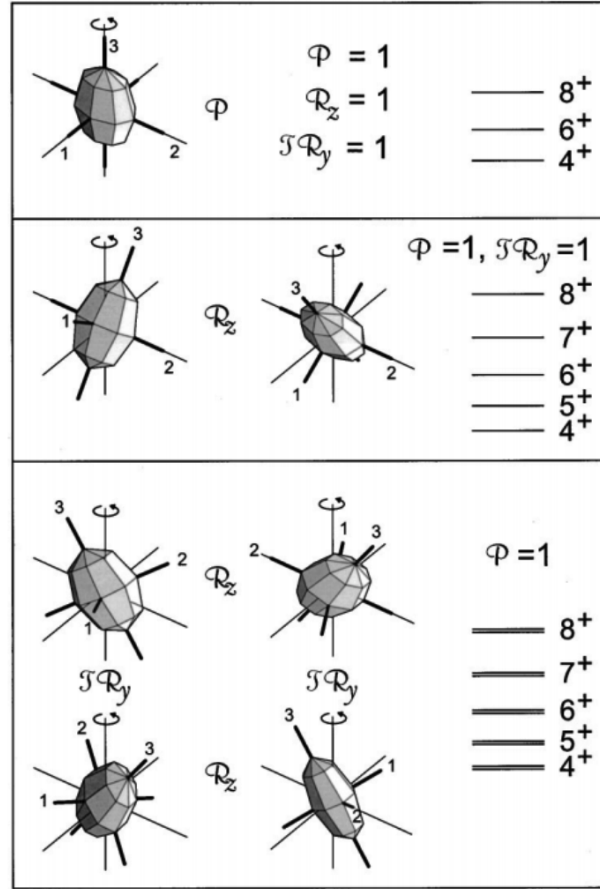


Figure 2.10: Discrete symmetries of the mean field of a rotating triaxial reflection symmetric nucleus. The axis of rotation (z) is marked by the circular arrow. The rotational band structures associated with each symmetry type are presented on the right side. This figure was taken from Ref. [7].

Rotation around an axis in a principal plane

If the axis of rotation (z) does not coincide with any of the principal axes, but still lies in one of the three principal planes, we call such solution *planar*. The orientation angles satisfy the relations:

$$\theta \neq 0, \frac{\pi}{2}; \quad \phi = 0, \frac{\pi}{2},$$

or

$$\theta = 0, \frac{\pi}{2}; \quad \phi \neq 0, \frac{\pi}{2}.$$

The middle panel of Fig. 2.10 displays this case, in which the axis of rotation lies in one of the three principal planes 1-2, 2-3 or 1-3 and the $R_z(\pi)$ symmetry is broken, that is it satisfies the relation

$$R_z(\pi)|\rangle \neq e^{-i\alpha\pi}|\rangle, \quad (2.78)$$

which means the signature is not a good quantum number anymore and thus there is no restriction on the angular momentum I , giving rise to a band characterized by $\Delta I = 1$ transitions..

Rotation around an axis out of a principal plane

If the axis of rotation (z) is out of the three principal planes, we call such a solution *aplanar*, and the orientation angles satisfy the relations

$$\theta \neq 0, \frac{\pi}{2}; \quad \phi \neq 0, \frac{\pi}{2}. \quad (2.79)$$

The lower panel of Fig. 2.10 displays the aplanar case in which the rotational axis does not lie in one of the principal planes. In this case, $TR_y(\pi)$ symmetry is broken. The $TR_y(\pi)$ is the time-reversal operator combined with rotation about the y -axis by π . The two combinations have opposite chirality, corresponding the left- and right-handed frames. The breaking of the $TR_y(\pi)$ symmetry causes two degenerate doublet $\Delta I = 1$ bands with the same parity.

2.6.2 TAC-CDFT

The covariant density functional theory (CDFT) can be traced back to the successful relativistic mean-field (RMF) models introduced by Walecka and Serot [76,77], which was further developed by many physicists. In the following, we will give a brief description of the tilted axis cranking covariant density functional theory (TAC-CDFT) based on the point-coupling interaction [75].

The starting point of the CDFT is an effective Lagrangian density of the form

$$\mathcal{L} = \mathcal{L}^{\text{free}} + \mathcal{L}^{\text{4f}} + \mathcal{L}^{\text{hot}} + \mathcal{L}^{\text{der}} + \mathcal{L}^{\text{em}}, \quad (2.80)$$

which is divided into five terms. The Lagrangian density for free nucleons $\mathcal{L}^{\text{free}}$,

$$\mathcal{L}^{\text{free}} = \bar{\psi}(i\gamma_\mu \partial - m)\psi, \quad (2.81)$$

the four fermion point-coupling terms \mathcal{L}^{4f} ,

$$\begin{aligned} \mathcal{L}^{\text{4f}} = & -\frac{1}{2}\alpha_S(\bar{\psi}\psi)(\bar{\psi}\psi) - \frac{1}{2}\alpha_V(\bar{\psi}\gamma_\mu\psi)(\bar{\psi}\gamma_\mu\psi) \\ & - \frac{1}{2}\alpha_{TS}(\bar{\psi}\vec{\tau}\psi)(\bar{\psi}\psi) - \frac{1}{2}\alpha_{TV}(\bar{\psi}\vec{\tau}\gamma_\mu\psi)(\bar{\psi}\vec{\tau}\gamma^\mu\psi), \end{aligned} \quad (2.82)$$

the higher order terms \mathcal{L}^{hot} accounting for the medium effects,

$$\mathcal{L}^{\text{hot}} = -\frac{1}{3}\beta_S(\bar{\psi}\psi)^3 - \frac{1}{4}\gamma_S(\bar{\psi}\psi)^4 - \frac{1}{4}\gamma_V[(\bar{\psi}\gamma_\mu\psi)(\bar{\psi}\gamma^\mu\psi)]^2, \quad (2.83)$$

the derivative terms \mathcal{L}^{der} to simulate the effects of finite-range,

$$\begin{aligned} \mathcal{L}^{\text{der}} = & -\frac{1}{2}\delta_S\partial_\nu(\bar{\psi}\psi)\partial^\nu(\bar{\psi}\psi) - \frac{1}{2}\delta_V\partial_\nu(\bar{\psi}\gamma_\mu\psi)\partial^\nu(\bar{\psi}\gamma_\mu\psi) \\ & - \frac{1}{2}\delta_{TS}\partial_\nu(\bar{\psi}\vec{\tau}\psi)\partial^\nu(\bar{\psi}\psi) - \frac{1}{2}\delta_{TV}\partial_\nu(\bar{\psi}\vec{\tau}\gamma_\mu\psi), \end{aligned} \quad (2.84)$$

and the electromagnetic interaction term \mathcal{L}^{em} ,

$$\mathcal{L}^{\text{em}} = -\frac{1}{4}F^{\mu\nu}F_{\mu\nu} - e\frac{1-\tau_3}{2}\bar{\psi}\gamma^\mu\psi A_\mu, \quad (2.85)$$

where m is the nucleon mass and e is the charge unit for protons. A_μ and $F_{\mu\nu}$ are the four-vector potential and field strength tensor of the electromagnetic field, respectively. There are in total 11 coupling constants, α_S , α_V , α_{TS} , α_{TV} , β_S , γ_S , γ_V , δ_S , δ_V , δ_{TS} , and α_{TV} , in which α refers to the four-fermion term, β and γ respectively to the third- and fourth-order terms, and δ the derivative couplings. The subscripts S , V , and T respectively indicate the symmetries of the couplings, i.e., S stands for scalar, V for vector, and T for isovector [78].

The Hamiltonian density, i.e., the 00 components of the energy-momentum tensor, can be obtained by the Legendre transformation

$$\mathcal{H} = T^{00} - \frac{\partial \mathcal{L}}{\partial \dot{\phi}_i} \dot{\phi}_i - \mathcal{L}, \quad (2.86)$$

where ϕ_i is the nucleon or photon field. Thus, the total Hamiltonian is given as

$$H = \int d^3x \mathcal{H}. \quad (2.87)$$

In TAC-CDFT, it's assumed that the nucleus rotates around an axis in the xz plane, the Lagrangian in Eq. 2.80 is transformed into a frame rotating uniformly with a constant rotational frequency,

$$\Omega = (\Omega_x, 0, \Omega_z) = (\Omega \cos \theta_\Omega, 0, \Omega \sin \theta_\Omega), \quad (2.88)$$

where θ_Ω is the tilted angle between the cranking axis and the x -axis. The Dirac equation with nucleon potentials has the form

$$[\alpha \cdot (-i\nabla - V) + \beta(m + S(r)) + V(r) - \Omega \cdot \hat{J}] \psi_k = \epsilon_k \psi_k, \quad (2.89)$$

where \hat{J} is the total angular momentum of the nucleon spinors, ϵ_k represents the single-particle Routhians for nucleons, and the relativistic fields $S(r)$ and $V^\mu(r)$ are connected in a self-consistent way to the nucleon densities and current distributions, which are obtained from the single-nucleon spinors ψ_k .

The iterative solution of these equations yields single-particle energies, expectation values for the three components $\langle \hat{J}_i \rangle$ of the angular momentum, total energies, quadrupole moments, transition probabilities, etc. The magnitude of the angular velocity ω is connected to the angular momentum quantum number I by the semiclassical relation $\langle \hat{J} \rangle^2 = I(I+1)$, and its orientation is determined by minimizing the total Routhian self-consistently. The detailed formalism of TAC-CDFT can be seen in Refs. [71–75, 78].

In the present work, the TAC-CDFT calculations have been applied for the doublet bands built on the 4- and 6-quasiparticle configurations identified in ^{136}Nd , which will be presented in Section. 5.2.1.

2.7 Transition probabilities

The ratios of reduced transition probabilities ($B(M1)/B(E2)$) are crucial in the intrinsic nuclear structure studies. $B(M1)/B(E2)$ ratios can be extracted from the experimental transition energies and intensities, together with the multipole mixing ratio (angular distributions/correlations). It's also possible to obtain them from the measurement of the lifetime of nuclear states. Ratios of reduced transition probabilities can be extracted as

$$\frac{B(M1; I \rightarrow I - 1)}{B(E2; I \rightarrow I - 2)} = 0.697 \frac{E_\gamma^5(M1; I \rightarrow I - 1)}{E_\gamma^3(E2; I \rightarrow I - 2)} \frac{I_\gamma(M1)}{I_\gamma(E2)} \frac{1}{1 + \delta^2} \quad (2.90)$$

where $I_\gamma(M1)/I_\gamma(E2)$ is ratio of the the intensities of the γ rays, δ denotes the mixing ratio ration of the $\Delta I = 1$ transitions. The $B(M1)/B(E2)$ ratios are expressed in units of $(\mu_N/eb)^2$ and E_γ in MeV.

Theoretically, the $B(M1)/B(E2)$ ratios can be calculated using the semi-classic formalism of Dönau and Frauendorf [79, 80].

Chapter 3

Experimental techniques

One of the goals of the nuclear structure physics is to understand the properties of the high-spin states. Investigations on the nuclear structure at high spins require specific experimental techniques. The population of high-spin states in nuclei, the methods of measurements, and the experimental facilities used in this work are presented in this chapter.

3.1 Heavy-ion fusion-evaporation reactions

There are many types of reactions to produce excited nuclei, i.e., inelastic scattering, Coulomb excitation, heavy-ion fusion-evaporation reaction (a heavy-ion is defined as a nucleus with mass number $A > 4$). Among them, the fusion-evaporation is one of the most useful in the high-spin physics since it can produce excited nuclei in very high-spin states. To overcome the Coulomb barrier V_c form a compound nucleus, the minimum beam energy required is

$$V_c = 1.44 \frac{Z_b \cdot Z_t}{R_b + R_t} [\text{MeV}], \quad (3.1)$$

where the subscripts b and t denote projectile and target, respectively. $R_{b,t} = r_0 A_{b,t}^{1/3}$ is the radius of respective nucleus and $Z_{b,t}$ represent the atomic numbers. After fusion of the projectile and target, the compound nucleus is in a highly excited state, with the excitation energy of

$$E_{ex} = Q + E_{cm}, \quad (3.2)$$

where E_{cm} is the kinetic energy of the system in the center of the mass frame and the Q -value is the reaction energy. They are given by

$$Q = (M_b + M_t - M_{cn}), \quad E_{cm} = \frac{m_t}{m_b + m_t} E_{lab}. \quad (3.3)$$

We can also estimate the maximum angular momentum transferred in a fusion evaporation reaction, l_{max} , which can be expressed as

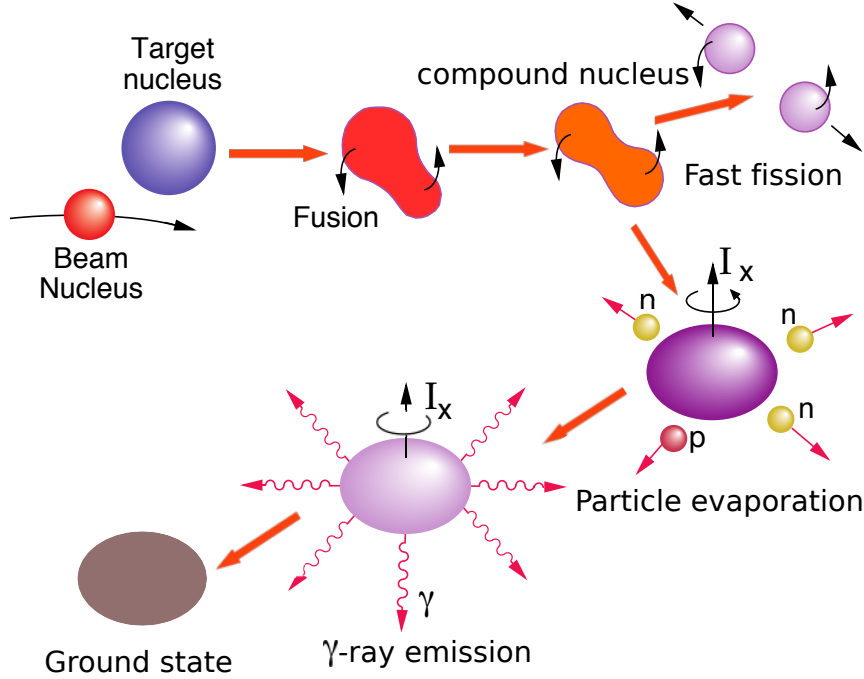


Figure 3.1: Schematic illustration the heavy-ion fusion-evaporation reaction forming a compound nucleus and its decay.

$$l_{max}^2 = \frac{2\mu R^2}{\hbar^2}(E_{cm} - V_c), \quad (3.4)$$

where $\mu = \frac{R_b R_t}{R_b + R_t}$ is the reduced mass of the compound nuclear system.

In fusion-evaporation reactions, a compound nucleus with very high excitation energy and angular momentum is formed when a heavy-ion beam bombards a target nucleus. If the compound nucleus does not fission, then the compound *hot* system will cool down by evaporation of particles, such as neutrons, protons, and α particles. Each of the emitted particles carries away an energy of ≈ 8 MeV and $1-2 \hbar$ of angular momentum. Finally, the residual nucleus produced after the evaporation of the particles loses the rest of excitation energy and almost all angular momentum via γ -ray emission, until it reaches the ground state. The dominant part of deexcitations of the residual nucleus proceeds by γ -ray emission. Therefore, the γ -ray spectroscopy as an efficient method was used to the study of excited states of nuclei. Generally, in the γ -ray spectroscopy one uses energy-sensitive HPGe detectors for the measurement of the γ rays emitted from a residual nucleus, and one analyzes the properties of γ rays, such as the energy, the multipolarity from angular distribution or angular correlation, the electromagnetic character from polarization. A schematic picture showing the formation and decay of the compound nucleus is given in Fig. 3.1.

3.2 Interaction mechanisms of the γ -rays with matter

In order to understand how to extract the information carried by the γ -rays, a knowledge of the γ -ray interactions with matter is important. Only three major types of interaction play a significant role in nuclear spectroscopy measurements: *photoelectric absorption*, *Compton scattering*, and *pair production*. These processes are schematically shown in Fig. 3.2.

3.2.1 Photoelectric absorption

Photoelectric absorption is an interaction in which the incident γ -ray photon disappears, namely, is fully absorbed. In this case, a photoelectron is emitted from one of the electron shells (E_b) of the absorber atom with a kinetic energy given by the incident photon energy E_γ minus the binding energy of the electron in its original shell, $E_e = E_\gamma - E_b$. The process is shown in Fig. 3.2 (a). After the electron has been emitted, a hole is created in the shell, X-rays are emitted in the process of filling the created hole, but it is also possible that the another electron, called *Auger electron*, is emitted. For typical γ -ray energies, the photoelectric effect is most likely to occur in the *K* shell, which has typical binding energies ranging from a few keV for low-*Z* materials to tens of keV for the materials with high-*Z*.

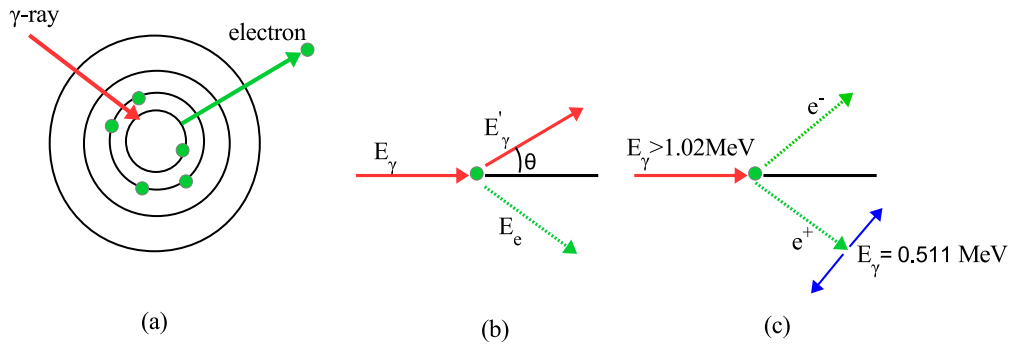


Figure 3.2: (a) Photoelectric absorption, (b) Compton scattering, (c) Pair production.

3.2.2 Compton scattering

In this process, the incident γ -ray with energy E_γ is scattered by an electron, creating a recoil electron and a scattered γ -ray photon deflected through an angle θ with respect to its original direction, with the energies of E_e and E'_γ , respectively. This process is illustrated in Fig. 3.2 (b).

The energy of the scattered photon is given by

$$E'_\gamma = \frac{E_\gamma}{1 + (\frac{E_\gamma}{m_0c^2})(1 - \cos\theta)}, \quad (3.5)$$

where $m_0c^2 = 0.511$ MeV is the rest mass energy of the electron. The kinetic energy of the recoil electron is

$$E_e = E_\gamma - E'_\gamma = E_\gamma \left[1 - \frac{1}{1 + (\frac{E_\gamma}{m_0c^2})(1 - \cos\theta)} \right]. \quad (3.6)$$

From the above equations, two extreme cases can be identified:

1. When the scattering angle $\theta = 180^\circ$, the incident γ -ray is backscattered towards its original direction, while the electron recoils along the incidence direction, the recoil electron having the maximum energy. This is the *so-called* "Compton edge" in a γ -ray spectrum, which corresponds to an energy

$$E_e|_{\theta=180^\circ} = E_\gamma \left(\frac{2 \frac{E_\gamma}{m_0c^2}}{1 + 2 \frac{E_\gamma}{m_0c^2}} \right). \quad (3.7)$$

2. When the scattering angle $\theta = 0^\circ$, $E_e \approx 0$.

For most γ -ray spectroscopy experiments, Compton scattering is the main cause of false events and decrease the P/T ratio of the spectra. To overcome these drawbacks anti-Compton shields were developed, which will be discussed in the section 3.3.

3.2.3 Pair production

The third effect shown in Fig. 3.2 (c) is pair production. The process occurs when an incident γ -ray within the strong electric field near the atomic nucleus, and results in the creation of an electron-positron pair. Since an energy of $2m_0c^2$ is required to create the pair, a minimum γ energy of 1.02 MeV is required to make the process energetically possible. After their production, both the electron and positron travel through the detector medium losing their energy. Once kinetic energy of the positron becomes very low, it will annihilate or combine with a electron in the absorbing medium and emission of two anti-parallel 0.511 MeV γ -rays. This process is shown in Fig. 3.2 (c).

3.3 High-purity Germanium γ -ray detector

In the 1960s, the Ge(Li) detectors were developed which marked the birth of high resolution γ -ray spectroscopy. In the 1980s, the more advanced HPGe

detectors became available widespread. The HPGe detector has many advantages over the Ge(Li) detector, i.e., HPGe offer the best compromise between energy resolution and efficiency; it also can be stored at room temperature which reduces storage costs and facilitates easier transportation, while Ge(Li) detectors must be continuously maintained at low temperature [81]. In addition, a detector system based on HPGe has good energy resolution, good P/T ratio, high efficiency and rather good timing properties which allow to extract the events of interest from complex γ spectra. In the 1990s, nuclear physicists built the next generation of γ -ray arrays, i.e., GAMMASPHERE and EUROBALL, with the aim to realize an ultimate 4π array of escape-suppressed Ge detectors. More recently the first phase of Advanced GAMMA Tracking Array (AGATA) was complete, as a new generation γ -ray spectrometer. AGATA is based on the technique of γ -ray energy tracking in electrically segmented high-purity germanium crystals [82].

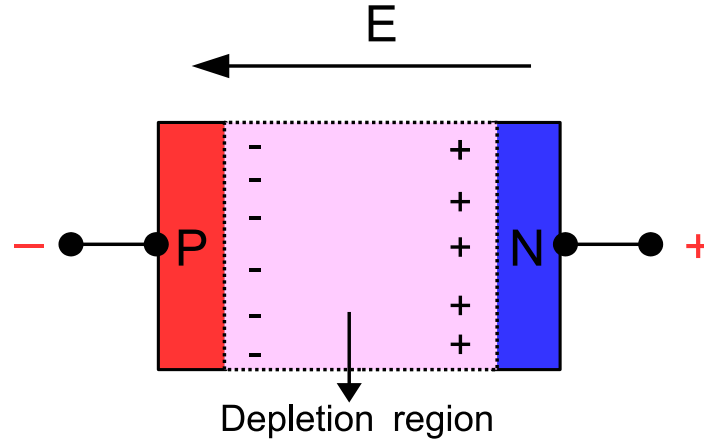


Figure 3.3: Reverse bias of the p-n junction.

A HPGe detector is generally operated as fully depleted detector. Reverse-biasing requires that a positive voltage be applied to the p-n junction, as shown in Fig. 3.3. At the p-n junction, the "built-in" electric field and the applied electric field are in the same direction. A thicker depletion region is created when these two fields add. The depletion region is a region of net zero charge, without free electrons and holes. The γ -ray interact with the germanium crystal within the depleted zone, producing electron-hole pairs which move towards the detector outer contacts. The produced charge induces a voltage pulse signal in a preamplifier. There are two major types of HPGe detectors: planar and coaxial. The planar detector usually used to measure the complex low-energy γ -ray in the range of 10 keV to a few hundred keV or X-rays. It achieves the best energy resolution due to low capacitance. Coaxial detectors have a large detection efficiency at high γ -ray energies, and are used to measure γ in the range of 10 keV to 10 MeV.

Compton suppression with BGO detectors

The dominating contribution to the background in γ -ray spectroscopy is come from the incomplete energy deposition of the incoming photon in the detector volume due to the Compton scattering. The Compton scattered γ -rays will result a continuous background in the γ -ray spectrum which consequently raises the detection limit for low energies and also decrease P/T ratio. In order to counteract these unwanted effects, we can suppress the Compton scattered γ -rays by surrounding the HPGe detector with a secondary veto detector, which usually is a scintillator. The majority of the γ -rays that are scattered out of the HPGe detector are then detected in the surrounding scintillator. Producing a veto signal that is used to eliminate the partially absorbed events from the spectra of the Ge detector. Generally speaking, the secondary detector is expected to have a high detection efficiency and high density to absorbe the escaping photons as much as possible. The bismuth germanate (BGO, $\text{Bi}_4\text{Ge}_3\text{O}_{12}$) material is the preferred choice, because of its excellent timing properties, high Z , high density (7.3 g/cm^3), and light output as compared with NaI(Tl) . If Compton scattered γ -rays escape from the HPGe detector and are detected in the BGO detector, which means that both detectors have signal, the event is rejected. Otherwise, if only the HPGe detector has signal, is stored. This technique is called "Compton suppression spectrometry". The BGO detector is also called "anti-Compton" detector. A schematic view of the Compton suppression is given in Fig. 3.4.

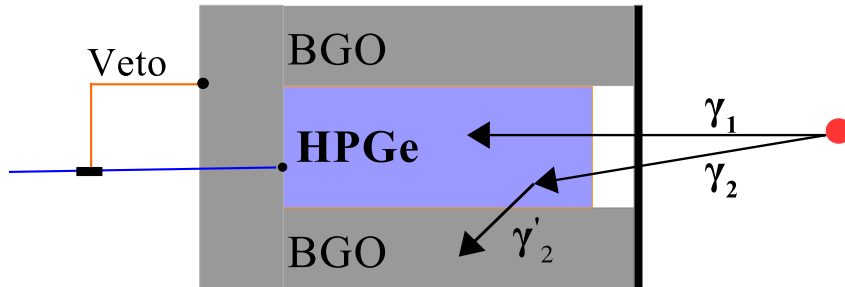


Figure 3.4: The schematic configuration of a BGO anti-Compton shield of a HPGe detector.

3.4 The JUROGAM II array

The JUROGAM II array [83], a large γ -ray spectrometer consisting of 24 clover and 15 coaxial tapered detectors placed at the target position, has been used to detect prompt γ -rays. The clover detectors were placed on two rings at 75.5° (12 clovers) and 104.5° (12 clovers) symmetric with respect to 90° . The tapered detectors were also placed on two rings at 133.6° (10

detectors) and 157.6° (5 detectors). All Ge detectors of the array are equipped with Compton-suppression shields made of BGO and Hevimet collimators in front of the detectors to improve the P/T ratio. The add-back method of summing the coincident γ -ray energies in separate crystals in the same clover detector within a 200 ns time window was used in this work. For a γ -ray with the energy of 1.33 MeV, the full JUROGAM spectrometer with 39 detectors has a total photo-peak efficiency around 5% and energy resolution of 3.5 keV (FWHM) [83]. The schematic configuration of the JUROGAM II detector array is shown in Fig. 3.5.

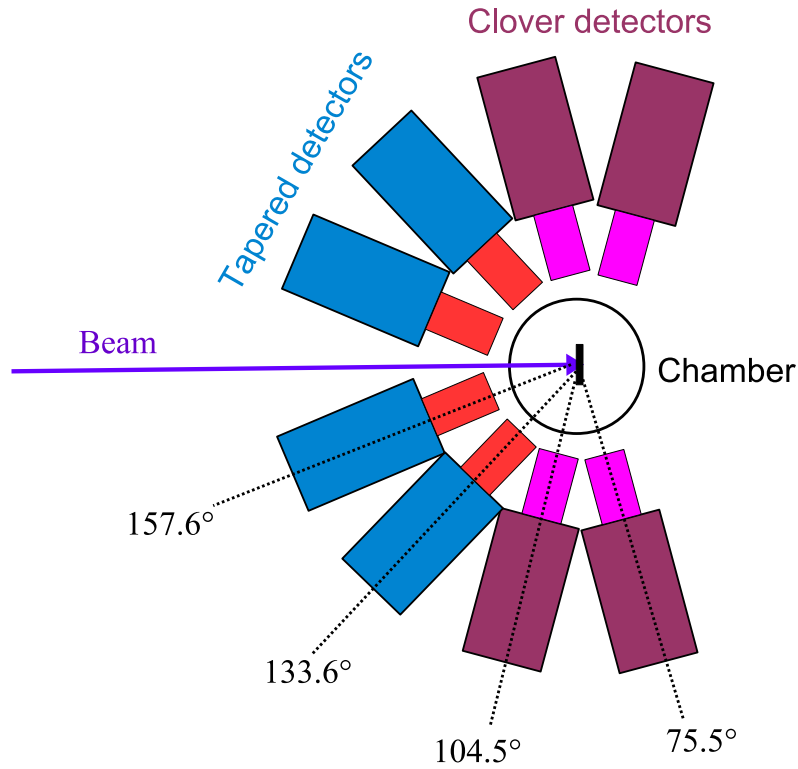


Figure 3.5: JUROGAM II array.

3.5 The RITU gas-filled recoil separator

Recoil separators for heavy-ion induced fusion products have become important tools to separate the fusion-evaporation residues from the primary beam and other unwanted reaction products, and then transport the recoils to the focal plane for further measurements (as for example, decay properties of heavy elements, search for long-lived isomeric states in nuclei). The Recoil Ion Transport Unit (RITU) is a gas-filled recoil separator [8, 84, 85], which is coupled to the JUROGAM II array, as is schematically shown in Fig. 3.6.

The typical separator is of the type DQQ with a magnetic dipole followed by a quadrupole doublet to focus the fusion products into the focal plane, the reason being that separation of primary beam immediately downstream from the target reduce the background at the focal plane. RITU is based on a standard DQQ magnetic configuration, it consists of a total of four focusing components that are in a $Q_1DQ_2Q_3$ configuration. The first magnetic quadrupole (Q_1) is vertically focusing to improves the dipole magnet acceptance, which leads to an increase of 30% in the angular acceptance [8]. The dipole magnet (D) is used to separate ions depending on their different magnetic rigidities $B\rho$. The Q_2 and Q_3 quadrupole magnets are horizontally and vertically focusing, respectively.

The relationship between the magnetic rigidity $B\rho$ and the average charge state q_{ave} of ions of a nuclear species Z is given by the formula [86]

$$B\rho = \frac{p}{q_{ave}} = \frac{mv}{(v/v_0)Z^{1/3}} = 0.0227A/Z^{1/3}Tm, \quad (3.8)$$

where B is the magnetic field strength, ρ is the curvature radius, p and mv is the momentum of the reaction product and v_o is the Bohr velocity $= c/137$ m/s $= 2.19 \times 10^6$ m/s, $q_{ave} = (v/v_o)Z^{1/3}$ is approximate and is given by the Thomas-Fermi model of the atom. Eq. 3.8 can be used for a rough estimate of the degree of separation residues.

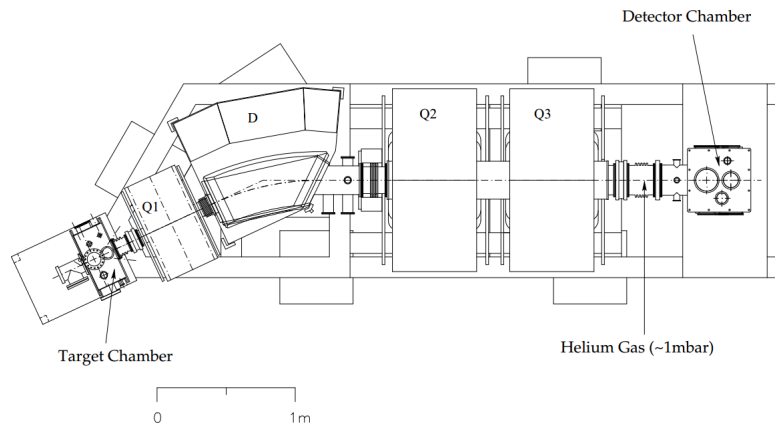


Figure 3.6: Scheme of gas-filled recoil separator RITU. The figure is taken from Ref. [8].

In heavy element studies, helium and hydrogen are the practical choices for filling gas due to their favourable scattering properties. The choice between these alternatives may be dictated by background suppression properties, safety considerations, or by the fact that higher field strengths are required in case of hydrogen and very asymmetric reactions [87]. The internal volume of the RITU is filled with a flow of helium gas with the pressure around 1 mbar.

Usually, pressures around 1 mbar lead to the minimum focal plane image size and also to increase of the recoil transmission.

3.6 The GREAT spectrometer

Gamma Recoil Alpha Tagging (GREAT) [88] spectrometer is placed at the focal plane of RITU separator. It is designed to measure the decay properties of reaction products transported to the focal plane of the recoil separator. In addition, GREAT can either be employed as a sensitive stand-alone device for decay measurements at the focal plane, or used to provide a effective tag for prompt conversion electrons or γ rays measured with arrays of detectors deployed at the target position [88].

The GREAT detector array is composed of several detector types: multi-wire proportional counter (MWPC), double-sided silicon strip detectors (DSSDs), PIN diodes, planar germanium detector and three clover detectors. A schematic view of the GREAT spectrometer is shown in Fig. 3.7.

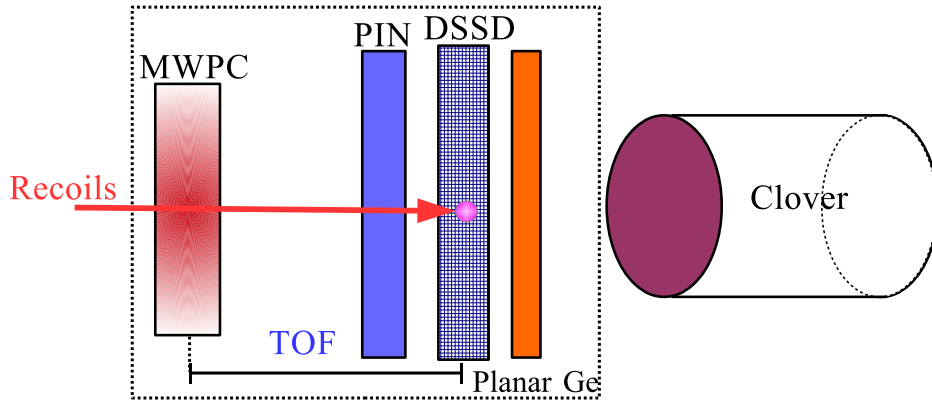


Figure 3.7: Schematic diagram of GREAT spectrometer.

The MWPC is placed at the entrance of GREAT, which can measure the position of the recoils and deliver the time reference for the delayed γ - γ coincidences, and for the time of flight (TOF) of the recoils between the MWPC and the DSSDs.

The recoils are implanted into DSSDs, which are used to measure the energies of ions, of subsequent emitted α particles, β particles and protons. Each DSSD has an active area of $60 \text{ mm} \times 40 \text{ mm}$ and a thickness of $300 \mu\text{m}$. The strip pitch is 1 mm in both directions, matching the position resolution of the MWPC and giving a total of 4800 pixels that can be used for correlation analysis. Reaction products are typically implanted into the DSSDs at depths of around $1\text{-}10 \mu\text{m}$, depending on the target-projectile combination [88].

An array of silicon PIN photodiode detectors to measure conversion electrons and α particles that escape from the DSSDs in the backward direction.

The active area of each detector element is $28 \text{ mm} \times 28 \text{ mm}$ with a thickness of $500 \text{ }\mu\text{m}$.

Behind the DSSD, a planar Ge strip detector is mounted, which is used to for the measurement of X-rays and low-energy γ rays. The active area of each detector element is $120 \text{ mm} \times 60 \text{ mm}$ with a thickness of $15 \text{ }\mu\text{m}$. The strip pitch on both faces is 5 mm , providing position information that can be correlated with other GREAT detectors. It can also be used to detect high-energy β particles ($\geq 2 \text{ MeV}$) that penetrate through the DSSDs [88].

For the measurement of high-energy γ -rays, a set of three clover detectors have been placed around the focal plane reaction chamber. Each of the four crystals has a diameter of 70 mm and a length is of 105 mm . The detectors are surrounded by BGO suppression shields to improve their P/T ratio.

3.7 Total-Data Readout (TDR)

In general, nuclear experiments are using data-acquisition systems which are triggered by an event in a pre-defined detector. The main problem of a conventional trigger method is that the dead-time causing a loss of events and the data written to tape include both good and random data, which later must be separated. The random data also increase the readout time and the data rate to tape.

To overcome dead-time limitations due to reading all the data, the one of the solution is time stamping them, and then collecting the event fragments together in software in the event builder using spatial and temporal correlations. Total-Data Readout (TDR) [89] data-acquisition systems are needed. In TDR acquisition systems all channels run independently and are associated in software to reconstruct events. The correlation in the event builder can be simple. For example, in order to eliminate random γ rays measured with JUROGAM II at the target position, one can tag with recoils, and then looking back in time using a window centred on the time of flight [89].

The most important and valuable feature of the TDR is that it is triggerless and the data is timestamped from a global 100-MHz clock giving a time resolution of 10 ns . The data from TDR are not structured or filtered, apart from the time-ordered, it allows the offline process data more flexible and events reconstructed in real time in the event builder using temporal and spatial associations depend on the physics of the experiment.

In the experiment of the present work, all the data were recorded by the triggerless TDR data acquisition and the events were time-stamped using a 100-MHz clock. The data acquisition system employs an OR gate in the GREAT spectrometer as a software trigger. It requires a signal in any of the GREAT detectors to be recorded for an event to start, and JUROGAM II data are only stored if they arrive within a give time window relative to the signal in GREAT. The data from the JUROGAM II detectors were buffered

for $5 \mu\text{s}$ if there was a signal at the focal plane, and provided a JUROGAM II detector fired within the time period preceding the signal in GREAT, the data was stored to disc [9].

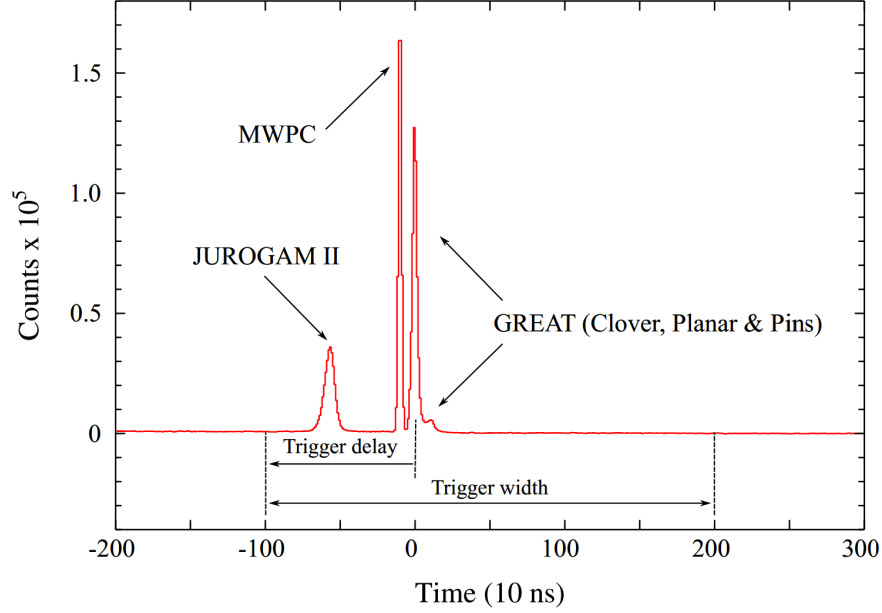


Figure 3.8: Schematic illustration of a typical RDT setup and the signal times for each detector relative to an event stamp in the DSSDs. This figure is adapted from Ref. [9].

A typical time structure for each detector relative to the event stamp in the DSSDs ($T=0$) is presented in Fig. 3.8. In this case, data would be stored on disc if a signal within the trigger width of $3 \mu\text{s}$, and if it is registered $1 \mu\text{s}$ before or $2 \mu\text{s}$ after an event in the DSSDs. There is no limit to choose the trigger or delay widths due to the signals are collected with a 10 ns time stamp, except for the upper limit of $5 \mu\text{s}$ resulting from the software trigger delay. Although there is a maximum correlation time of $5 \mu\text{s}$ for each event, there is no limitation in the correlation time between separate events [9]. The data processed using the GRAIN [90] software package will be discussed in the next chapter.

Chapter 4

Experimental details and processing of the data

4.1 Experimental details

The experiment was performed at the University of Jyväskylä, Finland, using the JUROGAM II + RITU + GREAT setup. High-spin states in $^{135,136}\text{Nd}$ were populated using the fusion-evaporation reaction $^{100}\text{Mo}(^{40}\text{Ar}, xn)$. The ^{40}Ar ion beam was produced in an ECR ion source and accelerated by the K130 cyclotron to final energy of 152 MeV, the beam intensity was around 14 pA. One week beam time was allocated for this experiment. We used as target a self-supporting enriched ^{100}Mo foil of 0.5 mg/cm^2 thickness. The ^{135}Nd and ^{136}Nd nuclei were the most strongly populated in the reaction, with cross sections of around 100 mb each, for a total reaction cross section calculated with PACE4 of 480 mb.

4.2 Data processing

In this experiment ≈ 4000 Gb of data spread across ≈ 2000 files were stored. A total of 5.1×10^{10} prompt γ -ray coincidence events with fold ≥ 3 were collected. All the data were recorded by the triggerless TDR data acquisition system and the events were time-stamped using a 100 MHz clock with the time resolution of 10 ns.

4.2.1 Energy calibrations and gain matching

During the experiment, the gain of each detector could drift. Hence, it is important to calibrate (establish the relation ADC channel-energy) each detector and to gain match all detectors. In this work, the JUROGAM II detectors, the focal plane planar, and the clover detectors were calibrated before and after the experiment using the standard γ -ray sources ^{152}Eu and

^{133}Ba . To calibrate the detectors a polynomial expression was used of the form

$$E_\gamma = a + bx + cx^2, \quad (4.1)$$

where E_γ is the γ -ray energy, x is the ADC channel number associated with the centroid position of the photopeak; a , b , and c are coefficients of the polynomial used for obtaining the calibrated energy.

In the present work, we used a program *ENCAL* from the RADWARE [91, 92] analysis package to obtain the coefficients a , b , and c . Fig. 4.1 shows a sample of overlaid some Ge detectors of JUROGAM II array after calibration.

In addition, each strips of the DSSDs was calibrated using a combination of ^{239}Pu , ^{241}Am , and ^{244}Cm sources.

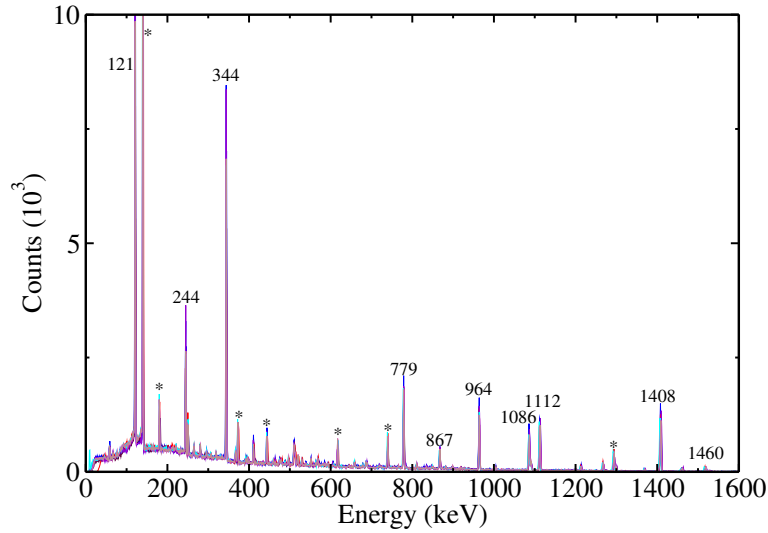


Figure 4.1: A sample of calibrated overlaid energy spectra of ^{152}Eu for some Ge detectors of the JUROGAM II array. The peaks corresponding to the contaminating transitions are indicated with asterisks.

4.2.2 Efficiency calibrations for Ge detectors

In order to make the correction of the measured γ -ray intensities for the detection efficiency of the JUROGAM II array, we used the program *EFFIT* from the RADWARE [91, 92] analysis package. The efficiency of the detectors was obtained by fitting the data points using the equation,

$$\ln(\epsilon) = [(A + Bx + Cx^2)^{-G} + (D + Ey + Fy^2)^{-G}]^{-1/G}, \quad (4.2)$$

with

$$x = \ln\left(\frac{E_\gamma}{100}\right), \quad y = \ln\left(\frac{E_\gamma}{1000}\right), \quad (4.3)$$

where ϵ is the efficiency and E_γ is the γ -ray energy in keV. The A, B, and C parameters are used to control the low energy region efficiency curve. The parameter C is often fixed to 0, and D, E, and F are the parameters that are used to adjust the high energy part of the efficiency curve. G is the parameter which determines the shape of the region between the high and low energy efficiency curves. In present experiment, the following parameters were used to obtain the best fit of JUROGAM II efficiency: $A = 6.2, B = 1.8, C = 0.0, D = 5.5, E = 0.6, F = 0.0$ and $G = 20.0$.

4.2.3 Doppler shift correction

For fusion-evaporation reactions, the γ -rays emitted by a in-flight recoil nuclei are Doppler-shifted when a stationary detector is used. The γ line width is also broadened due to the Doppler effect, hence, it is necessary to Doppler correct the γ -ray energies. The shifted γ energy is determined by the formula:

$$E'_\gamma = E_\gamma \frac{\sqrt{1 - \beta^2}}{1 - \beta \cos \theta}, \quad (4.4)$$

where E_γ is the unshifted γ -ray energy, $\beta = \frac{v}{c}$, v is the velocity of the recoil, c is the speed of light, and the detector angle θ is defined with respect to the beam direction.

If $\beta \ll 1$, the shifted γ energy is calculated using the following formula:

$$E'_\gamma = E_\gamma (1 + \beta \cos \theta). \quad (4.5)$$

In present work, the best resolution was obtained for a value $\beta = 0.0245$ which was therefore used to correct the Doppler shift of all γ rays detected in JUROGAM II.

4.2.4 Add-back for the clover detectors

The clover HPGe detector consists of four crystals. As the four crystals are close-packed and put in a single cryostat, there is the possibility that γ -rays Compton scatter from one crystal to another. In a Compton scattering event it can happen that the γ -ray deposits part of its energy in one crystal and then enter a neighbouring crystal to deposit a part or the remainder of its energy. In practice, the energy signals of the crystals that hit simultaneously the crystals are recorded in an event-by-event mode which are time correlated [93]. Thus, these events can be used to reconstruct the full γ -ray energy by summing the individual events in a procedure called "add-back" technique. The main advantage of the clover HPGe detector with add-back is the increase of the photo-peak efficiency (P/T) ratio.

4.2.5 Spin and parity assignments

After preparing the data as described above, we sorted all raw data using the GRAIN analysis package [90]. Fully symmetrized, three-dimensional (E_γ - E_γ - E_γ) coincidence cubes were analyzed using the *levit8r* program from the RADWARE analysis package [91, 92]. The program allows for a double gate to be set on two mutual coincident transition energies. The double gate will produce a slice on the third axis of the cube showing a one-dimensional γ -ray spectrum with all the detected γ -rays which are in coincidence with the two γ -ray transitions that were selected in the double gate. Then, we constructed the level scheme of the two nuclei ^{135}Nd and ^{136}Nd . The multipolarities of the γ -rays were extracted using the Directional Correlation from Oriented states (DCO) ratios (R_{DCO}) and two-point Angular Correlation (anisotropy) ratios R_{ac} [94, 95], as is described in the following.

(i) DCO ratios

In the heavy-ion evaporation reaction, the angular momenta of the compound nucleus are aligned in a plane perpendicular to the beam direction. The angular correction of γ -rays emitted from oriented states depends on the spins of the involved levels. Thus, we can deduce the DCO values and assign the spin of one of the two levels linked by a given γ -ray if the spin of the other level is known. In the DCO method, the ratio between the intensities of two coincident γ -rays is analyzed. The angles between the two γ -rays and the beam direction are θ_1 and θ_2 , respectively. A third angle ϕ is also used to describe the angular position of the detectors. The intensity of the transition γ_2 , determined from a spectrum measured with the detector at θ_1 , gated on the transition γ_1 measured with the detector at θ_2 , is denoted by $W(\theta_1, \theta_2, \phi)$. The intensity of the transition γ_2 determined from a spectrum measured with the detector at θ_2 , gated on the transition γ_1 measured with the detector at θ_1 , is denoted by $W(\theta_2, \theta_1, \phi)$. The DCO ratio is defined as

$$R_{DCO} = \frac{W(\theta_2, \theta_1, \phi)}{W(\theta_1, \theta_2, \phi)}. \quad (4.6)$$

The corresponding experimental DCO ratio is then written as

$$R_{DCO} = \frac{I_{\theta_1}^{\gamma_2}(\text{gated by } \gamma_1 \text{ at } \theta_2)}{I_{\theta_2}^{\gamma_2}(\text{gated by } \gamma_1 \text{ at } \theta_1)}. \quad (4.7)$$

The DCO ratios depend on the angles θ_1 , θ_2 , and ϕ . In this experiment, JU-ROGAM II detectors are placed in four rings, as shown in Fig. 3.5. To extract the DCO ratios from the ring of detectors placed at different θ angles, we integrated over all angles ϕ . Then, the R_{DCO} values were extracted from γ - γ matrices, which were formed by sorting prompt coincidence events with the detectors at (157.6°) versus those at (75.5° and 104.5°), corresponding to

the angle $\approx 90^\circ$). The DCO ratio is defined as

$$R_{DCO} = \frac{I_\gamma(157.6^\circ, \approx 90^\circ)}{I_\gamma(\approx 90^\circ, 157.6^\circ)}. \quad (4.8)$$

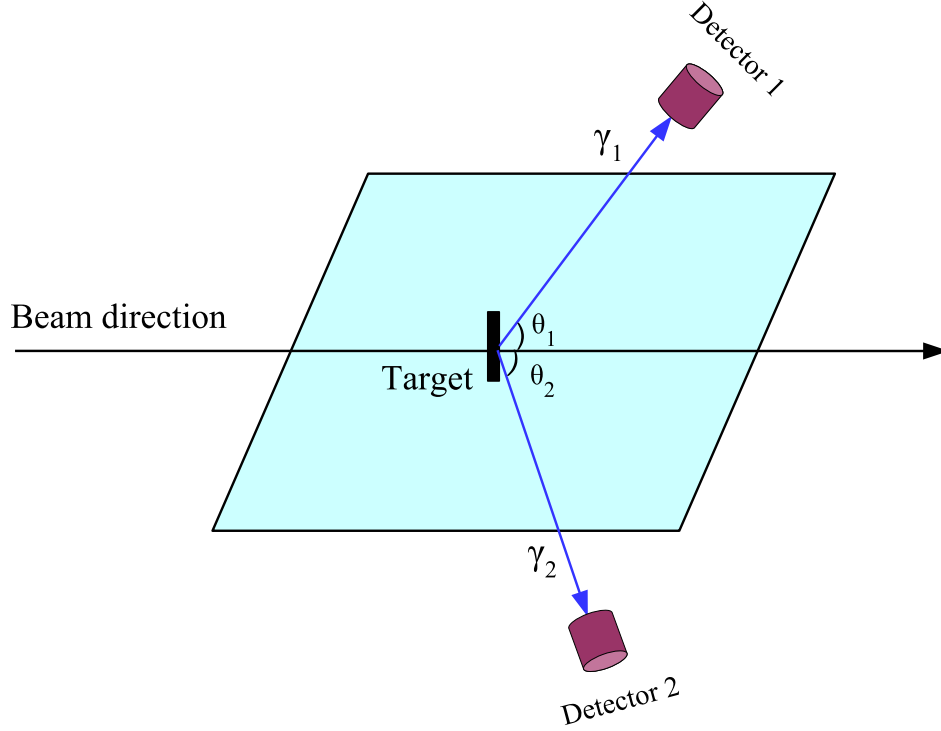


Figure 4.2: Geometry of the detector arrangement with the beam as orientation axis.

Note that the DCO ratios depend upon the type of transition gated on, and the measured transition DCO ratio will invert if exchange of the angles or of the gating.

(ii) Angular correlations ratio (R_{ac})

In addition of the DCO analysis, γ -ray multipolarities can also be obtained by measuring the two-point angular correlations ratios (R_{ac}), which is calculated by extracting the intensity of γ_1 in the detectors at θ_1 from a gate on γ_2 in all detectors and the intensity of γ_1 in the detectors at θ_2 from a gate on γ_2 in all detectors. The angular correlation ratio is

$$R_{ac} = \frac{I_{\theta_1}^{\gamma_1}(\text{gated by } \gamma_2 \text{ at all angles})}{I_{\theta_2}^{\gamma_1}(\text{gated by } \gamma_2 \text{ at all angles})}. \quad (4.9)$$

The R_{ac} method has some advantages, i.e., the value is independent of the gating transition character, can distinguish between $\Delta I = 2$ pure quadrupole and $\Delta I = 1$ pure dipole transitions. The two-point angular correlation ratio

is very useful for weak transition, which is the case of many new transitions identified in the ^{135}Nd and ^{136}Nd .

In the present data analysis, the values of R_{ac} were extracted from γ - γ matrices, which were formed by sorting prompt coincidence events with $(133.6^\circ \text{ and } 157.6^\circ)$ versus (all angles) and $(75.5^\circ \text{ and } 104.5^\circ)$ versus (all angles) combinations, by setting the same energy gates on the (all angles) projection spectrum in both matrices, and projecting on the another axis. Then, the R_{ac} ratio was calculated using the extracted intensities of the γ -rays of interest (I_γ) from these spectra, normalized by the different efficiency of the two sets of detectors. The R_{ac} is calculated using the formula

$$R_{ac} = \frac{I_\gamma(133.6^\circ + 157.6^\circ)}{I_\gamma(75.5^\circ + 104.5^\circ)} \quad (4.10)$$

The typical values for stretched dipole and quadrupole transitions are around 0.8 and 1.4, respectively.

It should be noted that both R_{DCO} and R_{ac} methods can only be used to deduce ΔI , but not their parity. To determine the electric or magnetic character of the emitted γ -rays, linear polarization measurements are required. A detailed description of the method applied to arrays of HPGe detectors can be found in Ref. [96].

Chapter 5

Towards complete spectroscopy of ^{136}Nd

In this chapter the experimental results obtained from the in beam γ -spectroscopy study of the even-even nucleus ^{136}Nd are presented. The structure of the various bands is discussed in the frameworks of the constrained and tilted axis cranking covariant density functional theory, the multi-j shell particle-rotor model, and the cranked Nilsson-Strutinsky model.

5.1 Experimental results and level scheme

The nucleus ^{136}Nd located near the center of the triaxial $A = 130$ region which has been previously investigated both in experimentally [97–108] and theoretically (see Refs. [109–113]). However, most of the experimental results were reported more than twenty years ago, being obtained with less efficient γ -ray arrays, which allowed to establish a limited level scheme.

In the present work, the level scheme of ^{136}Nd has been extended significantly. Many new bands have been identified both at low and high spin, among which five nearly degenerate bands which are interpreted as chiral partners. In addition of the excitation energies, the spins and parities of several previously known bands are revised and firmly established.

The level scheme of ^{136}Nd splitted into four partial level schemes is presented in Figs. 5.1, 5.6, 5.14 and 5.15. Most of the observed transitions were grouped in bands: the γ band, two bands of negative parity at low spins (N1-N2), nine bands at medium spins (L1-L9), six bands of dipole transitions (D1-D6) and five chiral partner bands (D1-chiral, D2-chiral, D3-chiral, D4-chiral, D5-chiral), four high-spin bands (T1-T4) and five highly-deformed bands (HD1-HD5). In addition, many new states have been newly identified and some previous states reported have been revised. The experimental information on the observed transitions is given in Table 5.1.

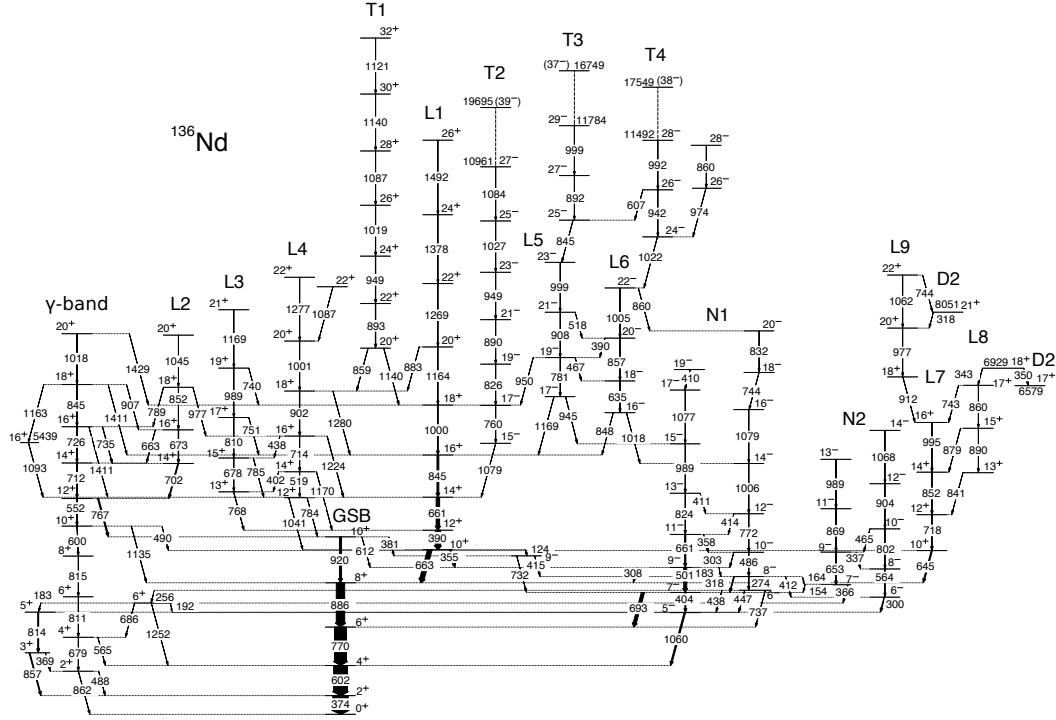


Figure 5.1: Partial level scheme of ^{136}Nd showing the low- and medium-spin bands.

5.1.1 The low-spin γ band and bands N1, N2

The γ band was first reported up to $I^\pi = 5^+$ [15], which now is extended to higher spins and linked by the 815- and 600-keV transitions to another previously known band built on the 10^+ state at 3768 keV [100]. The γ band is now observed up to $I^\pi = 20^+$: the previously reported 895-keV transition on top of the band has been replaced by the 1018-keV transition. The new transitions of 490, 735, 907, 1163, 1410.7, 1410.8, and 1429 keV have been identified connecting the γ band to the positive-parity bands L1 and L2, and to the 16^+ state deexcited by the 1093-keV transition. Coincidence spectra obtained by double-gating on selected transitions of the γ band are shown in Fig. 5.2.

For band N1, we newly identified the 1077-, 410-, 1079-, 744- and 832-keV transitions which were placed on the top of the previously known states of band N1. In addition, we observed two new transitions of 381 and 612 keV from the 10^+ state of the GSB towards the intermediate 9^- state, which in turn decays to the 7^- and 8^- states of band N1, and directly towards the 9^- state of band N1, respectively.

The new 6^+ state at 2228 keV has been identified, which decays to the ground-state band (GSB), to the γ band, and to band N1 via the 1252-keV, 686-keV and 192-keV transitions, respectively. The newly observed band N2

decays to the new 6^+ state, to the γ band, and to band N1 via the 366-keV, 300-keV and 154-keV transitions, respectively, and its 6^- and 7^- states are fed by the 412-keV and 164-keV transitions from band N1. The bandhead spin of the band N2 is fixed by the $\Delta I = 1$ transitions with energies of 366 and 300 keV. The negative parity of band N2 is fixed by the 412-keV $E2$ transition connecting the 8^- state of band N1 to the 6^- state of band N2. The negative-parity assignment to band N2 is further supported by the low-energy 154- and 164-keV transitions of $M1/E2$ character between bands N1 and N2. The double-gated spectra are given in Fig. 5.3 show the transitions of band N2.

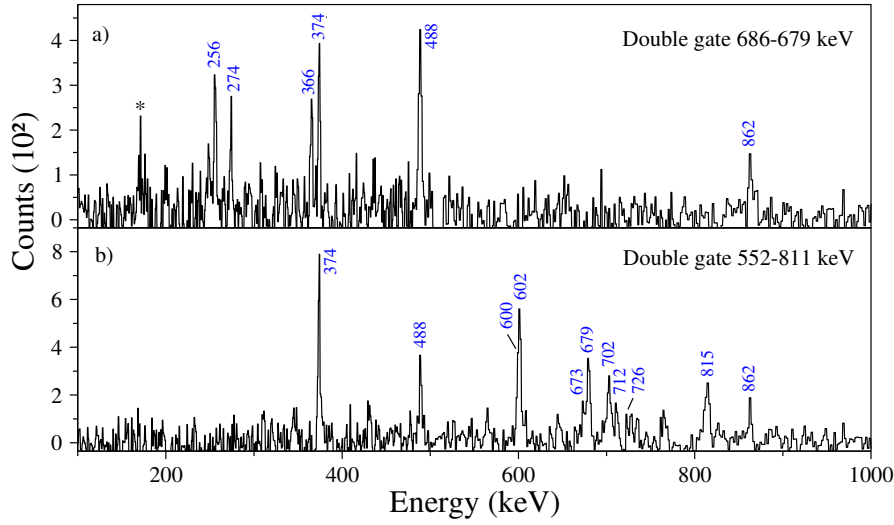


Figure 5.2: Double-gated spectra for the γ band of ^{136}Nd . The peaks corresponding to the γ rays of ^{136}Nd are indicated with their energies, while those of the contaminating transitions are indicated with an asterisk.

5.1.2 The medium-spin bands L and T

Band L1, which was previously known up to $I^\pi = 22^+$, has been extended up to $I^\pi = 26^+$ by adding two new transitions of 1378 ($22^+ \rightarrow 24^+$) and 1492 keV ($22^+ \rightarrow 26^+$). The transitions of band L1 reported previously are also confirmed in the present work.

Band L2 has been extended up to $I^\pi = 20^+$ by a new transition of 1045 keV ($18^+ \rightarrow 20^+$). Moreover, four transitions of 663, 735, 789, and 907 keV connecting band L2 to the γ band have been newly identified. Note that band L2 also decays via the weak transition of 977 keV to band L4.

Band L3, previously reported in Ref. [104], is confirmed. One new transition of 740 keV connecting the 19^+ state with the 18^+ state of band L1 has been identified.

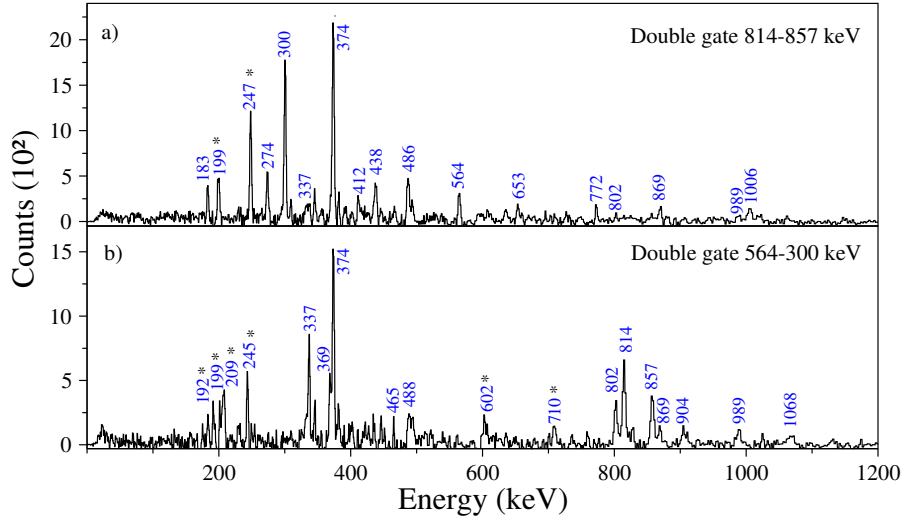


Figure 5.3: Double-gated spectra for the band N2 of ^{136}Nd . The peaks corresponding to the contaminating transitions are indicated with asterisks.

Band L4 has been revised due to the newly observed transitions of 519, 1001, 1277 and 1087 keV. It decays via the 438- and 402-keV transitions to band L3, via the 1041-, 1170-, 1224-, 1280-keV transitions to band L1, and via the 784-keV transition to the GSB. A double-gated spectrum showing the transitions of band L4 is presented in Fig. 5.4.

Bands L5 and L6 previously reported in Ref. [104] are confirmed by the present work. Three new transitions of 518, 390 and 467 keV connecting the two bands are newly identified. A new transition of 860 keV connects the 22^- state of band L6 to the 20^- state of band N1.

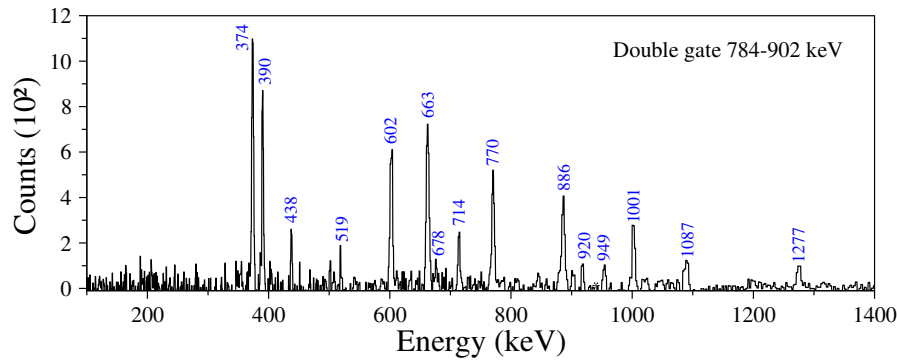


Figure 5.4: Double-gated spectrum for band L4 of ^{136}Nd .

Bands L7 and L8 previously reported in Ref. [104] are confirmed. One in-band transition of 890 keV and one out-of-band transition of 841 keV have

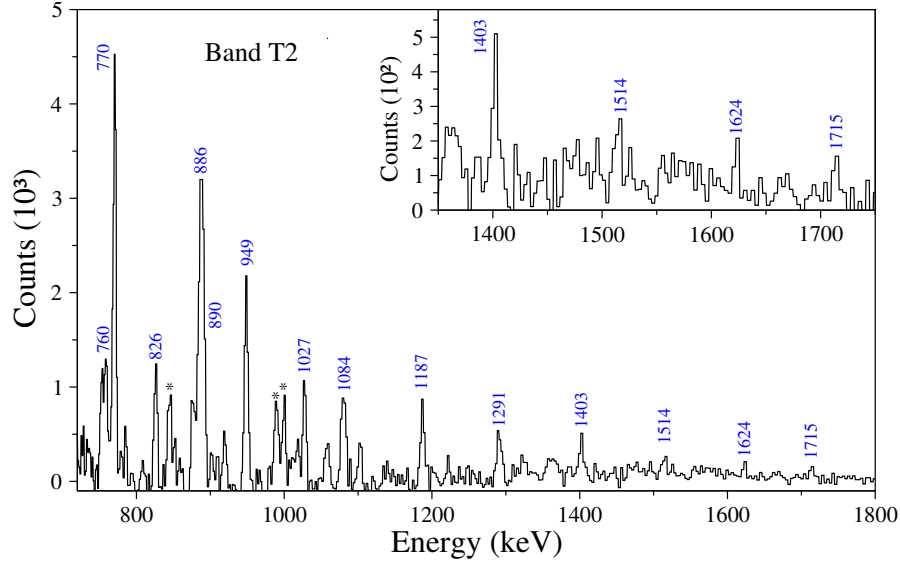


Figure 5.5: Sum of spectra obtained by double-gating on all combinations of in-band transitions of band T2. The peaks corresponding to the contaminating transitions are indicated with asterisks.

been added to band L8.

Band L9 is newly identified. It decays to band L7 via the 912-keV transition and its connected to band D2 via the 318- and 744-keV transitions.

Bands T1, T3 and T4 previously reported in Ref. [104] are confirmed, and several new transitions have been identified. A new relatively strong E2 transition of 1121 keV has been added on top of band T1 (see Fig. 5.1). The energies of the highest in-band transitions of bands T3 and T4 have been revised to 1391 and 1323 keV, respectively, whereas the spin and parity of the highest two and three levels, respectively, are tentative.

Band T2 is newly identified. It is built on the 15^- state and decays only to band T1 via the 1079-keV transition. It develops up to very high spin (39^-). A sum of doubly-gated spectra on the in-band transitions of band T2 is given in Fig. 5.5.

5.1.3 The dipole bands

A particular feature of the level scheme of ^{136}Nd is the existence of five pairs of nearly degenerate bands (D1 and D1-chiral, D2 and D2-chiral, D3 and D3-chiral, D4 and D4-chiral, D5 and D5-chiral) and the dipole band D6 without partner. The partial level scheme of ^{136}Nd showing the five pairs of chiral bands and band D6 is given in Fig. 5.6. One can observe that all these dipole bands decay to the yrast partners via high-energy quadrupole transi-

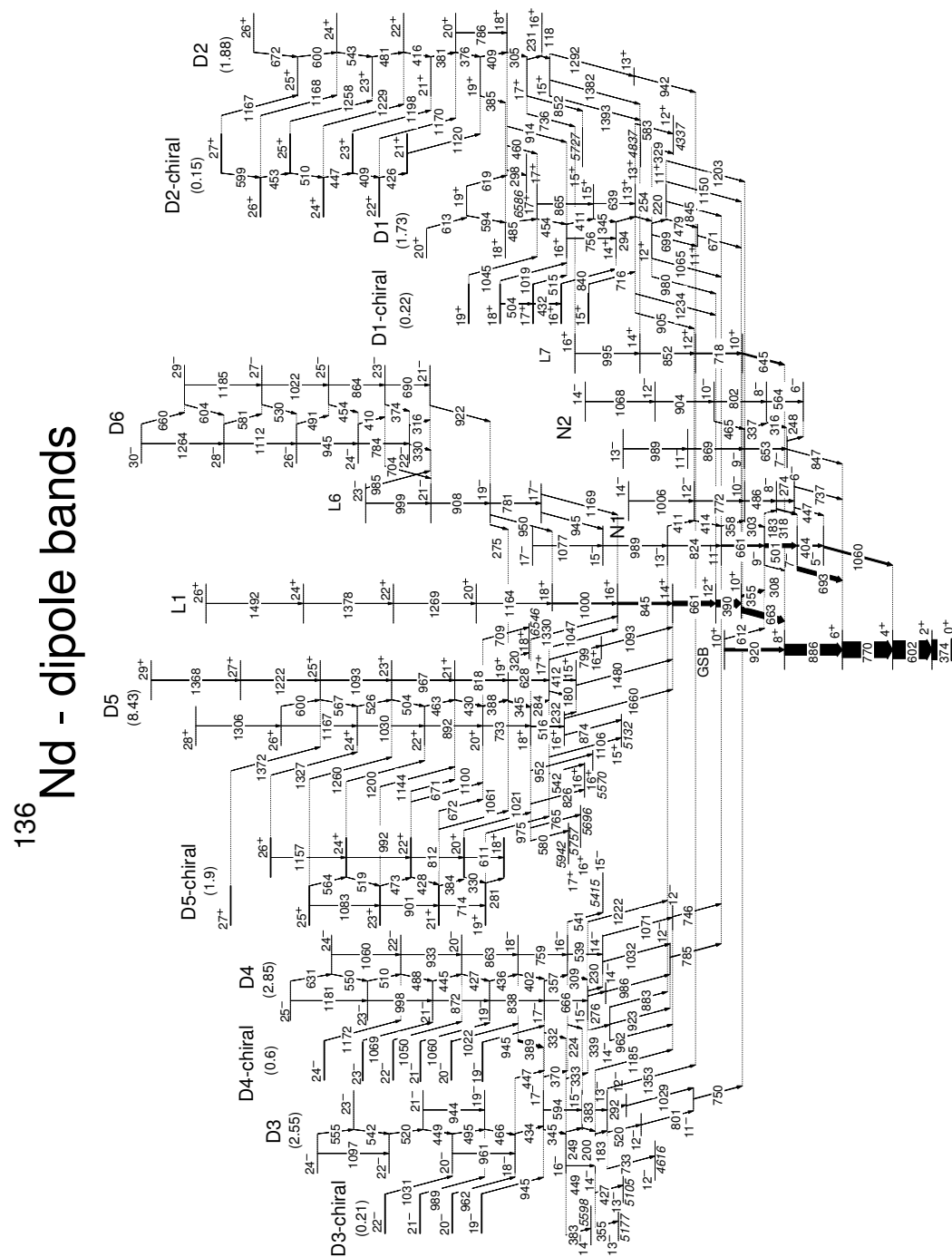


Figure 5.6: Partial level scheme of ^{136}Nd showing the dipole bands.

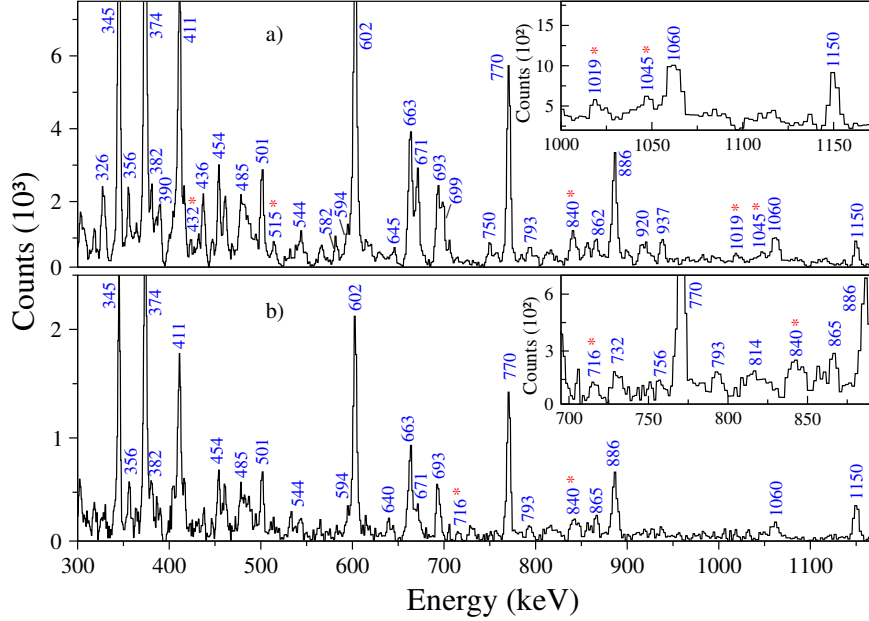


Figure 5.7: a) Sum of spectra obtained by double-gating on all combinations of the 220-, 254- and 294-keV transitions of band D1. b) Spectrum obtained by double-gating on the 220- and 254-keV transitions of band D1. The peaks corresponding to the in-band transitions of band D1-chiral and to the connecting transitions to band D1 are indicated with asterisks.

tions which, due to the E_γ^5 dependence, are stronger than the in-band dipole transitions which have low energy and E_γ^3 dependence, resulting in a factor of 10 to 20 in favor of the connecting transitions. This is the one of the reasons why many in-band dipole transitions of the non-yrast bands could not be observed with the present statistics.

Band D1, which was first reported in Ref. [105], is confirmed by the present study, but the spins and parity are revised. Three new crossover transitions of 639, 756 and 865 keV, and three new transitions of 485, 594 and 613 keV placed on top of the previously reported band, have been identified. Nine new decay-out transitions with energies of 329, 479, 583, 845, 905, 980, 1065, 1203 and 1234 keV have been identified, leading to a band-head of $I^\pi = 11^+$, with spin $2\hbar$ higher than that previously spin. The assigned positive parity is based on a series of the relatively strong connecting transitions to low-lying states. The new band D1-chiral decays to band D1 via high-energy E2 transitions (716 keV, 840 keV, 515 keV, 1019 keV, and 1045 keV). Double-gated spectra showing the transitions connecting one of the newly identified band D1-chiral to band D1 are given in Fig. 5.7.

Band D2 first reported in Ref. [105] is confirmed, with one new crossover

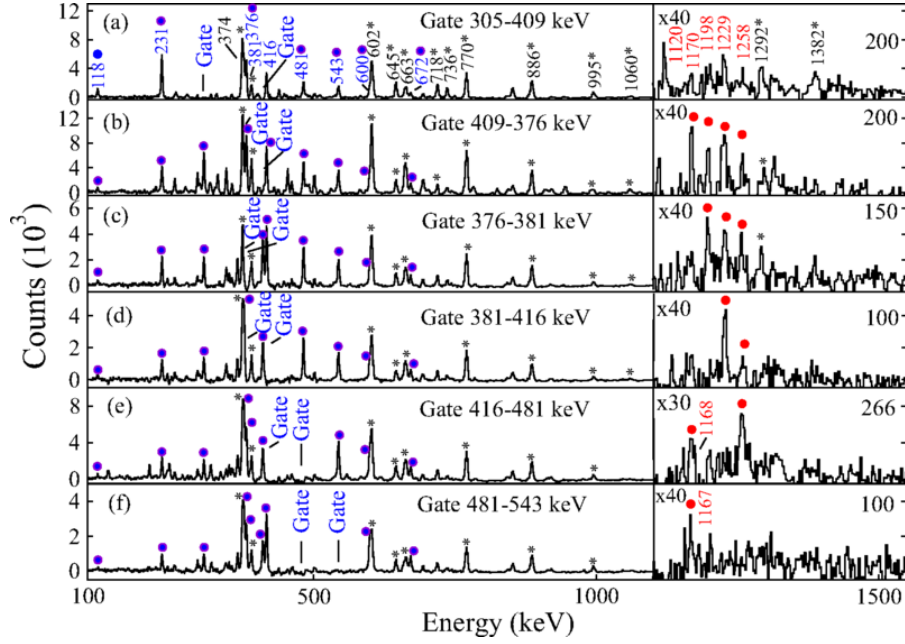


Figure 5.8: Spectra constructed by double-gating on transitions of band D2 which shows the connecting transitions of band D2-chiral. The transitions marked with asterisks indicate low-lying transitions in ¹³⁶Nd. The red lines show how the connecting transitions disappear when gating on successive higher-lying transitions of band D2.

transition of 786 keV. Three new transitions with energies of 385, 460 and 914 keV connect band D2 to band D1. The new band D2-chiral consists of a sequence of six dipole transitions. It decays to band D2 via seven high-energy E2 transitions. Double-gated spectra showing the bands D2 and D2-chiral is given in Fig. 5.8.

Band D3 first reported in Ref. [106] is confirmed, with a revision: one new in-band transition of 449 keV is inserted between the 520- and 495-keV transitions. The two new crossover transitions of 944 and 1097 keV, were useful to establish the order of the dipole in-band transitions. The band D3-chiral is new. It decays to band D3 via four E2 transitions of 945, 962, 989 and 1031 keV. No in-band dipole transitions have been observed in the present data. A double-gated spectrum showing the connecting transitions of band D3-chiral to band D3 is given in Fig. 5.9.

Band D4 first reported in Ref. [106] is confirmed, except the last two transitions of 624 and 1173 keV deexciting the 25⁻ state, which are replaced by the 631- and 1181-keV transitions. A new transition of 541 keV linking the 16⁻ state of band D4 to the 15⁻ state of band N1 has been also identified. The band D4-chiral consisting of six levels connected by high-energy transitions to band D4 is new. A spectrum showing these transitions is given in Fig. 5.10.

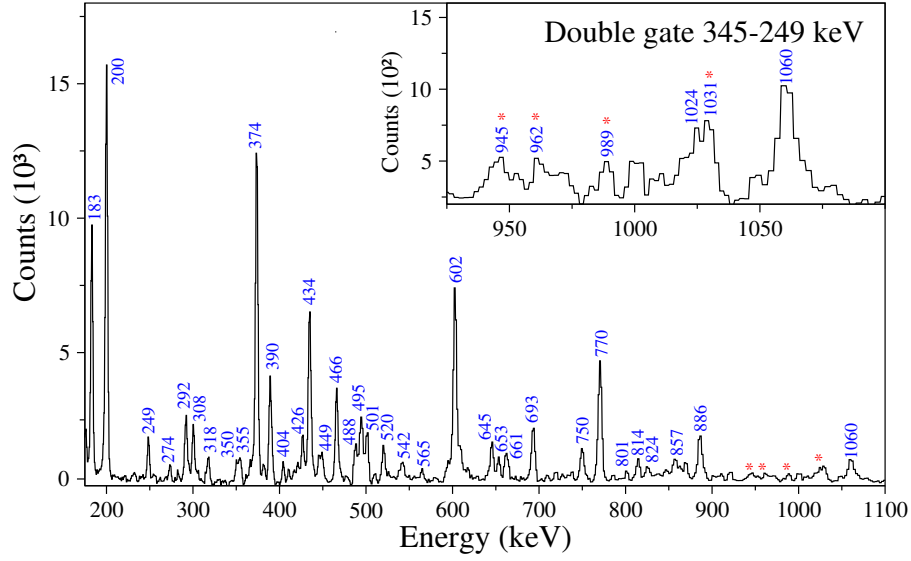


Figure 5.9: Double-gated spectrum on the 249- and 345-keV transitions of band D3, showing the connecting transitions of band D3-chiral to band D3, which are indicated with asterisks.

Band D5 first reported in Ref. [105] is confirmed. Several new decay-out transitions with energies of 180, 412, 709, 765, 952, 1480 and 1660 keV have been identified. Band D5-chiral consisting of in-band dipole and E2 crossover transitions is new. A sum of coincidence spectra obtained by double-gating on the transitions of band D5 is given in Fig. 5.11. Band D5-chiral is linked to band D5 by many dipole and quadrupole transitions. The relatively large intensities of the transitions of bands D5 and D5-chiral, made possible the extraction of the $B(M1)/B(E2)$ branching ratios for both bands, which are very similar and strongly support the chiral interpretation [114].

Band D6 first reported in Ref. [105] is confirmed. In the present work, we extended it up to $I^\pi = 30^-$ by adding on top of the previous band three dipole transitions of 581, 604 and 660 keV, and four crossover transitions of 945, 1112, 1185 and 1264 keV.

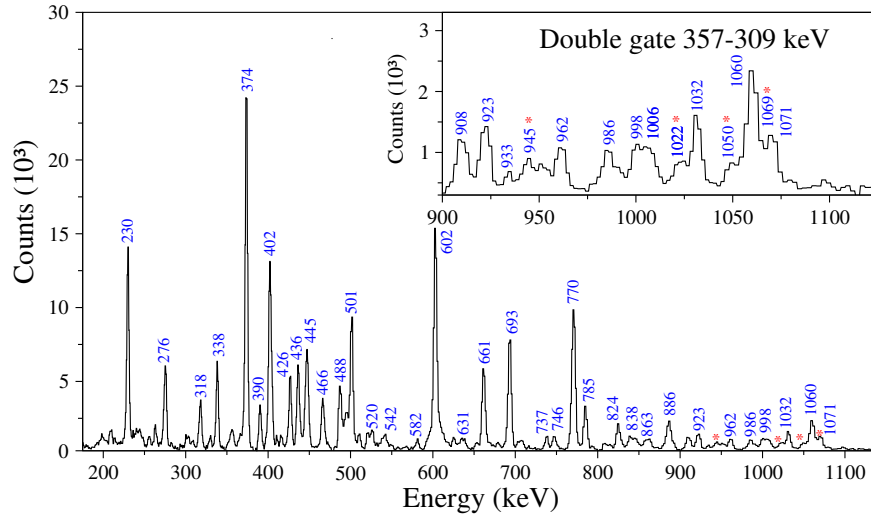


Figure 5.10: Double-gated spectrum on the 309- and 357-keV transitions of band D4. The peaks corresponding to the connecting transitions of band D4-chiral to band D4 are indicated with asterisks.

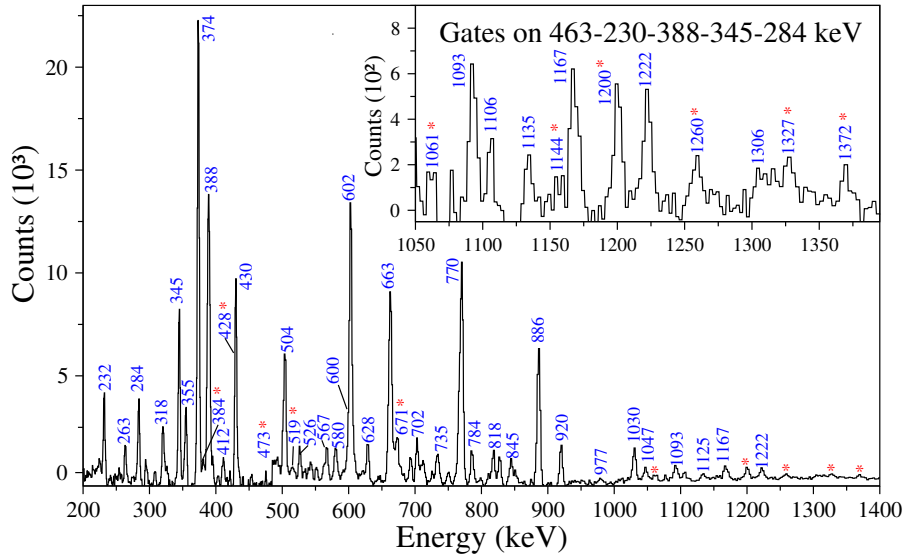


Figure 5.11: Sum of spectra obtained by double-gating on all combinations of the 230-, 284-, 345-, 388- and 463-keV transitions of band D5. The peaks corresponding to the in-band transitions of band D5-chiral and to the connecting transitions to band D5 are indicated with asterisks.

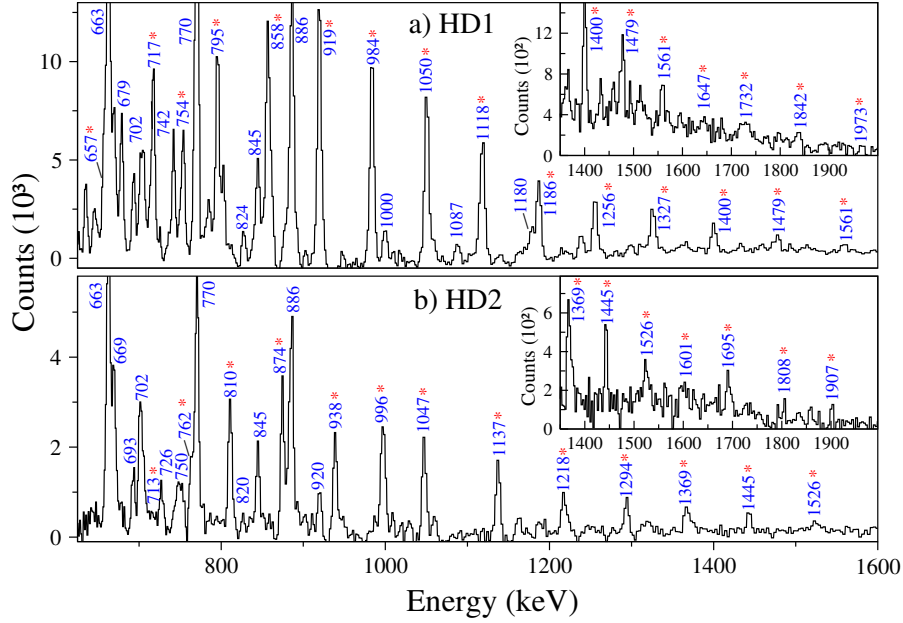


Figure 5.12: Sum of spectra obtained by double-gating on all combinations of in-band transitions of: a) band HD1 and b) band HD2. The peaks corresponding to the in-band transitions of each band are indicated with asterisks.

5.1.4 The highly-deformed bands

Five highly-deformed (HD) bands have been observed in ^{136}Nd in the present work. The three bands HD2, HD4 and HD5 are new. All bands are in coincidence with known low-lying transitions of ^{136}Nd . However, no linking transitions to the normal-deformed states have been found. Tentative spins, parities and excitation energies have been assigned based on the CNS model calculations (see the following sections). Spectra constructed by doubly-gating on all in-band transitions for the five bands are given in Figs. 5.12 and Fig. 5.13.

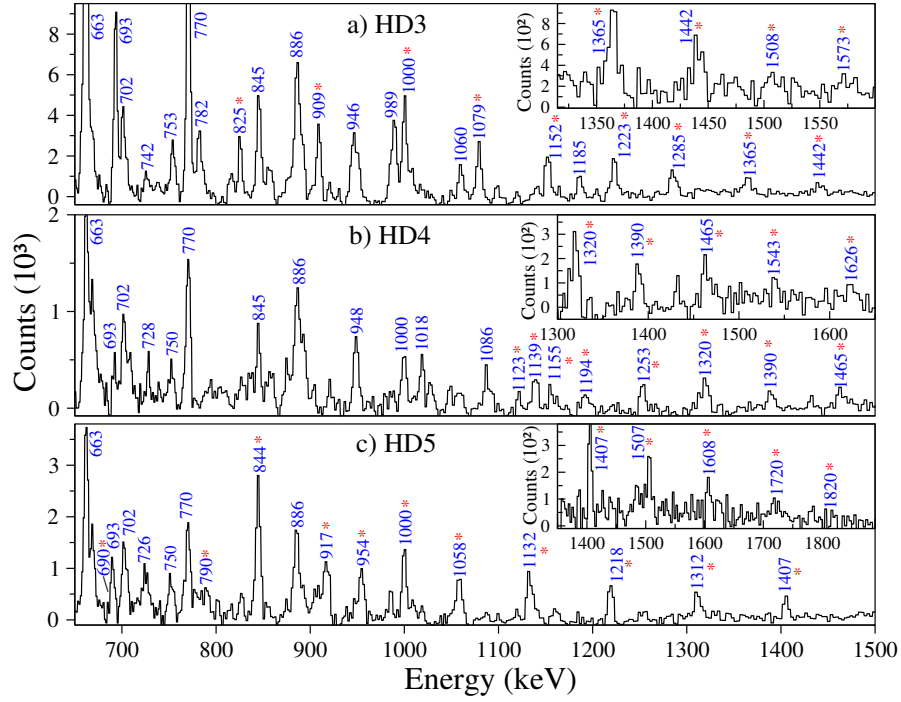


Figure 5.13: Sum of spectra obtained by double-gating on all combinations of in-band transitions of: a) band HD3, b) band HD4, and c) HD5. The peaks corresponding to the in-band transitions of each band are indicated with asterisks.

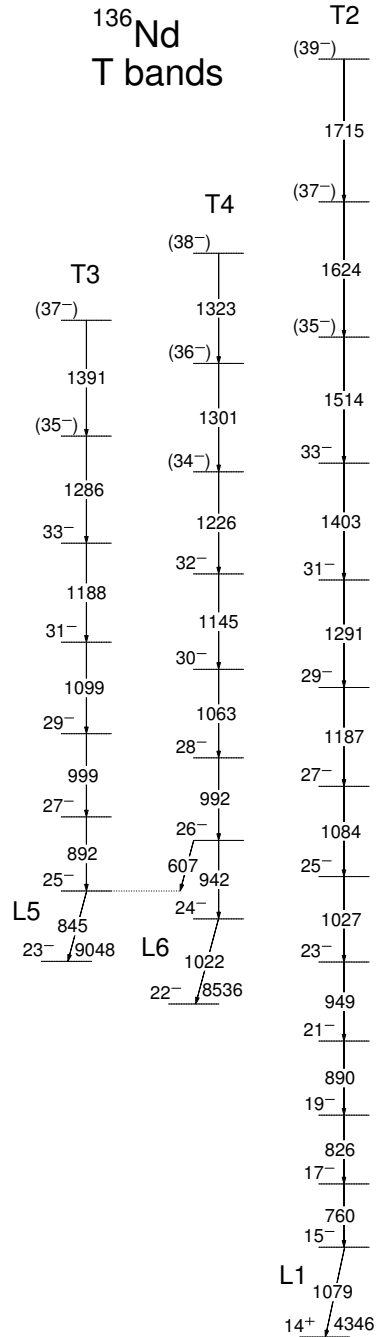
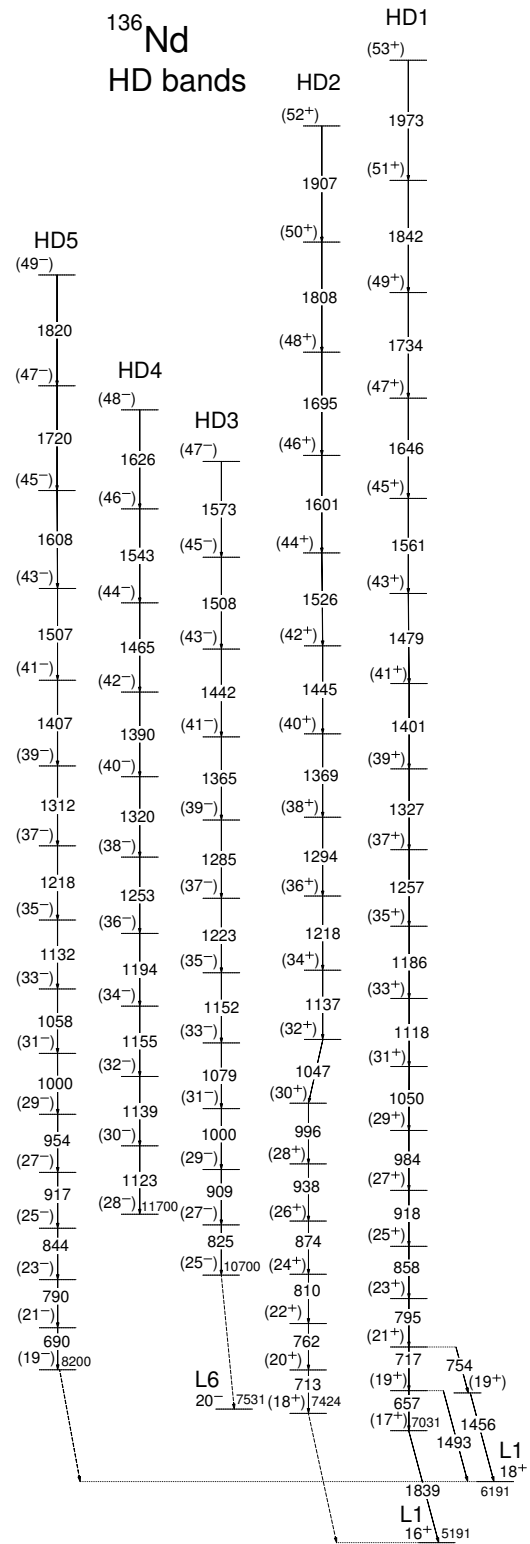
Figure 5.14: Partial level scheme of ^{136}Nd showing the T bands.Figure 5.15: Partial level scheme of ^{136}Nd showing the HD bands.

Table 5.1 – Experimental information including the γ -ray energies, energies of the initial levels E_i , intensities I_γ , anisotropies R_{DCO} and or R_{ac} , multipolarities, and the spin-parity assignments to the observed states in ^{136}Nd . The transitions listed with increasing energy are grouped in bands. The deduced values for R_{DCO} with a stretched quadrupole gate are ≈ 1 for stretched quadrupole and ≈ 0.46 for dipole transitions, while the ratio is close to 1 for a dipole and 2.1 for a quadrupole transition when the gate is set on a dipole transition. The R_{ac} values for stretched dipole and quadrupole transitions are ≈ 0.8 and ≈ 1.4 .

E_γ^a	E_i (keV)	I_γ^b	R_{DCO}^c	R_{ac}^d	Mult.	$J_i^\pi \rightarrow J_f^\pi$
GSB						
373.7	373.7	100.0	1.01(5) ^e		E2	$2^+ \rightarrow 0^+$
602.5	976.2	91(5)	1.06(11) ^e		E2	$4^+ \rightarrow 2^+$
770.2	1746.4	80(7)	0.97(9) ^e		E2	$6^+ \rightarrow 4^+$
886.3	2632.7	56(4)	1.01(15) ^e		E2	$8^+ \rightarrow 6^+$
920.1	3552.8	14(2)	0.99(16) ^e		E2	$10^+ \rightarrow 8^+$
γ band						
182.7	2227.8	0.25(2)		0.73(21)	M1	$6^+ \rightarrow 5^+$
191.9	2227.8	0.12(2)			E1	$6^+ \rightarrow 5^-$
368.7	1230.9	0.8(2)		1.10(25)	M1/E2	$3^+ \rightarrow 2^+$
488.5	862.2	1.7(3)		1.43(31)	E2	$2^+ \rightarrow 2^+$
490.3	3768.0	0.32(4)	0.71(9) ^e		M1/E2	$10^+ \rightarrow 10^+$
551.7	4319.7	2.7(2)	1.13(14) ^e		E2	$12^+ \rightarrow 10^+$
565.5	1541.7	1.3(4)		1.07(45)	M1/E2	$4^+ \rightarrow 4^+$
600.4	3768.0	0.7(2)	1.1(4) ^e		E2	$10^+ \rightarrow 8^+$
679.5	1541.7	1.8(3)	1.05(25) ^e		E2	$4^+ \rightarrow 2^+$
686.1	2227.8	0.71(6)		1.3(2)	E2	$6^+ \rightarrow 4^+$
711.8	5031.5	4.0(3)	1.08(17) ^e		E2	$14^+ \rightarrow 12^+$
725.7	5757.2	2.1(2)			E2	$16^+ \rightarrow 14^+$
735.2	5757.2	2.7(2)	1.1(2) ^e		E2	$16^+ \rightarrow 14^+$
766.9	4319.7	7.7(7)	1.0(2) ^e		E2	$12^+ \rightarrow 10^+$
811.0	2352.7	1.3(2)		1.38(23)	E2	$6^+ \rightarrow 4^+$
814.2	2045.1	6.5(6)		1.31(20)	E2	$5^+ \rightarrow 3^+$
814.9	3167.6	0.92(8)	1.05(15) ^e		E2	$18^+ \rightarrow 16^+$
844.8	6602.0	1.8(2)	0.98(25) ^e		E2	$18^+ \rightarrow 16^+$
857.2	1230.9	6.1(6)		1.16(15)	M1 /E2	$3^+ \rightarrow 2^+$
862.2	862.2	1.5(3)	1.1(3) ^e		E2	$2^+ \rightarrow 0^+$
907.1	6602.0	0.12(1)			E2	$18^+ \rightarrow 16^+$
1017.7	7619.7	0.83(5)	1.02(18) ^e		E2	$20^+ \rightarrow 18^+$
1135.3	3768.0	1.9(3)	0.98(25) ^e		E2	$10^+ \rightarrow 8^+$
1162.7	6603.2	0.21(2)			E2	$18^+ \rightarrow 16^+$

Table 5.1 – *Continued*

E_γ^a	E_i (keV)	I_γ^b	R_{DCO}^c	R_{ac}^d	Mult.	$J_i^\pi \rightarrow J_f^\pi$
1251.6	2227.8	0.31(3)		1.41(26)	E2	$6^+ \rightarrow 4^+$
1410.7	6602.0	0.12(3)			E2	$18^+ \rightarrow 16^+$
1410.8	5757.2	0.11(2)			E2	$16^+ \rightarrow 14^+$
1428.6	7619.7	0.15(2)			E2	$20^+ \rightarrow 18^+$
Band N1						
163.6	2757.3	0.05(1)			M1/E2	$8^- \rightarrow 7^-$
183.1	2940.4	0.65(8)		0.86(15)	M1	$9^- \rightarrow 8^-$
255.6	2483.4	0.65(5)		0.73(13)	E1	$6^- \rightarrow 6^+$
273.9	2757.3	4.1(4)	1.02(15) ^e		E2	$8^- \rightarrow 6^-$
302.8	3243.2	0.9(1)	0.42(8) ^e		M1	$10^- \rightarrow 9^-$
307.7	2940.4	1.1(3)	0.45(15) ^e		E1	$9^- \rightarrow 8^+$
317.7	2757.3	4.7(4)	0.54(7) ^e		M1	$8^- \rightarrow 7^-$
358.1	3601.3	0.72(8)		1.21(15)	M1/E2	$11^- \rightarrow 10^-$
403.7	2439.6	6.4(3)	0.99(8) ^e		E2	$7^- \rightarrow 5^-$
410.0	6903.2	0.18(4)			E2	$19^- \rightarrow 17^-$
410.7	4425.7	0.16(4)	0.42(11) ^e		M1	$13^- \rightarrow 12^-$
411.8	2757.3	0.7(1)		1.45(35)	E2	$8^- \rightarrow 6^-$
413.7	4015.0	0.10(2)			M1/E2	$12^- \rightarrow 11^-$
438.3	2483.4	1.24(7)		0.86(6)	E1	$6^- \rightarrow 5^+$
447.5	2483.4	1.6(2)		0.84(12)	M1	$6^- \rightarrow 5^-$
485.9	3243.2	3.6(4)		1.31(15)	E2	$10^- \rightarrow 8^-$
501.3	2940.4	20(1)	1.06(8) ^e		E2	$9^- \rightarrow 7^-$
660.9	3601.3	8(1)	1.0(1) ^e		E2	$11^- \rightarrow 9^-$
693.2	2439.6	21(2)	0.61(13) ^e		E1	$7^- \rightarrow 6^+$
737.0	2483.4	2.3(3)		1.07(20)	E1	$6^- \rightarrow 6^+$
743.8	6844.0	0.15(1)			E2	$18^- \rightarrow 16^-$
771.8	4015.0	3.3(3)		1.4(2)	E2	$12^- \rightarrow 10^-$
824.4	4425.7	2.7(3)	1.03(15) ^e		E2	$13^- \rightarrow 11^-$
832.0	7676.0	0.09(2)			E2	$(20^-) \rightarrow 18^-$
989.4	5415.1	2.2(2)	1.06(14) ^e		E2	$15^- \rightarrow 13^-$
1005.9	5020.9	2.5(3)	0.97(15) ^e		E2	$14^- \rightarrow 12^-$
1059.7	2035.9	9.3(8)	0.64(11) ^e		E1	$5^- \rightarrow 4^+$
1076.9	6492.0	0.47(4)	1.04(22) ^e		E2	$17^- \rightarrow 15^-$
1079.3	6100.2	0.31(2)		1.32(30)	E2	$16^- \rightarrow 14^-$
Band N2						
154.1	2593.7	0.21(2)		0.7(2)	M1	$7^- \rightarrow 7^-$
248.2	2593.7	2.6(2)		0.68(12)	M1	$7^- \rightarrow 6^-$
300.4	2345.5	4.7(3)		0.81(7)	E1	$6^- \rightarrow 5^+$
316.2	2909.9	0.41(2)	0.87(17) ^f		M1/E2	$8^- \rightarrow 7^-$

Table 5.1 – *Continued*

E_γ^a	E_i (keV)	I_γ^b	R_{DCO}^c	R_{ac}^d	Mult.	$J_i^\pi \rightarrow J_f^\pi$
337.0	3246.9	0.71(2)	0.63(7) ^f		M1/E2	$9^- \rightarrow 8^-$
365.9	2593.7	0.73(3)		0.71(13)	E1	$7^- \rightarrow 6^+$
465.3	3712.2	0.29(2)	0.61(5) ^f		M1/E2	$10^- \rightarrow 9^-$
564.4	2909.9	1.1(1)		1.40(18)	E2	$8^- \rightarrow 6^-$
653.2	3246.9	3.7(2)		1.40(8)	E2	$9^- \rightarrow 7^-$
802.3	3712.2	0.63(3)	1.97(11) ^f		E2	$10^- \rightarrow 8^-$
847.3	2593.7	0.94(5)		0.86(6)	E1	$7^- \rightarrow 6^+$
869.1	4116.0	3.0(2)	2.13(23) ^f		E2	$11^- \rightarrow 9^-$
904.2	4616.4	0.41(8)	2.17(45) ^f		E2	$12^- \rightarrow 10^-$
988.9	5104.9	1.47(6)	2.21(14) ^f		E2	$13^- \rightarrow 11^-$
1068.0	5684.4	0.22(1)	2.0(3) ^f		E2	$14^- \rightarrow 12^-$
Band L1						
123.7	3295.7	0.5(1)	0.47(12) ^e		E1	$10^+ \rightarrow 9^-$
355.3	3295.7	9.7(3)	0.58(8) ^e		E1	$10^+ \rightarrow 9^-$
389.9	3685.6	34(2)	1.01(20) ^e		E2	$12^+ \rightarrow 10^+$
414.7	3172.0	0.63(5)	0.45(12)		M1	$9^- \rightarrow 8^-$
660.8	4346.4	23(2)	1.1(1) ^e		E2	$14^+ \rightarrow 12^+$
663.0	3295.7	30(3)	1.12(24) ^e		E2	$10^+ \rightarrow 8^+$
732.4	3172.0	0.55(2)	1.08(13)		E2	$9^- \rightarrow 7^-$
844.9	5191.3	12.2(7)	1.10(16) ^e		E2	$16^+ \rightarrow 14^+$
883.1	7354.9	0.41(5)		1.5(2)	E2	$20^+ \rightarrow 18^+$
999.8	6191.1	5.7(4)	1.07(15) ^e		E2	$18^+ \rightarrow 16^+$
1163.8	7354.9	1.13(9)		1.47(24)	E2	$20^+ \rightarrow 18^+$
1268.7	8623.6	0.65(4)		1.53(21)	E2	$22^+ \rightarrow 20^+$
1378.2	10001.8	0.10(1)			E2	$(24^+) \rightarrow 22^+$
1492.3	11494.1	0.05(1)			E2	$(26^+) \rightarrow (24^+)$
Band L2						
663.4	5694.9	1.9(2)	1.12(16) ^e		E2	$16^+ \rightarrow 14^+$
672.9	5694.9	3.3(2)	1.04(20) ^e		E2	$16^+ \rightarrow 14^+$
702.3	5022.0	6.1(3)	1.13(17) ^e		E2	$14^+ \rightarrow 12^+$
789.5	6546.7	0.31(2)		1.46(29)	E2	$18^+ \rightarrow 16^+$
851.8	6546.7	1.5(3)	1.03(30) ^e		E2	$18^+ \rightarrow 16^+$
976.7	6546.7	<0.01			E2	$18^+ \rightarrow 16^+$
1044.7	7591.4	0.43(2)		1.44(25)	E2	$20^+ \rightarrow 18^+$
Band L3						
487.3	4454.0	0.10(5)			E2	$13^+ \rightarrow 11^+$
678.5	5131.6	0.63(7)		1.33(23)	E2	$15^+ \rightarrow 13^+$
739.9	6931.0	0.52(4)		0.63(12)	M1	$19^+ \rightarrow 18^+$

Table 5.1 – *Continued*

E_γ^a	E_i (keV)	I_γ^b	R_{DCO}^c	R_{ac}^d	Mult.	$J_i^\pi \rightarrow J_f^\pi$
750.7	5942.0	1.75(6)	0.46(6) ^e		M1	$17^+ \rightarrow 16^+$
768.4	4454.0	1.8(3)		1.54(50)	M1/E2	$13^+ \rightarrow 12^+$
785.2	5131.6	1.9(1)	0.58(12) ^e		M1/E2	$15^+ \rightarrow 14^+$
810.4	5942.0	1.35(8)	0.98(9) ^e		E2	$17^+ \rightarrow 15^+$
989.0	6931.0	1.5(1)	1.01(15) ^e		E2	$19^+ \rightarrow 17^+$
1168.8	8099.8	0.34(3)		1.37(24)	E2	$21^+ \rightarrow 19^+$
Band L4						
370.3	4337.0	0.11(1)			M1/E2	$12^+ \rightarrow 11^+$
401.6	4855.6	0.35(2)		1.05(23)	M1/E2	$14^+ \rightarrow 13^+$
438.4	5570.0	0.42(3)		0.77(14)	M1	$16^+ \rightarrow 15^+$
518.6	4855.6	0.41(2)			E2	$14^+ \rightarrow 12^+$
714.4	5570.0	1.43(7)	0.97(13) ^e		E2	$16^+ \rightarrow 14^+$
784.2	4337.0	0.38(2)		1.33(25)	E2	$12^+ \rightarrow 10^+$
901.8	6471.8	3.1(2)	1.05(18) ^e		E2	$18^+ \rightarrow 16^+$
1001.3	8256.7	0.57(4)	1.1(2) ^e		E2	$20^+ \rightarrow 18^+$
1041.3	4337.0	0.7(2)	1.12(27) ^e		E2	$12^+ \rightarrow 10^+$
1088.4	9345.1	0.21(2)		1.49(29)	E2	$22^+ \rightarrow 20^+$
1170.0	4855.6	1.23(6)	1.11(19) ^e		E2	$14^+ \rightarrow 12^+$
1223.6	5570.0	2.5(2)	0.97(13) ^e		E2	$16^+ \rightarrow 14^+$
1276.7	10621.8	0.17(2)		1.5(2)	E2	$22^+ \rightarrow 20^+$
1280.4	6471.8	0.58(5)	1.10(20) ^e		E2	$18^+ \rightarrow 16^+$
Band L5						
275.1	7141.5	0.11(1)	0.47(9) ^e		E1	$19^- \rightarrow 19^+$
467.4	7141.5	0.03(1)			M1/E2	$19^- \rightarrow 18^-$
518.1	8049.5	< 0.01			M1/E2	$21^- \rightarrow 20^-$
781.4	7141.5	1.5(1)	1.03(19) ^e		E2	$19^- \rightarrow 17^-$
908.0	8049.5	1.35(11)	0.94(12) ^e		E2	$21^+ \rightarrow 19^+$
945.0	6360.1	1.15(9)	1.07(24) ^e		E2	$17^- \rightarrow 15^-$
950.4	7141.5	1.11(7)	0.53(10) ^e		E1	$19^- \rightarrow 18^+$
984.9	9048.4	0.30(2)		1.37(21)	E2	$23^- \rightarrow 21^-$
998.9	9048.4	0.40(4)	1.0(2) ^e		E2	$23^- \rightarrow 21^-$
1168.8	6360.1	0.53(5)	0.49(8) ^e		E1	$17^- \rightarrow 16^+$
Band L6						
390.1	7531.4	0.10(5)			M1/E2	$20^- \rightarrow 19^-$
635.2	6674.1	1.3(1)	1.03(15) ^e		E2	$18^- \rightarrow 16^-$
847.6	6038.9	0.31(1)	0.47(12) ^e		E1	$16^- \rightarrow 16^+$
857.3	7531.4	1.23(14)	0.98(22) ^e		E2	$20^- \rightarrow 18^-$
860.0	8536.0	0.05(1)			E2	$22^- \rightarrow 20^-$

Table 5.1 – *Continued*

E_γ^a	E_i (keV)	I_γ^b	R_{DCO}^c	R_{ac}^d	Mult.	$J_i^\pi \rightarrow J_f^\pi$
1004.6	8536.0	1.1(1)	1.01(18) ^e		E2	$22^- \rightarrow 20^-$
1018.0	6038.9	1.1(2)	1.03(37) ^e		E2	$16^- \rightarrow 14^-$
Band L7						
645.0	3277.7	7.5(6)	1.04(12) ^e		E2	$10^+ \rightarrow 8^+$
718.3	3996.0	4.6(3)	1.05(20) ^e		E2	$12^+ \rightarrow 10^+$
851.6	4848.6	2.9(2)	1.02(15) ^e		E2	$14^+ \rightarrow 12^+$
995.2	5842.8	1.63(17)		1.52(26)	E2	$16^+ \rightarrow 14^+$
Band L8						
342.7	6929.5	0.11(1)		0.71(22)	M1	$18^+ \rightarrow 17^+$
350.0	6929.5	0.45(4)	0.72(15) ^f		M1/E2	$18^+ \rightarrow 17^+$
743.5	6586.3	0.34(2)		0.64(16)	M1	$17^+ \rightarrow 16^+$
841.0	4837.0	0.48(3)		0.68(9)	M1	$13^+ \rightarrow 12^+$
859.7	6586.3	0.19(4)		1.58(45)	E2	$17^+ \rightarrow 15^+$
879.0	5726.6	0.58(2)		1.21(25)	M1/E2	$15^+ \rightarrow 14^+$
889.6	5726.6	0.19(2)		1.5(3)	E2	$15^+ \rightarrow 13^+$
Band L9						
438.7	7732.3	0.13(5)			M1/E2	$20^+ \rightarrow 19^+$
743.9	8794.3	0.05(1)			M1/E2	$22^+ \rightarrow 21^+$
912.1	6754.9	0.74(3)		1.49(23)	E2	$18^+ \rightarrow 16^+$
977.4	7732.3	0.20(1)		1.43(25)	E2	$20^+ \rightarrow 18^+$
1062.3	8794.3	0.10(1)		1.44(22)	E2	$22^+ \rightarrow 20^+$
Band D1						
219.9	4665.9	0.82(6)	0.95(9) ^f		M1	$12^+ \rightarrow 11^+$
254.1	4920.0	1.72(15)	0.48(11) ^e		M1	$13^+ \rightarrow 12^+$
293.8	5213.8	1.42(8)	0.71(7) ^f		M1	$14^+ \rightarrow 13^+$
328.9	4665.9	0.30(3)	1.24(29) ^f		M1/E2	$12^+ \rightarrow 12^+$
345.3	5559.1	1.1(1)	0.66(9) ^f		M1/E2	$15^+ \rightarrow 14^+$
411.1	5970.2	0.75(4)	0.98(10) ^f		M1	$16^+ \rightarrow 15^+$
453.8	6424.0	0.37(9)	0.81(25) ^f		M1/E2	$17^+ \rightarrow 16^+$
479.3	4446.0	0.13(2)		0.83(17)	M1	$11^+ \rightarrow 11^+$
485.0	6909.0	0.23(3)	0.94(20) ^f		M1/E2	$18^+ \rightarrow 17^+$
583.0	4920.0	0.11(1)			M1/E2	$13^+ \rightarrow 12^+$
594.1	7503.1	0.14(2)		1.09(19)	M1/E2	$19^+ \rightarrow 18^+$
613.0	8116.1	0.05(2)			M1/E2	$20^+ \rightarrow 19^+$
618.7	7503.1	0.10(1)			M1/E2	$19^+ \rightarrow 18^+$
639.1	5559.1	0.04(2)			E2	$15^+ \rightarrow 13^+$
671.0	3966.7	0.8(1)	1.21(18) ^f		M1/E2	$11^+ \rightarrow 10^+$

Table 5.1 – *Continued*

E_γ^a	E_i (keV)	I_γ^b	R_{DCO}^c	R_{ac}^d	Mult.	$J_i^\pi \rightarrow J_f^\pi$
699.2	4665.9	0.49(3)	1.1(3) ^f		M1/E2	12 ⁺ \rightarrow 11 ⁺
756.4	5970.2	0.06(3)			E2	16 ⁺ \rightarrow 14 ⁺
844.7	4446.0	0.09(1)			(E1)	11 ⁺ \rightarrow 11 ⁻
864.9	6424.0	0.25(10)			E2	17 ⁺ \rightarrow 15 ⁺
905.0	4920.0	0.15(2)			(E1)	13 ⁺ \rightarrow 12 ⁻
980.3	4665.9	0.16(3)	1.60(45) ^f		M1/E2	12 ⁺ \rightarrow 12 ⁺
1064.6	4665.9	0.26(4)	1.16(36) ^f		E1	12 ⁺ \rightarrow 11 ⁻
1150.3	4446.0	0.62(6)		0.81(8)	M1	11 ⁺ \rightarrow 10 ⁺
1202.8	4446.0	0.05(1)			(E1)	11 ⁺ \rightarrow 10 ⁻
1234.4	4920.0	0.12(3)			M1/E2	13 ⁺ \rightarrow 12 ⁺
D1 – c						
431.7	6485.4	0.15(5)		0.93(50)	M1/E2	17 ⁺ \rightarrow 16 ⁺
503.9	6989.3	<0.01			M1/E2	18 ⁺ \rightarrow 17 ⁺
515.2	6485.4	0.11(3)		0.73(28)	M1	17 ⁺ \rightarrow 16 ⁺
716.4	5636.4	0.03(2)			E2	15 ⁺ \rightarrow 13 ⁺
839.9	6053.7	0.22(4)		1.4(3)	E2	16 ⁺ \rightarrow 14 ⁺
1019.1	6989.3	0.10(3)		1.43(32)	E2	18 ⁺ \rightarrow 16 ⁺
1045.2	7469.2	0.12(2)		1.31(29)	E2	19 ⁺ \rightarrow 17 ⁺
Band D2						
117.9	6347.9	0.25(10)	0.72(37) ^f		M1/E2	16 ⁺ \rightarrow 15 ⁺
231.1	6579.0	0.89(6)		0.78(7)	M1	17 ⁺ \rightarrow 16 ⁺
298.1	6884.4	0.11(1)		0.86(15)	M1	18 ⁺ \rightarrow 17 ⁺
305.4	6884.4	1.41(15)		1.06(20)	M1/E2	18 ⁺ \rightarrow 17 ⁺
318.3	8050.6	0.21(2)		1.10(14)	M1/E2	21 ⁺ \rightarrow 20 ⁺
364.6	7293.6	0.50(4)	1.17(18) ^f		M1	19 ⁺ \rightarrow 18 ⁺
376.4	7670.0	1.9(3)	1.54(60) ^f		M1/E2	20 ⁺ \rightarrow 19 ⁺
380.6	8050.6	1.4(2)		0.85(12)	M1	21 ⁺ \rightarrow 20 ⁺
384.6	7293.6	0.12(2)	1.02(17) ^f		M1	19 ⁺ \rightarrow 18 ⁺
409.2	7293.6	1.72(9)	0.84(8) ^f		M1/E2	19 ⁺ \rightarrow 18 ⁺
416.3	8466.9	1.15(3)	0.98(9) ^f		M1	22 ⁺ \rightarrow 21 ⁺
460.4	6884.4	0.21(1)		1.16(13)	M1/E2	18 ⁺ \rightarrow 17 ⁺
481.2	8948.1	0.89(4)	0.88(9) ^f		M1/E2	23 ⁺ \rightarrow 22 ⁺
543.3	9491.4	0.52(1)	1.15(15) ^f		M1	24 ⁺ \rightarrow 23 ⁺
600.0	10091.4	0.37(10)			M1/E2	25 ⁺ \rightarrow 24 ⁺
671.8	10763.2	0.27(4)	0.85(22) ^f		M1/E2	26 ⁺ \rightarrow 25 ⁺
736.2	6579.0	0.55(4)		1.13(18)	M1/E2	17 ⁺ \rightarrow 16 ⁺
785.6	7670.0	0.08(2)			E2	20 ⁺ \rightarrow 18 ⁺
852.4	6579.0	0.5(2)		1.3(4)	E2	17 ⁺ \rightarrow 15 ⁺
914.2	6884.4	0.15(2)			E2	18 ⁺ \rightarrow 16 ⁺

Table 5.1 – *Continued*

E_γ^a	E_i (keV)	I_γ^b	R_{DCO}^c	R_{ac}^d	Mult.	$J_i^\pi \rightarrow J_f^\pi$
942.0	4938.0	0.35(5)		0.8(2)	M1	$13^+ \rightarrow 12^+$
1292.0	6230.0	0.17(3)		1.41(42)	E2	$15^+ \rightarrow 13^+$
1393.0	6230.0	0.10(2)			E2	$15^+ \rightarrow 13^+$
1382.4	6230.0	0.14(2)		1.0(3)	M1/E2	$15^+ \rightarrow 14^+$
D2 – c						
408.7	9248.7	0.10(3)		1.25(40)	M1/E2	$23^+ \rightarrow 22^+$
(426.0)	8840.0	<0.01			M1/E2	$22^+ \rightarrow 21^+$
447.2	9695.9	<0.02			M1/E2	$24^+ \rightarrow 23^+$
453.1	10659.2	0.04(1)			M1/E2	$26^+ \rightarrow 25^+$
510.2	10206.1	0.05(2)			M1/E2	$25^+ \rightarrow 24^+$
599.4	11258.6	0.05(2)			M1/E2	$27^+ \rightarrow 26^+$
1120.4	8414.0	0.14(3)		1.31(42)	E2	$21^+ \rightarrow 19^+$
1167.2	11258.6	0.10(3)		1.42(60)	E2	$27^+ \rightarrow 25^+$
1167.8	10659.2	0.03(2)			E2	$26^+ \rightarrow 24^+$
1170.0	8840.0	0.18(4)		1.4(3)	E2	$22^+ \rightarrow 20^+$
1198.1	9248.7	0.15(3)		1.37(50)	E2	$23^+ \rightarrow 21^+$
1229.0	9696.9	0.10(3)		1.40(45)	E2	$24^+ \rightarrow 22^+$
1258.0	10206.1	0.05(1)			E2	$25^+ \rightarrow 23^+$
Band D3						
134.2	5732.2	0.13(1)		0.76(13)	M1	$15^- \rightarrow 14^-$
183.1	5532.1	1.64(7)		0.75(8)	M1	$14^- \rightarrow 13^-$
200.1	5732.2	1.53(15)	1.02(15) ^f		M1/E2	$15^- \rightarrow 14^-$
248.7	5980.9	1.33(10)	1.05(17) ^f		M1	$16^- \rightarrow 15^-$
292.0	5349.0	1.71(5)		0.79(5)	M1	$13^- \rightarrow 12^-$
333.4	5980.9	0.07(1)			M1/E2	$16^- \rightarrow 15^-$
345.4	6326.3	1.7(2)		0.74(11)	M1	$17^- \rightarrow 16^-$
355.1	5532.1	0.3(1)	1.14(43) ^f		M1	$14^- \rightarrow 13^-$
369.9	6326.3	0.23(1)			M1/E2	$17^- \rightarrow 16^-$
382.4	5980.9	1.03(7)	1.94(29) ^f		E2	$16^- \rightarrow 14^-$
383.2	5732.2	0.15(3)	1.9(4) ^f		E2	$15^- \rightarrow 13^-$
421.5	5598.5	0.31(1)		0.79(11)	M1	$14^- \rightarrow 13^-$
427.2	5532.1	0.05(1)			M1/E2	$14^- \rightarrow 13^-$
434.2	6760.5	1.23(9)	1.1(2) ^f		M1	$18^- \rightarrow 17^-$
447.3	6760.5	0.41(3)		0.8(1)	M1	$18^- \rightarrow 17^-$
448.8	8169.9	0.36(1)	1.07(17) ^f		M1	$21^- \rightarrow 20^-$
448.8	5980.9	0.27(12)			E2	$16^- \rightarrow 14^-$
465.7	7226.2	0.74(5)	1.19(18) ^f		M1	$19^- \rightarrow 18^-$
493.6	5598.5	0.42(3)		1.01(13)	M1/E2	$14^- \rightarrow 13^-$
494.9	7721.1	0.57(7)	0.92(12) ^f		M1	$20^- \rightarrow 19^-$

Table 5.1 – *Continued*

E_γ^a	E_i (keV)	I_γ^b	R_{DCO}^c	R_{ac}^d	Mult.	$J_i^\pi \rightarrow J_f^\pi$
520.0	5349.0	0.35(4)		1.11(28)	M1/E2	$13^- \rightarrow 12^-$
520.2	8690.1	0.25(4)	$1.28(27)^f$		M1/E2	$22^- \rightarrow 21^-$
542.0	9232.1	0.15(1)	$1.6(3)^f$		M1/E2	$23^- \rightarrow 22^-$
555.1	9787.2	0.04(1)			M1/E2	$24^- \rightarrow 23^-$
557.0	5734.0	0.12(1)		1.1(1)	M1/E2	$14^- \rightarrow 13^-$
560.6	5177.0	< 0.01			M1/E2	$13^- \rightarrow 12^-$
594.1	6326.3	0.27(2)		1.3(2)	E2	$17^- \rightarrow 15^-$
732.6	5349.0	0.09(1)			E2	$13^+ \rightarrow 12^-$
750.1	4027.8	$2.36(20)$		$0.74(10)$	E1	$11^- \rightarrow 10^+$
750.9	5598.5	$0.58(3)$	$1.02(15)^f$		M1	$14^- \rightarrow 14^+$
801.2	4829.0	$0.41(2)$		$0.77(14)$	M1	$12^- \rightarrow 11^-$
943.7	8169.9	$0.07(2)$			E2	$21^- \rightarrow 19^-$
960.6	7721.1	$0.08(3)$			E2	$20^- \rightarrow 18^-$
1029.2	5057.0	$1.95(4)$		$1.08(15)$	M1/E2	$12^- \rightarrow 11^-$
1061.0	5177.0	$1.2(3)$		$1.1(3)$	M1/E2	$13^- \rightarrow 12^-$
1097.1	9787.2	$0.02(1)$			E2	$24^- \rightarrow 23^-$
1185.7	5532.1	$0.26(2)$		$0.92(25)$	E1	$14^- \rightarrow 14^+$
1353.0	5349.0	$0.4(1)$		$0.89(30)$	E1	$13^- \rightarrow 12^+$
D3 – c						
945.1	7271.4	$0.21(5)$		$1.44(55)$	E2	$19^- \rightarrow 17^-$
962.1	7722.6	$0.11(5)$		$1.5(4)$	E2	$20^- \rightarrow 18^-$
988.9	8215.1	$0.07(2)$		$1.39(32)$	E2	$21^- \rightarrow 19^-$
1030.6	8751.7	$0.16(3)$		$1.35(26)$	E2	$22^- \rightarrow 20^-$
Band D4						
224.2	5956.4	$0.07(2)$			M1/E2	$16^- \rightarrow 15^-$
229.7	5647.5	$1.29(10)$	$0.75(10)^f$		M1/E2	$15^- \rightarrow 14^-$
275.7	5647.5	$0.54(3)$	$0.77(5)^f$		M1/E2	$15^- \rightarrow 14^-$
308.9	5956.4	$2.3(2)$	$0.48(8)^e$		M1	$16^- \rightarrow 15^-$
332.3	6313.2	$0.77(5)$		$0.84(8)$	M1	$17^- \rightarrow 16^-$
338.7	5647.5	$0.82(7)$	$0.83(11)^f$		M1/E2	$15^- \rightarrow 14^-$
356.8	6313.2	$1.7(2)$	$0.93(24)^f$		M1	$17^- \rightarrow 16^-$
388.7	6715.0	$0.61(18)$			M1/E2	$18^- \rightarrow 17^-$
401.8	6715.0	$1.9(2)$	$1.09(19)^f$		M1	$18^- \rightarrow 17^-$
426.6	7577.7	$1.1(1)$	$0.97(13)^f$		M1	$20^- \rightarrow 19^-$
436.1	7151.1	$1.82(20)$	$0.45(6)^e$		M1	$19^- \rightarrow 18^-$
445.3	8023.0	$0.88(10)$	$0.95(27)^f$		M1	$21^- \rightarrow 20^-$
487.6	8510.6	$0.61(6)$	$1.17(29)^f$		M1/E2	$22^- \rightarrow 21^-$
510.0	9020.6	$0.30(5)$		$0.73(21)$	M1	$23^- \rightarrow 22^-$
538.6	5956.4	$0.33(6)$		$1.39(42)$	E2	$16^- \rightarrow 14^-$
541.3	5956.4	$0.24(1)$		$1.16(18)$	M1/E2	$16^- \rightarrow 15^-$

Table 5.1 – *Continued*

E_γ^a	E_i (keV)	I_γ^b	R_{DCO}^c	R_{ac}^d	Mult.	$J_i^\pi \rightarrow J_f^\pi$
549.8	9570.4	0.21(2)		1.13(25)	M1/E2	$24^- \rightarrow 23^-$
630.8	10201.2	0.05(2)			M1/E2	$25^- \rightarrow 24^-$
665.7	6313.2	0.23(6)		1.32(33)	E2	$17^- \rightarrow 15^-$
745.7	4347.0	0.58(3)	0.51(11) ^e		M1	$12^- \rightarrow 11^-$
758.6	5715.0	0.3(1)	1.94(26) ^f		E2	$18^- \rightarrow 16^-$
784.7	4386.0	2.9(2)	0.51(7) ^f		M1/E2	$12^- \rightarrow 11^-$
837.9	7151.1	0.21(4)	1.83(38) ^f		E2	$19^- \rightarrow 17^-$
862.7	7577.7	0.17(4)	1.98(27) ^f		E2	$20^- \rightarrow 18^-$
871.9	8023.0	0.15(3)		1.42(36)	E2	$21^- \rightarrow 19^-$
883.1	5308.8	0.24(3)	1.13(16) ^f		M1	$14^- \rightarrow 13^-$
922.8	5308.8	0.61(5)	1.9(2) ^f		E2	$14^- \rightarrow 12^-$
932.9	8510.6	0.15(3)		1.33(31)	E2	$22^- \rightarrow 20^-$
961.8	5308.8	0.25(2)	1.97(24) ^f		E2	$14^- \rightarrow 12^-$
985.8	5371.8	0.81(4)	2.01(19) ^f		E2	$14^- \rightarrow 12^-$
997.6	9020.6	0.15(5)			E2	$23^- \rightarrow 21^-$
1031.8	5417.8	1.4(1)	1.91(20) ^f		E2	$14^- \rightarrow 12^-$
1059.8	9570.4	0.12(4)		1.4(3)	E2	$24^- \rightarrow 22^-$
1070.8	5417.8	0.33(2)		1.41(21)	E2	$14^- \rightarrow 12^-$
1180.6	10201.2	0.07(2)			E2	$25^- \rightarrow 23^-$
1221.8	5647.5	0.20(2)		1.38(18)	E2	$15^- \rightarrow 13^-$
D4 – c						
945.0	7258.2	0.10(3)		1.36(45)	E2	$19^- \rightarrow 17^-$
1022.0	7737.0	0.25(4)		1.41(27)	E2	$20^- \rightarrow 18^-$
1059.9	8211.0	0.6(3)			(E2)	$21^- \rightarrow 19^-$
1050.3	8628.0	0.14(4)		1.26(37)	E2	$22^- \rightarrow 20^-$
1069.2	9092.2	0.10(2)		1.45(30)	E2	$23^- \rightarrow 21^-$
1172.4	9683.0	<0.01			E2	$24^- \rightarrow 22^-$
Band D5						
180.2	6006.2	0.17(3)		1.51(36)	M1/E2	$16^+ \rightarrow 15^+$
231.8	6238.0	1.8(2)	0.71(12) ^f		M1/E2	$17^+ \rightarrow 16^+$
283.8	6521.8	2.5(4)	0.84(15) ^f		M1/E2	$18^+ \rightarrow 17^+$
319.7	6866.4	1.05(10)	0.39(8) ^e		M1/E2	$19^+ \rightarrow 18^+$
344.6	6866.4	5.9(4)		0.81(9)	M1	$19^+ \rightarrow 18^+$
388.2	7254.6	5(1)			M1/E2	$20^+ \rightarrow 19^+$
412.0	6238.0	0.15(5)		1.3(3)	E2	$17^+ \rightarrow 15^+$
429.7	7684.3	2.8(2)	0.86(13) ^f		M1/E2	$21^+ \rightarrow 20^+$
462.7	8147.0	1.5(1)	0.96(14) ^f		M1	$22^+ \rightarrow 21^+$
504.0	8651.0	1.1(1)	0.97(11) ^f		M1	$23^+ \rightarrow 22^+$
515.6	6521.8	0.35(10)	0.92(33) ^e		E2	$18^+ \rightarrow 16^+$

Table 5.1 – *Continued*

E_γ^a	E_i (keV)	I_γ^b	R_{DCO}^c	R_{ac}^d	Mult.	$J_i^\pi \rightarrow J_f^\pi$
526.3	9177.3	0.47(5)		0.99(15)	M1/E2	$24^+ \rightarrow 23^+$
543.1	6238.0	0.72(3)	0.74(8) ^e		M1/E2	$17^+ \rightarrow 16^+$
567.1	9744.4	0.31(2)		0.74(16)	M1	$25^+ \rightarrow 24^+$
579.8	6521.8	1.01(8)	1.22(18) ^f		M1/E2	$18^+ \rightarrow 17^+$
599.6	10344.0	0.2(1)			M1/E2	$26^+ \rightarrow 25^+$
628.4	6866.4	1.3(2)	1.02(19) ^e		E2	$19^+ \rightarrow 17^+$
707.9	7254.6	0.25(3)		1.41(26)	E2	$20^+ \rightarrow 18^+$
732.8	7254.6	0.8(2)		1.4(3)	E2	$20^+ \rightarrow 18^+$
764.6	6521.8	1.9(2)	2.16(29) ^f		E2	$18^+ \rightarrow 16^+$
798.7	6238.0	0.81(7)	1.34(16) ^e		M1/E2	$17^+ \rightarrow 16^+$
817.9	7684.3	1.6(2)	2.39(35) ^f		E2	$21^+ \rightarrow 19^+$
826.9	6521.8	2.7(3)	2.15(30) ^f		E2	$18^+ \rightarrow 16^+$
874.6	6006.2	0.16(4)		1.11(25)	M1/E2	$16^+ \rightarrow 15^+$
892.4	8147.0	0.94(5)	2.28(22) ^f		E2	$22^+ \rightarrow 20^+$
951.8	6521.8	0.16(2)		1.31(22)	E2	$18^+ \rightarrow 16^+$
966.7	8651.0	0.78(7)	2.13(27) ^f		E2	$23^+ \rightarrow 21^+$
1030.3	9177.3	0.38(5)		1.49(34)	E2	$24^+ \rightarrow 22^+$
1046.7	6238.0	1.04(7)	0.46(7) ^e		M1	$17^+ \rightarrow 16^+$
1092.9	5439.3	1.5(1)	0.92(14) ^e		M1	$16^+ \rightarrow 15^+$
1093.4	9744.4	0.5(1)		1.27(23)	E2	$25^+ \rightarrow 23^+$
1106.4	6238.0	0.5(1)	0.93(21) ^e		E2	$17^+ \rightarrow 15^+$
1166.7	10344.0	0.52(5)		1.51(22)	E2	$25^+ \rightarrow 23^+$
1221.6	10966.0	0.12(4)			E2	$27^+ \rightarrow 25^+$
1306.1	11650.1	<0.01			E2	$28^+ \rightarrow 26^+$
1330.5	6521.8	<0.01			E2	$18^+ \rightarrow 16^+$
1368.3	12334.3	<0.01			E2	$29^+ \rightarrow 27^+$
1479.6	5826.0	0.31(2)		1.11(26)	M1/E2	$15^+ \rightarrow 14^+$
1659.8	6006.2	0.23(2)		1.34(28)	E2	$16^+ \rightarrow 14^+$
D5 – c						
281.4	7213.0	0.3(1)		1.17(22)	M1/E2	$19^+ \rightarrow 18^+$
330.0	7543.0	0.42(9)		0.69(15)	M1	$20^+ \rightarrow 19^+$
384.1	7927.1	0.6(1)		0.71(13)	M1/E2	$21^+ \rightarrow 20^+$
428.0	8355.1	1.5(5)	1.10(37) ^f		M1	$22^+ \rightarrow 21^+$
473.0	8828.1	0.5(1)		1.13(24)	M1/E2	$23^+ \rightarrow 22^+$
519.1	9347.2	0.31(10)			M1/E2	$24^+ \rightarrow 23^+$
563.9	9911.1	0.10(3)			M1/E2	$25^+ \rightarrow 24^+$
611.4	7543.0	0.21(10)			E2	$20^+ \rightarrow 18^+$
670.8	8355.1	0.65(6)	0.93(18) ^e		M1/E2	$22^+ \rightarrow 21^+$
672.5	7927.1	0.5(2)	1.45(48) ^f		M1/E2	$21^+ \rightarrow 20^+$
714.1	7927.1	0.18(4)		1.33(40)	E2	$21^+ \rightarrow 19^+$
812.1	8355.1	0.62(20)		1.4(3)	E2	$22^+ \rightarrow 20^+$

Table 5.1 – *Continued*

E_γ^a	E_i (keV)	I_γ^b	R_{DCO}^c	R_{ac}^d	Mult.	$J_i^\pi \rightarrow J_f^\pi$
901.0	8828.1	0.3(1)			E2	$23^+ \rightarrow 21^+$
975.0	7213.0	0.3(1)		1.33(35)	E2	$19^+ \rightarrow 17^+$
992.1	9347.2	0.25(10)			E2	$24^+ \rightarrow 22^+$
1021.2	7543.0	0.6(1)		1.42(21)	E2	$20^+ \rightarrow 18^+$
1060.7	7927.1	0.8(4)			E2	$21^+ \rightarrow 19^+$
1083.0	9911.1	0.10(2)			E2	$25^+ \rightarrow 23^+$
1100.5	8355.9	0.2(1)	2.1(6) ^f		E2	$22^+ \rightarrow 20^+$
1143.8	8828.1	0.15(5)	1.06(21) ^e		E2	$23^+ \rightarrow 21^+$
1156.8	10504.0	<0.01			E2	$26^+ \rightarrow 24^+$
1200.2	9347.2	0.4(1)		1.37(28)	E2	$24^+ \rightarrow 22^+$
1260.1	9911.1	0.19(4)		1.50(36)	E2	$25^+ \rightarrow 23^+$
1326.7	10504.0	0.02(1)			E2	$26^+ \rightarrow 24^+$
1371.6	11116.0	<0.01			E2	$27^+ \rightarrow 25^+$
Band D6						
315.7	8379.2	0.60(5)	0.35(5) ^e		M1/E2	$22^- \rightarrow 21^-$
329.7	8379.2	0.60(4)	0.68(12) ^e		M1/E2	$22^- \rightarrow 21^-$
374.0	8753.2	0.82(7)			M1/E2	$23^- \rightarrow 22^-$
410.3	9063.5	0.91(8)	0.51(6) ^e		M1	$24^- \rightarrow 23^-$
453.7	9617.2	0.49(4)	0.45(7) ^e		M1	$25^- \rightarrow 24^-$
491.4	10108.6	0.38(3)	0.28(9) ^e		M1/E2	$28^- \rightarrow 26^-$
530.4	10639.0	0.18(2)		0.77(17)	M1	$27^- \rightarrow 26^-$
581.2	11220.2	0.07(2)			M1/E2	$28^- \rightarrow 27^-$
603.8	11824.0	0.03(1)			M1/E2	$29^- \rightarrow 28^-$
660.1	12484.1	0.02(1)			M1/E2	$30^- \rightarrow 29^-$
689.7	8753.2	0.10(1)			E2	$23^- \rightarrow 21^-$
703.7	8753.2	0.41(3)	0.85(16) ^e		E2	$23^- \rightarrow 21^-$
784.3	9163.5	0.22(2)	0.95(14) ^e		E2	$24^- \rightarrow 22^-$
864.0	9617.2	0.30(3)	1.10(22) ^e		E2	$25^- \rightarrow 23^-$
922.2	8063.5	1.15(6)	0.98(15) ^e		E2	$21^- \rightarrow 19^-$
945.1	10108.6	0.52(3)	1.08(13) ^e		E2	$26^- \rightarrow 24^-$
1021.8	10639.0	0.32(3)		1.30(21)	E2	$27^- \rightarrow 25^-$
1111.6	11220.2	0.17(2)		1.53(28)	E2	$28^- \rightarrow 26^-$
1185.0	11824.0	0.10(1)		1.37(36)	E2	$29^- \rightarrow 27^-$
1263.9	12484.1	0.08(2)			E2	$30^- \rightarrow 28^-$
Band T1						
858.9	7330.7	1.73(16)	1.09(19) ^e		E2	$20^+ \rightarrow 18^+$
893.2	8223.9	2.9(3)		1.35(20)	E2	$22^+ \rightarrow 20^+$
948.9	9172.8	2.1(1)		1.43(15)	E2	$24^+ \rightarrow 22^+$
1018.8	10191.6	1.5(2)		1.42(22)	E2	$26^+ \rightarrow 24^+$

Table 5.1 – *Continued*

E_γ^a	E_i (keV)	I_γ^b	R_{DCO}^c	R_{ac}^d	Mult.	$J_i^\pi \rightarrow J_f^\pi$
1086.8	11278.4	0.92(9)		1.54(20)	E2	$28^+ \rightarrow 26^+$
1121.5	13539.5	0.28(2)		1.39(21)	E2	$32^+ \rightarrow 30^+$
1139.6	7330.7	2.0(3)		1.56(30)	E2	$20^+ \rightarrow 18^+$
Band T2						
759.5	6184.7	0.58(5)		1.51(27)	E2	$17^- \rightarrow 15^-$
826.0	7010.7	0.70(7)		1.46(21)	E2	$19^- \rightarrow 17^-$
890.3	7901.0	0.73(8)		1.42(30)	E2	$21^- \rightarrow 19^-$
948.6	8849.6	0.7(1)		1.46(27)	E2	$23^- \rightarrow 21^-$
1027.4	9877.0	0.67(6)		1.4(2)	E2	$25^- \rightarrow 23^-$
1078.8	5425.2	0.65(15)		0.99(29)	E1	$15^- \rightarrow 14^+$
1084.0	10961.0	0.6(1)		1.41(25)	E2	$27^- \rightarrow 25^-$
1186.9	12147.9	0.44(4)		1.45(20)	E2	$29^- \rightarrow 27^-$
1290.9	13438.8	0.36(3)		1.36(34)	E2	$31^- \rightarrow 29^-$
1402.6	14841.4	0.22(3)		1.33(27)	E2	$33^- \rightarrow 31^-$
1514.0	16355.4	0.09(2)			E2	$(35^-) \rightarrow 33^-$
1624.4	17979.8	0.07(2)			E2	$(37^-) \rightarrow (35^-)$
1715.3	19695.1	0.03(1)			E2	$(39^-) \rightarrow (37^-)$
Band T3						
845.1	9893.5	0.6(1)	1.0(2) ^e		E2	$25^- \rightarrow 23^-$
892.4	10785.9	0.42(3)	0.96(10) ^e		E2	$27^- \rightarrow 25^-$
998.6	11784.5	0.31(4)		1.4(2)	E2	$29^- \rightarrow 27^-$
1099.4	12883.9	0.20(3)	1.08(21) ^e		E2	$31^- \rightarrow 29^-$
1188.4	14072.3	0.11(2)	0.93(25) ^e		E2	$33^- \rightarrow 31^-$
1286.1	15358.3	0.05(1)			E2	$(35^-) \rightarrow 33^-$
1390.6	16748.9	<0.01			E2	$(37^-) \rightarrow (35^-)$
Band T4						
606.9	10499.2	0.03(1)			M1/E2	$26^- \rightarrow 25^-$
860.0	11392.0	0.10(2)			E2	$(28^-) \rightarrow 26^-$
941.8	10499.2	0.27(2)	0.98(19) ^e		E2	$26^- \rightarrow 24^-$
973.6	10532.0	0.16(1)		1.44(33)	E2	$26^- \rightarrow 24^-$
991.6	11490.8	0.23(3)	0.99(16) ^e		E2	$28^- \rightarrow 26^-$
1022.4	9558.4	0.66(6)	1.11(15) ^e		E2	$24^- \rightarrow 22^-$
1062.7	12553.5	0.18(3)	0.95(18) ^e		E2	$30^- \rightarrow 28^-$
1145.1	13698.6	0.11(1)		1.38(20)	E2	$32^- \rightarrow 30^-$
1226.3	14924.9	0.09(2)			E2	$(34^-) \rightarrow 32^-$
1301.1	16226.0	0.05(1)			E2	$(36^-) \rightarrow (34^-)$
1323.3	17549.3	<0.01			E2	$(38^-) \rightarrow (36^-)$

^a The error on the transition energies is 0.2 keV for transitions below 1000 keV of the ^{136}Nd reaction channel, 0.5 keV for transitions above 1000 keV and 1 keV for transitions above 1200 keV.

^b Relative intensities corrected for efficiency, normalized to the intensity of the 373.7 keV transition. The transition intensities were obtained from a combination of total projection and gated spectra.

^c R_{DCO} has been deduced from an asymmetric γ - γ coincidence matrices sorted with detectors at 157.6° on one axis, and detectors at $\approx 90^\circ$ on the other axis. The tentative spin-parity of the states are given in parenthesis.

^d R_{ac} has been deduced from two asymmetric γ - γ coincidence matrices sorted with all detectors at 133.6° and 157.6° on one axis, and detectors at $\approx 90^\circ$ on the other axis. The tentative spin-parity of the states are given in parenthesis.

^e DCO ratio from spectrum gated on stretched quadrupole transition.

^f DCO ratio from spectrum gated on stretched dipole transition.

Table 5.2 – Experimental information including the γ ray energies, energies of the initial levels E_i and the tentative spin-parity assignments to the observed states in ^{136}Nd .

E_γ	E_i (keV)	$J_i^\pi \rightarrow J_f^\pi$	E_γ	E_i (keV)	$J_i^\pi \rightarrow J_f^\pi$
HD1			825.1	11525.1	$(25^-) \rightarrow (27^-)$
656.8	7687.8	$(17^+) \rightarrow (19^+)$	908.9	12434.0	$(27^-) \rightarrow (29^-)$
717.1	8404.9	$(19^+) \rightarrow (21^+)$	1000.2	13434.2	$(29^-) \rightarrow (31^-)$
795.2	9200.1	$(21^+) \rightarrow (23^+)$	1079.4	14513.6	$(31^-) \rightarrow (33^-)$
857.4	10057.5	$(23^+) \rightarrow (25^+)$	1152.5	15666.1	$(33^-) \rightarrow (35^-)$
919.4	10976.9	$(25^+) \rightarrow (27^+)$	1222.7	16888.8	$(35^-) \rightarrow (37^-)$
983.6	11960.5	$(27^+) \rightarrow (29^+)$	1285.2	18174.0	$(37^-) \rightarrow (39^-)$
1050.1	13010.6	$(29^+) \rightarrow (31^+)$	1365.4	19539.4	$(39^-) \rightarrow (41^-)$
1117.8	14128.4	$(31^+) \rightarrow (33^+)$	1442.1	20981.5	$(41^-) \rightarrow (43^-)$
1186.5	15314.9	$(33^+) \rightarrow (35^+)$	1508.5	22490.0	$(43^-) \rightarrow (45^-)$
1256.2	16571.1	$(35^+) \rightarrow (37^+)$	1573.1	24063.1	$(45^-) \rightarrow (47^-)$
1326.9	17898.0	$(37^+) \rightarrow (39^+)$	HD4		
1400.5	19298.5	$(39^+) \rightarrow (41^+)$	1122.7	12822.7	$(28^-) \rightarrow (30^-)$
1479.2	20777.7	$(41^+) \rightarrow (43^+)$	1139.2	13961.9	$(30^-) \rightarrow (32^-)$
1561.1	22338.8	$(43^+) \rightarrow (45^+)$	1155.1	15117.0	$(32^-) \rightarrow (34^-)$
1646.8	23985.6	$(45^+) \rightarrow (47^+)$	1194.0	16311.0	$(34^-) \rightarrow (36^-)$
1732.4	25718.0	$(47^+) \rightarrow (49^+)$	1252.9	17563.9	$(36^-) \rightarrow (38^-)$
1841.9	27559.9	$(49^+) \rightarrow (51^+)$	1320.4	18884.3	$(38^-) \rightarrow (40^-)$
1973.2	29533.1	$(51^+) \rightarrow (53^+)$	1390.3	20274.6	$(40^-) \rightarrow (42^-)$
HD2			1464.8	21739.4	$(42^-) \rightarrow (44^-)$
713.2	8137.2	$(18^+) \rightarrow (20^+)$	1542.7	23282.1	$(44^-) \rightarrow (46^-)$
762.5	8899.7	$(20^+) \rightarrow (22^+)$	1626.4	24908.5	$(46^-) \rightarrow (48^-)$
810.1	9709.8	$(22^+) \rightarrow (24^+)$	HD5		
873.8	10583.6	$(24^+) \rightarrow (26^+)$	690.5	8890.5	$(19^-) \rightarrow (21^-)$
938.4	11522.0	$(26^+) \rightarrow (28^+)$	790.4	9680.9	$(21^-) \rightarrow (23^-)$
996.5	12518.5	$(28^+) \rightarrow (30^+)$	844.2	10525.1	$(23^-) \rightarrow (25^-)$
1047.2	13565.7	$(30^+) \rightarrow (32^+)$	917.5	11442.6	$(25^-) \rightarrow (27^-)$
1137.5	14703.2	$(32^+) \rightarrow (34^+)$	953.9	12396.5	$(27^-) \rightarrow (29^-)$
1217.8	15921.0	$(34^+) \rightarrow (36^+)$	1000.3	13396.8	$(29^-) \rightarrow (31^-)$
1294.5	17215.5	$(36^+) \rightarrow (38^+)$	1058.1	14454.9	$(31^-) \rightarrow (33^-)$
1368.9	18584.4	$(38^+) \rightarrow (40^+)$	1132.5	15597.4	$(33^-) \rightarrow (35^-)$
1445.2	20029.6	$(40^+) \rightarrow (42^+)$	1218.5	16805.9	$(35^-) \rightarrow (37^-)$
1525.7	21555.3	$(42^+) \rightarrow (44^+)$	1368.9	18174.8	$(37^-) \rightarrow (39^-)$
1601.4	23156.7	$(44^+) \rightarrow (46^+)$	1407.3	19582.1	$(39^-) \rightarrow (41^-)$
1695.4	24852.1	$(46^+) \rightarrow (48^+)$	1507.2	21089.3	$(41^-) \rightarrow (43^-)$
1808.5	26660.6	$(48^+) \rightarrow (50^+)$	1608.4	22697.7	$(43^-) \rightarrow (45^-)$
1906.9	28567.5	$(50^+) \rightarrow (52^+)$	1720.5	24418.2	$(45^-) \rightarrow (47^-)$
HD3			1820.1	26238.3	$(47^-) \rightarrow (49^-)$

5.2 Discussion

As mentioned above, a particularly important feature of level scheme of ^{136}Nd is the observation of the five pairs of doublet bands (see Fig. 5.6). These five pairs of doublet bands is the most extended set of chiral bands observed until now, and therefore represent an important support for the existence of the multiple chiral doublet ($M\chi D$) phenomenon. The constrained and tilted axis cranking covariant density functional theory (TAC-CDFT) and particle-rotor model (PRM) calculations were performed to describe the identified doublet bands [55, 114]. In addition, all rotational bands of ^{136}Nd were discussed within the cranked Nilsson-Strutinsky (CNS) framework [115]. In this part of the thesis, the results of these calculations are presented.

5.2.1 $M\chi D$ interpretation of the chiral bands within TAC-CDFT framework

Generally speaking, in order to describe the chiral rotations, three-dimensional tilted axis cranking covariant density functional theory (3D TAC-CDFT) is required, which has been used to investigate the chiral modes of ^{106}Rh [116]. For the doublet bands built on the 4- and 6-quasiparticle configurations identified in ^{136}Nd , the 3D TAC-CDFT calculations are very challenging. For simplicity, the observed five pairs of rotational bands are investigated within the two-dimensional framework of TAC-CDFT [117–120]. However, the chiral nature of the assigned configurations was tested by performing 3D TAC-CDFT calculations for one of chiral doublet bands D3 as an example. In calculations, the relativistic density functional PC-PK1 [121] is adopted and the Dirac equation is solved in a 3D harmonic oscillator basis in Cartesian coordinates with 10 major shells which provide convergent results in TAC-CDFT calculations [120]. The contribution of the pairing correlations has also been investigated, concluding that they are negligible, in the discussed multi-quasiparticle configurations: the changes of total energy and total angular momentum at the rotational frequency 0.2 MeV are within 0.005% and 4.5% for configuration A. Thus, the pairing correlations can be safely neglected within the TAC-CDFT framework [114].

In order to understand the nature of the observed band structure in ^{136}Nd , by minimizing the energy with respect to the deformation γ , both adiabatic and configuration-fixed β -constrained calculations similar to those in Ref. [122] were performed to search for the possible configurations and deformations. The results are provided in Table 5.3. One can see that three positive-parity configurations (labels A, B, and C) and five negative-parity configurations (labels D, D*, E, F, and H) are candidates for the observed nearly degenerate partner bands. One can also see that all these configurations with particle-hole excitations possess remarkable triaxial deformation, which is the typical feature for the chiral rotational bands. Subsequently, the assignment of configura-

tions listed in Table 5.3 were justified based on the quasiparticle alignments. Furthermore, the configurations and deformations of the assigned configurations were reexamined by TAC-CDFT calculations. The obtained results in Table 5.3 were also used to calculate the $B(M1)/B(E2)$ ratios.

Table 5.3 – Unpaired nucleon configurations labeled A-H and the corresponding parities, calculated by constrained CDFT. The excitation energies E_x (unit MeV) and quadrupole deformation parameters (β, γ) are also presented.

State	E_x	Parity	(β, γ)	Unpaired nucleons
G	0.000	+	(0.24, 27°)	-
A	0.335	+	(0.21, 21°)	$\pi(h_{11/2})^1(d_{5/2}g_{7/2})^{-1} \otimes \nu(h_{11/2})^{-1}(s_{1/2}d_{3/2})^{-1}$
B	3.419	+	(0.22, 19°)	$\pi(h_{11/2})^3(d_{5/2}g_{7/2})^{-1} \otimes \nu(h_{11/2})^{-1}(s_{1/2}d_{3/2})^{-1}$
C	3.704	+	(0.26, 23°)	$\pi(h_{11/2})^2(g_{7/2})^{-2} \otimes \nu(h_{11/2})^{-1}(f_{7/2}h_{9/2})^1$
D	1.173	-	(0.22, 19°)	$\pi(h_{11/2})^2 \otimes \nu(h_{11/2})^{-1}(s_{1/2}d_{3/2})^{-1}(\Omega \sim +\frac{3}{2})$
D*	1.346	-	(0.21, 22°)	$\pi(h_{11/2})^2 \otimes \nu(h_{11/2})^{-1}(s_{1/2}d_{3/2})^{-1}(\Omega \sim -\frac{3}{2})$
E	1.937	-	(0.21, 23°)	$\pi(h_{11/2})^2(d_{5/2}g_{7/2})^{-2} \otimes \nu(h_{11/2})^{-1}(s_{1/2}d_{3/2})^{-1}$
F	2.778	-	(0.20, 35°)	$\pi(h_{11/2})^1(d_{5/2}g_{7/2})^{-1} \otimes \nu(h_{11/2})^{-2}$
H	3.494	-	(0.20, 37°)	$\pi(h_{11/2})^1(d_{5/2}g_{7/2})^{-3} \otimes \nu(h_{11/2})^{-2}$

Fig. 5.16 shows the calculated excitation energies and $\hbar\omega$ versus spin I for the bands D1-D5 using the TAC-CDFT formalism, in comparison with the experimental data. One can see that the theoretical results based on the assigned configurations agree with experimental data, the chiral partner having similar behavior. In detail, for band D1, the theoretical results based on configuration A agree with experimental data well, the configuration assignment being thus validated. Meanwhile, no other configuration can be found to reproduce band D1-C, which indicates that bands D1 and D1-C are based on the same intrinsic state, and therefore that the bands D1 and D1-C are good candidates for chiral partner bands; Similarly, one can conclude that D2 and D2-C, D5 and D5-C, D3 and D3-C, as well as D4 and D4-C are good candidates of chiral doublets bands built on the same intrinsic configurations B, C, D*, and D, respectively. This is one of the evidences in favor of the chiral interpretation.

It should be pointed that the energy references for the positive- and negative-parity calculated bands are taken as those of band D1 at $I = 11 \hbar$ and of band D4 at $I = 15 \hbar$, respectively. One should note that the back-bending phenomenon observed in bands D2, D3, and D4 can be due to crossing with 8-, 6-, and 6-qp configurations, respectively, which is beyond the current TAC-CDFT calculation.

The quasiparticle alignments calculated by TAC-CDFT are shown in Fig. 5.17 in comparison with the experimental data. The parameters $\mathcal{J}_0 = 11 \hbar^2 \text{MeV}^{-1}$ and $\mathcal{J}_1 = 20 \hbar^4 \text{MeV}^{-3}$ for the Harris formula $\mathcal{J} = \mathcal{J}_0 + \mathcal{J}_1 \omega^2$ have been adopted. It is clearly seen that the calculated results based on the assigned configurations reproduce the experimental data very well.

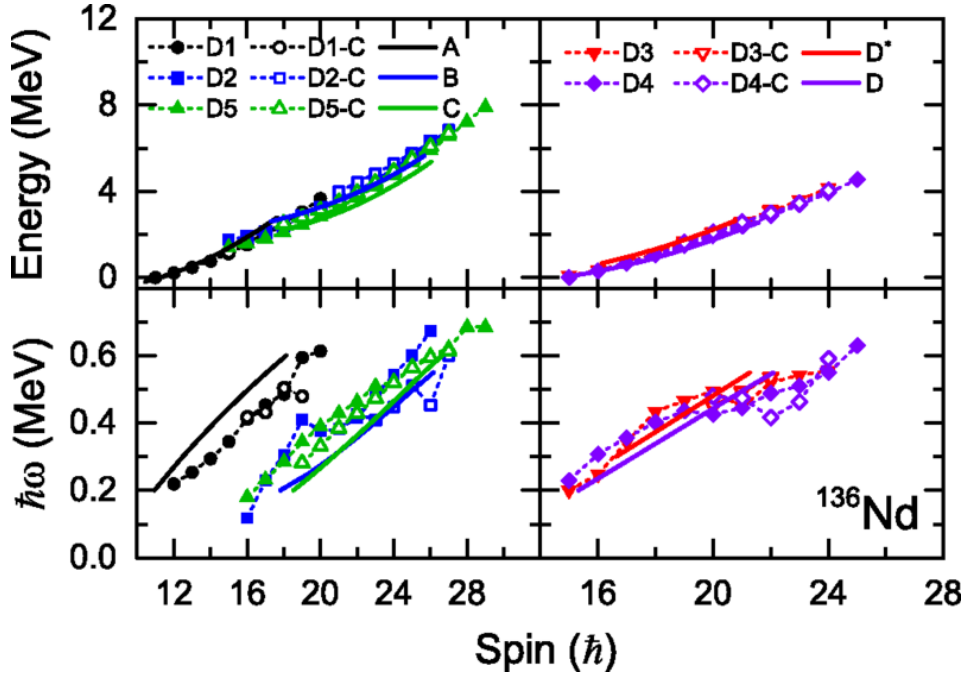


Figure 5.16: Excitation energies and $\hbar\omega$ vs I calculated by TAC-CDFT for the positive (left panel) and negative (right panel) chiral rotational bands of ^{136}Nd .

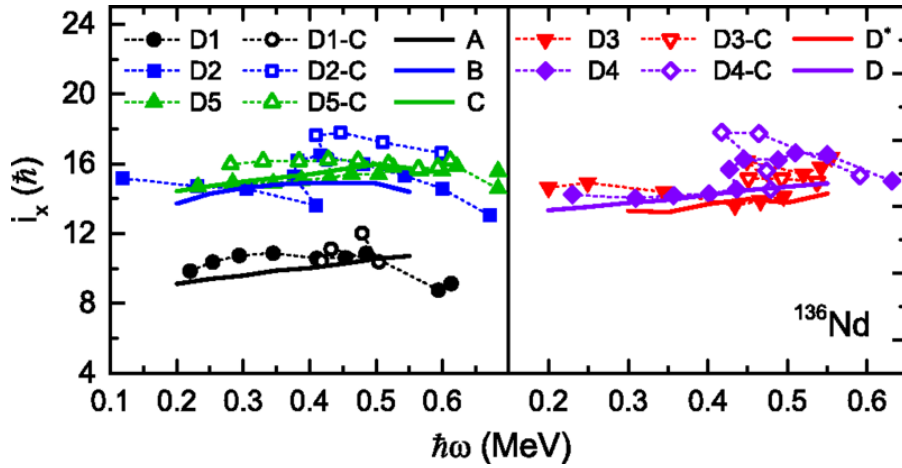


Figure 5.17: Quasiparticle alignments calculated by TAC-CDFT for the positive-parity (left panel) and negative-parity (right panel) chiral rotational bands of ^{136}Nd . Solid and open circles with the same color represent experimental data of one pair of nearly degenerate bands, and different lines denote the theoretical results based on different configurations.

The calculated $B(M1)/B(E2)$ ratios together with some of the measured experimental results are shown in Fig. 5.18. For bands D2, D3, and D4, one can observe that $B(M1)/B(E2)$ ratios firstly increase with increasing spin; at spin around 20, it reaches the maximum and then has a decreasing behavior which is coherent with the behavior of the single-particle alignments. Note that only for the strongest pair of bands D5 and D5-chiral, we could extract the $B(M1)/B(E2)$ values for both bands, which are nearly identical within errors in the observed spin range. This is a strong evidence that D5 and D5-C are chiral bands. One can also see that the calculated $B(M1)/B(E2)$ values based on the configurations A and B underestimate the experimental data of bands D1 and D2, while the theoretical $B(M1)/B(E2)$ values of the assigned configuration are in good agreement with the experimental data of band D5 over all the observed spin range. As for bands D3 and D4, a satisfactory agreement with experimental is only present in the low- and high-spin parts. An abrupt increase of $B(M1)/B(E2)$ values in bands D3 and D4 is observed near back-bending and can not be reproduced by the calculations. As mentioned above, a back-bending also exists in band D2, which induces an abrupt increase of the $B(M1)/B(E2)$ values. It should be noted that although the absolute $B(M1)/B(E2)$ values for bands D1 and D2 are not reproduced, the relative differences agree with the experimental data well.

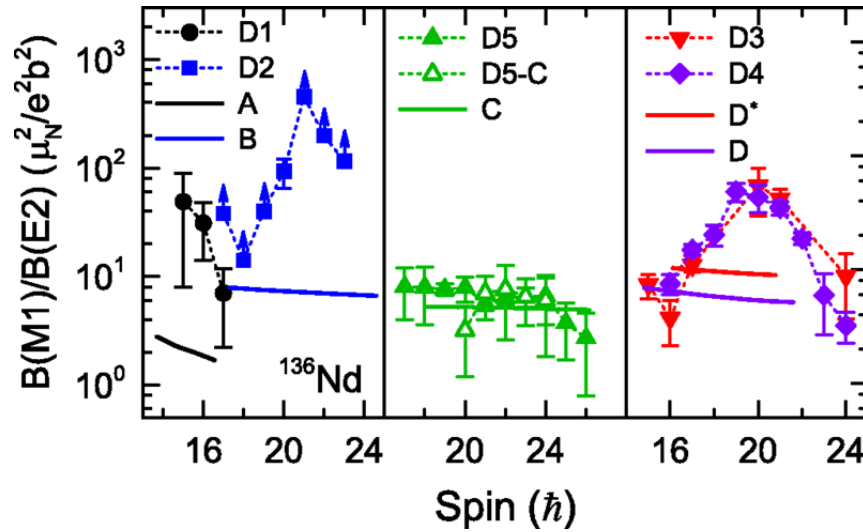


Figure 5.18: Values of transition probabilities $B(M1)/B(E2)$ of ^{136}Nd calculated by TAC-CDFT, in comparison with experimental data (solid and open symbols).

In order to give more strongly theoretical support for the chiral interpretation of the observed doublet bands in ^{136}Nd , our collaborators performed challenging calculations based on 3D TAC-CDFT. Here, we only use band D3 as an example to show the calculated results. In 3D TAC-CDFT calculations, the D^* configuration was assigned to the band D3. Fig. 5.19 shows

the orientation angle ϕ for the total angular momentum of band D3 calculated with 3D TAC-CDFT. It is found that the azimuth angle ϕ for band D3 vanishes at low rotational frequencies, providing a planar solution. Above the critical rotational frequency 0.5 MeV, a nonzero angle ϕ appears, corresponding to an aplanar solution, namely, chiral rotation. Furthermore, for band D3, the observed excitation energies and total angular momenta are also in good agreement with the 3D TAC-CDFT calculations. Although the $B(M1)/B(E2)$ values are not available, these results also provide very strong support for the existence of chiral rotation in band D3.

Summarizing, the observed doublet bands in ^{136}Nd have been compared with results of calculations involving adiabatic and configuration-fixed constrained CDFT, TAC-CDFT, and 3D TAC-CDFT. One can see that the observed energy spectra and alignments are well reproduced for the five pairs of nearly degenerate bands D1-D5 which exhibits the chiral character. Moreover, the band D5 and its partner $B(M1)/B(E2)$ values are in good agreement with the experimental data. The other four doublet bands which are weakly populated, have no measured $B(M1)/B(E2)$ values, but the calculated assigned configurations show chiral geometry. Hence, we suggest that D5 and D5-chiral are chiral doublet bands and the four others doublet bands are chiral candidates, which can contribute to the realization of the multiple pairs of chiral doublet bands ($M\chi D$) phenomenon. It is the first time that chiral bands are observed in an even-even nucleus at high spins, and the set of five nearly degenerate bands is the largest observed in a single nucleus until now.

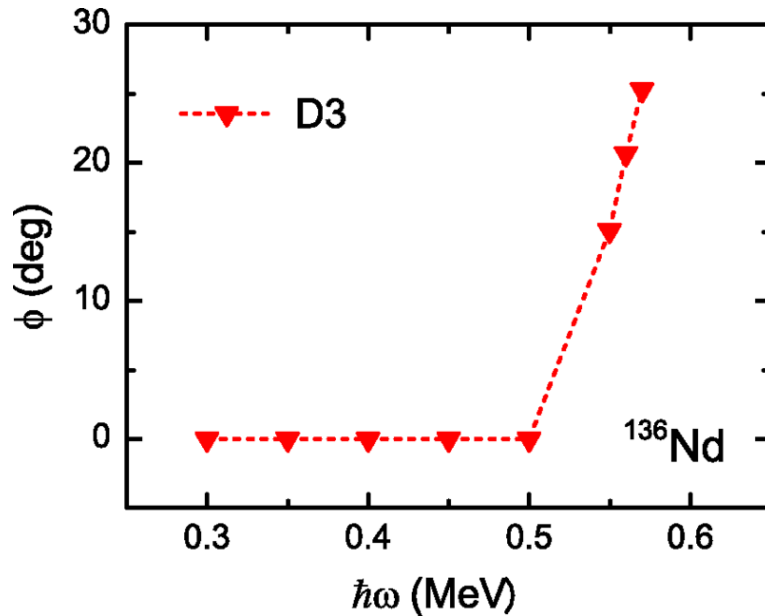


Figure 5.19: Evolution of the azimuth angle ϕ as a function of rotational frequency, for the total angular momentum of the configuration D^* assigned to band D3, calculated by 3D TAC-CDFT

5.2.2 $M\chi D$ interpretation of the chiral bands within PRM framework

To investigate in detail to what extent the chiral geometry of the observed doublet bands in ^{136}Nd is realized, a particle-rotor model (PRM) which couples nucleons in four single- j shells to a triaxial rotor core has been developed [55].

In the performed PRM calculations, the unpaired nucleon configurations are consistent with those in TAC-CDFT used for the doublet bands D1-D5, and the corresponding quadrupole deformation parameters (β, γ) are obtained from triaxial constrained CDFT calculations [122]. The moments of inertia \mathcal{J}_0 and Coriolis attenuation factors ξ are adjusted to reproduce the trend of the energy spectra. The corresponding details are listed in Table 5.4. In addition, for the electromagnetic transitions, the empirical intrinsic quadrupole moment $Q_0 = (3/\sqrt{5\pi})R_0^2 Z\beta$, and gyromagnetic ratios for rotor $g_R = Z/A$ and for nucleons $g_{p(n)} = g_l + (g_s - g_l)/(2l + 1)$ ($g_l = 1(0)$ for protons (neutrons) and $g_s = 0.6g_s(\text{free})$) [3] are adopted.

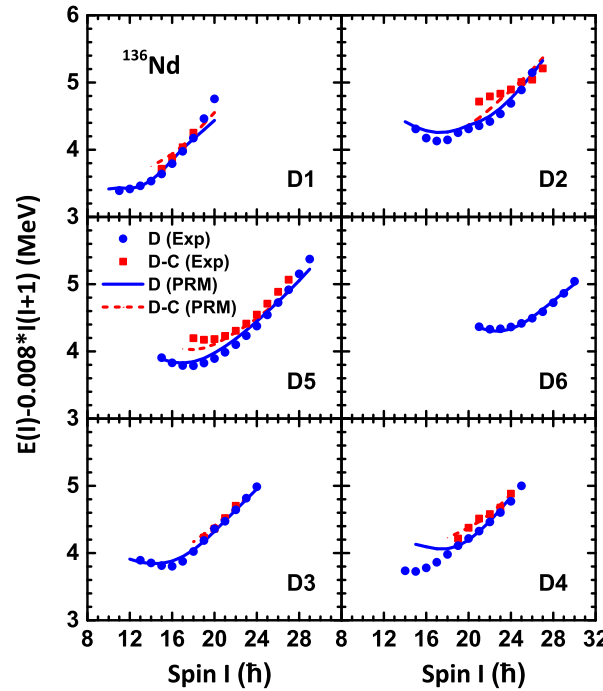


Figure 5.20: (Color online) The energy spectra of bands D1-D6 and their partners calculated by PRM in comparison with corresponding data. The excitation energies are relative to a rigid-rotor reference.

The calculated excitation energies relative to a rigid-rotor reference for the bands D1-D6 in ^{136}Nd are compared with the experimental data, in Fig. 5.20. The experimental values are reproduced well by the PRM calculations except the low spin part of band D4 which is not suitable for the description of

the lower part of band D4, which can have another configuration. One can see that for the doublet bands (D1,D1-C), (D3,D3-C), and (D4,D4-C), the energy separations are around 70, 40, and 120 keV, respectively, and nearly do not change with the increasing spin. For bands (D2,D2-c) and (D5,D5-c) the energy differences between the doublet bands decreasing with increasing spin and finally merge together. These rather small energy differences between doublet doublets support their chiral interpretation.

The staggering parameters $S(I)$, is one of the more sensitive parameters to examine the energy spectra. The standard fingerprints for chiral bands outlined in Ref. [123] require that $S(I)$ is independent of spin. Fig. 5.21 displays staggering parameters $S(I)$ are extracted from data, compared with theoretical results. The PRM obtained values can reproduce the experimental $S(I)$ result. Moreover, the $S(I)$ values of all bands vary smoothly and don't change too much with spin. The behavior of $S(I)$ represent therefore another support for the chiral interpretation of band D1-D5.

The $B(M1)/B(E2)$ values of bands D1-D6 calculated by PRM in comparison with the corresponding experimental data are presented in Fig. 5.22. One can see that the PRM results are in impressive good agreement with the experimental values. In detail, for band D1 and D6, one observes that the decreasing $B(M1)/B(E2)$ values with increasing spin are well reproduced by model. For band D2, one observes that the $B(M1)/B(E2)$ values firstly increase and then an abruptly decrease at $I = 21\hbar$. To understand it, after analyzing the corresponding PRM wave function, we found that, at $I < 20\hbar$, the largest component of the state is $I_s \sim I$ (I_s the angular momentum component along the short axis), while for $I \geq 20\hbar$, the largest one is $I_s \sim I - 2$. This structure change causes the small $B(M1)$ value at $I = 20\hbar$ and small $B(E2)$ values at $I = 20$ and $21\hbar$, and hence large $B(M1)/B(E2)$ value at $I = 21\hbar$. For bands D3 and D4, one observes a similar behavior of the $B(M1)/B(E2)$ values. It seems that they are $M\chi D$ built on identical configuration as in ^{103}Rh [26]. However, as their spectra are interweaved

Table 5.4 – The parities, unpaired nucleon configurations, quadrupole deformation parameters (β , γ), moments of inertia \mathcal{J}_0 (unit \hbar^2/MeV), and Coriolis attenuation factors ξ used in the PRM calculations for bands D1-D6 and their partners.

Band	Parity	Unpaired nucleons	(β, γ)	\mathcal{J}_0	ξ
D1	+	$\pi(1h_{11/2})^1(2d_{5/2})^{-1} \otimes \nu(1h_{11/2})^{-1}(2d_{3/2})^{-1}$	(0.21, 21°)	32	0.96
D2	+	$\pi(1h_{11/2})^3(2d_{5/2})^{-1} \otimes \nu(1h_{11/2})^{-1}(2d_{3/2})^{-1}$	(0.22, 19°)	35	0.96
D5	+	$\pi(1h_{11/2})^2(1g_{7/2})^{-2} \otimes \nu(1h_{11/2})^{-1}(1f_{7/2})^1$	(0.26, 23°)	40	0.93
D3	–	$\pi(1h_{11/2})^2 \otimes \nu(h_{11/2})^{-1}(2d_{3/2})^{-1}$	(0.22, 19°)	32	0.97
D4	–	$\pi(1h_{11/2})^2(2d_{5/2})^{-2} \otimes \nu(h_{11/2})^{-1}(2d_{3/2})^{-1}$	(0.22, 19°)	33	0.97
D6	–	$\pi(1h_{11/2})^3(2d_{5/2})^{-1} \otimes \nu(1h_{11/2})^{-1}(1f_{7/2})^1$	(0.23, 25°)	42	0.95

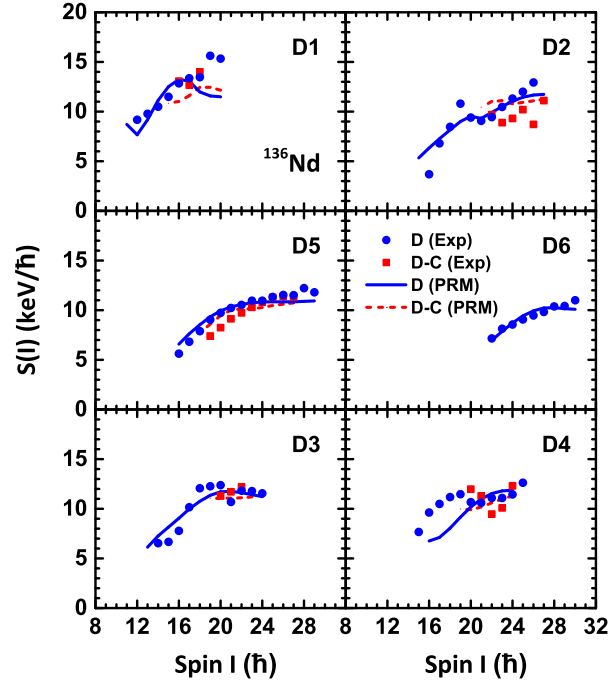


Figure 5.21: (Color online) The staggering parameters of bands D1-D6 calculated by PRM in comparison with corresponding data.

each other at several spins, this possibility is excluded. In the calculations, $\pi(1h_{11/2})^2 \otimes \nu(h_{11/2})^{-1}(2d_{3/2})^{-1}$ configuration with three single- j shells is used to describe D3 and $\pi(1h_{11/2})^2(2d_{5/2})^{-2} \otimes \nu(h_{11/2})^{-1}(2d_{3/2})^{-1}$ configuration with four single- j shells is used to describe D4, respectively. As shown in Fig. 5.22, we can observe that the present PRM calculations do not agree very well with the data of D3, while for band D4, the calculated results reproduce very well the experimental data for $I \geq 19\hbar$. For D5 and D5-C, their $B(M1)/B(E2)$ values are quite similar and in very good agreement with the PRM calculations fulfilling thus the characteristics of chiral doublet bands [51, 123].

The great successes in reproducing the energy spectra and $B(M1)/B(E2)$ ratios for the doublet bands in ^{136}Nd motivate us to examine the angular momentum geometries in PRM for the observed doublet bands. To exhibit their chiral geometry, we calculated the expectation values of the squared angular momentum components along the intermediate (i -), short (s -), and long (l -) axes for the rotor, valence protons, and valence neutrons. The obtained results of bands D2, D4, and D5 are shown in Figs. 5.23, 5.24, and 5.25, respectively.

Fig. 5.23 shows for both bands D2 and D2-C. that the collective core angular momentum mainly aligns along the i -axis at $I \geq 25\hbar$, because the largest moment of inertia is for rotation around the i -axis under the assumption of hydrodynamic moment of inertia. Note that the s -component of the collective core angular momentum is large and cannot be ignored. Moreover,

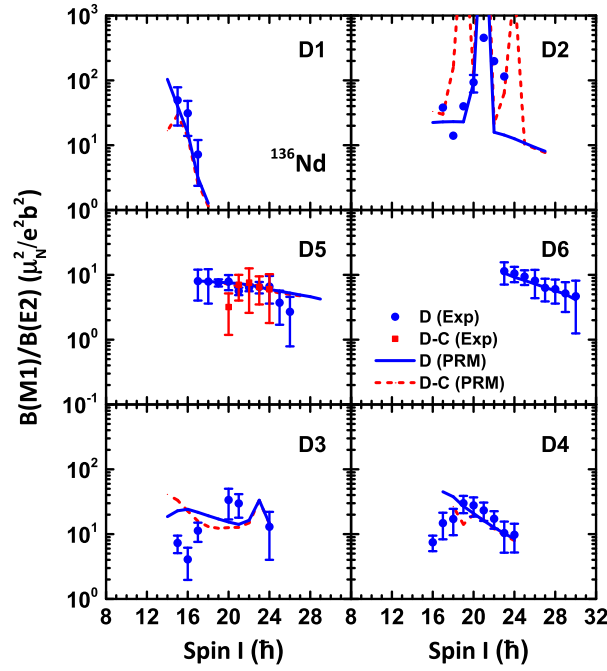


Figure 5.22: (Color online) The $B(M1)/B(E2)$ of bands D1-D6 and their partners calculated by PRM in comparison with corresponding data.

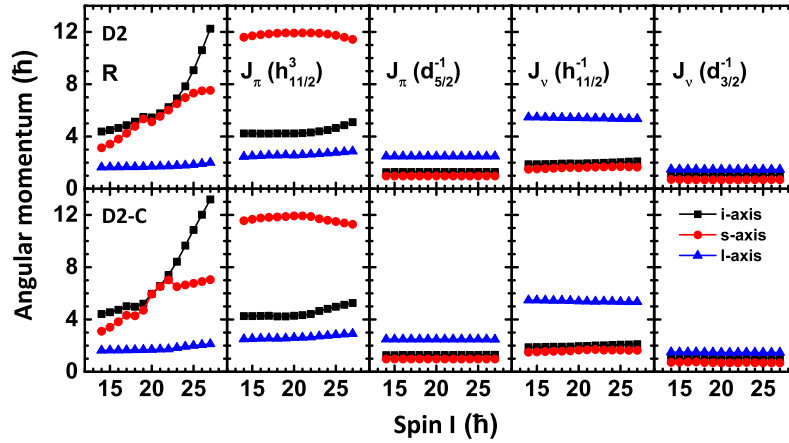


Figure 5.23: (Color online) The root mean square components along the intermediate (i -, squares), short (s -, circles) and long (l -, triangles) axes of the rotor, valence protons, and valence neutrons angular momenta calculated as functions of spin by PRM for the doublet bands D2 and D2-C in ^{136}Nd .

it shows a discontinuous behavior between $I = 19$ and $20\hbar$ in band D2, and between $I = 17$ and $18\hbar$ and $I = 22$ and $23\hbar$ in band D2-C, respectively. This is the reason why we observed an abrupt increase of $B(M1)/B(E2)$ values, as

discussed previously. The angular momentum of the three $h_{11/2}$ valence proton particles mainly aligns along the s -axis, and those of valence proton and neutron holes mainly along the l -axis. Such orientations form the chiral geometry of aplanar rotation. This is a further strong evidence to support the band D2 and D2-C being chiral bands. Note that due to the large s -component of the rotor and proton, the total angular momentum lies close to the s - i plane.

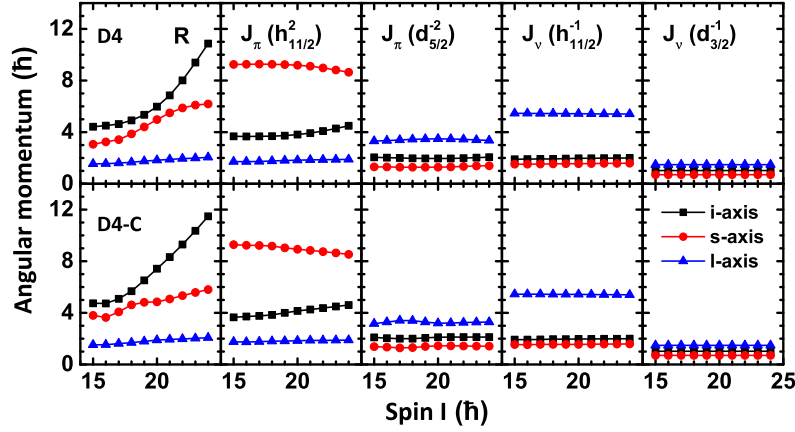


Figure 5.24: (Color online) Same as Fig. 5.23, but for D4 and D4-C.

As shown in Fig. 5.23, for the bands D4 and D4-C, the similar aplanar orientation were observed as in band D2. The angular momentum of the rotor mainly aligns along the i -axis, that of the two $h_{11/2}$ valence proton particles mainly aligns along the s -axis, that of the two $d_{5/2}$ valence protons holes, and that of the two valence neutron holes mainly aligns along the l -axis. Such orientations form a chiral geometry of aplanar rotation. This supports the D4 and D4-C being chiral doublets. A particular feature was observed that at $I \geq 19\hbar$, the angular momenta of the two $h_{11/2}$ valence proton particles tend to align along i -axis. This leads to the increase of $B(E2)$, and hence the decrease of $B(M1)/B(E2)$ with increasing spin as shown in Fig. 5.22. Note that there is a band-crossing at $I = 19\hbar$ as discussed previously, and the adopted configuration is only suitable for describing the data above band-crossing.

For the chiral doublet bands D5 and D5-C, as shown in Fig. 5.25, the angular momenta have similar orientation at $I \geq 21\hbar$ as in D2. In detail, the angular momentum of the rotor mainly aligns along the i -axis, the two $h_{11/2}$ valence proton and one $f_{7/2}$ valence neutron particles mainly align along the s -axis, and two $g_{7/2}$ valence proton and one neutron $h_{11/2}$ valence holes mainly align along the l -axis. Compared with those in D2, the s -axis components of the angular momenta of the rotor and $h_{11/2}$ valence proton particles in D5 are about $2\hbar$ smaller. Such orientations form a better chiral geometry of aplanar rotation than that of D2. One observes that at $I \leq 21\hbar$, the l -axis component

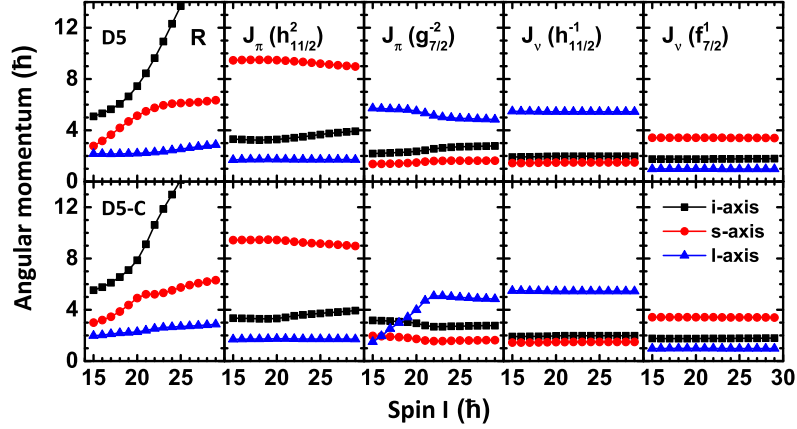


Figure 5.25: (Color online) Same as Fig. 5.23, but for D5 and D5-C.

of angular momenta of two $g_{7/2}$ valence proton holes are different in bands D5 and D5-C. For D5, the two proton holes are aligned and contribute $\approx 5\hbar$. However, for D5-C, the alignment happens when the spin increases from $17\hbar$ to $21\hbar$. At $I = 17\hbar$, the two proton holes contribute angular momenta $\approx 2\hbar$. At $I = 21\hbar$, the two proton holes contribute $\approx 5\hbar$. Such difference causes the energy difference between the doublet bands in this spin region ≈ 400 keV as shown in Fig. 5.20.

From the discussion above, it is clear that the PRM is applied to investigate the five pairs of nearly degenerate doublet bands in the even-even nucleus ^{136}Nd reproduces well the experimental energy spectra and available $B(M1)/B(E2)$ values. The angular momentum geometries of the valence nucleons and the core support the chiral rotation interpretation for all the five pairs.

5.2.3 CNS interpretation of all rotational bands

In order to globally understand the structure of all rotational bands in ^{136}Nd , we performed CNS calculations. The ^{136}Nd nucleus, with 60 protons and 76 neutrons, can be considered to arise from an interaction between ten valence proton particles above the $Z = 50$ major shell closure, and six neutron holes in the $N = 82$ major shell closure. In the low-energy regime, the nucleus is expected to have a small deformation, $\varepsilon_2 \sim 0.15-0.20$. Thus, it is convenient to express the single-particle configuration in terms of j -shell quantum numbers.

In the CNS formalism the nucleus rotates about one of its principal axes and in the present calculations the pairing correlations are neglected. The deformation is optimized for each single particles configuration explored. The configurations are labelled by the number of particles in low- j and high- j orbitals, respectively, in the different N -shells. The configurations can be defined

relative to a ^{132}Sn core as

$$\pi(g)^{-p_1}(dg)^{p_2}(h_{11/2})^{p_3} \\ \nu(sd)^{-n_1}(h_{11/2})^{-n_2}(hf)^{n_3}(i_{13/2})^{n_4},$$

for which we will use the short hand notation $[(p_1)p_2p_3, n_1n_2(n_3n_4)]$. The pseudo-spin partners $d_{5/2}g_{7/2}$ (dg), $s_{1/2}d_{3/2}$ (sd) and $h_{9/2}f_{7/2}$ (hf) are not distinguished in the CNS formalism. Note that all particles are listed, i.e. not only the particles considered as active (unpaired). Note also that the labels do not refer to the pure j -shells, but rather to the dominating amplitudes in the Nilsson orbitals. In some cases, for an odd number of particles in a group, the signature will be specified as a subscript $+$ ($\alpha = +1/2$) or $-$ ($\alpha = -1/2$). The $A = 130$ parameters introduced in Refs. [60, 61] have been used for the calculation on ^{136}Nd .

In the nucleus ^{136}Nd , the lowest proton configuration has 10 protons in the $\pi g_{7/2}$ and $\pi d_{5/2}$ orbitals which interact and are strongly mixed. Higher angular momenta from proton configurations can be obtained by exciting one, two or three protons from $\pi g_{7/2}$ and $\pi d_{5/2}$ to the $\pi h_{11/2}$ orbitals. The lowest observed bands are characterized by the configurations with the active neutron holes in the $\nu d_{3/2}$ and $\nu s_{1/2}$ orbitals which interact and are strongly mixed. Higher angular momenta from neutron configurations can be generated from neutron configurations with one, two or three active holes in the $\nu h_{11/2}$ orbital instead. Much more excited states and very high angular momenta can be obtained from neutron excitations above the $N = 82$ shell gap into the $\nu f_{7/2}$, $\nu h_{9/2}$ and $\nu i_{13/2}$ orbitals and proton excitations from the $\pi g_{9/2}$ orbital across the $Z = 50$ shell gap.

Before discussing the various observed structures, it is instructive to draw the observed bands relative to a standard rotating liquid drop reference, $E - E_{rid}(\text{def})$. The resulting figures reveal not only the relative excitation of the bands, but also details which otherwise are hard to observe in the $E - I$ plots. However, the multitude of bands identified in ^{136}Nd makes their visualisation in a single figure cumbersome. Therefore, we divided them in four groups, which are drawn in different figures of Fig. 5.26, Fig. 5.27, Fig. 5.28, and Fig. 5.29.

As shown in Fig. 5.26, one can observe the up-sloping pattern with increasing spin of all the bands, which is induced by the large difference between the moments of inertia of the low-spin bands and that of the rotating liquid drop. One can also observe the change of slope of the γ band above spin 10^+ , and of the even-spin branch of band N1 above spin 18^+ , which are evidently induced by configuration and/or deformation changes.

As shown in Fig. 5.27, one can see that the yrast nature of band L1 in the spin range $10\hbar$ to $20\hbar$, while just above 10^+ the lowest excited band is L7. There are three positive-parity yrare bands L2, L3 and L4, two nearly degenerate negative-parity bands L5 and L6 connected to band L1, and two

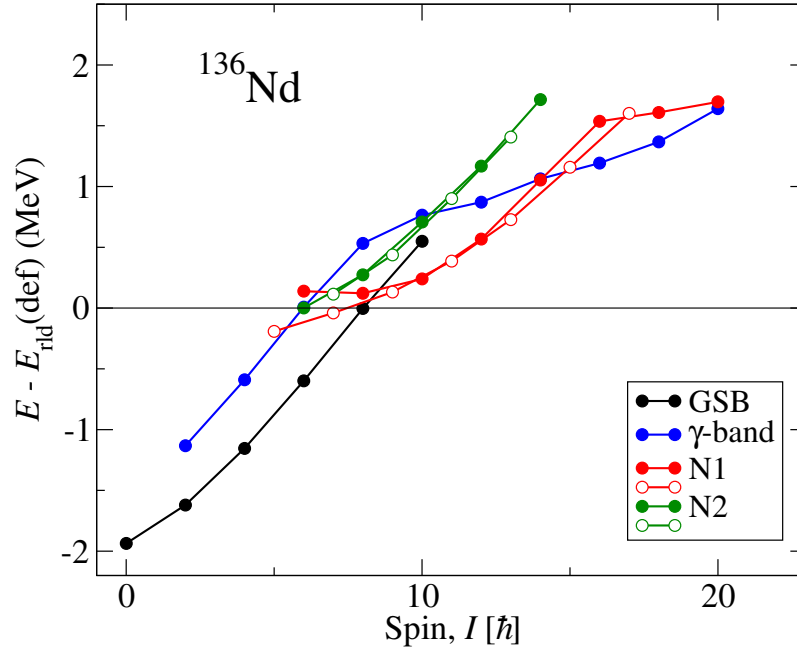


Figure 5.26: (Color online) Energies relative to a standard rotating liquid drop reference calculated for the experimental bands observed in ^{136}Nd . With an odd number of $h_{11/2}$ neutron holes, two signature degenerate bands are formed which are shown by the same color and symbols.

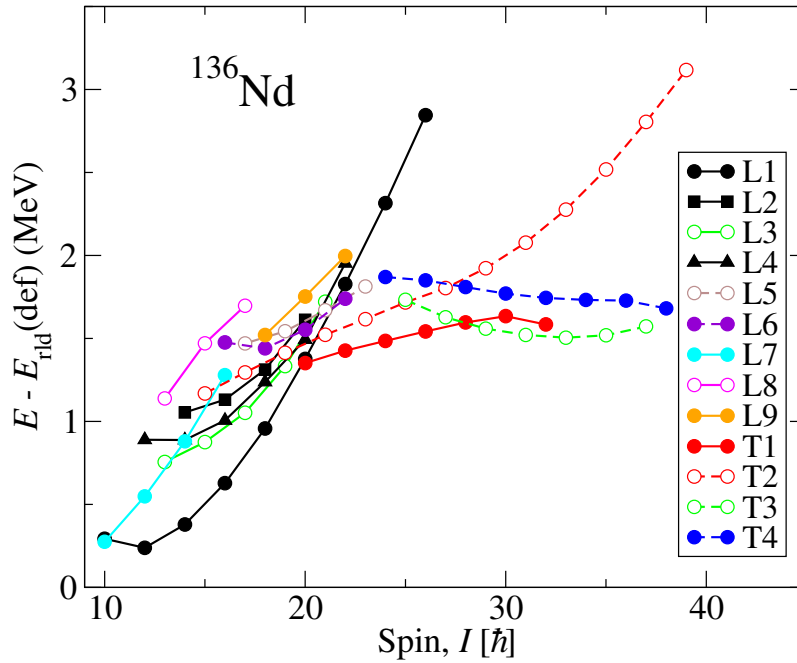


Figure 5.27: The same as in Fig. 5.26 but for the bands L and T.

yrare positive-parity bands L8 and L9 which decay to band L7. At spins higher than 20^+ there are four bands, labeled T1-T4 to emphasize their interpretation in terms of triaxial bands (see the following sections). Band T2 develops over the largest spin interval, from 15^+ to 39^+ ; at the highest spins it develops up to ≈ 1.7 MeV above yrast, which is a feature similar to that observed in the neighboring ^{137}Nd [124]. The bands T1, T3 and T4 have a nearly flat behavior, with moments of inertia which are similar to that of the liquid drop in the observed spin interval.

As shown in Fig. 5.28, one can observe the well known parabolic behavior of the $E - E_{\text{rid}}$ plots, which is induced by the mismatch between the calculated moment of inertia of the drop and that of a given band: for a perfect matching one would have a flat horizontal line (see e.g. [125]). The chiral doublets are drawn with the same color, but different symbols (circles for the yrast, squares for the yrare bands). The spin of the minimum of each parabola is indicative of the total single-particle spin of the contributing nucleons in the configuration. All bands show nearly degenerate branches with even and odd spins, which indicate the presence in the configurations of one unpaired high- Ω Nilsson orbital. One can observe that the chiral doublets develop only at high spins for the bands D2, D3, D4, that the energy separation is different for the different doublets, and that the chiral doublet observed over the largest spin interval is that of band D5.

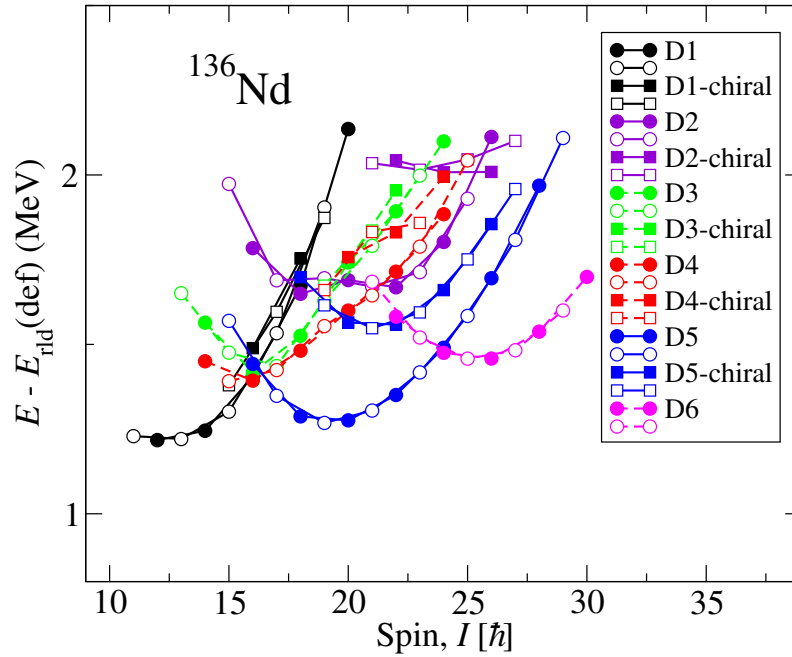


Figure 5.28: The same as in Fig. 5.26 but for the dipole bands.

As shown in Fig. 5.29, we can see the characteristic down-sloping behavior

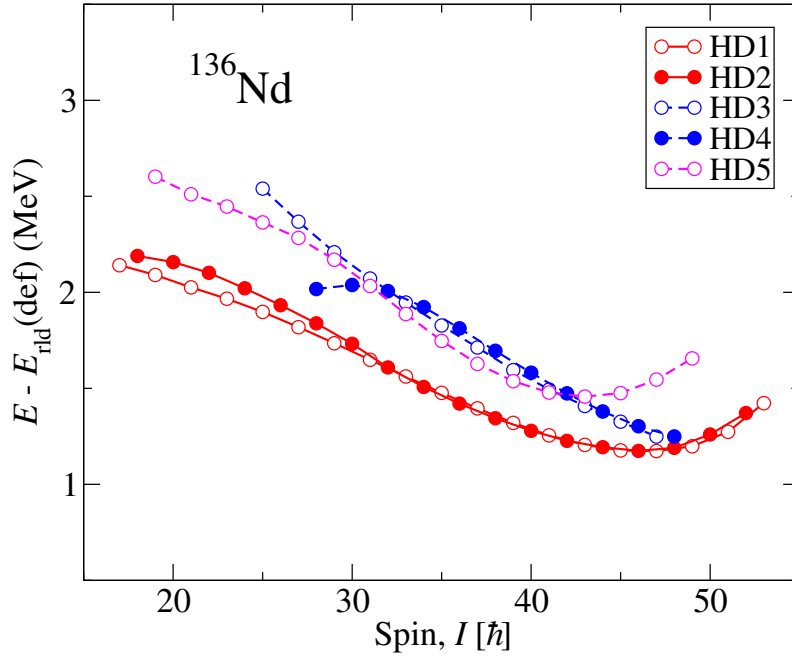


Figure 5.29: The same as in Fig. 5.26 but for the bands HD.

with increasing spin of the HD bands, which is induced by the calculations without pairing. The excitation energies of the bands HD2-HD5 are not known experimentally. They are adjusted such that to form two nearly degenerate partners HD1-HD2 and HD3-HD4. This adjustment is in agreement with the yrastness criteria and is supported by the theoretical interpretation presented in the following sections.

The low- and medium-spin bands L and T

The γ band of ^{136}Nd exhibits a crossing at spin $I^\pi = 10^+$ similar to that observed in the neighboring ^{134}Nd nucleus [126]. The $B(E2; 2_2^+ \rightarrow 0^+)$ and $B(E2; 2_2^+ \rightarrow 2_1^+)$ values extracted from the relativistic Coulomb excitation measurement reported in Ref. [107] clearly show the large triaxiality ($\gamma \approx 23^\circ$) and pronounced γ softness of ^{136}Nd at low spins. The γ softness is well documented in the $A \approx 130$ mass region, in particular in the ^{134}Nd nucleus, for which the measured transition probabilities are in good agreement with the O(6) symmetry of the interacting boson model which is adequate for the description of γ -soft nuclei [127]. Above the crossing at spin $I^\pi = 10^+$, the γ band exhibits a regular increase of the transition energies as expected for a rotational band, but also several transitions towards the bands L1 and L2, which is a clear indication of an important mixing with the configurations of these bands. The same behavior of the γ bands has been reported in ^{134}Nd [126].

As one can observe in Figs. 5.30 and 5.31, the bands L1, L2, L4, and the high-spin part of the γ band exhibit a similar behavior, are all reasonably well reproduced by the same configuration $[82, 42]$, or $[\pi h_{11/2}^2]$ in terms of spherical single-particle orbitals. The calculated deformations in the observed spin range shows their enhanced quadrupole deformation ($\varepsilon_2 \approx 0.20$) relative to that of the GSB ($\varepsilon_2 \approx 0.16$), and their pronounced triaxiality $\gamma \approx +25^\circ$ (see Table 5.5).

The configuration assigned to bands N1 and N2 is $[9_{+,-}1_{-}, 42]$, or $[\pi(dg)^1 h^1]$

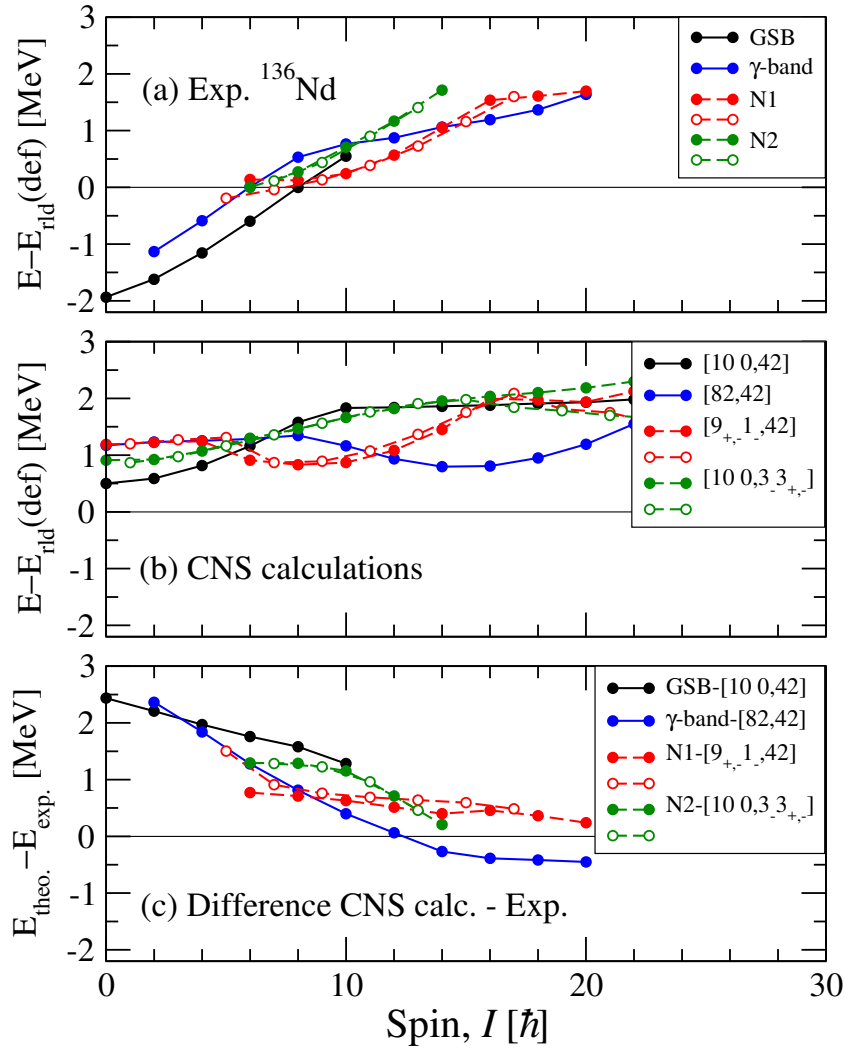


Figure 5.30: (Color online) The observed low-spin bands of ^{136}Nd are shown relative to a rotating liquid drop reference in panel (a), with the calculated configurations assigned to these bands given relative to the same reference in panel (b). The panel (c) provides the difference between calculations and experiment.

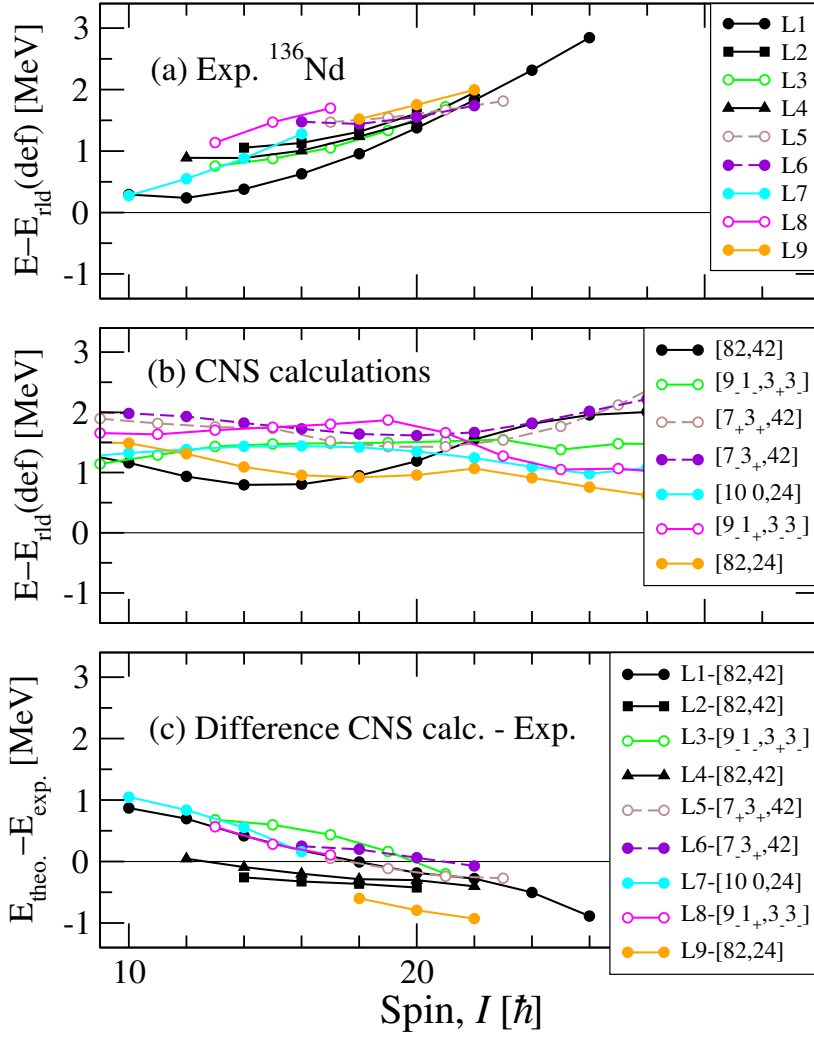


Figure 5.31: (Color online) The same as in Fig. 5.30 but for the medium-spin bands L.

$\otimes \nu 0]$ in terms of spherical single-particle orbitals, where $\nu 0$ represents the vacuum for neutrons) and $[10 0, 3_+ 3_+, -]$, or $[\pi 0 \otimes \nu h^{-1}(sd)^{-1}]$ in terms of spherical single-particle orbitals, where $\pi 0$ represents the vacuum for protons, respectively. The bands have different deformations, which are induced by the different types of active nucleons. As one can observe in Fig. 5.30, a nice global agreement with the experimental bands N1 and N2 is obtained. In addition, band N1 has higher quadrupole deformation ($\varepsilon_2 \approx 0.18$) than band N2 ($\varepsilon_2 \approx 0.16$), and positive triaxiality ($\gamma \approx +25^\circ$) which is opposite to that of band N2 ($\gamma \approx -25^\circ$). The larger quadrupole deformation and positive triaxiality of band N1 are induced by the low- Ω $h_{11/2}$ proton present in its configuration. The high- Ω $h_{11/2}$ neutron present in the configuration of

band N2 induces a smaller increase of the quadrupole deformation and negative triaxiality. Interestingly, the high-spin part of band N1 which exhibits a change of slope in the $E - E_{rld}$ plot of Fig. 5.26, is nicely reproduced by the $[9_{+,-}1_{-}, 42]$ CNS configuration, which shows a jump from the minimum at positive triaxiality ($\varepsilon_2 \approx 0.18$, $\gamma \approx +25^\circ$) to the minimum at negative triaxiality ($\varepsilon_2 \approx 0.17$, $\gamma \approx -85^\circ$), indicating a drastic change of the rotation axis, from the intermediate to the long axis, respectively.

The medium-spin bands L5 and L6 are the continuation of the odd- and even-spin cascades composing band N1. The configuration assigned to these bands is $[7_{+,-}3_{+}, 42]$ in CNS framework. They have the same neutron configuration as band N1 and two additional $h_{11/2}$ aligned protons. In addition, they have pronounced triaxiality, as expected due to the presence of three low- Ω $h_{11/2}$ protons, larger quadrupole deformation ($\varepsilon_2 \approx 0.20$) than band N1 ($\varepsilon_2 \approx 0.18$).

The configuration assigned to bands L7, $[10\ 0, 24]$, or νh^2 in terms of spherical orbitals, is the same as proposed in Ref. [100]. It has a smaller deformation ($\varepsilon_2 \approx 0.15$) than the GSB and negative triaxiality ($\gamma \approx -35^\circ$), induced by the presence of two high- Ω $h_{11/2}$ neutrons. The continuation of band L7 to higher spins is band L9, to which we assign the $[82, 24]$ configuration involving two $h_{11/2}$ aligned protons, which induce a larger quadrupole deformation ($\varepsilon_2 \approx 0.18$) and positive triaxiality ($\gamma \approx +27^\circ$).

Band L8 has odd spins and is linked to band L7 by weak $\Delta I = 1$ transitions, which most probably have $M1/E2$ character. For band L8, a possible configuration $[9_{-}1_{+}, 3_{-}3_{-}]$ is proposed, which is quite different from that of band L7 to which it decays and can explain the weak connecting transitions.

The T bands

In the high-spin region, we observed four bands that are called T bands to underline their pronounced triaxiality, which distinguish them from the other high-spin bands based on nearly axial shapes and are dominated by HD configurations.

Band T1 decays only to the bands L1 and L4, which are well reproduced by the $[82, 42]$ configuration involving two $h_{11/2}$ aligned protons. As it is not linked through several transitions to the other bands, one reasonably can assume that its configuration is quite different from the configurations of the medium-spin bands. One possible configuration is $[7_{-}3_{-}, 3_{-}3_{-}]$, which involved one $h_{11/2}$ proton and one $h_{11/2}$ neutron. One can see in Fig. 5.32, with the configuration $[7_{-}3_{-}, 3_{-}3_{-}]$, the CNS model can reproduce the band well.

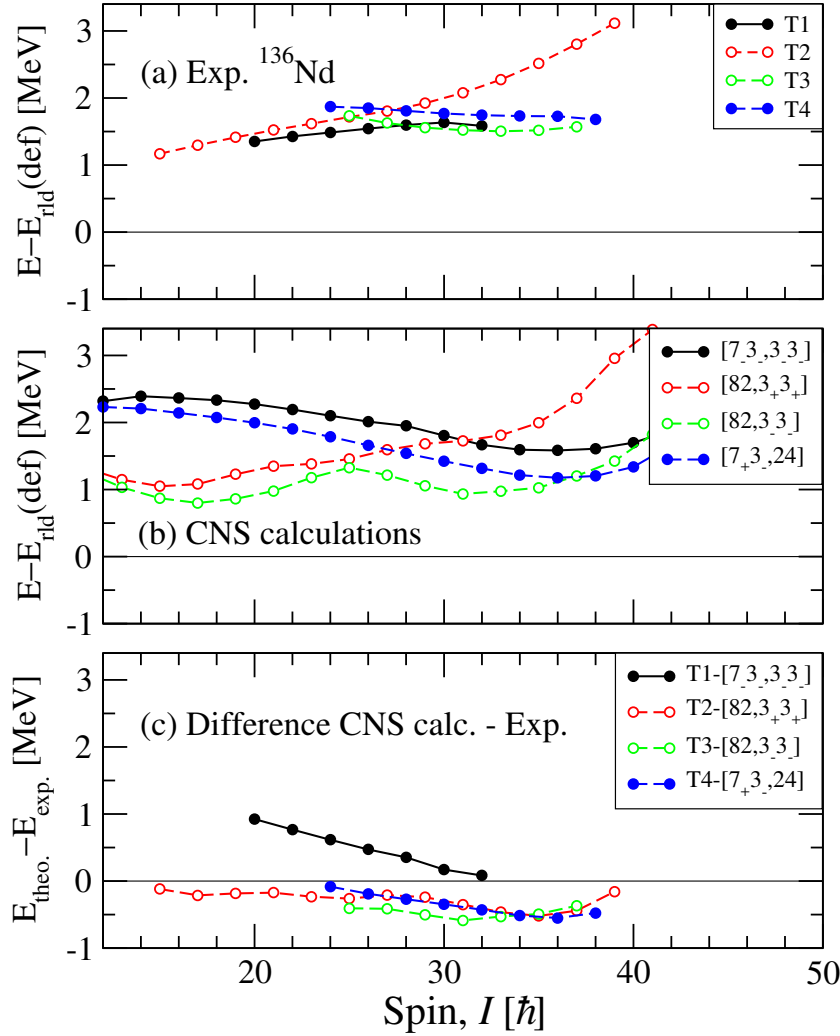


Figure 5.32: (Color online) The same as in Fig. 5.30 but for the medium-spin bands T.

Band T2 is observed over a wide spin range from $I = 15$ to $I = 39$, and decays only to band L1. Its increasing excitation energy relative to the other high-spin bands (see Figs. 5.26 and 5.32) is an intriguing behavior that has been recently observed in a band in the neighboring ^{137}Nd nucleus [124] and interpreted in terms of rotation of an oblate shape. The suggest possible configuration for band T2 is $[82, 3_+3_+]$, which involves one more neutron in the $h_{11/2}$ orbital. The calculated deformation is $(\varepsilon_2 \approx 0.19, \gamma \approx +26^\circ)$ up to spin 19^- , while in the range $I = 21^-$ to $I = 39^-$ the deformation changes gradually from $(\varepsilon_2 \approx 0.17, \gamma \approx -20^\circ)$ to $(\varepsilon_2 \approx 0.09, \gamma \approx -54^\circ)$. This decreasing quadrupole deformation and increase of the triaxiality with increasing spin is a behavior similar to band O of ^{137}Nd [124].

To bands T3 and T4, the possible configuration $[82, 3-3_-]$ and $[7_+3_-, 24]$ have been assigned, respectively. Their quadrupole deformations decrease gradually with increasing spin at quasiconstant triaxiality, from $(\varepsilon_2 \approx 0.20, \gamma \approx -70^\circ)$ to $(\varepsilon_2 \approx 0.12, \gamma \approx -68^\circ)$ for band T3, and from $(\varepsilon_2 \approx 0.17, \gamma \approx -30^\circ)$ to $(\varepsilon_2 \approx 0.12, \gamma \approx -45^\circ)$ for band T4.

The dipole bands

The CNS configurations assigned to the dipole bands of ^{136}Nd are presented in Table 5.5, which are in global agreement with those calculated with the CDFT model in Ref. [114] and with the PRM in Ref. [55]. In the CNS model, we can only describe the configurations for yrast partners of the chiral doublets, which assumes the rotation around one of the principal axes. As one can see in Table 5.5, all dipole bands D1-D6 have a pronounced triaxiality, close to the maximum of 30° . The calculated triaxiality is positive for all bands excepting for band D1. The configuration assignment is quite straightforward, being based on the measured energies, spin-parities and decay patterns. The configuration assignments are as follows:

The positive-parity band D1 decays to band L7 and the bottom of band L1, which are based on $\nu h_{11/2}^2$ and $\pi h_{11/2}^2$ configurations, respectively. The assigned $[9_-1_{+,-}, 3_+3_-]$ configuration is the simplest single-particle excitation leading to a low-lying positive-parity band, which, however maintain one low- Ω proton and one high- Ω neutron in the $h_{11/2}$ orbitals to assure the perpendicular geometry of the angular momenta required by dipole and chiral bands.

The positive-parity band D2 is developed above spin $I = 15^+$ and has a fragmented decay to many low-lying bands, including band D1. A two-quasiparticle excitation with respect to band D1 appears as the natural choice, and we therefore assign the $[7_+3_+, 3_-3_{+,-}]$ configuration, involving two additional $h_{11/2}$ protons relative to band D1.

The negative-parity bands D3 and D4 are connected through several transitions and decay via a multitude of transitions towards the low-lying bands. Their spins and excitation energies are similar to those of band D2. The most probable configurations are $[82, 3_+3_{+,-}]$ and $[82, 3_-3_{+,-}]$, which are in good agreement with experiment.

The positive parity band D5 is the strongest dipole bands in ^{136}Nd which decays mainly to band L1. Its properties are nicely reproduced by the $[82, 43_{+,-}(1_-0)]$ configuration (see Fig. 5.33) which involves one neutron in the intruder $(h_{9/2}, f_{7/2})$ orbital. As a consequence, its quadrupole deformation is larger ($\varepsilon_2 \approx 0.23$) than those of the bands D1-D4, due to the polarizing force of the $(h_{9/2}, f_{7/2})$ intruder orbital.

The negative-parity band D6 is the highest excited dipole band which decays to band L6. The configuration assigned to band D6 is $[7_+3_+, 43_{+,-}(1_-0)]$, which has one neutron excited from $h_{11/2}$ to the $(h_{9/2}, f_{7/2})$ intruder orbital relative to band L6. As one can see in the panel (c) of Fig. 5.33, the data are

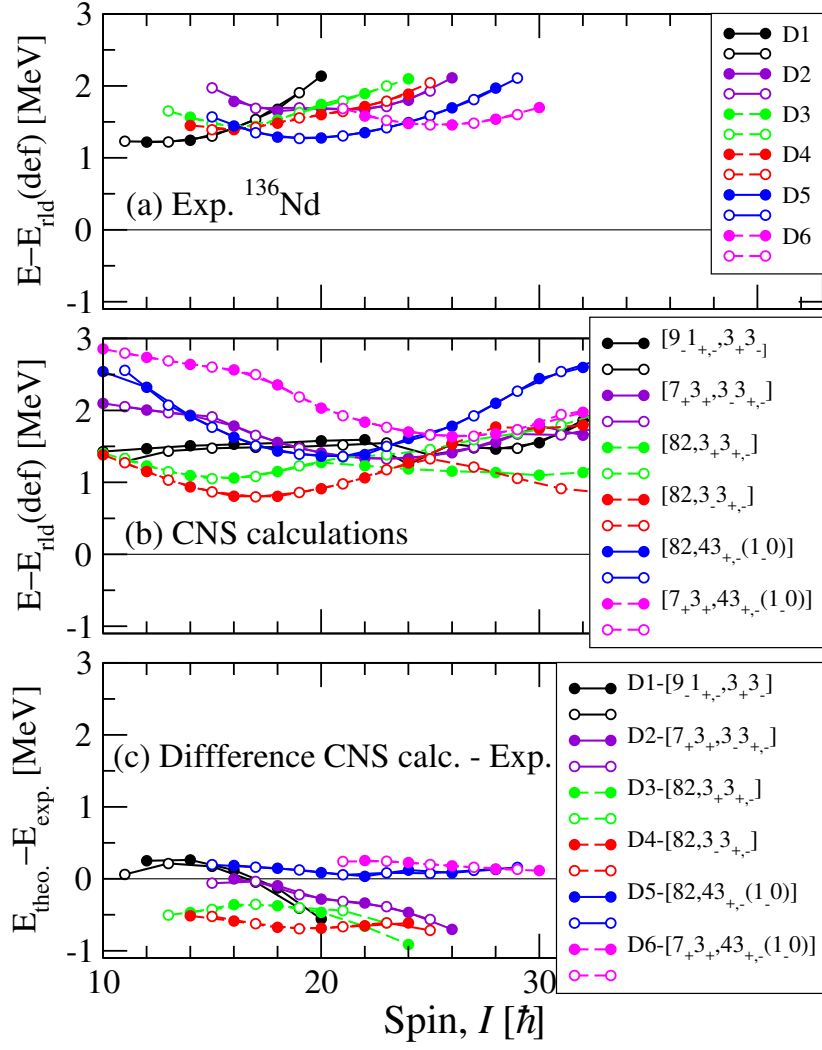


Figure 5.33: (Color online) The same as in Fig. 5.30 but for the bands D.

well reproduced by CNS model calculations.

Table 5.5 – Configuration assignments and deformation information to the bands of ^{136}Nd .

Band	I(%)	Parity	Configuration	States	(ε_2, γ)
GSB	100	+	[10 0,42]	0^+-10^+	$(\approx 0.16, \approx -20^\circ)$
γ -band	6	+	[82,42]	2^+-20^+	$(\approx 0.20, \approx 26^\circ)$
N1	9	-	$[9_{+,-}1_{-},42]$	5^--20^-	$(\approx 0.18, \approx 25^\circ)$
N2	5	-	$[10\ 0, 3_{-}3_{+,-}]$	6^--14^-	$(\approx 0.16, \approx -25^\circ)$
L1	34	+	[82,42]	10^+-26^+	$(\approx 0.20, \approx 25^\circ)$
L2	6	+	[82,42]	14^+-20^+	$(\approx 0.20, \approx 25^\circ)$
L3	2	+	$[9_{-}1_{-},3_{+}3_{-}]$	13^+-21^+	$(\approx 0.16, \approx -25^\circ)$
L4	3	+	[82,42]	12^+-22^+	$(\approx 0.20, \approx 25^\circ)$
L5	1.4	-	$[7_{+}3_{+},42]$	17^--23^-	$(\approx 0.20, \approx 25^\circ)$
L6	1.2	-	$[7_{-}3_{+},42]$	16^--20^-	$(\approx 0.20, \approx 20^\circ)$
L7	7.5	+	[10 0,24]	10^+-16^+	$(\approx 0.15, \approx -35^\circ)$
L8	0.2	+	$[9_{-}1_{+},3_{-}3_{-}]$	13^+-18^+	$(\approx 0.17, \approx -33^\circ)$
L9	0.7	+	[82,24]	18^+-22^+	$(\approx 0.18, \approx 27^\circ)$
T1	3	+	$[7_{-}3_{-},3_{-}3_{-}]$	20^+-32^+	$(\approx 0.18, \approx -35^\circ)$
T2	0.7	-	$[82,3_{+}3_{+}]$	$15^--(39^-)$	$(\approx 0.19, \approx 26^\circ)$
T3	0.6	-	$[82,3_{-}3_{-}]$	$26^--(37^-)$	$(\approx 0.17, \approx -30^\circ)$
T4	0.7	-	$[7_{+}3_{-},24]$	$24^--(38^-)$	$(\approx 0.20, \approx -70^\circ)$
D1	1.7	+	$[9_{-}1_{+,-},3_{+}3_{-}]$	11^+-20^+	$(\approx 0.18, \approx -25^\circ)$
D2	1.9	+	$[7_{+}3_{+},3_{-}3_{+,-}]$	15^+-26^+	$(\approx 0.20, \approx 21^\circ)$
D3	2.6	-	$[82,3_{+}3_{+,-}]$	13^--23^-	$(\approx 0.20, \approx 25^\circ)$
D4	2.9	-	$[82,3_{-}3_{+,-}]$	14^--25^-	$(\approx 0.20, \approx 25^\circ)$
D5	8.4	+	$[82,3_{-}3_{+,-}(1_{-}0)]$	15^+-29^+	$(\approx 0.23, \approx 27^\circ)$
D6	1.2	-	$[7_{+}3_{+},3_{-}3_{+,-}(1_{-}0)]$	21^--31^-	$(\approx 0.23, \approx 25^\circ)$
HD1	2	+	$[64,5_{-}4(21)]$	$(17^+)-(53^+)$	$(\approx 0.29, \approx 5^\circ)$
HD2	0.6	+	$[64,5_{+}4(21)]$	$(18^+)-(52^+)$	$(\approx 0.29, \approx 5^\circ)$
HD3	0.4	-	$[64,45_{-}(21)]$	$(25^--)(47^-)$	$(\approx 0.27, \approx 15^\circ)$
HD4	0.1	-	$[64,45_{+}(21)]$	$(28^--)(50^-)$	$(\approx 0.27, \approx 15^\circ)$
HD5	0.3	-	$[64,44(1_{+}1)]$	$(19^--)(49^-)$	$(\approx 0.27, \approx 17^\circ)$

The highly-deformed bands

The highly-deformed bands of ^{136}Nd have been studied relatively long time ago [102–104,108]. The decay out of band HD1 has been identified [108] and a negative-parity involving two neutrons in the intruder orbitals $i_{13/2}$ and $(h_{9/2}, f_{7/2})$ was assigned based on TRS calculations [104]. In the present work we identified three more bands developing to very high spins, with behaviors similar to that of the band HD1. Unfortunately, we were not able to identify the

decay out of the new HD bands. However, based on their intensity, normal-

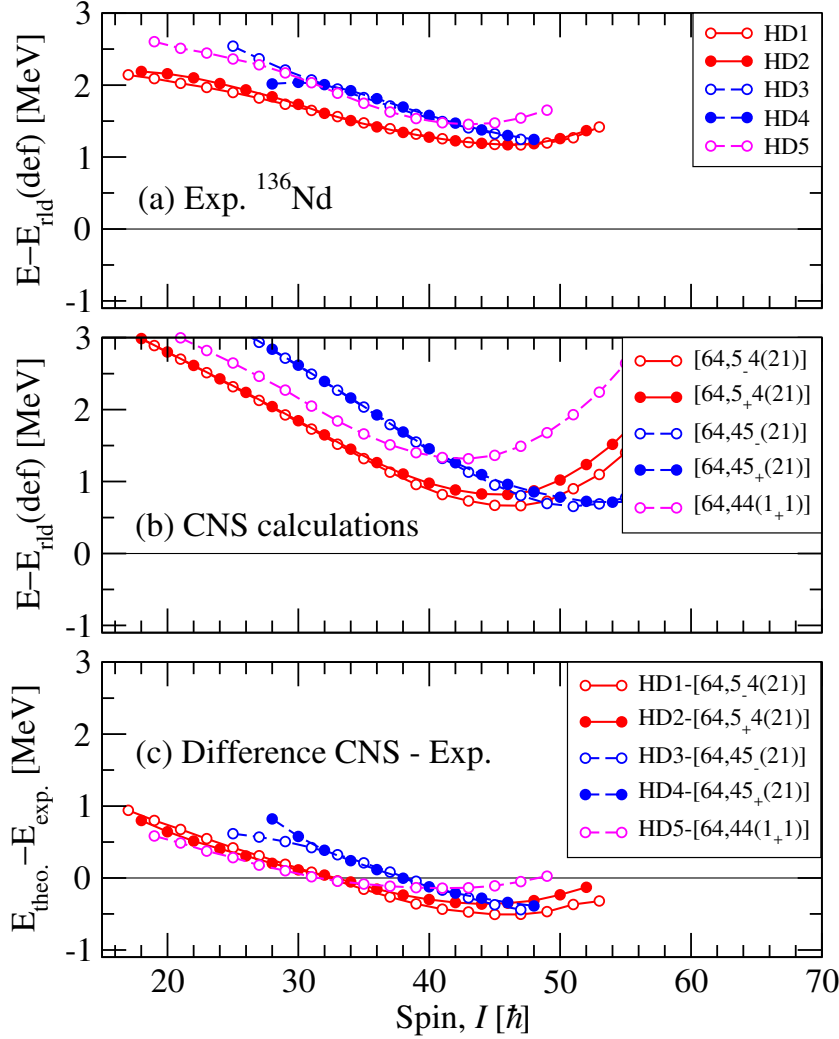


Figure 5.34: (Color online) The same as in Fig. 5.30 but for the HD bands.

deformed entry states and the calculated yrast HD configurations at high spins, we assigned tentative configurations, which compose a quite convincing scenario of the single-particle excitations in the HD well. As can be seen in Fig. 5.34, the yrast configuration with minimum at the right spin and adequate slope for the band HD1 is $[64, 5_4(21)]$, which has positive parity and a close lying $[64, 5_+4(21)]$ signature partner. One can adjust the excitation energy and spin of band HD2 such that it fits the $[64, 5_+4(21)]$ configuration. One obtains therefore a new interpretation of the band HD1 of ^{136}Nd , which now has two neutrons in $(h_{9/2}, f_{7/2})$ and one in $i_{13/2}$, and has positive parity.

The situation is a bit more complicated for the configuration assignment to the bands HD3, HD4 and HD5. However, guided by the CNS calcula-

tions and properly adjusting the excitation energies and spins of the bands, while keeping in mind their smaller intensity, we assigned the $[64, 45_-(21)]$ and $[64, 45_+(21)]$ configurations to the bands HD3 and HD4, respectively, and the $[64, 44(1_+1)]$ configuration to band HD5. With these configuration assignments we obtain a relatively coherent picture of the single-particle excitations in the HD well, which involve always one neutron in the $i_{13/2}$ intruder orbital, and one or two neutrons in the $(h_{9/2}, f_{7/2})$ orbitals.

Chapter 6

Evidence of $M\chi D$ in the odd-A nucleus ^{135}Nd

In this chapter the details of the experimental results and discussion related to the odd-A nucleus ^{135}Nd are presented. The structure of doublet bands is discussed in the frameworks of the covariant density functional theory and the particle-rotor model.

6.1 Introduction

In the $A \approx 130$ mass region, a series of low lying $\Delta I = 1$ chiral bands based on the $\pi h_{11/2} \otimes \nu h_{11/2}^{-1}$ configuration have been identified in the $N = 75$ nuclei [21]. Recently, the multiple chiral doublet ($M\chi D$) have been reported in the odd-A nucleus ^{133}Ce [25]. $M\chi D$ bands are also expected to exist in the ^{135}Nd nucleus, which is an isotone of ^{133}Ce . We therefore performed a careful investigation of the experimental data obtained in our JUROGAM II experiment to possibly identify chiral partners of the previously known bands.

Prior to this study, the chirality in ^{135}Nd has been investigated both experimentally [32, 33, 128] and theoretically [51, 129, 130].

Experimentally, the nearly degenerate doublet bands of negative parity observed in ^{135}Nd are considered as best examples of chiral bands in the $A=130$ mass region [33]. These bands have been interpreted as chiral doublet bands within the 3D TAC framework. Later, in Ref. [32] were reported the lifetime measurement results of intraband and interband transition probabilities of the doublet bands. A microscopic calculation based on the combination of tilted-axis cranking (TAC) model with random phase approximation (RPA) reproduces all experimental observables quite well, substantiating the theoretical interpretation: at the bottom of the bands, the angular momentum vector oscillates perpendicular to the plane spanned by the long and short axes of the triaxial nuclear shape, executing a motion that was called chiral vibration. These oscillations slow down with increasing angular momentum, resulting

in a decreasing energy splitting between the bands and an increase in the interband $B(E2)$ values. The vibration, then, becomes strongly anharmonic, changing into tunneling between well-established left- and right-handed configurations (chiral rotation). This behavior shows how the chirality changes from chiral vibration to nearly static chirality with increasing spin.

A n -particle- n -hole PRM was developed to investigate the chirality in ^{135}Nd [51] in a fully quantal approach. For the two negative-parity chiral bands, the observed energies and the $B(M1)$ and $B(E2)$ values for the in-band as well as interband transitions were reproduced excellently. Furthermore, to study in detail the chiral geometry of the aplanar rotation and its evolution with angular momentum, root mean square values of the angular momentum components and their probability distributions were used. The chirality was shown to be a transient phenomenon. The chiral partner bands start as a soft vibration of the angular momentum perpendicular to the plane spanned by the short and long axes, where the band and its partner realized as the zero- and one-phonon state. With increasing angular momentum the vibration becomes strongly anharmonic, progressively localizing in left- and right-handed configurations. Maximal chirality is reached at $I = 39/2$, where the two bands approach each other closest. At this spin they have very similar distributions of the angular momenta of the core, the valence neutron, and the valence protons in the left- and right-handed sectors, which reflect reduced left right tunneling. With further increasing spin the two bands again develop into the zero and one-phonon states of a chiral vibration of the angular momentum about the intermediate axis [51]. In addition, the doublet bands were also investigated in the framework of interacting boson-fermion model. It has been shown that they can be interpreted as twin chiral bands based on the $\pi h_{11/2}^2 \otimes \nu h_{11/2}^{-1}$ configuration [130].

6.2 Experimental results and level scheme

In the present work, we succeeded to identify one new pair of chiral doublet bands in ^{135}Nd , namely D3 and D4, in addition to the previously known one composed of bands D5 and D6 (see Fig. 6.1), which raises to two the number of chiral doublet bands in this nucleus. In addition, many new transitions have also been observed linking the new bands between them and with the other levels.. The partial level scheme of ^{135}Nd showing two pairs of doublet bands and their decay toward low-lying states is shown in Fig. 6.1. The experimental information on the observed transitions is given in Table 6.1.

Band D2-3qp, first reported in Ref. [131], is confirmed up to spin $39/2^+$. Three new levels are added on top of the band up to spin $45/2^+$, which together with the previously known $39/2^+$ level form a new band labelled D2-5qp. The spins of band D2 are established based on the dipole character of the several connecting transitions to band D1. The parity of band D2 is not experimentally

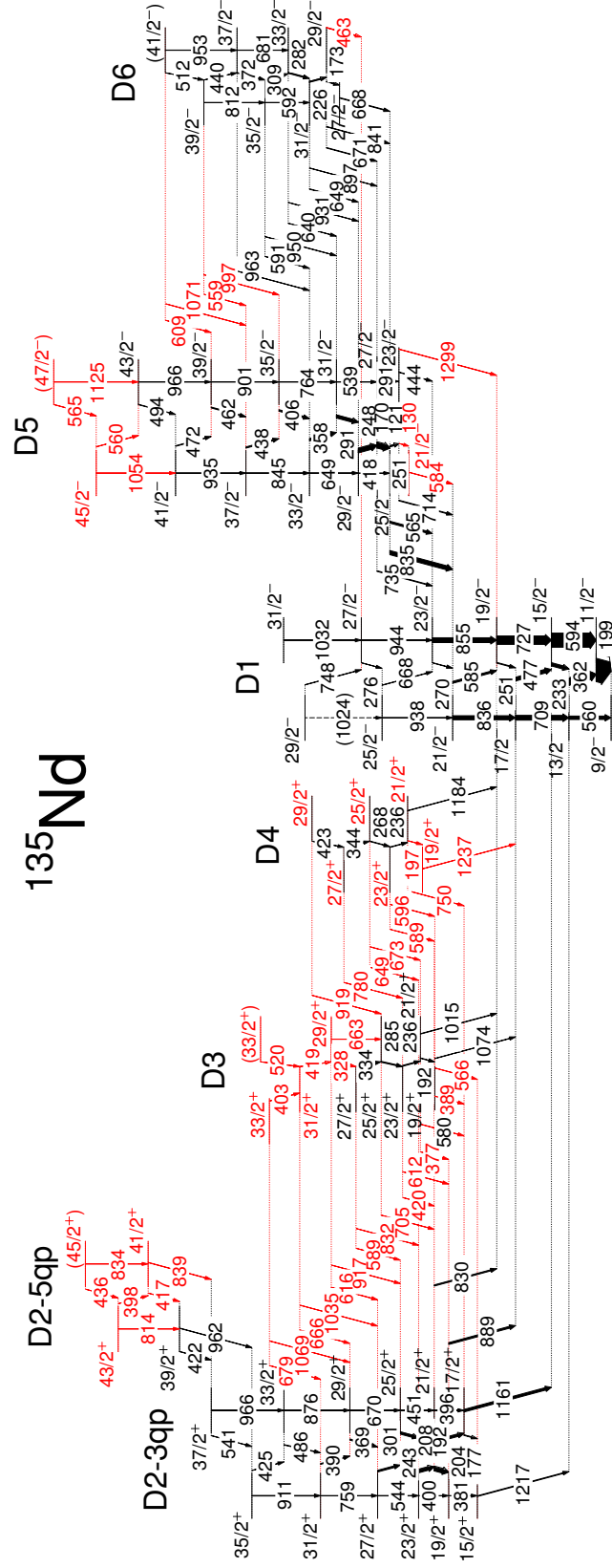


Figure 6.1: (Color online) Partial level scheme of ^{135}Nd showing the newly identified doublet bands.

established. However, based on the R_{DCO} values of the 830-, 889- and 1161-keV transitions which are in agreement within errors with pure E1 character (see Table. 6.1), and also on the theoretical interpretation here below, we assign a positive parity to band D2.

Band D3, previously known up to the level de-excited by the 334-keV transition [128], is extended by three more levels up to spin $33/2^+$. Another $33/2^+$ level decaying to both the $31/2^+$ level of band D3 and to band D2-3qp is also identified. Fourteen new transitions of 377, 389, 420, 566, 589, 612, 616, 666, 679, 705, 832, 917, 1035 and 1069 keV connecting band D3 to band D2-3qp are also identified. The parity of band D3 is changed to positive based on the R_{DCO} and R_{ac} values of the multitude of connecting transitions to band D1 and D2-3qp. In particular, the extracted values for the five connecting transitions of 566, 705, 832, 1035, and 1069 keV clearly indicate their E2 character (see Table. 6.1), therefore firmly establishing the parity of band D3 as identical to the assigned positive parity of band D2.

Band D4, previously known up to the state de-excited by the 423-keV transition is confirmed [128], but based on R_{DCO} values of the connecting transitions to bands D1 and D3, the spins are decreased by one unit and the parity is changed to positive. We added one new level with spin $19/2^+$ at the bottom of the band, one transition of 1237 keV towards band D1, four transitions of 596, 673, 780, and 919 keV towards band D3, and three transitions of 589, 649 and 750 keV towards band D2-3qp. The parity of band D4 is the same as the assigned positive parity of band D3, because the three connecting transitions of 589, 649, and 780 keV between bands 3 and 2 have firmly established E2 character (see Table. 6.1). We therefore adopt a negative parity for band D4. Spectra showing the newly identified transitions in the bands D3 and D4 are given in Fig. 6.2.

We confirm all previously reported levels of bands D5 and D6 in Refs. [32, 33]. Three new levels with spins $21/2^-$, $45/2^-$ and $(47/2^-)$ are identified at the bottom and at the top of band D5, connected by the new transitions of 130, 560, 565, 1054, and 1125 keV. The two tentative transitions of 557 keV and 963 keV reported previously in Ref. [33] are confirmed, but our data show that the energy of the 557-keV transition is instead 559 keV. Three new transitions connecting band D6 to D5 with energies of 609, 997 and 1071 keV are newly identified. Three transitions of 463, 584, and 1299 keV from bands D5 and D6 to band D1 have been also newly identified. The spins and negative parity of band D5 are well established based on the E2 character of the 735-, 835-, and 1299-keV transitions towards band D1, deduced from the measured R_{DCO} and R_{ac} ratios (see Table. 6.1). The spins and negative parity of band D6 are also well established based on the E2 character of the 897-, 931-, 950-, 963-, and 997-keV transitions towards band D5 (see Table. 6.1).

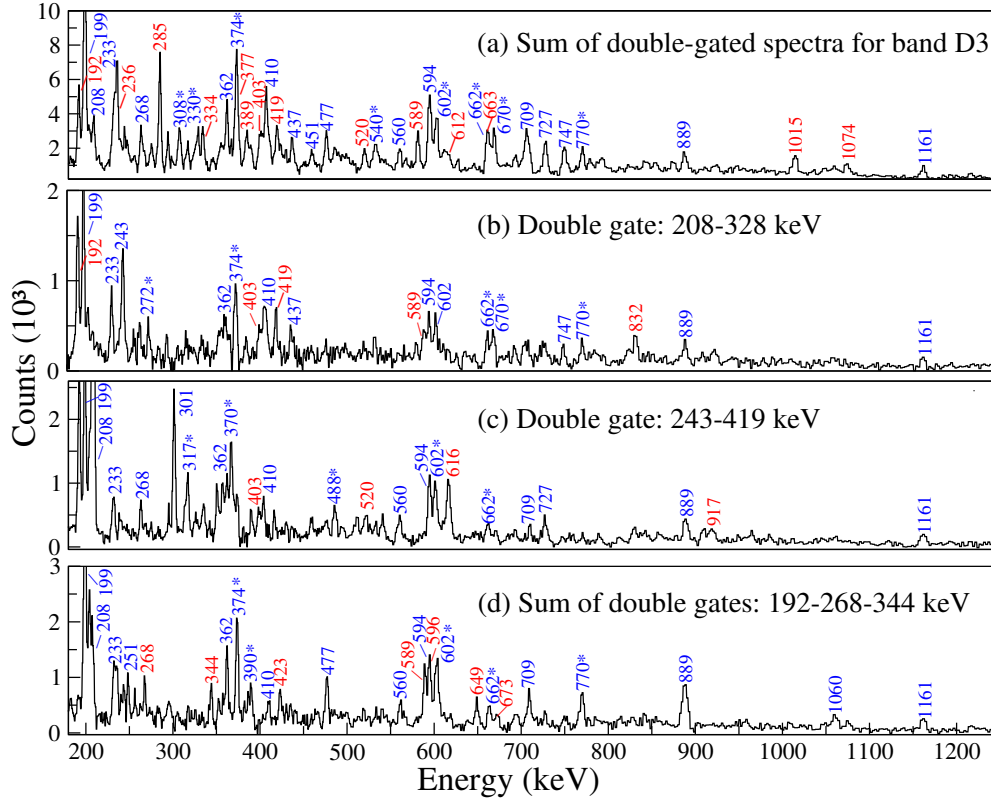


Figure 6.2: (Color online) Spectra for the bands D3 and D4 of ^{135}Nd showing the newly identified transitions (in red color). The peaks marked with an asterisk are contaminants from ^{136}Nd .

6.3 Discussion

To understand the nature of the observed band structure in ^{135}Nd , we analyzed the excitation energies of the bands, which reveal their detailed structure when drawn relative to a standard rotor reference, like in Fig. 6.3. One can observe a significant signature splitting between the two signatures of the yrast one-quasiparticle band built on the $\nu 9/2^- [514]$ Nilsson orbital, which indicates that ^{135}Nd has a large triaxiality close to the ground state. One can also observe the parabolic behavior of the bands D2-D6, with a difference in excitation energy between the bands D2, D3 and D4 of around 200 keV, and between the bands D5 and D6 of around 500 keV at low spins, which decreases steadily with increasing spin. Band D2 is observed over a much longer spin range than the bands D3, D4. It exhibits a markedly different slope at high spins, indicating a band crossing, and induced us to use the two labels D2-3qp and D2-5qp for the low- and high-spin parts, as they are interpreted as three (3qp) and five-quasiparticle (5qp) bands, respectively (see the discussion below).

Another quantity which reveals the properties of the bands is the single-

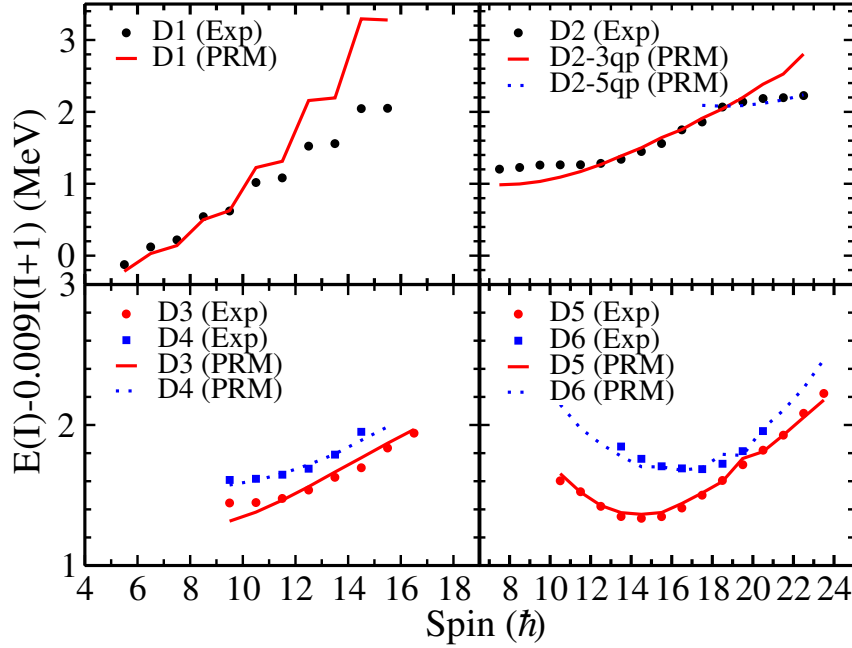


Figure 6.3: (Color online) Comparison between the experimental excitation energies relative to a reference rotor (symbols) and the particle-rotor model calculations (lines) for the bands D1-D6.

particle alignment i_x , which is given in Fig. 6.4. The used Harris parameters $\mathcal{J}_0 = 11 \hbar^2 \text{MeV}^{-1}$ and $\mathcal{J}_1 = 20 \hbar^4 \text{MeV}^{-3}$ which induce a flat behavior of band D2-D4 in the medium spin range, at difference with respect to that of band D1 which is up-sloping with increasing frequency. This clearly shows the polarizing effect of the two additional nucleons contributing to the 3qp configurations of bands D2-D4, which induces a larger deformation. Particular features are exhibited by band D2 at both low and high spins. At low spins one observes a decrease of i_x , most probably induced by the interaction with other positive-parity levels not shown in the partial level scheme given in Fig. 6.1. At high spins one observes a backbending with a spin gain of at least $7\hbar$, indicating the alignment of two more nucleons, most probably protons occupying the $h_{11/2}$ orbital. Furthermore, the very similar values of around $9\hbar$ exhibited by the bands D2-D4, suggest similar 3qp configurations. The difference of $\approx 7\hbar$ at low frequency between the bands D2-D4 and D1, strongly suggests the involvement of two more nucleons placed on opposite parity orbitals in the bands D2-D4, most probably protons occupying the $h_{11/2}$ and the strongly mixed ($d_{5/2}, g_{7/2}$) orbitals. The single-particle alignment i_x of the bands D5 is larger by $2-3\hbar$ than that of the bands D2-D4, while that of band D6 is larger than that of band D5 by $\approx 2\hbar$. The higher spin alignment of the bands D5, D6 relative to that of bands D2-D4 clearly shows the involvement of a pair of protons in the $h_{11/2}$ orbital.

A third quantity revealing the properties of the band is the ratio of reduced transition probabilities $B(M1)/B(E2)$, which are given together with the calculated values in Fig. 6.5. One can observe the big difference between the $B(M1)/B(E2)$ values of the bands D1 and D2-D6 which are based on 1qp and 3qp (5qp) configurations, respectively.

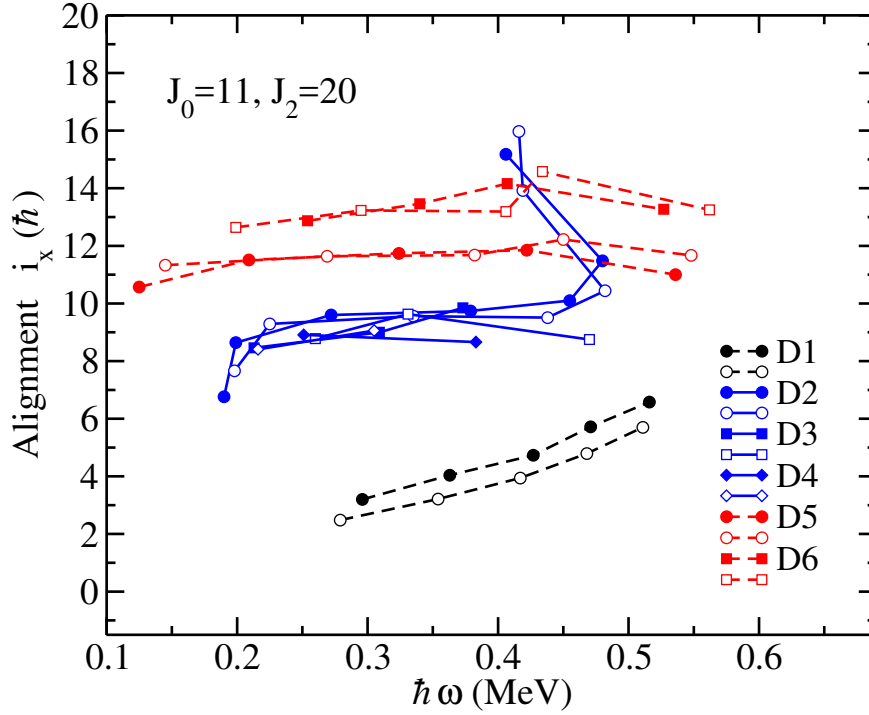


Figure 6.4: (Color online) The experimental quasi-particle alignments for the chiral rotational bands of ^{135}Nd .

In order to examine in detail the chiral character of the observed bands, the recently developed particle-rotor model has been used [51, 55]. The input deformation parameters (β_2, γ) for PRM calculations are obtained from constrained CDFT calculations [23]. In addition, for the electromagnetic transitions, the empirical intrinsic quadrupole moment $Q_0 = (3/\sqrt{5\pi})R_0^2 Z\beta$ with $R_0 = 1.2A^{1/3}$ fm, and gyromagnetic ratios for rotor $g_R = Z/A$ and for nucleons $g_{p(n)} = g_l + (g_s - g_l)/(2l + 1)$ [$g_l = 1(0)$ for protons (neutrons) and $g_s = 0.6g_{free}$] [3] are adopted.

The ground state band D1 with the configuration $\nu(1h_{11/2})^{-1}$ has been studied previously [33, 131, 132]. The deformation parameters obtained from the CDFT calculations are $\beta_2 = 0.19$ and $\gamma = 25.5^\circ$, which are similar to those used in Ref. [133], in which the measured transition probabilities were well reproduced. The obtained energy spectra, which are shown in Fig. 6.3, are in excellent agreement with the data in the low spin region. The deviation from the experimental data at high spin is due to the interaction with band D5

and to the variation of the moment of inertia which is not taken into account in the calculation. The corresponding calculated $B(M1)/B(E2)$ ratios, shown in Fig. 6.5 (a), are in very good agreement with the measured values.

The configurations assigned to band D2-3qp and its continuation at high spins D2-5qp are $\pi[(1h_{11/2})^1(2d_{5/2})^{-1}] \otimes \nu(1h_{11/2})^{-1}$ and $\pi[(1h_{11/2})^3(2d_{5/2})^{-1}] \otimes \nu(1h_{11/2})^{-1}$, respectively. The deformation parameters obtained from the CDFT calculations are $(\beta_2, \gamma) = (0.23, 22.5^\circ)$ and $(0.25, 15.6^\circ)$, respectively. To reproduce the $B(M1)/B(E2)$ for D2-3qp, a slightly smaller triaxial deformation 17.0° is used in the PRM calculations. In both calculations, a Coriolis attenuation factor $\xi = 0.92$ is introduced. In addition, the used moments of inertia for D2-3qp and D2-5qp are $\mathcal{J}_l = 25.0$ and $40 \hbar^2 \text{MeV}^{-1}$, respectively. A larger \mathcal{J}_l needed for D2-5qp is consistent with its larger single-particle alignment, as shown in Fig. 6.2. As one can see in Fig. 6.2, the calculated excitation energies for band D2 are in excellent agreement with the experimental values in the central and high spins ranges. At low spins, the calculated energies are lower than the experimental values by around 200 keV, which can be ascribed to the interaction with other low-lying levels. The calculated $B(M1)/B(E2)$ ratios of band D2 are compared with the experimental data in Fig. 6.5 (b), in which we can see a good agreement for both D2-3qp and D2-5qp bands.

The configuration assigned to the positive-parity doublet bands D3 and D4 is $\pi[(1h_{11/2})^1(1g_{7/2})^{-1}] \otimes \nu(1h_{11/2})^{-1}$, similar to that assigned to the corresponding bands 2 and 3 of the isotone nucleus ^{133}Ce [25]. In the PRM calculations, $(\beta_2 = 0.23, \gamma = 21.0^\circ)$, $\mathcal{J}_l = 28 \hbar^2 \text{MeV}^{-1}$, and $\xi = 0.94$ are employed. The calculated energy spectra presented in Fig. 6.3 reproduce well the experimental data. The energy separation between the bands is nearly constant at ≈ 200 keV, reflecting similar moments of inertia, and supporting thus the chiral doublet bands interpretation. Due to very weak in-band crossover transitions, we could extract the $B(M1)/B(E2)$ ratio only for the level with spin $I = 29\hbar$ of band D3, which is similar to that of band D2. The theoretical calculation is in agreement with the experimental values within the error bars [see Fig. 6.5 (b)]. Based on this similarity between the observed bands in the two isotones ^{133}Ce and ^{135}Nd , we safely can interpret the bands D3 and D4 of ^{135}Nd as chiral doublet bands based on the $\pi[(1h_{11/2})^1(1g_{7/2})^{-1}] \otimes \nu(1h_{11/2})^{-1}$ configuration.

The configuration adopted for the bands D5 and D6, which are among the best examples of chiral vibration, is $\pi(1h_{11/2})^2 \otimes \nu(1h_{11/2})^{-1}$ [32, 33, 51]. The deformation parameters from the CDFT are $(\beta_2, \gamma) = (0.24, 22.2^\circ)$, which are the same as those used in Ref. [32]. To reproduce the rapid increase of experimental $B(M1)/B(E2)$ value at $I = 39/2\hbar$, a slightly smaller triaxial deformation $\gamma = 20.2^\circ$ is used in the PRM calculations. In addition, $\mathcal{J}_l = 23.5 \hbar^2 \text{MeV}^{-1}$, and $\xi = 0.98$ are adopted. As one can see in Fig. 6.3, the calculated excitation energies of the two bands are in very good agreement with the experimental data. The measured transition probabilities $B(M1)$ and $B(E2)$ of the two bands were published in Ref. [32]. The $B(M1)/B(E2)$ ratios of the

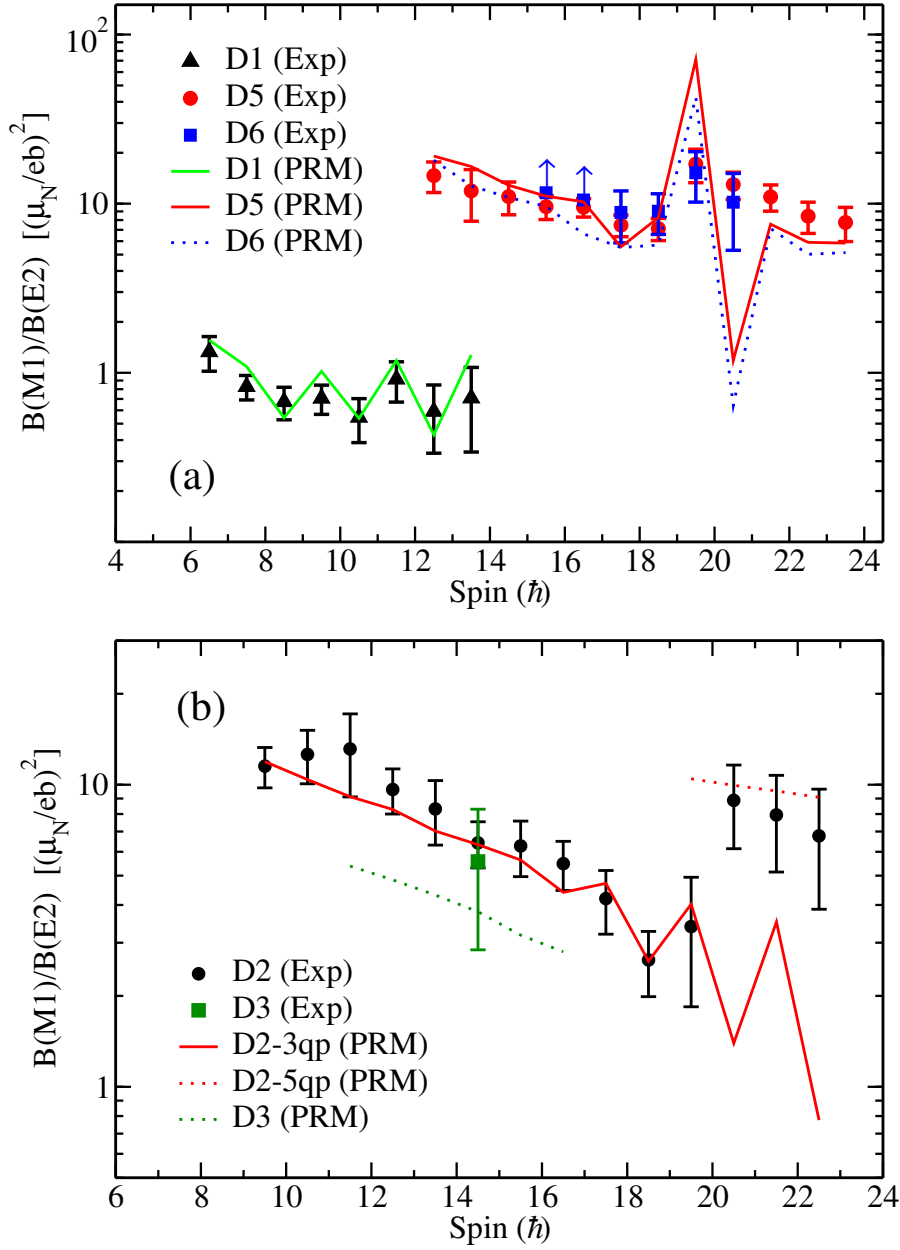


Figure 6.5: (Color online) Comparison between experimental ratios of transitions probabilities $B(M1)/B(E2)$ (symbols) and the particle-rotor calculations (lines) for the bands D1-D6.

present work are very similar to those obtained from the results published in Ref. [32]. The calculated and experimental $B(M1)/B(E2)$ ratios are showed in Fig. 6.5 (a). One can see that the PRM values are in good agreement with the experimental data, including the sudden increase occurring at spin 39/2, which is induced by a sudden decrease of the $B(E2)$ values at spins above 39/2, and was interpreted as due to the transition from chiral vibration to chiral rotation.

The success in reproducing the excitation energies and the electromagnetic transition probabilities of the bands D5 and D6 by the PRM calculations give a strong support to the configuration assignment of $\pi(1h_{11/2})^2 \otimes \nu(1h_{11/2})^{-1}$.

In order to investigate to what extent the 3D chiral geometry is present in the two chiral doublets, we plotted the components of the angular momenta on the three axes (short, intermediate and long) of the intrinsic reference system. The results for bands D3 and D4 are shown in Fig. 6.6. Those for bands D5 and D6 are similar to those reported in Ref. [32], hence here we do not present them once again. One can observe a significative difference between the two chiral doublets: the positive-parity configuration assigned to bands D3 and D4 fulfils much better the chiral geometry, exhibiting equilibrated single-particle angular momenta along the three axes. The negative-parity configuration assigned to band D5 and D6 exhibits a higher single-particle angular momentum along the short axis, which brings the total angular momentum closer to the short-long principal plane and facilitates the chiral vibration at low spin.

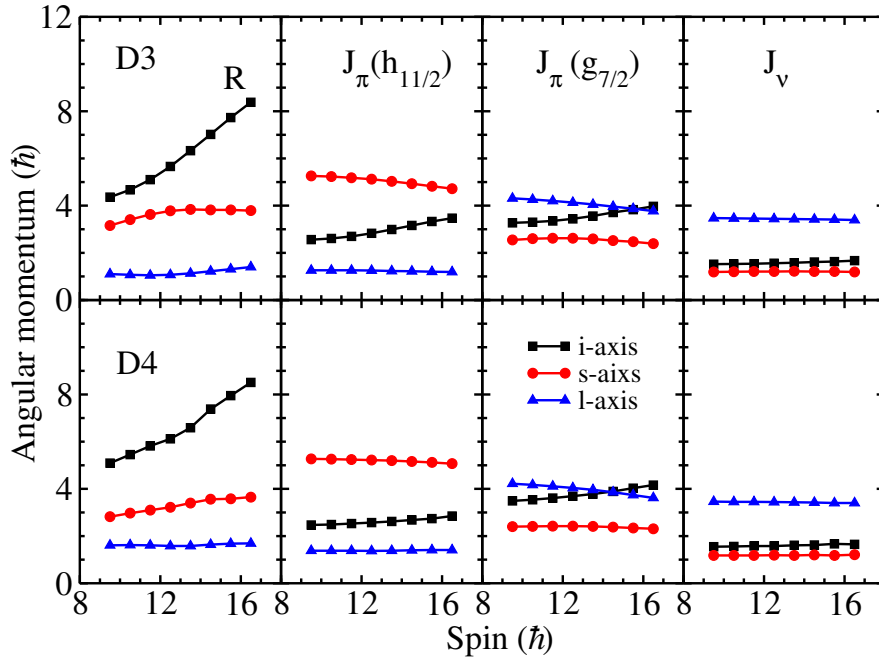


Figure 6.6: (Color online) The root mean square components along the intermediate (i –, squares), short (s –, circles) and long (l –, triangles) axes of the rotor, valence protons, and valence neutrons angular momenta calculated as functions of spin by PRM for the doublet bands D3 and D4 of ^{135}Nd .

The observation of a second set of chiral doublet bands with positive-parity in addition to the previously known negative-parity chiral doublet, reveals the existence of the M χ D phenomenon in ^{135}Nd . The presence of the M χ D phenomenon in several nuclei of the $A \approx 130$ mass region (^{133}Ce , ^{135}Nd , ^{136}Nd), put in evidence the importance and solidity of the chiral symmetry in

nuclei.

In summary, a new pair of chiral doublet bands based on the $3\text{qp } \pi[(1h_{11/2})^1(1g_{7/2})^{-1}] \otimes \nu(1h_{11/2})^{-1}$ in addition to the previously known pair of chiral bands based on the $\pi(1h_{11/2})^2 \otimes \nu(1h_{11/2})^{-1}$ configuration has been identified in ^{135}Nd . The observed doublet bands are compared with CDFT and PRM calculations, which nicely reproduce the experimental data. According to these results, the existence of the M χ D phenomenon in nuclei of the $A \approx 130$ mass region is strongly supported. The present results encourage us to continue the study of chirality in nuclei, both experimentally (measurement of lifetimes and search for chiral doublets in other nuclei) and theoretically.

Table 6.1 – Experimental information including the γ -ray energies, energies of the initial levels E_i , intensities I_γ , anisotropies R_{DCO} and or R_{ac} , multipolarities, and the spin-parity assignments to the observed states in ^{135}Nd . The transitions listed with increasing energy are grouped in bands and the transitions connecting a given band to low-lying states are listed at the end of each band separated by a blank line. The deduced values for R_{DCO} with a stretched quadrupole gate are ≈ 1 for stretched quadrupole and ≈ 0.46 for dipole transitions, while the ratio is close to 1 for a dipole and 2.1 for a quadrupole transition when the gate is set on a dipole transition. The R_{ac} values for stretched dipole and quadrupole transitions are ≈ 0.8 and ≈ 1.4 .

E_γ^a	E_i (keV)	I_γ^b	R_{DCO}^c	R_{ac}^d	Mult.	$J_i^\pi \rightarrow J_f^\pi$
Band D1						
198.8	198.8	100.0	0.49(5) ^e		M1	11/2 ⁻ \rightarrow 9/2 ⁻
232.6	793.1	12.5(19)	0.82(4) ^e		M1/E2	15/2 ⁻ \rightarrow 13/2 ⁻
250.6	1520.4	2.9(5)	0.47(8) ^e		M1	19/2 ⁻ \rightarrow 17/2 ⁻
270.1	2375.6	1.2(3)	0.24(5) ^e		M1/E2	23/2 ⁻ \rightarrow 21/2 ⁻
276.2	3319.5	0.10(5)				27/2 ⁻ \rightarrow 25/2 ⁻
361.7	560.5	31(3)	0.43(6) ^e		M1	13/2 ⁻ \rightarrow 11/2 ⁻
476.7	1269.8	14.0(25)	0.45(4) ^e		M1	17/2 ⁻ \rightarrow 15/2 ⁻
560.5	506.5	19(4)	0.90(10) ^e		E2	13/2 ⁻ \rightarrow 9/2 ⁻
585.1	1520.4	7.3(9)	0.55(3) ^e		M1/E2	21/2 ⁻ \rightarrow 19/2 ⁻
594.3	793.1	62(4)	1.00(8) ^e		E2	15/2 ⁻ \rightarrow 11/2 ⁻
667.7	3043.3	0.8(3)	0.82(9) ^e		M1/E2	25/2 ⁻ \rightarrow 23/2 ⁻
709.3	1269.8	24(3)	1.08(8) ^e		E2	17/2 ⁻ \rightarrow 13/2 ⁻
727.3	1520.4	37.0(35)	1.08(9) ^e		E2	19/2 ⁻ \rightarrow 15/2 ⁻
748.2	4067.7	1.12(6)	0.65(3) ^e		M1/E2	29/2 ⁻ \rightarrow 27/2 ⁻
835.7	2105.5	19(5)	0.90(13) ^e		E2	21/2 ⁻ \rightarrow 17/2 ⁻
855.2	2375.6	21.2(20)	1.15(17) ^e		E2	23/2 ⁻ \rightarrow 19/2 ⁻
937.8	3043.3	2.3(5)	1.06(11) ^e		E2	25/2 ⁻ \rightarrow 21/2 ⁻
943.9	3319.5	3.5(5)	1.12(20) ^e		E2	27/2 ⁻ \rightarrow 23/2 ⁻
(1024.4)	4067.7					(29/2 ⁻) \rightarrow 27/2 ⁻

Table 6.1 – *Continued*

E_γ^a	E_i (keV)	I_γ^b	R_{DCO}^c	R_{ac}^d	Mult.	$J_i^\pi \rightarrow J_f^\pi$
1032.3	4351.8	1.2(1)	0.83(23) ^e		E2	$31/2^- \rightarrow 27/2^-$
Band D2						
177.2	1954.5	2.0(1)		0.66(7)	M1/E2	$17/2^+ \rightarrow 15/2^+$
192.4	2350.8	17(2)	0.64(3) ^e		M1/E2	$21/2^+ \rightarrow 19/2^+$
203.9	2158.4	9.5(8)	0.85(9) ^e		M1/E2	$19/2^+ \rightarrow 17/2^+$
207.5	2588.3	13.5(25)	0.65(7) ^e		M1/E2	$23/2^+ \rightarrow 21/2^+$
243.2	2801.5	9.2(9)	0.64(9) ^e		M1/E2	$25/2^+ \rightarrow 23/2^+$
301.1	3102.6	7.5(6)	0.34(7) ^e		M1/E2	$27/2^+ \rightarrow 25/2^+$
369.1	3471.7	4.9(4)	0.82(36) ^e		M1/E2	$29/2^+ \rightarrow 27/2^+$
381.1	2158.4	0.55(7)		1.32(23)	E2	$19/2^+ \rightarrow 15/2^+$
390.0	3861.7	3.6(4)		0.65(5)	M1/E2	$31/2^+ \rightarrow 29/2^+$
396.3	2350.8	1.29(21)		1.37(17)	E2	$21/2^+ \rightarrow 17/2^+$
397.7	6550.0	0.4(1)		0.79(11)	M1/E2	$43/2^+ \rightarrow 41/2^+$
399.9	2588.3	0.82(20)		1.36(16)	E2	$23/2^+ \rightarrow 19/2^+$
416.7	6152.3	0.6(1)		0.86(20)	M1/E2	$41/2^+ \rightarrow 39/2^+$
421.9	5735.6	0.31(11)		1.09(16)	M1/E2	$39/2^+ \rightarrow 37/2^+$
425.4	4773.2	1.20(21)		1.07(14)	M1/E2	$35/2^+ \rightarrow 33/2^+$
436.3	6986.3	0.20(3)				$(45/2^+) \rightarrow 43/2^+$
450.7	2801.5	0.86(12)		1.38(11)	E2	$25/2^+ \rightarrow 21/2^+$
486.1	4347.8	2.10(25)		0.75(2)	M1/E2	$33/2^+ \rightarrow 31/2^+$
540.5	5313.7	0.85(15)		1.22(10)	M1/E2	$37/2^+ \rightarrow 35/2^+$
544.3	3102.6	1.10(25)	1.08(12) ^e		E2	$27/2^+ \rightarrow 23/2^+$
670.2	3471.7	1.43(22)	0.95(16) ^e		E2	$29/2^+ \rightarrow 25/2^+$
759.1	3861.7	1.7(3)		1.42(12)	E2	$31/2^+ \rightarrow 27/2^+$
814.4	6550.0	0.20(5)		1.36(10)	E2	$43/2^+ \rightarrow 39/2^+$
834.0	6986.3	0.10(4)				$(45/2^+) \rightarrow 41/2^+$
838.6	6152.3	0.27(7)		1.34(21)	E2	$41/2^+ \rightarrow 37/2^+$
876.1	4347.8	1.20(17)		1.50(17)	E2	$33/2^+ \rightarrow 29/2^+$
911.5	4773.2	1.7(3)		1.41(15)	E2	$35/2^+ \rightarrow 31/2^+$
962.4	5735.6	0.7(2)		1.43(16)	E2	$39/2^+ \rightarrow 35/2^+$
965.9	5313.7	1.2(2)		1.37(25)	E2	$37/2^+ \rightarrow 33/2^+$
513.0	2158.4	0.28(2)		0.74(7)	E1	$19/2^+ \rightarrow 17/2^-$
514.8	2350.8	0.20(2)		0.77(9)	E1	$21/2^+ \rightarrow 19/2^-$
747.2	2158.4	1.4(2)		0.87(11)	E1	$19/2^+ \rightarrow 17/2^-$
827.4	1954.5	1.87(8)		0.83(10)	E1	$17/2^+ \rightarrow 15/2^-$
830.4	2350.8	5.0(3)	0.48(5) ^e		E1	$21/2^+ \rightarrow 19/2^-$
888.6	2158.4	8.1(6)	0.58(15) ^e		E1	$19/2^+ \rightarrow 17/2^-$
1060.4	1777.3	0.11(2)				$15/2^+ \rightarrow 13/2^-$
1161.4	1954.5	11(1)	0.60(16) ^e		E1	$17/2^+ \rightarrow 15/2^-$

Table 6.1 – *Continued*

E_γ^a	E_i (keV)	I_γ^b	R_{DCO}^c	R_{ac}^d	Mult.	$J_i^\pi \rightarrow J_f^\pi$
1216.8	1777.3	3.2(2)		0.83(10)	E1	$15/2^+ \rightarrow 13/2^-$
Band D3						
191.5	2535.0	1.4(2)		1.10(16)	M1/E2	$21/2^+ \rightarrow 19/2^+$
235.7	2770.7	3.4(2)	$0.62(11)^f$		M1/E2	$23/2^+ \rightarrow 21/2^+$
285.0	3055.7	4.0(3)	$0.35(8)^f$		M1/E2	$25/2^+ \rightarrow 23/2^+$
328.5	3718.6	1.1(1)	$0.87(7)^f$		M1/E2	$29/2^+ \rightarrow 27/2^+$
334.4	3390.1	2.1(1)	$0.61(14)^f$		M1/E2	$27/2^- \rightarrow 25/2^+$
419.3	4137.9	0.39(5)		1.10(25)	M1/E2	$31/2^+ \rightarrow 29/2^+$
520.3	4658.2	0.13(2)				$(33/2^+) \rightarrow 31/2^+$
662.9	3718.6	0.5(2)				$29/2^+ \rightarrow 25/2^+$
376.6	2535.0	0.17(2)				$21/2^+ \rightarrow 19/2^+$
389.0	2343.5	0.43(6)				$19/2^+ \rightarrow 17/2^+$
402.9	4540.8	0.30(4)				$33/2^+ \rightarrow 31/2^+$
419.9	2770.7	0.44(4)		1.04(16)	M1/E2	$23/2^+ \rightarrow 21/2^+$
566.2	2343.5	0.25(2)	$0.85(25)^e$		E2	$19/2^+ \rightarrow 15/2^+$
580.5	2535.0	0.9(1)		1.34(21)	E2	$21/2^+ \rightarrow 17/2^+$
588.6	3390.1	0.26(2)				$27/2^+ \rightarrow 25/2^+$
612.3	2770.7	0.81(5)		1.44(23)	E2	$23/2^+ \rightarrow 19/2^+$
616.0	3718.6	1.19(11)		1.02(14)	M1/E2	$29/2^+ \rightarrow 27/2^+$
666.2	4137.9	0.58(5)		0.65(8)	M1/E2	$31/2^+ \rightarrow 29/2^+$
679.1	4540.8	0.43(2)		0.58(4)	M1/E2	$33/2^+ \rightarrow 31/2^+$
704.9	3055.7	0.57(2)	$1.11(16)^e$		E2	$25/2^+ \rightarrow 21/2^+$
831.8	3390.1	0.36(2)	$1.2(3)^e$		E2	$27/2^+ \rightarrow 23/2^+$
917.1	3718.6	0.26(3)				$29/2^+ \rightarrow 25/2^+$
1014.6	2535.0	1.7(1)	$0.51(6)^e$		E1	$21/2^+ \rightarrow 19/2^-$
1035.3	4137.9	0.19(2)		1.30(18)	E2	$31/2^+ \rightarrow 27/2^+$
1069.1	4540.8	0.29(2)		1.43(15)	E2	$33/2^+ \rightarrow 29/2^+$
1073.7	2343.5	1.2(1)	$0.64(25)^e$		E1	$19/2^+ \rightarrow 17/2^-$
Band D4						
197.3	2704.3	0.40(5)				$21/2^+ \rightarrow 19/2^+$
235.7	2940.0	1.7(2)	$0.31(3)^e$		M1/E2	$23/2^+ \rightarrow 21/2^+$
267.6	3207.6	1.9(2)	$0.22(6)^e$		M1/E2	$25/2^+ \rightarrow 23/2^+$
343.5	3551.1	1.2(1)	$0.44(7)^e$		M1	$27/2^+ \rightarrow 25/2^+$
423.4	3974.5	0.25(3)		1.08(16)	M1/E2	$29/2^+ \rightarrow 27/2^+$
589.2	2940.0	0.21(3)		1.45(30)	E2	$23/2^+ \rightarrow 19/2^+$
596.5	2940.0	0.13(5)				$23/2^+ \rightarrow 19/2^+$
649.3	3207.6	0.35(3)		1.41(17)	E2	$25/2^+ \rightarrow 21/2^+$
672.6	3207.6	0.11(2)				$25/2^+ \rightarrow 21/2^+$

Table 6.1 – *Continued*

E_γ^a	E_i (keV)	I_γ^b	R_{DCO}^c	R_{ac}^d	Mult.	$J_i^\pi \rightarrow J_f^\pi$
749.8	2704.3	0.15(2)				$21/2^+ \rightarrow 17/2^+$
780.4	3551.1	0.13(4)	0.90(20) ^e		E2	$27/2^+ \rightarrow 23/2^+$
918.8	3974.5	0.21(5)				$29/2^+ \rightarrow 25/2^+$
1183.9	2704.3	1.3(1)	0.61(16) ^e		E1	$21/2^+ \rightarrow 19/2^-$
1237.2	2507.0	0.45(4)		0.72(15)	E1	$19/2^+ \rightarrow 17/2^-$
Band D5						
121.0	2940.6	6.0(5)	0.41(5) ^e		M1	$25/2^- \rightarrow 23/2^-$
129.8	2819.6	0.12(2)				$23/2^- \rightarrow 21/2^-$
170.4	3111.0	24.5(20)	0.44(3) ^e		M1	$27/2^- \rightarrow 25/2^-$
247.9	3358.9	18.8(17)	0.55(9) ^e		M1/E2	$29/2^- \rightarrow 27/2^-$
250.8	2940.6	0.16(3)				$25/2^- \rightarrow 21/2^-$
291.1	3650.0	12.7(14)	0.53(7) ^e		M1/E2	$31/2^- \rightarrow 29/2^-$
291.4	3111.0	0.61(20)				$27/2^- \rightarrow 23/2^-$
358.2	4008.2	9.9(6)	0.58(15) ^e		M1/E2	$33/2^- \rightarrow 31/2^-$
406.3	4414.5	6.6(5)	0.63(5) ^e		M1/E2	$35/2^- \rightarrow 33/2^-$
418.3	3358.9	1.0(2)	0.94(9) ^e		E2	$29/2^- \rightarrow 25/2^-$
438.2	4852.7	5.2(5)	0.43(3) ^e		M1	$37/2^- \rightarrow 35/2^-$
462.4	5315.2	3.9(3)	0.70(5) ^e		M1/E2	$39/2^- \rightarrow 37/2^-$
472.4	5787.6	2.5(2)		0.79(6)	M1	$41/2^- \rightarrow 39/2^-$
493.9	6281.5	1.53(15)		1.11(12)	M1/E2	$43/2^- \rightarrow 41/2^-$
539.0	3650.0	1.7(2)	1.04(12) ^e		E2	$31/2^- \rightarrow 27/2^-$
560.1	6841.6	0.85(7)				$45/2^- \rightarrow 43/2^-$
565.0	7406.6	0.5(1)				$(47/2^-) \rightarrow 45/2^-$
649.3	4008.2	1.82(20)	0.89(11) ^e		E2	$33/2^- \rightarrow 29/2^-$
764.5	4414.5	2.4(3)	1.23(26) ^e		E2	$35/2^- \rightarrow 31/2^-$
844.5	4852.7	2.6(3)		1.34(15)	E2	$37/2^- \rightarrow 33/2^-$
900.7	5315.2	0.95(20)		1.51(19)	E2	$39/2^- \rightarrow 35/2^-$
934.9	5787.6	0.91(15)		1.46(23)	E2	$41/2^- \rightarrow 37/2^-$
966.3	6281.5	0.68(10)		1.39(17)	E2	$43/2^- \rightarrow 39/2^-$
1054.0	6841.6	0.52(10)		1.64(33)	E2	$45/2^- \rightarrow 41/2^-$
1125.1	7406.6	0.45(5)				$(47/2^-) \rightarrow 43/2^-$
84.6	2819.6	0.30(5)				$23/2^- \rightarrow 21/2^-$
444.0	2819.6	1.7(1)	1.22(19) ^e		M1/E2	$23/2^- \rightarrow 23/2^-$
565.0	2940.6	8.4(6)	0.37(5) ^e		M1/E2	$25/2^- \rightarrow 23/2^-$
584.3	2689.6	0.50(4)	0.48(5) ^e		M1	$21/2^- \rightarrow 21/2^-$
640.6	2819.6	0.11(2)				$23/2^- \rightarrow 19/2^-$
714.1	2819.6	2.9(2)	0.68(7) ^e		M1/E2	$23/2^- \rightarrow 21/2^-$
735.4	3111.0	2.9(2)	0.97(12) ^e		E2	$27/2^- \rightarrow 23/2^-$
738.3	2819.6	2.0(2)		1.23(14)	M1/E2	$23/2^- \rightarrow 21/2^-$

Table 6.1 – *Continued*

E_γ^a	E_i (keV)	I_γ^b	R_{DCO}^c	R_{ac}^d	Mult.	$J_i^\pi \rightarrow J_f^\pi$
835.1	2940.6	17.9(18)	1.02(13) ^e		E2	25/2 ⁻ \rightarrow 21/2 ⁻
1044.4	2689.8	0.10(1)				21/2 ⁻ \rightarrow 17/2 ⁻
1299.2	2819.6	0.76(4)	1.14(16) ^e		E2	23/2 ⁻ \rightarrow 19/2 ⁻
Band D6						
173.0	3782.0	2.3(2)	0.7(2) ^e		M1/E2	29/2 ⁻ \rightarrow 27/2 ⁻
225.8	4007.8	3.8(4)	0.85(9) ^e		M1/E2	31/2 ⁻ \rightarrow 29/2 ⁻
282.4	4290.2	4.5(3)		0.61(9)	M1/E2	33/2 ⁻ \rightarrow 31/2 ⁻
309.4	4599.6	3.1(2)		0.66(7)	M1/E2	35/2 ⁻ \rightarrow 33/2 ⁻
371.6	4971.2	2.5(5)				37/2 ⁻ \rightarrow 35/2 ⁻
440.4	5411.6	0.95(17)		1.09(22)	M1/E2	39/2 ⁻ \rightarrow 37/2 ⁻
512.4	5924.0	0.20(6)				(41/2 ⁻) \rightarrow 39/2 ⁻
591.8	4599.6	0.6(2)				35/2 ⁻ \rightarrow 31/2 ⁻
681.0	4971.2	0.55(10)				37/2 ⁻ \rightarrow 33/2 ⁻
812.0	5411.6	0.18(5)				39/2 ⁻ \rightarrow 35/2 ⁻
952.8	5924.0	0.08(3)				(41/2 ⁻) \rightarrow 37/2 ⁻
463.0	3782.0	1.12(13)		0.67(8)	M1/E2	29/2 ⁻ \rightarrow 27/2 ⁻
591.4	4599.6	0.8(2)				35/2 ⁻ \rightarrow 33/2 ⁻
608.8	5924.0	0.25(4)				(41/2 ⁻) \rightarrow 39/2 ⁻
640.2	4290.2	0.57(3)		1.38(23)	M1/E2	33/2 ⁻ \rightarrow 31/2 ⁻
648.9	4007.8	1.8(2)		0.22(3)	M1/E2	31/2 ⁻ \rightarrow 29/2 ⁻
668.4	3609.0	2.5(2)	0.66(12) ^e		M1/E2	27/2 ⁻ \rightarrow 25/2 ⁻
671.0	3782.0	2.1(2)	0.73(16) ^e		M1/E2	29/2 ⁻ \rightarrow 27/2 ⁻
841.4	3782.0	1.58(17)	0.55(9) ^e		M1/E2	29/2 ⁻ \rightarrow 27/2 ⁻
896.8	4007.8	0.79(6)	1.02(16) ^e		E2	31/2 ⁻ \rightarrow 27/2 ⁻
931.3	4290.2	0.50(3)		1.53(17)	E2	33/2 ⁻ \rightarrow 29/2 ⁻
934.9	5787.6	0.70(20)		1.46(23)	E2	41/2 ⁻ \rightarrow 37/2 ⁻
949.6	4599.6	0.69(8)		1.51(27)	E2	35/2 ⁻ \rightarrow 31/2 ⁻
963.0	4971.2	0.53(5)		1.47(14)	E2	37/2 ⁻ \rightarrow 33/2 ⁻
966.3	6281.5	0.68(10)		1.39(17)	E2	43/2 ⁻ \rightarrow 39/2 ⁻
998.1	5412.6	0.85(6)		1.42(16)	E2	39/2 ⁻ \rightarrow 35/2 ⁻
1071.3	5924.0	0.22(3)				(41/2 ⁻) \rightarrow 37/2 ⁻

^a The error on the transition energies is 0.2 keV for transitions below 1000 keV of the ^{135}Nd reaction channel, 0.5 keV for transitions above 1000 keV and 1 keV for transitions above 1200 keV.

^b Relative intensities corrected for efficiency, normalized to the intensity of the 198.8 keV transition. The transition intensities were obtained from a combination of total projection and gated spectra.

^c R_{DCO} has been deduced from asymmetric γ - γ coincidence matrix sorted with detectors at 157.6° on one axis, and detectors at $\approx 90^\circ$ on the other axis. The tentative spin - parity of the states are given in parenthesis.

^d R_{ac} has been deduced from two asymmetric γ - γ coincidence matrices sorted with detectors at 133.6° and 157.6° on one axis, and detectors at $\approx 90^\circ$ on the other axis, respectively. The tentative spin - parity of the states are given in parenthesis.

^e DCO ratio from spectrum gated on stretched quadrupole transition.

^f DCO ratio from spectrum gated on stretched dipole transition.

Chapter 7

Search for long-lived isomeric states

In this chapter, the recoil-decay tagging technique will be briefly introduced. Then, the experimental results obtained from the analysis of the data collected at the focal plane will be presented.

7.1 Introduction

The nuclei around the $N = 82$ shell closure can have a variety of shapes, such as spherical at low spins, triaxial, highly deformed and superdeformed at high spins. At difference with respect to the well deformed nuclei which can exhibit long and regular rotational bands up to very high spins, the decay flux in the nearly spherical nuclei is often fragmented and interrupted by isomeric states, which renders more difficult their observation. Such a situation is encountered in the weakly deformed Nd nuclei, i.e., ^{139}Nd ($I^\pi = 23/2^+$, $T_{1/2} = 272$ ns) and ^{140}Nd ($I^\pi = 7^-$, $T_{1/2} = 600$ μs) [15], with neutron numbers close to $N = 82$ shell closure, which exhibit irregular sequences of transitions and possible yrast traps. Moreover, isomeric states were also observed in the well deformed Nd nuclei, i.e., ^{134}Nd ($I^\pi = 8^-$, $T_{1/2} = 410$ μs), ^{137}Nd ($I^\pi = 11/2^-$, $T_{1/2} = 1.6$ s) [15]. This encouraged us to search for possible long-lived isomeric states in the present experimental populated nuclei, in particular in ^{135}Nd and ^{136}Nd nuclei.

7.2 The recoil-decay tagging technique

The recoil-decay tagging (RDT) [134–136] is based on the use of temporal and spatial correlations of events in the measurement. The JUROGAM II + RITU + GREAT setup offers such a possibility. The fusion-evaporation reaction produces excited residual nuclei at the target position where they emit prompt γ rays in the de-excitation process to the ground state. These

prompt events are detected by JUROGAM II array. The reaction recoils then flight through the RITU separator are implanted into the focal plane GREAT array where one can measure delayed events resulting from long-lived isomers, with lifetimes sufficiently long to allow their observation after the flight time through the spectrometer. To correlate the events recorded by the detectors placed at different locations, the TDR data acquisition system was always used. In the RDT method, the "tag" can be charged particles, i.e., proton, α and β .

In the prompt and delayed spectroscopy, to correlate the prompt and delayed γ ray transitions across isomeric states and identify the lifetime of the isomer, the RDT technique can be applied. In addition, the γ rays following deexcitation of an isomeric state and detected at the focal plane of a recoil separator can be used to identify prompt γ ray transitions feeding the isomeric state. This method have been turned out to well suit for identifying the isomers with a half-live larger than the flight time through RITU [136].

7.3 Results of the focal plane

In the present work, initially, for the identification of the the γ rays of a specific nucleus we produced γ - γ matrices between the delayed transition detected by the clovers placed at the focal plane. In addition, to search for the transitions feeding a long-lived isomer we also produced γ - γ matrices between the JUROGAM II array (detecting prompt γ rays) and the clovers detectors (detecting delayed γ rays) placed at the focal plane. Various time conditions can be applied to these matrices to optimize the sensitivity for the isomeric decay with different half-lives. These matrices allowed the study of correlated prompt and delayed γ rays across isomeric states. Note that the time of the γ -ray emission measured at the focal plane is relative to the time of implantation of the recoiling nucleus in the DSSD detector.

After a careful analysis of the matrix obtained from the focal plane Ge detectors, we can select the cleanest transitions to extract the prompt-delayed spectra between JUROGAM II and the detectors at the focal plane. Thus, we can link the "new" transitions to the known level scheme of nucleus in this step.

To identify and extract the lifetime of the isomeric states, matrices can be constructed of delayed γ ray energy versus the time of the focal plane clovers (see Fig. 7.1). The time defined by a start induced by a recoil event in the DSSD detector and a stopped induced by a delayed γ ray detected in the focal plane clover detectors. The half-life can be obtained by gating on the γ rays de-exciting the isomeric states of interest and then fitting the time spectra.

Fig. 7.1 shows a 2D γ -Time matrix constructed from the clovers of the focal plane in this work. One can see delayed components of different lengths for the 729-, 884- and 973-keV transitions below the 10^+ , $T_{1/2} = 370$ ns

isomer of ^{138}Nd , and for the 640-, 815- and 948-keV transitions below the 10^+ , $T_{1/2} = 308$ ns isomer of ^{134}Ce .

By constructing several γ -Time matrices with various constraints on the time of the delayed γ ray, we also observed and confirmed the $11/2^-$, $T_{1/2} = 2.7$ μs isomer of ^{137}Pr and the 6^+ , $T_{1/2} = 90$ ns isomer of ^{136}Pr , but we could not extract lifetimes more precise than those already known [15]. However, no long-lived isomeric states have been found in ^{135}Nd and ^{136}Nd in the present data.

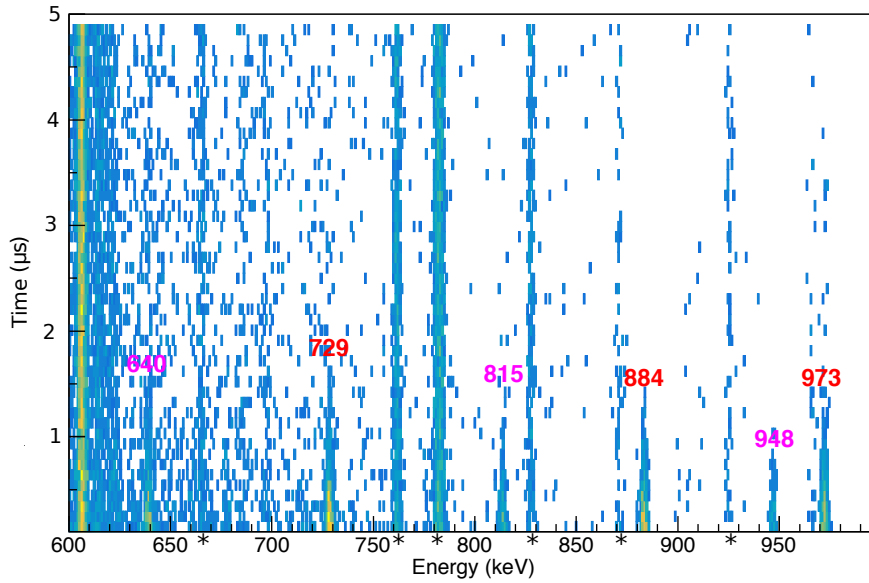


Figure 7.1: γ -Time matrix for the clovers at the focal plane. The transitions marked with asterisks represent the β -decay contaminants from the nuclei produced in this experiment: 665 keV, 783 keV, 828 keV and 872 keV from the β -decay of ^{135}Ce , 761 keV and 925 keV from the β -decay of ^{137}Nd .

In order to show the details of application of the RDT method in this work, we discuss here the already known 10^+ , $T_{1/2} = 370$ ns isomer of ^{138}Nd as an example. A partial level scheme of ^{138}Nd relative to the isomeric state is given in Fig. 7.2.

In the first step, we identified the 521-, 729-, 884- and 973-keV transitions of ground state band in ^{138}Nd from the γ - γ matrices of the delayed γ rays detected by the clovers placed at the focal plane.

In the second step, the clean 521-, 729-, 884- and 973 transitions were selected to extract the prompt-delayed spectra between JUROGAM II and the detectors at the focal plane. An example of a prompt spectrum from JUROGAM II obtained by gating on selected transitions of ^{138}Nd measured at the focal plane is shown in Fig. 7.3. One can see the 193-, 231-, 286-, 381- and 647 keV transitions in this spectrum, which belong to the prompt transitions above the isomer of the ^{138}Nd .

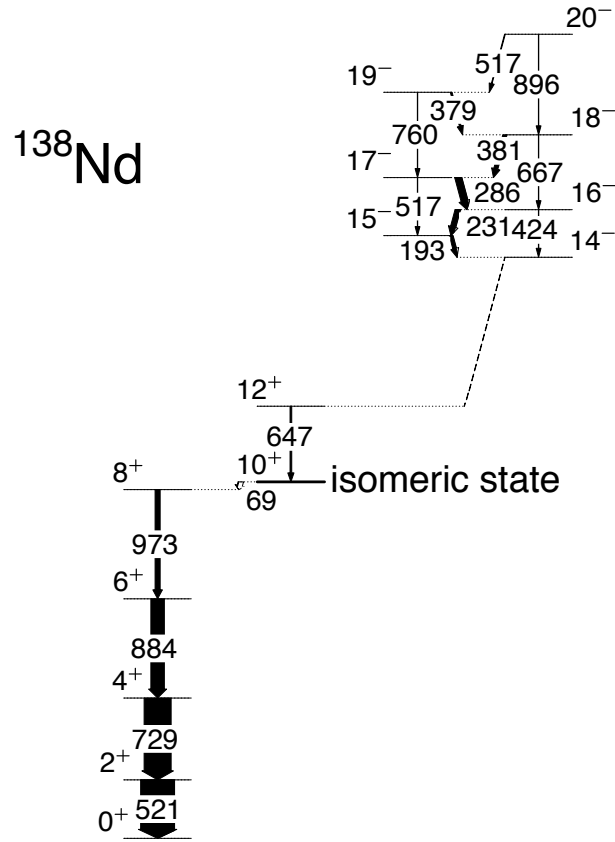


Figure 7.2: Partial level scheme of ^{138}Nd related to the isomeric state.

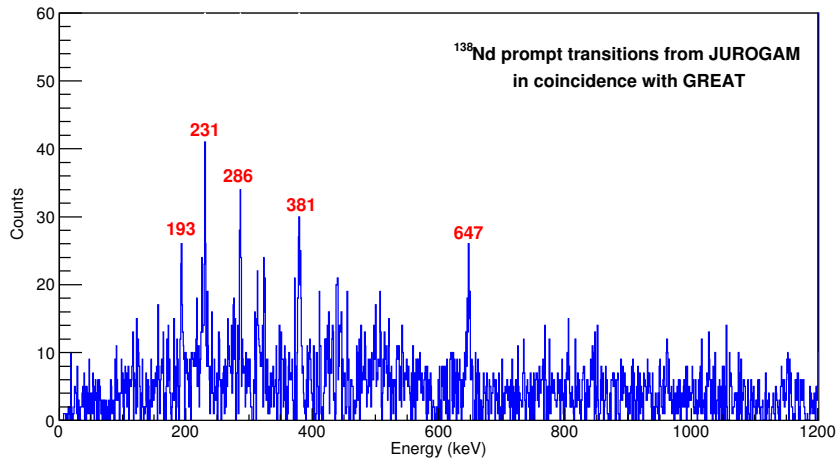


Figure 7.3: Spectrum of prompt transitions measured by JUROGAM II gated with selected clean transitions in ^{138}Nd (521, 729, 884, and 973 keV) measured by the clovers placed at the focal plane.

Finally, we can extract the lifetime from time spectra of γ rays in the deexcitation cascade below the isomeric state, after proper background subtraction and fit with an exponential decay curve. In the nucleus ^{138}Nd , the lifetime of 10^+ , $T_{1/2} = 370$ ns isomer is deduced from sum spectra of the 521, 729, 884, and 973 keV transitions below the isomeric state. Time spectra of the transitions deexciting the isomeric states and a representative fit are shown in Fig. 7.4. The half-life of the 10^+ isomer is 374 ± 15 ns in present work could not be more precise than previously reported result 370 ± 5 [15].

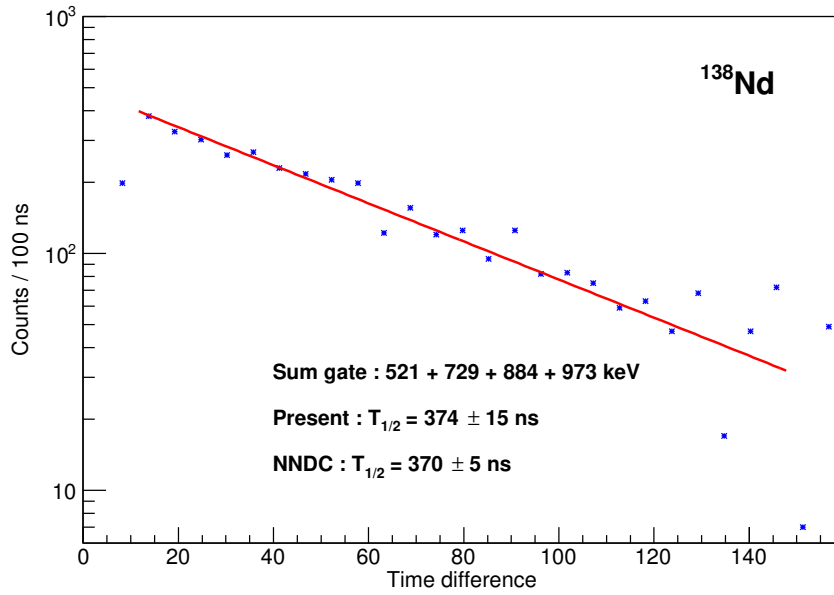


Figure 7.4: Time spectra extracted from γ -T matrix at the focal plane transitions (521, 729, 884, and 973 keV) deexciting the 10^+ isomer in ^{138}Nd . The red line is fitted to the data.

Synthèse

Introduction

Le terme chiralité a été introduit pour la première fois par Lord Kelvin en 1904 dans ses conférences à Baltimore:

« J'appelle n'importe quelle figure géométrique, ou groupe de points, chirale, et dis qu'elle a la chiralité, si son image dans un miroir plan, idéalement réalisée, ne peut être amenée à coïncider avec elle-même. »

La chiralité existe généralement dans la nature et a des conséquences importantes dans des domaines scientifiques aussi divers que la biologie, la chimie et la physique. Les exemples les plus connus d'objets géométriquement chiraux sont les mains humaines et le caractère microscopique de certaines molécules. La symétrie chirale est également bien connue en physique des particules, où elle est de nature dynamique et distingue les deux orientations possibles du spin intrinsèque par rapport à la quantité de mouvement de la particule. En physique nucléaire, la chiralité a été suggérée en 1997 par Frauendorf et Meng. Il apparaît dans un noyau triaxial qui tourne autour d'un axe situé hors des trois plans principaux de la forme nucléaire ellipsoïdale.

Des approches adiabatiques et à champ moyen relativiste triaxial contraint à configuration fixée ont été développées pour étudier la coexistence de formes triaxiales et les bandes de doublets chirales possibles en 2006, qui prédit un nouveau phénomène, à savoir l'existence de multiples doublets chiraux ($M\chi D$), c'est-à-dire plusieurs paires de doublet chiraux dans un seul noyau. Ce phénomène a été suggéré pour ^{106}Rh après avoir examiné l'existence possible d'une déformation triaxiale et de la configuration correspondante de trous de proton et de particules de neutron à j élevé. Cette étude a été étendue aux autres isotopes du rhodium et l'existence de $M\chi D$ a été suggérée dans les noyaux Rh. L'étude a prédit $M\chi D$ non seulement dans ^{106}Rh , mais également dans d'autres régions de masse, c'est-à-dire $A \approx 80$ et $A \approx 130$.

Il convient de noter que, jusqu'à présent, toutes les bandes $M\chi D$ observées ne sont que dans des noyaux impair-impair, impair-pair et pair-impair. Cela nous a inspiré à rechercher les bandes $M\chi D$ dans les noyaux pairs. C'est l'un des objectifs principaux de l'expérience présentée dans cette thèse.

D'un point de vue expérimental, les bandes de doublets doivent répondre à un ensemble de critères pour être reconnues en tant que bandes chirales, parmi lesquelles les plus importantes sont la séparation de l'énergie entre les partenaires, leurs taux de transitions électromagnétiques et les géométries de moment angulaire des bandes doublet observées, investigués en calculant les valeurs moyennes des composantes en moment angulaire du noyau, des protons de valence et des neutrons de valence, le long des axes intermédiaire, court et long.

L'essentiel du travail actuel a été entrepris dans le but de rechercher plusieurs bandes chirales dans le ^{136}Nd , un noyau qui est le voisin le plus proche du premier candidat chirale ^{134}Pr et du premier wobblé ^{135}Pr rapporté en dehors de la région $A \approx 160$. De plus, un effort important a été consacré à la spectroscopie détaillée du ^{136}Nd , car la plupart des résultats expérimentaux rapportés précédemment ont été obtenus il y a plus de vingt ans avec des matrices de détecteurs moins efficaces.

L'autre objectif du présent travail de thèse était axé sur une étude détaillée de la chiralité dans ^{135}Nd , afin de rechercher plusieurs bandes chirales similaires à celles observées dans l'isotone du ^{133}Ce . Le noyau ^{135}Nd est l'un des exemples les plus connus de vibrations chirales.

Outre l'étude des bandes chirales de ^{135}Nd et ^{136}Nd , nous avons consacré un effort important à la recherche d'isomères à longue durée de vie dans les noyaux peuplés, en particulier dans ^{135}Nd et ^{136}Nd , en utilisant la configuration JURIGAM II + RITU + GREAT et la technique de marquage par noyaux de recul.

Détails expérimentaux et traitement des données

L'expérience a été réalisée à l'Université de Jyväskylä, en Finlande, avec l'installation JUROGAM II + RITU + GREAT. Des états de spin élevé dans $^{135,136}\text{Nd}$ ont été peuplés en utilisant la réaction de fusion-évaporation ^{100}Mo (^{40}Ar , xn). Le faisceau d'ions ^{40}Ar a été produit dans une source d'ions ECR et accéléré par le cyclotron K130 jusqu'à une énergie finale de 152 MeV. L'intensité du faisceau était d'environ 14 pnA. Une semaine de temps de faisceau a été allouée à cette expérience. Nous avons utilisé comme cible une feuille autoportante enrichie de ^{100}Mo d'une épaisseur de 0.5 mg/cm². Les noyaux ^{135}Nd et ^{136}Nd étaient les plus fortement peuplés dans la réaction, avec des sections efficaces d'environ 100 mb chacune, pour une section efficace totale de la réaction calculée avec PACE4 de 480 mb.

La boule de détecteurs Germanium JUROGAM II, un spectromètre composé de 24 détecteurs trèfle et 15 détecteurs coaxiaux tronconiques placés à la position de la cible, a été utilisé pour détecter des rayons gamma prompts. Les détecteurs de trèfle ont été placés sur deux anneaux à 75.5° (12 détecteurs) et 104.5° (12 détecteurs) symétriques par rapport à 90°. Les détecteurs coniques ont également été placés sur deux anneaux à 133.6° (10 détecteurs) et 157.6° (5 détecteurs). Tous les détecteurs Ge sont équipés d'écrans anti-Compton constitués de collimateurs BGO et Hevimet placés devant les détecteurs afin d'améliorer le rapport P/T. La méthode d'addition consistant à additionner les énergies de rayons gamma coïncidentes dans des cristaux séparés dans le même détecteur de trèfle dans une fenêtre temporelle de 200 ns a été utilisée dans ce travail. Pour un rayon gamma avec une énergie de 1.33 MeV, le spectromètre complet JUROGAM avec 39 détecteurs a une efficacité de photopic totale d'environ 5% et une résolution en énergie de 3.5 keV (FWHM).

Les séparateurs de recul pour les produits de fusion induits par les ions lourds sont devenus des outils importants pour séparer les résidus d'évaporation produits par la fusion du faisceau primaire avec la cible des d'autres produits de réaction indésirables, puis pour transporter les reculs sur le plan focal en vue de mesures ultérieures (comme par exemple les propriétés de désintégration de éléments lourds, recherche d'états isomériques à longue durée de vie dans les noyaux). L'unité de transport des ions de recul (RITU) est un séparateur de recul rempli de gaz, qui est couplé au multi-détecteur JUROGAM II. Il se compose d'un total de quatre éléments focalisants qui sont dans une configuration Q₁DQ₂Q₃.

Le spectromètre GREAT (Gamma REcoil Alpha Tagging) est placé dans le plan focal du séparateur RITU. Il est conçu pour mesurer les propriétés de désintégration des produits de réaction transportés dans le plan focal du séparateur à recul. En outre, GREAT peut être utilisé en tant que dispositif autonome sensible pour les mesures de désintégration dans le plan focal ou pour fournir une étiquette efficace permettant une conversion rapide des électrons ou des rayons mesurés avec des réseaux de détecteurs déployés à la position cible. Le réseau de détecteurs GREAT est composé de plusieurs types de détecteurs: compteur proportionnel multifils (MWPC), détecteurs segmentés de silicium double face (DSSD), diodes PIN, un détecteur planaire et trois détecteurs trèfle en Germanium.

Dans cette expérience, ≈ 4000 Go de données réparties sur 2000 fichiers ont été stockées. Un total

de 5.1×10^{10} événements de coïncidence des rayons gamma avec multiplicité ≥ 3 ont été recueillis. Toutes les données ont été enregistrées par le système d'acquisition de données TDR sans déclenchement et les événements ont été horodatés en utilisant une horloge de 100 MHz avec une résolution temporelle de 10 ns. Dans mon analyse de données, j'ai effectué un étalonnage en énergie, une adaptation du gain et étalonnages d'efficacité pour les détecteurs Ge, correction de déplacement Doppler, addition de des signaux pour les détecteurs de trèfle.

Afin d'attribuer le spin et la parité pour les nouveaux niveaux identifiés, les multipolarités des rayons gamma ont été extraites à l'aide des rapports DCO (Corrélation Directionnelle à états Orientés) et des rapports de corrélation angulaire à deux points (Anisotropie) R_{ac} .

Dans ce travail, les valeurs de R_{DCO} ont été extraites de matrices gamma-gamma qui ont été formées en triant les événements de coïncidence rapides avec les détecteurs à (157.6°) par rapport à ceux à $(75.5^\circ$ et $104.5^\circ)$ correspondant à l'angle autour de 90° .

Dans la présente analyse des données, les valeurs de R_{ac} ont été extraites de matrices gamma-gamma, qui ont été formées en triant les événements de coïncidence rapides avec des combinaisons $(133.6^\circ$ et $157.6^\circ)$ versus (tous les angles) et $(75.5^\circ$ et $104.5^\circ)$ versus (tous les angles), en définissant les mêmes fenêtres d'énergie sur le spectre de projection (tous les angles) dans les deux matrices et en projetant sur l'autre axe. Ensuite, le ratio de R_{ac} a été calculé en utilisant les intensités extraites des rayons gamma d'intérêt de ces spectres, normalisées par l'efficacité différente des deux ensembles de détecteurs.

Les valeurs déduites pour R_{DCO} avec une fenêtre sur une transition quadripolaire étirée sont 1 pour un quadripôle étiré et 0.46 pour des transitions dipolaires, tandis que le rapport est proche de 1 pour un dipôle et de 2.1 pour une transition quadripolaire lorsque la fenêtre est posée sur une transition dipolaire. Les valeurs de R_{ac} pour les transitions dipolaires et quadripolaires étirées sont 0.8 et 1.4.

Résultats expérimentaux

Dans notre travail, le schéma de niveaux de ^{136}Nd a été considérablement étendu. De nombreuses nouvelles bandes ont été identifiées à la fois à bas et à haut spin, parmi lesquelles cinq bandes presque dégénérées interprétées comme des partenaires chiraux. En outre, les énergies d'excitation, les spins et les parités de plusieurs bandes connues auparavant sont révisés et fermement établis. La plupart des transitions observées ont été regroupées en bandes: la bande γ , deux bandes de parité négative à bas spins (N1, N2), neuf bandes à spin moyen (L1-L9), six bandes de transitions dipolaires (D1-D6) et cinq bandes partenaires chirales (D1-chirale, D2-chirale, D3-chirale, D4-chirale, D5-chirale), quatre bandes à spin élevé (T1-T4) et cinq bandes fortement déformées (HD1-HD5).

La bande γ , précédemment connue jusqu'au spin $I = 5^+$, est maintenant étendue à des spins plus élevés et liée par les transitions de 815 et 600 keV à une autre bande précédemment connue, construite sur l'état 10^+ à 3768 keV. La bande γ est maintenant observée jusqu'à $I = 20^+$. Pour la bande N1, nous avons récemment identifié les transitions de 1077, 410, 1079, 744 et 832 keV placées au dessus des états précédemment connus. De plus, nous avons observé deux nouvelles transitions de 381 et 612 keV de l'état 10^+ du GSB vers l'état intermédiaire 9^- , qui à leur tour se désintègrent vers les états 7^- et 8^- de la bande N1, et directement vers l'état 9^- état de la bande N1, respectivement. La bande N2 est observée pour la première fois. Nous avons beaucoup étendu les bandes L1-L9, dans lesquelles de nombreux nouveaux états ont été observés. Une caractéristique particulière du schéma de niveau de ^{136}Nd est l'existence de cinq paires de bandes presque dégénérées (D1 et D1-chirale, D2 et D2-chirale, D3 et D3-chirale, D4 et D4-chirale, D5 et D5-

chirale) et la bande dipolaire D6 sans partenaire. Nous avons récemment identifié les partenaires chiral des bandes D1-D5. Cinq bandes hautement déformés (HD) ont été observés dans le ^{136}Nd dans le présent travail. Les trois bandes HD2, HD4 et HD5 sont nouvelles. Toutes les bandes coïncident avec les transitions connues de ^{136}Nd . Cependant, aucune transition de liaison vers les états normaux déformés n'a été trouvée. Les spins, les parités et les énergies d'excitation ont été attribués sur la base des calculs du modèle CNS.

De plus, nous avons réussi à identifier une nouvelle paire de bandes chirales dans ^{135}Nd , à savoir D3 et D4, en plus de la précédente, composée des bandes D5 et D6, ce qui porte à deux le nombre doublets chirales dans ce noyau. En outre, de nombreuses nouvelles transitions ont également été observées reliant les nouvelles bandes entre elles et avec les autres niveaux. La bande D2-3qp, connue précédemment, est confirmée jusqu'au spin $39/2^+$. Trois nouveaux niveaux sont ajoutés au sommet de la bande jusqu'à spin $45/2^+$, qui, avec le niveau précédemment connu $39/2^+$, forment une nouvelle bande nommée D2-5qp. La bande D3, jusque-là connue jusqu'au niveau désexcité par la transition à 334 keV, est étendue de trois niveaux supplémentaires jusqu'au spin $33/2^+$. Un autre niveau de $33/2^+$ qui se désexcite à la fois vers le niveau $31/2^+$ de la bande D3 et vers la bande D2-3qp est également identifié. Quatorze nouvelles transitions de 377, 389, 420, 566, 589, 612, 616, 666, 679, 705, 832, 917, 1035 et 1069 keV reliant la bande D3 à la bande D2-3qp sont également identifiées. La bande D4, connue jusqu'à l'état désexcité par la transition à 423 keV, est confirmée, mais sur la base des valeurs R_{DCO} des transitions de connexion aux bandes D1 et D3, les spins sont diminués d'une unité et la parité est changé en positive. Nous avons ajouté un nouveau niveau avec spin $19/2^+$ au bas de la bande, une transition de 1237 keV vers la bande D1, quatre transitions de 596, 673, 780 et 919 keV vers la bande D3 et trois transitions de 589, 649. et 750 keV vers la bande D2-3qp. La parité de la bande D4 est identique à la parité positive assignée de la bande D3, car les trois transitions de connexion de 589, 649 et 780 keV entre les bandes 3 et 2 ont un caractère E2 bien établi. Nous confirmons tous les niveaux précédemment rapportés des bandes D5 et D6. Trois nouveaux niveaux avec les spins $21/2^-$, $45/2^-$ et $(47/2^-)$ sont identifiés en bas et en haut de la bande D5, reliés par les nouvelles transitions 130, 560, 565, 1054 et 1125 keV. Les deux transitions provisoires de 557 keV et 963 keV rapportées précédemment sont confirmées, mais nos données montrent que l'énergie de la transition à 557 keV est plutôt de 559 keV. Trois nouvelles transitions reliant les bandes D6 à D5 avec des énergies de 609, 997 et 1071 keV sont récemment identifiées. Trois transitions de 463, 584 et 1299 keV des bandes D5 et D6 à la bande D1 ont également été identifiées.

Conclusion et perspectives

La présente thèse présente l'étude spectroscopique des noyaux triaxiaux $^{135,136}\text{Nd}$, avec un accent particulier sur le phénomène des doublets chiraux multiples ($M\chi D$). Un effort important a également été consacré à la recherche d'isomères à longue durée de vie possibles dans les ^{135}Nd et ^{136}Nd , en utilisant la configuration JUROGAM II + RITU + GREAT et la technique de marquage par décroissance de recul.

Dans ^{136}Nd , la caractéristique la plus importante du schéma de niveau est l'observation des cinq paires de bandes rotationnelles presque dégénérées, qui ont des propriétés en accord avec un caractère chiral. Les bandes observées ont été étudiées par la théorie fonctionnelle de densité covariante avec rotation contrainte autour d'un axe incliné (TAC-CDFT). Les configurations possibles ont été explorées. Les spectres d'énergie expérimentaux, les moments cinétiques et les valeurs $B(M1)/B(E2)$ des configurations attribuées sont globalement bien reproduits par les calculs TAC-CDFT. Les résultats théoriques soutiennent l'interprétation chirale des bandes observées, qui correspondent à des formes avec une triaxialité presque maximale induite par différentes configurations multi-quasi-particules dans ^{136}Nd . Plus tard, inspiré par nos résultats expérimentaux,

Qibo Chen *et al.* ont mis au point un modèle particule-rotor (PRM) couplant les nucléons de quatre couches j à un rotor triaxial. Il a été constaté que les propriétés de ces bandes doublet sont en bon accord avec les résultats des calculs de PRM. Par conséquent, le phénomène $M\chi D$ dans le noyau ^{136}Nd a été confirmé. A noter que c'est pour la première fois que des bandes $M\chi D$ sont observées dans un noyau à des spins élevés. De plus, les cinq paires de bandes chirales observées dans ^{136}Nd est le plus grand nombre de bandes chirales observées dans un seul noyau jusqu'à présent. Tout récemment, un nouveau travail théorique inspiré par nos résultats a également été consacré à l'étude des cinq bandes chirales de ^{136}Nd , dans lequel le modèle en couche projeté triaxial incluant des configurations avec plus de quatre quasi-particules dans l'espace de configuration a été développé.

En outre, le schéma de niveau de ^{136}Nd a été considérablement étendu à des spins bas, moyens et très élevés. Beaucoup de nouveaux états et de nouvelles bandes ont été identifiés dans ce noyau. Les énergies d'excitation, les spins et les parités des bandes précédemment connues ont été révisés et fermement établis. Des configurations ont été attribuées aux bandes observées sur la base de calculs Nilsson-Strutinsky en rotation contrainte. La structure de bande de ^{136}Nd a été clarifiée et les différents types d'excitations uni-particule et collectives ont été bien compris.

Dans ^{135}Nd , une nouvelle paire de bandes chirales à parité positive a été identifiée qui, avec les bandes chirales à parité négative précédemment rapportées, constitue un troisième cas de bandes $M\chi D$ dans la région de masse $A \approx 130$. Ces bandes chirales comprennent des transitions dipolaires et sont caractérisées par la même parité, des énergies d'excitation des niveaux très proches et une variation régulière du paramètre $S(I)$. Les caractéristiques des bandes doublet soutiennent l'interprétation chirale. De plus, les bandes doublet observées ont été comparées à la théorie fonctionnelle de densité covariante sous contrainte (CDFT) et aux calculs PRM reproduisant fidèlement les données expérimentales, confirmant le phénomène $M\chi D$ dans ce noyau. Les bandes $M\chi D$ nouvellement observées dans ^{135}Nd représentent une forte support de l'existence de $M\chi D$ dans les noyaux.

La recherche d'états isomériques à longue durée de vie dans ^{135}Nd et ^{136}Nd n'a pas conduit à l'identification de nouveaux isomères, mais nous avons pu confirmer les isomères rapportés dans les noyaux ^{138}Nd , ^{134}Ce , ^{136}Pr et ^{137}Pr dans nos données.

Selon ces résultats, l'existence du phénomène $M\chi D$ dans les noyaux de la région de masse $A \approx 130$ est fortement confirmée. Les présents résultats nous incitent à poursuivre l'étude de la chiralité dans les noyaux, à la fois expérimentalement (mesure de la durée de vie et la recherche de doublets chiraux dans d'autres noyaux) et théoriquement.

Conclusions and Outlook

The present thesis presents the spectroscopic study of the triaxial nuclei $^{135,136}\text{Nd}$, with particular emphasise on the multiple chiral doublets ($\text{M}\chi\text{D}$) phenomenon. An important effort was also devoted to search for possible long-lived isomers in ^{135}Nd and ^{136}Nd , using the RITU+GREAT setup and the recoil decay tagging technique.

The high-spin states in the nuclei $^{135,136}\text{Nd}$ were populated using the fusion-evaporation reaction $^{100}\text{Mo}(^{40}\text{Ar}, xn)$ at a beam energy of 152 MeV, provided by the K130 Cyclotron at the University of Jyväskylä, Finland. The high efficiency JUROGAM II array was used to detect prompt γ rays, resulting in a high statistics data set which allowed us to extend the level scheme of $^{135,136}\text{Nd}$ significantly. The RITU spectrometer and its focal plane array GREAT were used to measure delayed events, allowing us to search for long-lived isomers in the populated nuclei.

In ^{136}Nd , the most important feature of the level scheme is the observation of the five pairs of nearly degenerate rotational bands, which have properties in agreement with a chiral character. The observed bands were investigated by the constrained and tilted axis cranking covariant density functional theory (TAC-CDFT). Possible configurations have been explored. The experimental energy spectra, angular momenta, and $B(M1)/B(E2)$ values for the assigned configurations are globally well reproduced by the TAC-CDFT calculations. The theoretical results support the chiral interpretation of the observed bands, which correspond to shapes with nearly maximum triaxiality induced by different multiquasiparticle configurations in ^{136}Nd . Later, inspired by our experimental results, a particle-rotor model (PRM), which couples nucleons in four single- j shells to a triaxial rotor core was developed by QiBo Chen *et al* [55], to investigate the five pairs of nearly degenerate doublet bands of ^{136}Nd . It was found that the properties of these doublet bands are in good agreement with results of the PRM calculations. Therefore, the $\text{M}\chi\text{D}$ phenomenon in the nucleus ^{136}Nd was further confirmed. Note that it was the first time that $\text{M}\chi\text{D}$ bands were observed in an even-even nucleus at high spins, and also five pairs of chiral doublet bands is the largest observed in a single nucleus until now. Very recently, a new theoretical work was also devoted to the study of the five chiral doublet bands of ^{136}Nd [137], in which the triaxial projected shell model including configurations with more than four quasiparticles in the

configuration space was developed.

In addition, the level scheme of the ^{136}Nd has been extended considerably at low, medium, and very high spins. Many new states and new bands have been identified in this nucleus. Excitation energies, spins, and parities of the previously known bands have been revised and firmly established. Configurations have been assigned to the observed bands based on cranked Nilsson-Strutinsky calculations. The band structure of ^{136}Nd was clarified and the various types of single-particle and collective excitations were well understood.

In ^{135}Nd , one new pair of positive-parity chiral doublet bands have been identified which together with the previously reported negative-parity chiral doublet bands constitute a third case of $M\chi D$ bands in the $A \approx 130$ mass region. The characteristics of the doublet bands support the chiral interpretation. Furthermore, the observed doublet bands were compared with constrained covariant density functional theory (CDFT) and PRM calculations which nicely reproduce the experimental data, confirming the $M\chi D$ phenomenon in this nucleus. The newly observed $M\chi D$ bands in ^{135}Nd represents an important milestone in supporting the existence of $M\chi D$ in nuclei.

The search for long-lived isomeric states in ^{135}Nd and ^{136}Nd did not lead to the identification of new isomers, but we could confirm the reported isomers in the nuclei ^{138}Nd , ^{134}Ce , ^{136}Pr , and ^{137}Pr in our data.

According to these results, the existence of the $M\chi D$ phenomenon in nuclei of the $A \approx 130$ mass region is strongly supported. The present results encourage us to continue the study of chirality in nuclei, both experimentally (measurement of lifetimes and search for chiral doublets in other nuclei) and theoretically.

Appendix A

JUROGAM II detector angles

Table A.1 – The information of JUROGAM II detector angles.

Detector ID ^a	θ^b	ϕ^c
T01	157.6	0
T02	157.6	72
T03	157.6	144
T04	157.6	216
T05	157.6	288
T06	133.6	18
T07	133.6	54
T08	133.6	90
T09	133.6	126
T10	133.6	162
T11	133.6	198
T12	133.6	234
T13	133.6	270
T14	133.6	306
T15	133.6	342
Q01	104.5	15
Q02	104.5	45
Q03	104.5	75
Q04	104.5	105
Q05	104.5	135
Q06	104.5	165
Q07	104.5	195
Q08	104.5	225
Q09	104.5	255
Q10	104.5	285
Q11	104.5	315
Q12	104.5	345

Table A.1 – <i>Continued</i>		
Detector ID ^a	θ^b	ϕ^c
Q13	75.5	15
Q14	75.5	45
Q15	75.5	75
Q16	75.5	105
Q14	75.5	135
Q18	75.5	165
Q19	75.5	195
Q20	75.5	225
Q21	75.5	255
Q22	75.5	285
Q23	75.5	315
Q24	75.5	345

^a T is tapered detector, Q is Clover detector.

^b The θ is defined with respect to the beam direction.

^c $\phi = 0^\circ$ is defined as vertically upwards, increases in a clockwise direction when the array is viewed from a position upstream.

Bibliography

- [1] Jie Meng and SQ Zhang. Open problems in understanding the nuclear chirality. *Journal of Physics G: Nuclear and Particle Physics*, 37(6):064025, 2010.
- [2] B.W. Xiong and Y.Y. Wang. Nuclear chiral doublet bands data tables. *Atomic Data and Nuclear Data Tables*, 125:193 – 225, 2019.
- [3] Peter Ring and Peter Schuck. *The nuclear many-body problem*. Springer Science & Business Media, 2004.
- [4] Anwar Kamal. *Nuclear physics*. Springer, 2014.
- [5] Walter Greiner and Joachim A Maruhn. *Nuclear models*. Springer, 1996.
- [6] Lee James Angus. *Spectroscopy of Exotic Proton-Rich Nuclei Close to $A = 120$* . PhD thesis, University of the West of Scotland, 2012.
- [7] Stefan Frauendorf. Spontaneous symmetry breaking in rotating nuclei. *Reviews of Modern Physics*, 73:463, 2001.
- [8] M. Leino *et al.* Gas-filled recoil separator for studies of heavy elements. *Nucl. Instrum. Meth. Phys. Res. A*, 99(1):653–656, 1995.
- [9] M. Sandzelius. *PhD thesis, 2009*.
- [10] P. Möller, R. Bengtsson, B.G. Carlsson, P. Olivius, and T. Ichikawa. Global calculations of ground-state axial shape asymmetry of nuclei. *Phys. Rev. Lett.*, 97:162502, 2006.
- [11] C. M. Petrache, I. Ragnarsson, Hai-Liang Ma, R. Leguillon, T. Zerrouki, D. Bazzacco, and S. Lunardi. Multiple triaxial bands in ^{138}Nd . *Phys. Rev. C*, 91:024302, 2015.
- [12] C. M. Petrache *et al.* Triaxiality and exotic rotations at high spins in ^{134}Ce . *Phys. Rev. C*, 93:064305, 2016.
- [13] C. M. Petrache *et al.* Search for the terminating 27^- state in ^{140}Nd . *Phys. Rev. C*, 92:034314, 2015.
- [14] A. Neusser *et al.* Superdeformed band at very high spin in ^{140}Nd . *Phys. Rev. C*, 70:064315, 2004.
- [15] ENSDF database, NNDC Online Data Service, <http://www.nndc.bnl.gov/ensdf/>.
- [16] A Bohr and Ben R Mottelson. *Nuclear structure*, Vol. II, 1998.

- [17] J. T. Matta *et al.* Transverse wobbling in ^{135}Pr . *Phys. Rev. Lett.*, 114:082501, 2015.
- [18] William Thomson Baron Kelvin. *Baltimore lectures on molecular dynamics and the wave theory of light*. C J Clay and Sons, 1904.
- [19] Meng Jie. *Relativistic density functional for nuclear structure*. World Scientific, 2016.
- [20] S. Frauendorf and Jie Meng. Tilted rotation of triaxial nuclei. *Nuclear Physics A*, 617(2):131–147, 1997.
- [21] K. Starosta and T. Koike, *et al.* Chiral doublet structures in odd-odd $N = 75$ isotones: Chiral vibrations. *Phys. Rev. Lett.*, 86:971–974, 2001.
- [22] C. Vaman, D. B. Fossan, T. Koike, K. Starosta, I. Y. Lee, and A. O. Macchiavelli. Chiral degeneracy in triaxial ^{104}Rh . *Phys. Rev. Lett.*, 92:032501, 2004.
- [23] J. Meng, J. Peng, S. Q. Zhang, and S.-G. Zhou. Possible existence of multiple chiral doublets in ^{106}Rh . *Phys. Rev. C*, 73:037303, 2006.
- [24] J. Peng, H. Sagawa, S. Q. Zhang, J. M. Yao, Y. Zhang, and J. Meng. Search for multiple chiral doublets in rhodium isotopes. *Phys. Rev. C*, 77:024309, 2008.
- [25] A. D. Ayangeakaa *et al.* Evidence for multiple chiral doublet bands in ^{133}Ce . *Phys. Rev. Lett.*, 110:172504, 2013.
- [26] I. Kuti, Q. B. Chen, and J. Timár, *et al.* Multiple chiral doublet bands of identical configuration in ^{103}Rh . *Phys. Rev. Lett.*, 113:032501, 2014.
- [27] C. Liu *et al.* Evidence for octupole correlations in multiple chiral doublet bands. *Phys. Rev. Lett.*, 116:112501, 2016.
- [28] AA Raduta. Specific features and symmetries for magnetic and chiral bands in nuclei. *Progress in Particle and Nuclear Physics*, 90:241–298, 2016.
- [29] T. Koike, K. Starosta, and I. Hamamoto. Chiral bands, dynamical spontaneous symmetry breaking, and the selection rule for electromagnetic transitions in the chiral geometry. *Phys. Rev. Lett.*, 93:172502, 2004.
- [30] B. Qi, S. Q. Zhang, S. Y. Wang, J. M. Yao, and J. Meng. Examining $B(M1)$ staggering as a fingerprint for chiral doublet bands. *Phys. Rev. C*, 79:041302, 2009.
- [31] E. Grodner *et al.* ^{128}Cs as the best example revealing chiral symmetry breaking. *Phys. Rev. Lett.*, 97:172501, 2006.
- [32] S. Mukhopadhyay *et al.* From chiral vibration to static chirality in ^{135}Nd . *Phys. Rev. Lett.*, 99:172501, 2007.
- [33] S. Zhu *et al.* A composite chiral pair of rotational bands in the odd-A nucleus ^{135}Nd . *Phys. Rev. Lett.*, 91:132501, 2003.

- [34] P. Joshi *et al.* Stability of chiral geometry in the odd–odd rh isotopes: spectroscopy of ^{106}Rh . *Physics Letters B*, 595(1-4):135–142, 2004.
- [35] J. A. Alcántara-Núñez, J. R. B. Oliveira, E. W. Cybulska, N. H. Medina, M. N. Rao, R. V. Ribas, M. A. Rizzutto, W. A. Seale, F. Falla-Sotelo, K. T. Wiedemann, V. I. Dimitrov, and S. Frauendorf. Magnetic dipole and electric quadrupole rotational structures and chirality in ^{105}Rh . *Phys. Rev. C*, 69:024317, 2004.
- [36] J. Timar *et al.* Experimental evidence for chirality in the odd–A nucleus ^{105}Rh . *Physics Letters B*, 598(3-4):178–187, 2004.
- [37] E. Grodner *et al.* Partner bands of ^{126}Cs - first observation of chiral electromagnetic selection rules. *Physics Letters B*, 703(1):46–50, 2011.
- [38] S.Y Wang *et al.* The first candidate for chiral nuclei in the $A \approx 80$ mass region: ^{80}Br . *Physics Letters B*, 703(1):40–45, 2011.
- [39] D. Tonev *et al.* Candidates for twin chiral bands in ^{102}Rh . *Phys. Rev. Lett.*, 112:052501, 2014.
- [40] George Gamow. Mass defect curve and nuclear constitution. *Proc. R. Soc. Lond. A*, 126(803):632–644, 1930.
- [41] CF V Weizsäcker. Zur theorie der kernmassen. *Zeitschrift für Physik*, 96(7-8):431–458, 1935.
- [42] Hans Albrecht Bethe and Robert Fox Bacher. Nuclear physics a. stationary states of nuclei. *Reviews of Modern Physics*, 8(2):82, 1936.
- [43] Ingemar Ragnarsson and Sven Gvsta Nilsson. *Shapes and shells in nuclear structure*. Cambridge University press, 2005.
- [44] Maria Goeppert Mayer. On closed shells in nuclei. II. *Physical Review*, 75(12):1969, 1949.
- [45] Otto Haxel, J. Hans D. Jensen, and Hans E. Suess. On the "magic numbers" in nuclear structure. *Phys. Rev.*, 75:1766–1766, 1949.
- [46] Roger D Woods. Diffuse surface optical model for nucleon-nuclei scattering. *Phys. Rev.*, 95:577, 1954.
- [47] Sven Gösta Nilsson. Binding states of individual nucleons in strongly deformed nuclei. *Dan. Mat. Fys. Medd.*, 29(CERN-55-30):1–69, 1955.
- [48] David Lawrence Hill and John Archibald Wheeler. Nuclear constitution and the interpretation of fission phenomena. *Phys. Rev.*, 89:1102–1145, Mar 1953.
- [49] G. Andersson *et al.* Nuclear shell structure at very high angular momentum. *Nuclear Physics A*, 268(2):205–256, 1976.
- [50] Aage Niels Bohr and Benjamin Roy Mottelson. Collective and individual-particle aspects of nuclear structure. *Dan. mat. fys. Medd.*, 27(CERN-57-38):1–174, 1953.

- [51] B. Qi, S. Q. Zhang, J. Meng, S. Y. Wang, and S. Frauendorf. *Phys. Lett. B*, 675:175, 2009.
- [52] B. Qi, S. Q. Zhang, S. Y. Wang, J. Meng, and T. Koike. Chirality in odd- a rh isotopes within the triaxial particle rotor model. *Phys. Rev. C*, 83:034303, 2011.
- [53] E. O. Lieder *et al.* Resolution of chiral conundrum in ^{106}Ag : Doppler-shift lifetime investigation. *Phys. Rev. Lett.*, 112:202502, 2014.
- [54] B. Qi, H. Jia, N. B. Zhang, C. Liu, and S. Y. Wang. Possible multiple chiral doublet bands in ^{107}Ag . *Phys. Rev. C*, 88:027302, 2013.
- [55] Q. B. Chen, B. F. Lv, C. M. Petrache, and J. Meng. *Phys. Lett. B*, 782:744, 2018.
- [56] Wang Shou-Yu, Qi Bin, and Zhang Shuang-Quan. Coupling parameter in the single- j shell model. *Chinese Physics Letters*, 26(5):052102, 2009.
- [57] S. Q. Zhang, B. Qi, S. Y. Wang, and J. Meng. Chiral bands for a quasi-proton and quasi-neutron coupled with a triaxial rotor. *Phys. Rev. C*, 75:044307, 2007.
- [58] J.Y. Zeng and T.S. Cheng. Particle-number-conserving method for treating the nuclear pairing correlation. *Nuclear Physics A*, 405(1):1 – 28, 1983.
- [59] Z. Shi, Z. H. Zhang, Q. B. Chen, S. Q. Zhang, and J. Meng. Shell-model-like approach based on cranking covariant density functional theory: Band crossing and shape evolution in ^{60}Fe . *Phys. Rev. C*, 97:034317, 2018.
- [60] A.V. Afanasjev, D.B. Fossan, G.J. Lane, and I. Ragnarsson. Termination of rotational bands: disappearance of quantum many-body collectivity. *Physics Reports*, 322(1):1 – 124, 1999.
- [61] Tord Bengtsson and Ingemar Ragnarsson. Rotational bands and particle-hole excitations at very high spin. *Nucl. Phys. A*, 436(1):14 – 82, 1985.
- [62] B. G. Carlsson and I. Ragnarsson. Calculating the nuclear mass in the very high angular momentum regime. *Phys. Rev. C*, 74:011302, 2006.
- [63] A.V. Afanasjev and I. Ragnarsson. Gradual loss of collectivity in rotational bands in the $A \sim 110$ ($Z \geq 50, N \sim 60$) mass region. *Nuclear Physics A*, 591(3):387 – 420, 1995.
- [64] D. R. Inglis. Particle derivation of nuclear rotation properties associated with a surface wave. *Phys. Rev.*, 96:1059–1065, 1954.
- [65] D. R. Inglis. Nuclear moments of inertia due to nucleon motion in a rotating well. *Phys. Rev.*, 103:1786–1795, 1956.
- [66] S E Larsson. The nuclear potential-energy surface with inclusion of axial asymmetry. *Physica Scripta*, 8(1-2):17, 1973.

- [67] V. M. Strutinsky. Shell effects in nuclear masses and deformation energies. *Nuclear Physics A*, 95(2):420–442, 1967.
- [68] A.O. Macchiavelli, R.M. Clark, M.A. Deleplanque, R.M. Diamond, P. Fallon, I.Y. Lee, F.S. Stephens, and K. Vetter. The competition between the shears mechanism and core rotation in a classical particles-plus-rotor model. *Physics Letters B*, 450(1):1–6, 1999.
- [69] S. Frauendorf. Tilted cranking. *Nuclear Physics A*, 557:259 – 276, 1993.
- [70] S. Frauendorf. Description of multi-quasiparticle bands by the tilted axis cranking model. *Nuclear Physics A*, 677(1):115 – 170, 2000.
- [71] Jie Meng, Jing Peng, Shuang-Quan Zhang, and Peng-Wei Zhao. Progress on tilted axis cranking covariant density functional theory for nuclear magnetic and antimagnetic rotation. *Frontiers of Physics*, 8(1):55–79, 2013.
- [72] Dario Vretenar, AV Afanasjev, GA Lalazissis, and P Ring. Relativistic hartree–bogoliubov theory: static and dynamic aspects of exotic nuclear structure. *Physics reports*, 409(3-4):101–259, 2005.
- [73] Jie Meng, H Toki, Shan-Gui Zhou, SQ Zhang, WH Long, and LS Geng. Relativistic continuum hartree bogoliubov theory for ground-state properties of exotic nuclei. *Progress in Particle and Nuclear Physics*, 57(2):470–563, 2006.
- [74] A Sulaksono, T Bürvenich, JA Maruhn, P-G Reinhard, and W Greiner. The nonrelativistic limit of the relativistic point coupling model. *Annals of Physics*, 308(1):354–370, 2003.
- [75] Peng-Wei Zhao, Shuang-Quan Zhang, Jing Peng, HZ Liang, P Ring, and J Meng. Novel structure for magnetic rotation bands in ^{60}Ni . *Physics Letters B*, 699(3):181–186, 2011.
- [76] D Serot, Brian *et al.* The relativistic nuclear many body problem. *Adv. Nucl. Phys.*, 16:1, 1986.
- [77] Brian D Serot and John Dirk Walecka. Recent progress in quantum hadrodynamics. *International Journal of Modern Physics E*, 6(04):515–631, 1997.
- [78] P. W. Zhao, Z. P. Li, J. M. Yao, and J. Meng. New parametrization for the nuclear covariant energy density functional with a point-coupling interaction. *Phys. Rev. C*, 82:054319, 2010.
- [79] F Dönaau and S Frauendorf. Proceedings of the conference on high angular momentum properties of nuclei, oak ridge, 1982. 1983.
- [80] F Dönaau. Electromagnetic radiation of rotating nuclei. *Nuclear Physics A*, 471(3-4):469–488, 1987.
- [81] J Eberth and J Simpson. From ge (li) detectors to gamma-ray tracking arrays–50 years of gamma spectroscopy with germanium detectors. *Progress in Particle and Nuclear Physics*, 60(2):283–337, 2008.

- [82] S Akkoyun, Alejandro Algora, B Alikhani, F Ameil, G De Angelis, L Arnold, A Astier, Ayse Ata, Y Aubert, C Aufranc, et al. Agata-advanced gamma tracking array. *Nuclear Instruments and Methods in Physics Research Section A: Accelerators, Spectrometers, Detectors and Associated Equipment*, 668:26–58, 2012.
- [83] P. J. Nolan, F. A. Beck, and D. B. Fossan. Large arrays of escape-suppressed gamma-ray detectors. *Annu. Rev. Nucl. Part. Sci.*, 99(1):561–607, 1994.
- [84] J Sarén, J Uusitalo, M Leino, and J Sorri. Absolute transmission and separation properties of the gas-filled recoil separator ritu. *Nuclear Instruments and Methods in Physics Research Section A: Accelerators, Spectrometers, Detectors and Associated Equipment*, 654(1):508–521, 2011.
- [85] Matti Leino. In-flight separation with gas-filled systems. *Nuclear Instruments and Methods in Physics Research Section B: Beam Interactions with Materials and Atoms*, 126(1-4):320–328, 1997.
- [86] A. Ghiorso, S. Yashita, M.E. Leino, L. Frank, J. Kalnins, P. Armbruster, J.-P. Dufour, and P.K. Lemmertz. Sassy, a gas-filled magnetic separator for the study of fusion reaction products. *Nuclear Instruments and Methods in Physics Research Section A: Accelerators, Spectrometers, Detectors and Associated Equipment*, 269(1):192 – 201, 1988.
- [87] Yu Ts Oganessian, Yu V Lobanov, AG Popeko, F Sh Abdullin, Yu P Kharitonov, AA Ledovskoy, and Yu S Tsyganov. *Zeitschrift für Physik D Atoms, Molecules and Clusters*, 21(1):S357–S358, 1991.
- [88] R. D. Page *et al.* The GREAT spectrometer. *Nucl. Instrum. Meth. Phys. Res. A*, 204(1):634–637, 2003.
- [89] I. Lazarus *et al.* The GREAT triggerless total data readout method. *IEEE Transactions on Nuclear Science*, 48(3):567–569, 2001.
- [90] P. Rahkila. Grain-a java data analysis system for total data readout. *Nuclear Instruments and Methods in Physics Research Section A: Accelerators, Spectrometers, Detectors and Associated Equipment*, 595(3):637 – 642, 2008.
- [91] D.C Radford. {ESCL8R} and levit8r: Software for interactive graphical analysis of {HPGe} coincidence data sets. *Nucl. Instrum. Meth. Phys. Res. A*, 361(1–2):297 – 305, 1995.
- [92] D.C Radford. Background subtraction from in-beam {HPGe} coincidence data sets. *Nucl. Instrum. Meth. Phys. Res. A*, 361(1–2):306 – 316, 1995.
- [93] G Duchêne, FA Beck, PJ Twin, G De France, D Curien, L Han, CW Beausang, MA Bentley, PJ Nolan, and J Simpson. The Clover: a new generation of composite ge detectors. *Nuclear Instruments and Methods in Physics Research Section A: Accelerators, Spectrometers, Detectors and Associated Equipment*, 432(1):90–110, 1999.

- [94] A. Krämer-Flecken, T. Morek, R. M. Lieder, W. Gast, G. Hebbinghaus, H. M. Jäger, and W. Urban. Use of dco ratios for spin determination in γ - γ coincidence measurements. *Nucl. Instrum. Meth. Phys. Res. A*, 275(2):333 – 339, 1989.
- [95] C. J. Chiara *et al.* Probing *sd*-*fp* cross-shell interactions via terminating configurations in $^{42,43}\text{Sc}$. *Phys. Rev. C*, 75:054305, 2007.
- [96] K. Starosta *et al.* Experimental test of the polarization direction correlation method (PDCO). *Nuclear Instruments and Methods in Physics Research Section A: Accelerators, Spectrometers, Detectors and Associated Equipment*, 423(1):16 – 26, 1999.
- [97] D. Habs, H. Klewe-Nebenius, R. Löhken, S. Göring, J. van Klinken, H. Rebel, and G. Schatz. Quasirootational groundstate bands of even-even nuclei with $50 < N, Z < 82$. *Z. Physik*, 250:179–190, 1972.
- [98] M. M. Aléonard, Y. El Masri, I. Y. Lee, F. S. Stephens, M. A. Deleplanque, and R. M. Diamond. Experimental study of ^{136}Nd at high angular momentum. *Nucl. Phys. A*, 350:190–204, 1980.
- [99] V. Barci *et al.* Effective moment of inertia in ^{132}Ce , ^{134}Nd and ^{136}Nd . *Zeit. Phys. A*, 325:399–404, 1986.
- [100] E. S. Paul, C. W. Beausang, D. B. Fossan, R. Ma, W. F. Piel, Jr., P. K. Weng, and N. Xu. Band crossing in the gamma-soft nucleus ^{136}Nd . *Phys. Rev. C*, 36:153, Feb 1987.
- [101] J. Billowes, K. P. Lieb, J. W. Noe, W. F. Piel, Jr., S. L. Royston, G. D. Spouse, O. C. Kistner, and F. Christancho. Lifetime and g-factor measurements of yrast states in ^{134}Nd and ^{136}Nd . *Phys. Rev. C*, 36:974, 1987.
- [102] E. M. Beck, R. J. McDonald, and A. O. Superdeformed bands in Nd nuclei. *Phys. Lett. B*, 195:531, 1987.
- [103] R. M. Clark *et al.* A pair of identical superdeformed bands in ^{136}Nd . *Phys. Lett. B*, 343:59–63, 1995.
- [104] C. M. Petrache *et al.* Competing mechanism for generating high spin excitations in gamma-soft nuclei: the ^{136}Nd case. *Phys. Lett. B*, 373:275, 1996.
- [105] C. M. Petrache *et al.* Multiple dipole bands at prolate shapes in ^{136}Nd and their description through the projected shell model. *Phys. Rev. C*, 53:R2581–R2585, 1996.
- [106] E. Mergel *et al.* Candidates for chiral doublet bands in ^{136}Nd . *Eur. Phys. J. A*, 15:417, 2002.
- [107] T.R. Saito *et al.* Yrast and non-yrast $2+$ states of ^{134}Ce and ^{136}Nd populated in relativistic coulomb excitation. *Phys. Lett. B*, 669:19, 2008.

- [108] S. Perries *et al.* Decay-out of the yrast superdeformed band in ^{136}Nd : Towards an experimental extraction of the neutron pairing gap at large deformation. *Phys. Rev. C*, 60:064313, 1999.
- [109] G. L. Long. Collective backbending effect in the interacting boson model. *Phys. Rev. C*, 55:3163, 1997.
- [110] D. Vretenar, S. Brant, G. Bonsignori, L. Corradini, and C. M. Petrache. Interacting boson model plus broken-pair description of high-spin dipole bands. *Phys. Rev. C*, 57:675, 1998.
- [111] K. Tanabe and K. Sugawara-Tanabe. Microscopic properties of the superdeformed rotational states in light rare-earth nuclei ^{132}Ce and $^{134,136}\text{Nd}$. *Phys. Lett. B*, 259:12–18, 1991.
- [112] L. Próchniak, K. Zajac, K. Pomorski, S. G. Rohoziński, and J. Srebrny. Collective quadrupole excitations in the $50 < Z, N < 82$ nuclei with the general bohr hamiltonian. *Nucl. Phys. A*, 648:181–202, 1999.
- [113] J. A. Sheikh, G. H. Bhat, R. Palit, Z. Naik, and Y. Sun. Multi-quasiparticle γ -band structure in neutron-deficient Ce and Nd isotopes. *Nucl. Phys. A*, 824:58–69, 2009.
- [114] C. M. Petrache *et al.* Evidence of chiral bands in even-even nuclei. *Phys. Rev. C*, 97:041304, 2018.
- [115] B. F. Lv *et al.* Evolution from γ -soft to stable triaxiality in ^{136}Nd as a prerequisite of chirality. *Phys. Rev. C*, 98:044304, Oct 2018.
- [116] P.W. Zhao. Multiple chirality in nuclear rotation: A microscopic view. *Phys. Lett. B*, 773(Supplement C):1 – 5, 2017.
- [117] J. Peng, J. Meng, P. Ring, and S. Q. Zhang. Covariant density functional theory for magnetic rotation. *Phys. Rev. C*, 78:024313, 2008.
- [118] P.W. Zhao, S.Q. Zhang, J. Peng, H.Z. Liang, P. Ring, and J. Meng. Novel structure for magnetic rotation bands in ^{60}Ni . *Physics Letters B*, 699(3):181 – 186, 2011.
- [119] Jie Meng, Jing Peng, Shuang-Quan Zhang, and Peng-Wei Zhao. Progress on tilted axis cranking covariant density functional theory for nuclear magnetic and antimagnetic rotation. *Frontiers of Physics*, 8(1):55–79, 2013.
- [120] Jie Meng, Jing Peng, Shuang Quan Zhang, and Peng Wei Zhao. Progress on tilted axis cranking covariant density functional theory for nuclear magnetic and antimagnetic rotation. *Front. Phys.*, 8:55–79, 2013.
- [121] P. W. Zhao, Z. P. Li, J. M. Yao, and J. Meng. New parametrization for the nuclear covariant energy density functional with a point-coupling interaction. *Phys. Rev. C*, 82:054319, 2010.
- [122] J. Meng, J. Peng, S. Q. Zhang, and S.-G. Zhou. Possible existence of multiple chiral doublets in ^{106}Rh . *Phys. Rev. C*, 73:037303, 2006.

- [123] C. Vaman, D. B. Fossan, T. Koike, K. Starosta, I. Y. Lee, and A. O. Machiavelli. Chiral degeneracy in triaxial 104rh. *Phys. Rev. Lett.*, 92:032501, 2004.
- [124] C. M. Petrache *et al.* Collective rotation of an oblate nucleus at very high spin. *Phys. Rev. C*, 99:041301, 2019.
- [125] C. M. Petrache *et al.* Stable triaxiality at the highest spins in ^{138}Nd and ^{139}Nd . *Phys. Rev. C*, 61:011305(R), 1999.
- [126] C. M. Petrache *et al.* Smooth crossings between the $N = 4$ and $N = 6$ orbits and adiabatic configuration changes at high angular momentum in ^{134}Nd . *Phys. Lett. B*, 387:31–36, 1996.
- [127] T. Klemme *et al.* Lifetimes measurements for ^{134}Nd and neighboring nuclei with the coincidence-plunger technique. *Phys. Rev. C*, 60:034301, 1999.
- [128] S. Zhu. *PhD thesis*, 2004.
- [129] P. W. Zhao, S. Q. Zhang, and J. Meng. Impact of pairing correlations on the orientation of the nuclear spin. *Phys. Rev. C*, 92:034319, 2015.
- [130] S. Brant and C. M. Petrache. Chiral bands in ^{135}Nd : The interacting boson-fermion model approach. *Phys. Rev. C*, 79:054326, 2009.
- [131] W. F. Piel, C. W. Beausang, D. B. Fossan, L. Hildingsson, and E. S. Paul. *Phys. Rev. C*, 35:959, 1987.
- [132] E. M. Beck *et al.* Superdeformed band in ^{135}Nd . *Phys. Rev. Lett.*, 58:2182–2185, 1987.
- [133] T. Klemme *et al.* *Phys. Rev. C*, 60:034301, 1999.
- [134] K.H. Schmidt *et al.* Gamma-spectroscopic investigations in the radiative fusion reaction $^{90}\text{Zr} + ^{90}\text{Zr}$. *Physics Letters B*, 168(1):39 – 42, 1986.
- [135] R.S. Simon *et al.* Evidence for nuclear shape coexistence in ^{180}Hg . *Zeitschrift für Physik A Atomic Nuclei*, 325(2):197–202, 1986.
- [136] E. S. Paul *et al.* In-beam γ -ray spectroscopy above ^{100}Sn using the new technique of recoil decay tagging. *Phys. Rev. C*, 51:78–87, 1995.
- [137] Y. K. Wang, *et al.* Multichiral facets in symmetry restored states: Five chiral doublet candidates in the even-even nucleus ^{136}Nd . *Phys. Rev. C*, 99:054303, 2019.

Titre : Chiralité dans les noyaux ^{136}Nd et ^{135}Nd

Mots clés : Spectroscopie nucléaire, états de hauts spins, isomères, triaxialité, chiralité

Résumé : Le mode d'excitation collective exotique appelé chiralité a été étudié et des isomères de longue durée de vie ont été recherchés dans les noyaux ^{136}Nd et ^{135}Nd .

Cinq paires de bandes $\Delta I = 1$ presque dégénérées et de même parité ont été identifiées à des spins élevés dans ^{136}Nd . Les bandes observées ont été étudiées en utilisant la théorie de la fonctionnelle de densité covariante contrainte et rotation autour d'une axe incliné, et par un nouveau modèle de rotor plus particules développé pour décrire le couplage de particules dans quatre couches j à un rotor triaxial. Les propriétés de ces bandes doublet sont en bon accord avec les résultats des calculs théoriques. Par conséquent, l'existence de bandes chirales multiples ($M_{\chi}D$) dans le noyau ^{136}Nd a été établie. Il s'agit de la première preuve expérimentale de l'existence de bandes chirales dans des noyaux pairs. Les cinq paires de bandes chirales constituent le plus grand ensemble de bandes chirales observé jusqu'à présent dans un seul noyau. De plus, le schéma de niveaux de ^{136}Nd a été considérablement étendu aux spins bas, moyens et très élevés. Les configurations possibles de toutes les bandes rotationnelles ont été attribuées à l'aide du modèle Nilsson-Strutinsky en rotation. La

structure de ^{136}Nd a été clarifiée et les divers types d'excitations uni-particule et collectives ont été bien compris.

Une nouvelle paire de bandes chirales à parité positive a été identifiée dans ^{135}Nd . Les caractéristiques des bandes soutiennent leur interprétation en termes de bandes chirales. Des bandes chirales à parité négative ayant été identifiées précédemment, la présence de multiple bandes chirales dans ^{135}Nd est ainsi établie. Les bandes chirales observées ont été étudiées en utilisant la théorie avec fonctionnelle de densité covariante contrainte et avec le modèle rotor plus particules; elles reproduisent fidèlement les données expérimentales, confirmant ainsi le phénomène $M_{\chi}D$ dans ce noyau. Les bandes chirales nouvellement observées dans ^{135}Nd représentent une étape importante dans la confirmation de l'existence du phénomène $M_{\chi}D$ dans les noyaux.

La recherche d'états isomériques à longue durée de vie dans ^{135}Nd et ^{136}Nd a été aussi effectuée, mais n'a pas permis d'identifier de nouveaux isomères. Cependant, nous avons pu confirmer la présence des isomères déjà identifiés dans les noyaux ^{138}Nd , ^{134}Ce , ^{136}Pr , et ^{137}Pr dans nos données.

Title : Chirality in the ^{136}Nd and ^{135}Nd nuclei

Keywords : Nuclear spectroscopy, high-spin states, isomers, triaxiality, chirality

Abstract : The exotic collective excitation mode called chirality has been investigated and long-lived isomers have been searched for in the ^{136}Nd and ^{135}Nd nuclei. Five pairs of nearly degenerate $\Delta I=1$ bands with the same parity have been identified at high spins in ^{136}Nd . The observed bands were investigated by the constrained and tilted axis cranking covariant density functional theory and a new developed four single- j shells particle-rotor model. It was found that the properties of these doublet bands are in good agreement with results of the model calculations. Therefore, the multiple chiral doublets ($M_{\chi}D$) phenomenon in the nucleus ^{136}Nd was confirmed. This was the first experimental evidence for the $M_{\chi}D$ bands in even-even nuclei. The five pairs of chiral doublet bands is the largest observed in a single nucleus until now. In addition, the level scheme of the ^{136}Nd has been extended significantly at low, medium, and very high spins. Possible configurations of all rotational bands have been assigned by using the cranked Nilsson-Strutinsky model. The band structure of ^{136}Nd was clarified and the

various types of single-particle and collective excitations were well understood.

A new pair of positive-parity chiral doublet bands has been identified in ^{135}Nd . The characteristics of the doublet bands support the chiral interpretation. Together with the previously reported negative-parity chiral doublet bands show the presence of $M_{\chi}D$ bands in ^{135}Nd . The observed doublet bands were compared with constrained covariant density functional theory and particle-rotor model calculations which nicely reproduce the experimental data, confirming the $M_{\chi}D$ phenomenon in this nucleus. The newly observed $M_{\chi}D$ bands in ^{135}Nd represents an important milestone in supporting the existence of $M_{\chi}D$ in nuclei.

The search for long-lived isomeric states in ^{135}Nd and ^{136}Nd has also been performed. This did not lead to the identification of new isomers, but we could confirm the existence of the previously reported isomers in the nuclei ^{138}Nd , ^{134}Ce , ^{136}Pr , and ^{137}Pr in our data.

